UNIVERSITÀ DEGLI STUDI DI MILANO

DOTTORATO DI RICERCA IN SCIENZE DELLA TERRA

Curriculum "Sistema Terra: Processi e modellazione"

Ciclo XXXV

DIPARTIMENTO DI SCIENZE DELLA TERRA

QUASI STATIC GRAVITY SIGNATURES IN SLOW TECTONIC ZONES: ASSIMILATION OF NOVEL AEROSPACE DATA AND GEOPHYSICAL MODELING

GEO/10 – Geofisica della Terra Solida

Tesi di Dottorato di

Arcangela Bollino

Tutors

Chiar.ma Prof.ssa Anna Maria Marotta

Dott. Alessandro Regorda

Coordinatore del dottorato

Chiar.ma Prof.ssa Maria Iole Spalla

Anno Accademico

2021/2022

Contents

List of Figures

List of Tables

Abstract

The main aim of my Ph.D. research project was to investigate the gravitational signatures of the mechanisms that regulate slow rate tectonic deformation in areas where the earthquakes enucleate. 2D thermo-mechanical numerical models are used to simulate the crust-mantle dynamics; in particular, complexities such as compositional stratification of crust-lithosphere system, mantle hydration, phase changes and degree of plate coupling are investigated, exploring how they affect the gravity field and its rate of change in different tectonic environments.

A strongly integration between modelling, gravitational and GNSS (*Global Navigation Satellite System*) data has provided valuable constraints to the analysis. In fact, this work is part of the GravSeis-Gravitational Seismology project, an ESA-founded research project whose objective is to establish a theoretical framework for the detection and characterization of earthquake precursors based on the observations of the gravitational field made by satellite. Gravitational Seismology concept expresses the idea that earthquakes are not generated only by surface displacements but are closely connected to deep masses redistribution involved in the subduction systems. This rearrangement generates density anomalies, which in turn are responsible for the Earth's gravity field anomalies.

A first study has been conducted on the Sumatra and Mariana complexes, representative of the two major types of subduction: ocean–continent and ocean–ocean, respectively. In a first phase, a set of numerical tests has been developed, varying three main parameters:

prescribed subduction velocity, prescribed subduction dip angle and degree of plate coupling, exploiting how their variation affect the gravity pattern.

In a second phase, the study of the EIGEN-6C4 gravitational disturbance patterns of the Sumatra and Mariana subductions has been carried out, allowing to strengthen the analysis of the gravitational signature in ocean–continent and ocean–ocean subductions in terms of the physics of the processes occurring during the convergence of the plates. Model predictions show a good agreement with gravity data, both in terms of wavelengths and magnitude of the gravity anomalies measured in the surroundings of the Sumatra and Marina subductions, supporting that the differences in the style of the gravity anomaly observed in the two areas are attributable to the different environments – ocean-ocean or ocean-continental subduction – that drives a significantly different dynamic in the wedge area.

A second study has been carried out developing 2D finite-element thermo-mechanical models, in which the formation of oceanic crust and serpentinite due to the hydration of upwelling mantle peridotite is implemented, to simulate the evolution of the Gulf of Aden from the rift initiation to the development of an active oceanic spreading center.

The thermo-mechanical analysis support the hypothesis that the Gulf of Aden developed as a slow passive rift in thin lithosphere with thick crust and that the variations in features along the passive margins could be related to lateral variations in the amount of H_2O in the mantle, which determines the different times of mantle melting.

Chapter 1

GravSeis - Gravitational Seismology project

GravSeis is an ESA-funded research project led by Università degli Studi di Milano that aims to present a theoretical framework by which the Solid Earth processes leading to earthquakes can be recognized and interpreted from their gravity field signature as detected by satellites. The project expresses the idea that to fully understand the genesis of earthquakes it is necessary to have information from the deep masses redistribution and not to be limited to the displacements of the Earth's surface derived from seismometers and GNSS systems (Global Navigation Satellite System). In fact, every physical process that occurs within our planet includes both superficial displacements and deep mass redistributions. This rearrangement generates density anomalies, which in turn are responsible for the Earth's gravity field anomalies, according to Newton's law of gravitation.

The proposed approach builds on a method developed in recent years at the Università degli Studi di Milano, combining the physico-mathematical modelling of active tectonics and of the seismic cycle with geodetic data to constrain the mechanisms responsible for crustal deformation and stress accumulation. Distinctive time-varying gravity and geoid signals applied to the active tectonic processes (subduction, collision, extension) leading to earthquakes of different characteristics (thrust, normal and/or strike slip) throughout the

whole earthquake cycle, is categorized by a time scale and characteristic wavelength.
This global approach has already been successfully applied to the *a posteriori* detection of very large magnitude earthquakes (Mw = 9) with GOCE (*Gravity field and steady-state Ocean Circulation Explorer*) and GRACE (*Gravity Recovery and Climate Experiment*) data. Here, the main challenge will be to extend the method to lower magnitude earthquakes (Mw = 6 to 9) and adapt it to the Next Generation Gravity Mission (NGGM) type of data.
The GravSeis team is made up of the geophysics of Solid Earth research group of the Department of Earth Sciences "A. Desio "of the Università degli Studi di Milano, Thales Alenia Space, and the research group of the Institute of Geodesy of the University of Stuttgart. In particular, the research group of the Università degli Studi di Milano is involved in quantifying the signature that seismotectonic processes and earthquakes leave in the gravity field. Furthermore, it assists both Thales Alenia Space in fine-tuning the space mission to determine the gravity's changes with the utmost precision, and the University of Stuttgart in optimizing the software necessary to transform the raw data, provided by Thales Alenia Space, into the gravitational signal, to be compared with the signature of seismotectonic and earthquakes.

1.1 From GRACE to NGGM: between past and future

Earthquakes have been studied for a long time by means of seismometers recording the elastic waves travelling through the interior of our planet and, more recently, by means of GNSS and Synthetic Aperture Radar surveys, measuring surface displacements. This technique provides additional information on earthquakes, as well as on those solid Earth processes responsible for them, such as subduction, collision, and extension and the inter-seismic strain accumulation. This instrumentation is deployed over land and thus misses the seas, often surrounding regions where large earthquakes occur. This limitation is nowadays overcome by space gravity missions, thanks to their uniform coverage of the Earth, both inland and offshore. In fact, gravity constrains the motion of Earth's satellites, both natural and artificial. The study of the perturbations of the orbits of artificial satellites provided the first source of detailed information about the gravitational field. Measurement of the gravity field reveals Earth's state of mass balance and its dynamics and provides the geoid as

reference for sea level, global ocean circulation and height systems, and the variations of gravity and of the geoid provide information on mass exchange processes in the Earth system. Therefore, spaceborne gravimetry is a well-established tool of today's Earth Observation from space.

The first dedicated geodesy satellite, the Laser Geodynamics Satellite (LAGEOS), was launched in 1976 (*Tapley et al*., 1985) and its orbital path is precisely reconstructed via laser ranging.

Sampling the field with high spatial and temporal resolution requires very low altitude satellites and sophisticated measurement techniques, like satellite-to-satellite (SST) tracking and gravity gradiometry, studied since the Seventies (e.g., *Williamstown Report*, 1969; *Bender*, 1991; *Wells*, 1984). SST is the technique of choice for recovering the tiny time variable gravity field signal (*Silvestrin et al*., 2012). In this approach the ‘‘gravity sensor" consists of a pair of satellites flying in loose formation on a low Earth orbit (Figure 1.1).

With the Low-Low Satellite-to-Satellite Tracking (LL-SST), the Earth gravity field is determined from the distance variation between the centres of mass of two satellites (COMs) produced by the gravity acceleration, Δd_G, formally obtained as:

$$\Delta d_G = \Delta d - \Delta d_D$$

where:

- Δd is the total distance variation between the COMs, whatever the source, measured by a distance metrology,
- Δd_D is the distance variation produced by non-gravitational forces (mainly atmospheric drag, i.e., the atmospheric force acting opposite to the relative motion of the satellites) on the satellite COMs along the line joining the COMs themselves.

Therefore, the distance variation between the satellites and their non-gravitational accelerations, measured respectively by a laser interferometer (with nanometer resolution) and by ultra-sensitive accelerometers (of the same class of those embarked on GOCE), are the fundamental observables from which the Earth's gravity field anomalies are retrieved (*Dionisio et al*., 2018).

GRACE, a joint project between the *National Aeronautics and Space Administration* (NASA) and the *Deutsches Zentrum für Luft und Raumfahrt* (DLR), applied for the first

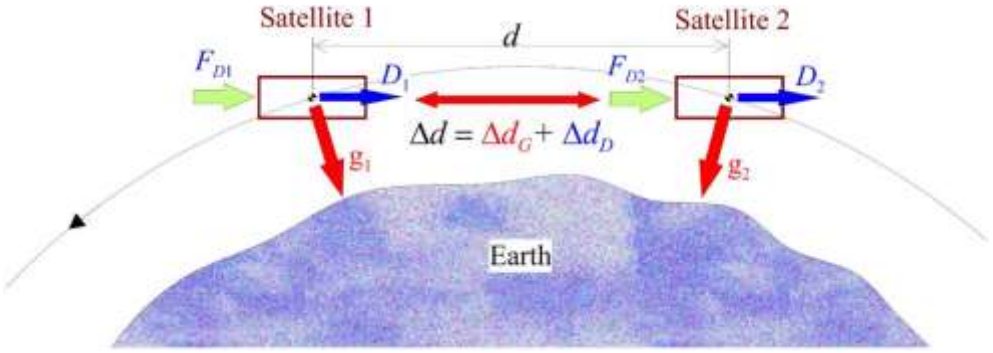

Figure 1.1: Principle of the SST technique (from *Cesare et al*., 2016).

time the SST tracking in low Earth orbit for measuring Earth's gravity using a microwave ranging instrument. In orbit from 2002 to 2017, GRACE consists of two identical spacecraft flying about 220 km apart in a near-polar orbit initially about 500 km high (*Cesare et al*., 2016), providing monthly estimates of Earth's global gravity field at scales of a few hundred kilometers and larger. The time variations in the gravity field were used to determine changes in Earth's mass distribution, with applications ranging from measurement of continental water content (seasonal changes in large river basins, groundwater extraction), to ice and snow accumulation and depletion in the polar regions and large glaciers, to monitoring of global mean eustatic sea-level variations. After GRACE proved the potential of satellite gravity missions for monitoring geodynamic processes, a large user community was formed: GRACE Follow-On, launched in 2017, provided data continuity with quality similar to GRACE (*Cesare et al*., 2016).

From its foundation, the European Space Agency (ESA) has been at the forefront of research into gravity estimation by satellite. The design, implementation and launch of GOCE, the first satellite to carry a gravity gradiometer in orbit, is its crowning achievement so far in this field.

GOCE, which flew between 2009 and 2013, delivered a gravity map of Earth with accuracy of 2-3 cm for the geoid and 0.7 mGal for the gravity anomalies, at spatial resolution of 100 km. GOCE's instruments measured full tensor gravity gradients (four high accuracy components, two of lower quality) and GPS positions while orbiting at mean orbit altitudes of 255 km (nominal mission) and 225 km (extended mission), in drag-free mode *(Cambiotti et al*., 2020). During the development of GOCE, ESA started preparatory studies for the

NGGM mission. While GOCE aimed to provide a high-resolution static map of the Earth's gravity, the objective of NGGM is long-term monitoring of the time-variable gravity fieldwith high temporal and spatial resolution, by SST technique. This allowed the investigation and monitoring of geophysical phenomena involving mass distribution and transport in the atmosphere, continental hydrosphere, oceans, cryosphere, and lithosphere.

Therefore, the scientific objectives for NGGM are the measurement of the geoid with an accuracy of 1 mm at a spatial resolution of 500 km every 3 days and 150 km every 10 days (*Haagmans et al*., 2020). The NGGM concept is thus expected to improve both spatial and temporal resolution of the time-variable gravity field with respect to previous and present missions. The key to improved the performance lies in implementing the range sensor at optical rather than microwave frequency, and in the selection of appropriate orbits enabling to exploit at best the techniques devised for reducing the effect of the temporal aliasing errors (*Cesare et al*., 2016).

The NGGM mission and system design will build on the experience of GOCE (in particular for the design of the attitude and orbit controls), GRACE (for the utilization of the SST measurement technique between two spacecrafts flying in low Earth orbit) and GRACE Follow-On (GRACE-FO) (for the utilization of the laser interferometry as inter-satellite metrology). The temporal resolution in sampling Earth's gravity is enhanced by having different satellite configurations. The simplest mission scenario for NGGM consists of a single pair of satellites flying on the same orbit, with different true anomalies (''in-line" or ''pearl string" formation, left panel of Figure 1.2). The in-line formation samples the gravity field in the along-track direction only. On a polar orbit, this formation is more sensitive to gravity field variations (and mass transport) in the North–South than in the East–West direction, producing an anisotropic signal structure leading to the North–South striations noted in the GRACE solutions (*Cesare et al*., 2016). In more complex scenarios, the two satellites fly on intersecting orbits with slightly different inclination or longitude of ascending node (''pendulum" formation) or slightly different eccentricity (''cartwheel" formation) as shown in Figure 1.2, capturing alternately both cross-track and along-track gravity signals.

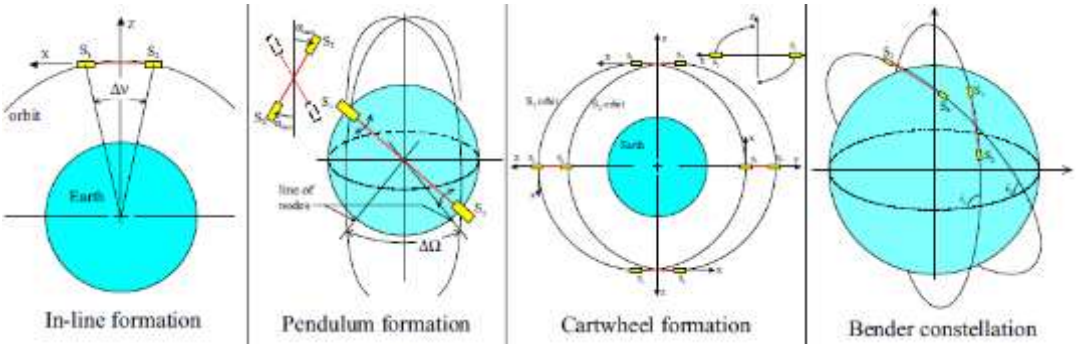

Figure 1.2: Satellite orbital configurations for NGGM (from Cesare *et al*., 2016).

However, the benefits on the gravity field retrieval brought by these scenarios are outweighed by their impacts on the design of the spacecraft and in particular its payload. Moreover, to increase the global coverage frequency (and therefore the temporal resolution of the gravity field monitoring), there are no alternatives than add more satellite pairs to the constellation.

To overcome these limitations, Bender *et al*., (2008) proposed the so-called Bender constellation consisting of two pairs of in-line satellites: one pair in a near-polar orbit (~88°) and one pair in a medium inclination orbit (~66°) (right panel of Figure 1.2) with an altitude of around 350 km (*Dionisio et al*., 2016). By using two pairs of satellites, a homogenous coverage of the Earth is achieved in a short time, sampling simultaneously the gravity fields in North–South and East–West directions at higher temporal frequency. This leads to a substantial reduction of spatial and temporal aliasing and of the anisotropic errors in the retrieval of gravity field models. The distance between the satellites forming a pair is 100 km, which was identified in simulations to be optimal, also noting that the laser ranging noise increases with the distance (*Haagmans et al*., 2020).

The contribution of the Gravitational Seismology project consists in providing information about the intensity of the gravitational signal and its rate of change over time, in order to make known to what extent both the tectonics and the different phases of earthquakes can be detected by the instrumentation of the NGGM.

1.2 Gravity disturbance and origin of gravity anomalies

Anomalies in the Earth's gravitational field play important roles in both geodesy and geophysics. In geodesy, they are used to define the figure of the Earth, notably the geoid (the equipotential surface of the Earth's gravity field that corresponds most closely to mean sea level). In geophysics, gravity anomalies are used to deduce variations in mass-density and hence subsurface geological structures for a wide variety of applications. Hence, geophysicists are usually only interested in the gravitational component of the observed gravity because it reflects the Earth's internal density distribution.

Considering a point mass *m*' at a point P located outside the Earth, and a small infinitesimal element of mass *dm* in position Q inside the Earth (Figure 1.3), the gravitational force df_m exerted by *dm* on *m*' is given by the Newton's law of gravitation and has intensity equal to:

$$df_m = G\frac{m'dm}{b^2} \tag{1.1}$$

where G= 6.6732×10^{-11} Nm^{2}kg^{-2} is the gravitational constant and *b* is the distance from *Q* to *P* (Figure 1.3).

The infinitesimal gravitational acceleration dg_m in *P*, produced by *dm*, is given by:

$$dg_m = \frac{df_m}{m'} = G\frac{dm}{b^2} \tag{1.2}$$

If the mass distribution within the Earth were known, the whole gravitational attraction of the Earth, on *m'*, would be obtained by integrating dg_m over the entire mass distribution as follow:

$$g_m = G\int\frac{dm}{b^2} \tag{1.3}$$

The element with mass *dm* can be expressed as the product between the volume *dV* and the density ρ of the element:

$$dm = \rho \cdot dV \tag{1.4}$$

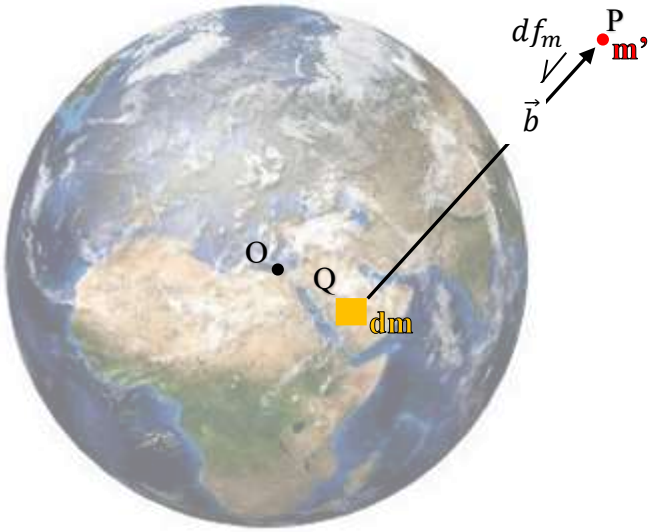

Figure 1.3: Gravitational force df_m exerted by an Earth's infinitesimal element of mass dm on a mass m 'placed at a point P external to the Earth.

It follows that:

$$g_m = G \int \rho \frac{dV}{b^2} \tag{1.5}$$

Therefore, a variation of the density $\Delta\rho$ within the volume V produces a variation of the gravitational acceleration expressed as:

$$\Delta g_m = G \int \Delta\rho \frac{dV}{b^2} \tag{1.6}$$

In particular, positive density anomalies generate positive gravity anomalies, while negative density anomalies generate negative gravity anomalies.

The gravity vector $\mathbf{g}_P$ acting on the unit of mass is defined as the gradient of the scalar *gravity potential*, which is the sum of a gravitational potential and a centrifugal potential. The Earth's gravity field is traditionally approximated by the gravity field of a reference ellipsoid (or level ellipsoid). This model is rigid and geocentric, with a minor axis c that coincides with the mean rotation axis Z of the Earth. The ellipsoid has the same total mass as the Earth (including the atmosphere), the same angular velocity, and its limiting surface coincides with a particular equipotential of its own gravity field.

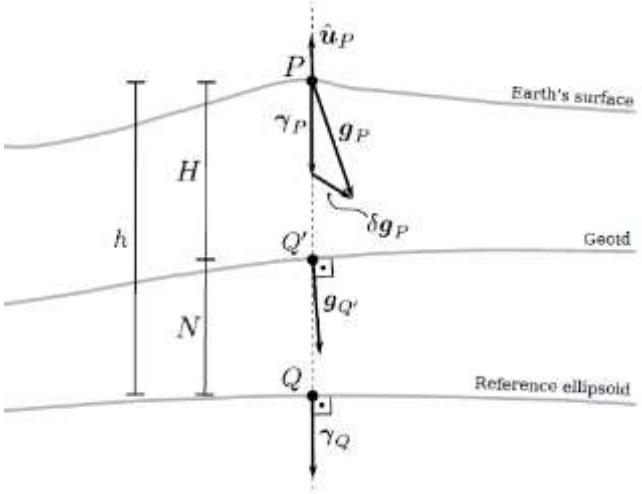

Figure 1.4: Parameters used to define gravity anomalies and gravity disturbances. $\mathbf{g}_P$ is the gravity vector; $\boldsymbol{\gamma}_P$ is the normal gravity vector; $\delta\mathbf{g}_P$ is the gravity disturbance vector. H and N are the orthometric and geoidal height, respectively. The dashed line passing through Q, Q' and P is normal to the surface of the reference ellipsoid at Q (from *Oliveira et al*., 2018).

This reference ellipsoid is called *normal Earth*. The *normal gravity vector* is the sum of the gravitational and centrifugal accelerations exerted by the normal Earth on a body at rest at a point P. The intensity of the normal gravity vector is called *normal gravity*.

Considering $\boldsymbol{\gamma}_P$ and $\mathbf{g}_P$ the *normal gravity vector* and the *Earth's gravity vector* (corrected from non-gravitational effects due to vehicle motion and time variations such as Earth tides and instrumental drift), the difference between $\mathbf{g}_P$ and $\boldsymbol{\gamma}_P$, which are located at the same point P, is the *gravity disturbance vector* (*Oliveira et al*., 2018) (Figure 1.4):

$$\delta\mathbf{g}_P = \mathbf{g}_P - \gamma_P \tag{1.7}$$

Because the centrifugal parts of both the normal gravity vector and the Earth's gravity vector are equal, the gravity disturbance vector $\delta\mathbf{g}_P$ represents a purely gravitational effect.
The *gravity disturbance* is defined by the difference between the magnitude of the gravity vector $g_P = \|\mathbf{g}_P\|$ and the normal gravity vector $\gamma_P = \|\boldsymbol{\gamma}_P\|$ at the same point:

$$\delta g_P = g_P - \gamma_P \tag{1.8}$$

The normal gravity vector value is computed by correcting the magnitude of normal gravity from the surface of the ellipsoid to the point of interest. This is simply the upward application of the free-air correction over the ellipsoidal height (*Hackney and Featherstone*, 2003), as explained below.

The difference between the gravity vector at a point Q' on the geoid (a particular equipotential surface of the gravity potential) and the normal gravity vector at a point Q on the surface of the ellipsoid, both located at the same geodetic latitude and longitude, is the *gravity anomaly vector* (*Oliveira et al*., 2018):

$$\Delta\mathbf{g} = \mathbf{g}_{Q'} - \gamma_Q \tag{1.9}$$

Therefore, similarly to Equation (1.8), it is possible to define the *gravity anomaly*:

$$\Delta g = g_{Q'} - \gamma_Q \tag{1.10}$$

where $g_{Q'}$ is the magnitude of the gravity vector on the geoid, and γ_Q is the magnitude of the normal gravity vector on the reference ellipsoid (*Oliveira et al*., 2018) (Figure 1.4).

The gravity anomaly is not defined at a particular point but it depends only on longitude and latitude and is not a function of height. Because gravity and normal gravity are located at different points, the gravity anomaly is a combination of gravitational and centrifugal effects, rather than purely gravitational effects like the gravity disturbance.

Different approximations (called gravity reductions) for the gravity anomaly can be calculated depending on the corrections applied to them. The *free-air anomaly*, for example, can be defined as:

$$\Delta g^F = g_P - \gamma_Q - \frac{\partial\gamma}{\partial h} H_P \tag{1.11}$$

where the rightmost term is called the free-air correction, $\frac{\partial\gamma}{\partial h} \approx 0.3086$ mGal/m is the derivative of the normal gravity with respect to the geometric height h, and H_P is the orthometric height (i.e., with respect to the geoid) of point P (*Oliveira et al*., 2018) (Figure 1.4). The free-air correction can be interpreted as a downward continuation of g_P to the geoid or as an upward continuation of Q to a height H_P .

The Bouguer correction can be applied to the free-air anomaly to remove the gravitational effect of the topographic masses between the observation point P and the point on the geoid Q'. The Bouguer anomaly is defined in the continents as:

$$\Delta g^B = g_P - \gamma_Q - \frac{\partial\gamma}{\partial h} H_P - 2\pi G \rho_t H_P \tag{1.12}$$

where ρ_t is the density of the topographic masses.

The Bouguer correction approximates the gravitational effect that all topographic masses above the geoid exert on point P by the effect of a homogeneous, infinitely extended slab of constant density ρ_t and thickness H_P (*Hackney and Featherstone*, 2003).

Chapter 2

The *SubMar* code

The use of numerical modelling in geosciences has transformed our understanding of the planet Earth, providing a powerful tool to investigate processes in the Earth's crust, mantle and core that are not directly observable.

Within computational geodynamics, a numerical model refers to a specific set of physical equations, which are discretised and solved numerically with initial and boundary conditions. In fact, a numerical model can be obtained by the resolution of discrete problems, such that the solution is determined dividing the system in a finite number of elements, or of continuous problems, for which problems can be solved by mathematical techniques. There are different methods of discretisation, developed by both engineers and mathematics, and all of them imply an approximation of the continuous system, which get better with the increase of the discrete variables. In particular, mathematics has developed a finite difference method, while engineers a finite element method (*Zienkiewicz and Taylor*, 2000). The *SubMar* code used in this work (Marotta *et al*., 2006 and successive upgrading in *Roda et al*., 2010 and *Regorda et al*., 2017) is based on the finite element method.

2.1 Governing equations of the *SubMar* code

The dynamics of the crust and mantle system are governed by the continuity, momentum and energy equations, which can be expressed as follows:

$$\frac{\delta p}{\delta t} + \nabla \cdot (\rho \boldsymbol{u}) = 0 \tag{2.1}$$

$$-\nabla p + \nabla \cdot \boldsymbol{\tau} + \rho \mathbf{g} = 0 \tag{2.2}$$

$$\rho C_p \left(\frac{\delta T}{\delta t} + \boldsymbol{u} \cdot \nabla T \right) = \nabla \cdot (K \nabla T) + H \tag{2.3}$$

where **u** is the velocity, p is the pressure, $\boldsymbol{\tau}$ is the deviatoric stress, ρ is the density, $\boldsymbol{g}$ is the gravity acceleration, C_p is the heat capacity at constant pressure, T is the temperature, K is the thermal conductivity and H is the total internal heating per mass unit.

Mantle dynamics is controlled by heat transfer, and the mantle properties are normally functions of temperature. The variations in density due to temperature variations are generally small and yet are the cause of the mantle motion. If the density depends only on temperature, the fluid can be assumed to be incompressible. Therefore, the density can be treated as constant ($\rho = \rho_0$) in the continuity Equation (2.1) and in the energy Equation (2.3), while it must be treated as a variable only in the gravitational (buoyancy) term of Equation (2.2) such that:

$$\rho = \rho_0 \left(1 - \alpha (T - T_0)\right) \tag{2.4}$$

where ρ_0 is the density at a reference temperature T_0 and α is the coefficient of thermal expansion. Equation 2.1 can be written as:

$$\nabla \cdot u = 0 \tag{2.5}$$

This simplification is known as the *Boussinesq approximation*.

2.2 Penalty formulation

In order to impose the incompressibility constraint, the penalty method is used thus allowing the elimination of the pressure variable from the momentum equation (resulting in a reduction of the matrix size).

The penalty formulation of the mass conservation equation is based on a relaxation of the incompressibility constraint and writes:

$$\nabla \cdot u + \frac{p}{\lambda} = 0 \tag{2.6}$$

where λ is the penalty parameter, which should be 6-7 orders of magnitude larger than the shear viscosity to ensure that mass conservation is satisfied (*Thieulot*, 2014).

The Sewell (1981)'s approach has been followed fixing $\lambda = \mu\sqrt{r_p}$ where r_p denotes the machine relative precision and μ is interpreted as a bulk viscosity (*Hughes et al.,* 1979; *Donea and Huerta*, 2003*; Marotta et al.,* 2006).

The deviatoric stress tensor in Equation 2.2 can be written in terms of the strain rate tensor as $\tau = 2\eta\dot{\epsilon}$, with $\dot{\epsilon} = \frac{1}{2}(\nabla \mathrm{v} + (\nabla v)^T)$. Therefore, Equation 2.2 can be written as:

$$-\nabla p + \nabla \cdot \left(\eta(\nabla v + (\nabla v)^T)\right) + \rho g = 0 \tag{2.7}$$

Finally, using pressure from Equation 2.6, Equation 2.7 can be written as:

$$\lambda \nabla(\nabla \cdot v) + \nabla \cdot \left(\eta(\nabla v + (\nabla v)^T)\right) + \rho g = 0 \tag{2.8}$$

To support large viscosities variations the penalty parameter is related to the effective elemental viscosity by means of a dimensionless coefficient, so that $\lambda = \lambda_e(e)\eta_{eff}(e)$ (*Marotta et al*., 2006).

2.3 Extended Boussinesq approximation

If density variations depend not only on temperature variations but also on pressure variations as considered herein, then compressibility must be taken into account. Accounting for compressibility can be achieved by using either the *extended Boussinesq approximation* or the anelastic approximation (*Gerya*, 2010; *Ismail-Zadeh and Tackley*, 2010). In the *SubMar* code the compressibility is achieved by using the *extended Boussinesq approximation.* In fact, the algorithm contemplates phase transitions both for the mantle and for all the lithologies considered for the crust (as explained in Appendix A), which introduce two main effects to be included in numerical models: variations in density, and latent heat release or absorption that is required by the extended Boussinesq approximation. Consequentially, in the extended Boussinesq approximation, the density is still assumed

constant in the continuity Equation but the effects of density variations on buoyancy force in the momentum Equation (2.8) are taken into account considering effective coefficient of thermal expansion (*Ismail-Zadeh and Tackley*, 2010). Similarly, effects of latent heat in the energy Equation (2.3) are taken into account by considering effective specific heat and coefficient of thermal expansion (*Christensen and Yuen*, 1985; *Gerya*, 2010; *Ismail-Zadeh and Tackley*, 2010).

In the energy Equation (2.3) the internal heating per mass unit can be expressed as follows:

$$H = H_r + H_s + H_a \tag{2.9}$$

where H_r is the radiogenic heating, $H_s = \tau_{ij}\dot{\varepsilon}$ is shear heating and $H_a = T\alpha\frac{Dp}{Dt}$, where α is the thermal expansion coefficient, is the adiabatic heating per mass unit (e.g., *Christensen and Yuen*, 1985; *Gerya*, 2010; *Ismail-Zadeh and Tackley*, 2010; *Thielmann and Kaus*, 2012).

2.4 Rheology

The model combines a linear viscous rheology for the sublithospheric mantle with a linear viscoplastic rheology for the lithosphere. To this purpose, for each material type *i*, we compute the following two viscosities:

$$\mu_i^{viscous} = \mu_{0,i} \cdot e\left[\frac{E_i}{R}\left(\frac{1}{T} - \frac{1}{T_0}\right)\right] \tag{2.10}$$

where $\mu_{0,i}$ and E_i are the reference viscosity at the reference temperature T_0 and the activation energy, respectively, for material type *i*:

$$\mu_i^{plastic} = min[\mu_1, \mu_2, \mu_3] \tag{2.11}$$

with μ_1, μ_2 and μ_3 computed combining the Byerlee's law criterion and the Tresca criterion as implemented in *Regorda et al.,* (2017):

$$\mu_1 = \frac{\sigma_y - p}{2\dot{\varepsilon}_1};\ \mu_2 = \frac{\sigma y - p}{2\dot{\varepsilon}_2};\quad \mu_2 = \frac{\sigma y}{2(\dot{\varepsilon}_1 - \dot{\varepsilon}_2)}, \tag{2.12}$$

where p is the pressure, ϵ_1, ϵ_2, ϵ_3 are the principal strain rates and σ_y is the yield stress, defines by the simplified formulation of Bayerlee's law criterion, $\sigma_y = \beta \cdot \gamma$, with β= 40 MPa km^{-1} (in compressive tectonic setting) and β= 16 MPa km^{-1} (in extensional tectonic setting) and y depth in kilometres. Outside the lithosphere, the effective viscosity is then calculated as follows:

$$\mu^{effective} = \mu_{viscous}. \tag{2.13}$$

Within the lithospheric layer the effective viscosity is instead defined as follows:

$$\mu^{effective} = min\left[\mu_i^{viscous}, \mu_i^{plastic}\right]. \tag{2.14}$$

Table 2.1 lists the values of the material and rheological parameters used in the analysis. Instantaneous erosion/sedimentation mechanism is simulated as in *Roda et al.,* (2010) by using the substitution technique, in which all the crustal particles lying above a prescribed height (h_t in Table 4.1) are replaced with air particles and, at the same time, an equal number of water particles buried into the trench region are transformed into sediments. This procedure reproduces an erosion and sedimentation rate variable in time, as function of the system dynamics. Further details can be found in *Roda et al.,* (2010).

2.5 Lagrangian markers

Elemental properties (density, viscosity, thermal conductivity, specific heat and thermal expansion) needed to solve Equations 2.2, 2.3 and 2.5 are related to the composition of each element, determined by means of Lagrangian markers that are characteristic of different materials in the domain. To compositionally differentiate the different types of materials, the marker-in-cell technique (e.g., *Christensen*, 1992) has been used.

At the beginning of the evolution, the markers are spatially distributed and identified by different code are to define the upper and lower oceanic crust, the upper and lower continental crust and the continental mantle. During the evolution of the system, each particle (marker) is advected using a fourth-order (both in time and in space) Runge–Kutta scheme. At each time the elemental density of each type of particle defines the composition of each element of the grid, C^e, such as:

$C^e = \sum_i C_i^e$,

where:

$C_i^e = \frac{N_i^e}{N_0^e}$,

	Continental crust		Oceanic crust		Sediments	Mantle	Serpentine	Air	Water
	Upper	Lower	Upper	Lower					
Lithology									
	Granite	Diorite	N-MORB Mid-Atlantic Ridge		Mica-schists	Dunite	Serpentine		
Density ρ (kg · m^{-3})	*pc*	*pc*	*pc*		*pc*	*pc*	3000	1.18	1000
Conductivity K (W · m^{-1} · K^{-1})	3.03		2.1		3.03	4.15	4.15	0.026	0.600
Heat production H (μW · m^{-3})	2.5		0.4		2.5	0.002	0.002	0	0
Rheology									
	Dry granite		Dry diabase		Dry granite	Dry dunite	Serpentinite	Sticky air/ water	
Activation energy E (kJ · mol^{-1})	38.4		103.2	103.2	38.4	130.2	0	0	
Reference viscosity μ_0 (Pa · s)	3.47· 10^{21}		1.61·10^{19}	1.61·10^{22}	3.47· 10^{20}	5· 10^{20}	10^{19}	10^{19}	
Based on	a, d, f, l		a, b, c, f, l	a, b, c, f, l	a, d, f, l	c, d, e, f, j	d, f, g, h, i	m	

Table 2.1: Values of the material and rheological parameters used in the analysis. References: (a) *Ranalli and Murphy*, (1987); (b) *Afonso and Ranalli*, (2004); (c) *Kirby*, (1983); (d) *Haenel et al.,* (1988); (e) *Chopra and Peterson*, (1981); (f) *Dubois and Diament*, (1997) and *Best and Christiansen*, (2001); (g) *Roda et al.,* (2011); (h) *Schmidt and Poli*, (1998); (i) Gerya and Stockhert, (2006); (j) Roda *et al.,* (2012); (k) *Gerya and Yuen*, (2003); (l) *Borghesan*, (2011); (m) *Schmeling et al.,* (2008). *pc*: Perple*X* derived.

where N_i^e and N_0^e are the number of particles of type *i* within element *e* and the maximum number of particles of any type that the element *e* contains, respectively. Each elemental property P^e (conductivity, specific heat at a constant pressure, density and viscosity) depends on the composition such that within each element *e*, P^e can be expressed as follows:

$$P^e = P_m \left[1 - \sum_i C_i^e \right] + \sum_i P_i \, C_i^e \tag{2.15}$$

where P_m and P_i are the property for mantle and for any particles of type i, respectively.

Chapter 3

Subduction zones

3.1 General features of subduction zones

Subduction zones, where the old and dense oceanic lithosphere sinks into the mantle, are complex regions of the Earth with challenging physical and chemical processes that impact on the global geodynamics, geochemistry, and thermal evolution of the planet. They represent a total of 55.000 km of the Earth's plate boundaries (*Lallemand*, 1999) and the most seismically active regions on Earth, producing 90% of the world's earthquakes both in terms of numbers and in quantity of seismic energy released (*Gutscher*, 2016) (Figure 3.1).

Although the term subduction is used interchangeably with convergent (destructive) plate margin or island arc, and while all three terms are intimately related, they are not synonymous. In fact, subduction zones (Figures 3.2 and 3.3), which are the three-dimensional manifestation of convective downwelling, are formally distinct from convergent plate margins, being, the latter, the surficial manifestations of downwelling (*Stern*, 2002). Further, convergent plate margins are required by plate tectonics, which is the motions of rigid spherical shells around the Euler pole of rotation, whereas none of the geometric rules of plate tectonics applies to the behavior of the lithosphere once it descends below the surface (*Stern*, 2002). Subduction zones are also distinct from arc-trench complexes that are the consequences of subduction zone processes preserved in the

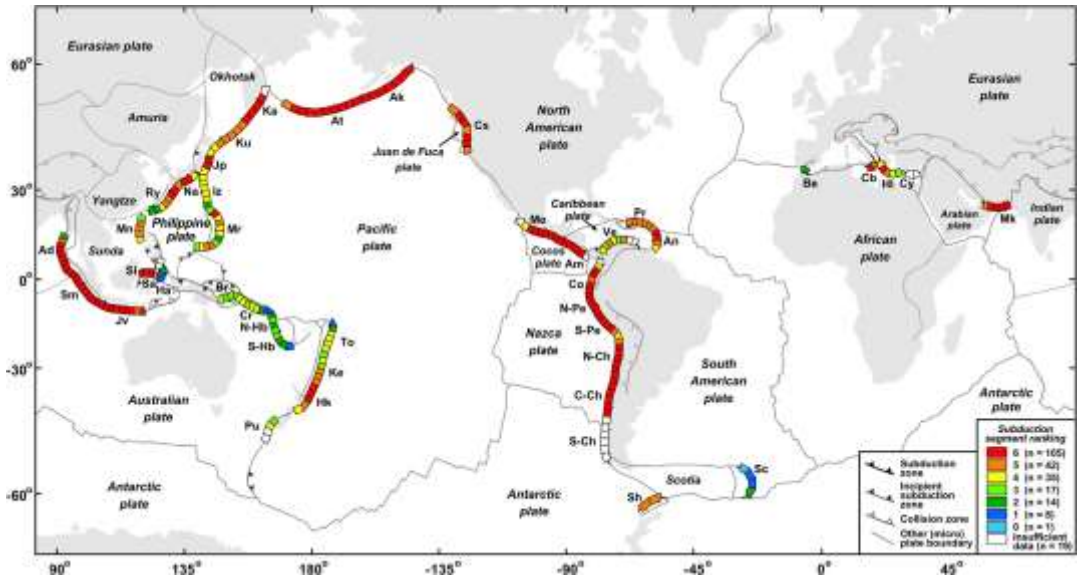

Figure 3.1: Map of convergent margins and active subduction zones on the Earth. The colored segments represent the 200 km trench that have been ranked in terms of their predicted capability of generating a giant subduction zone earthquake with MW > 8.5 (from *Schellart and Rawlinson*, 2013).

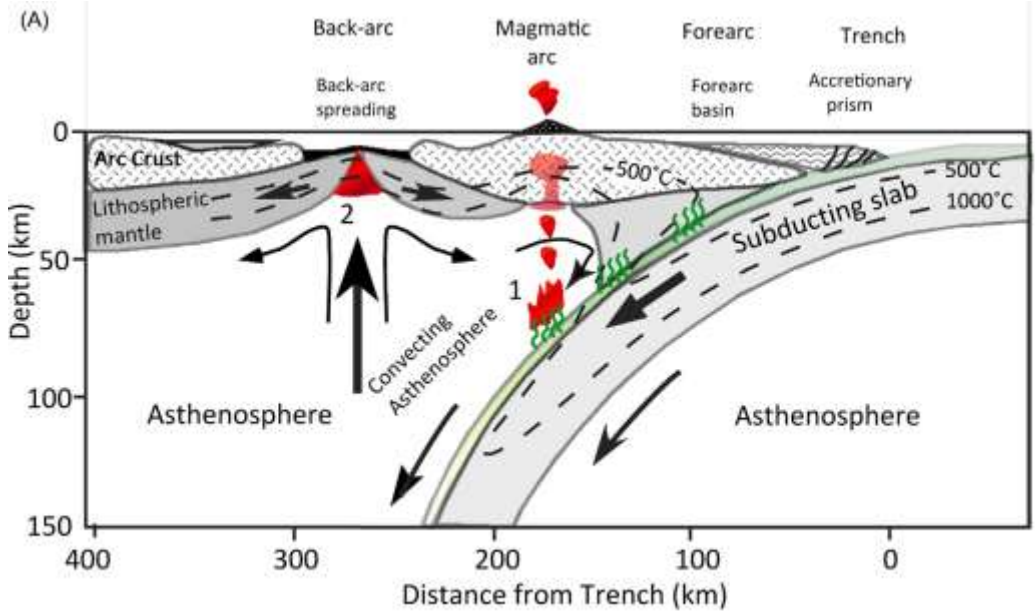

Figure 3.2: Schematic cross-section through the upper 140 km of a subduction zone, showing the principal crustal and upper mantle components and their interactions (from *Sen*, 2014).

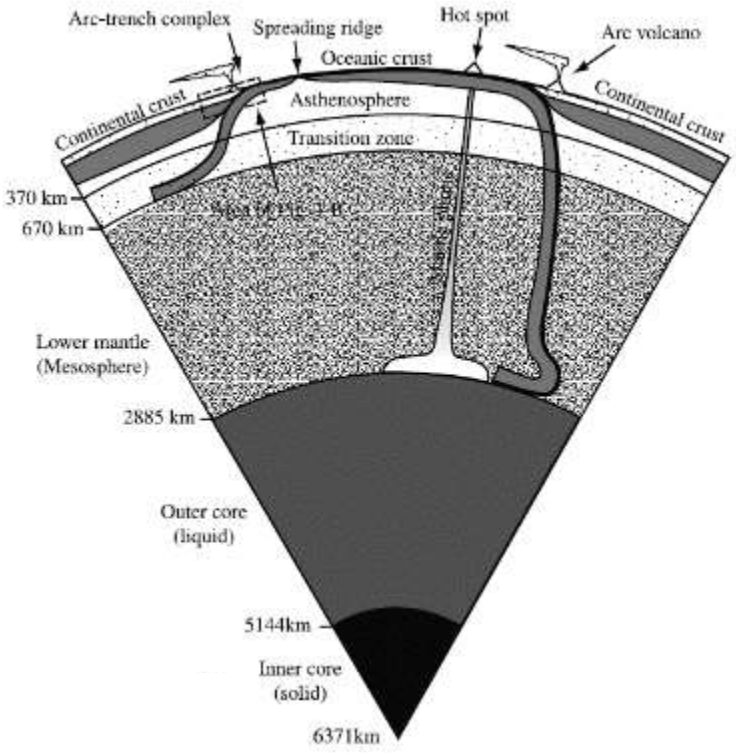

Figure 3.3: Vertical sketch of the Earth which shows better the scale of subduction zones. It shows both the subducted plates stagnating at the transition zone and the subducted plates sank to the core-mantle boundary (from *Stern*, 2002).

overlying crust and in the geological evidence of deformation and chemical recycling caused by subduction (*Stern*, 2002). Although arcs are a relatively minor components of subduction zones in terms of mass, they are important because they provide accessible samples of the products of interacting mantle and subducted materials and testify to the operation of ancient subduction zones (*Stern*, 2002).

The process of subduction is largely driven by subducted slabs of oceanic lithosphere in the underlying asthenosphere, as a consequence of the cooling and the relative increase of density, that occurs during the drifting from the positive thermal anomaly in the mid-ocean ridges. In fact, the subsidence of the ocean floor is proportional to the square root of the age. It is widely accepted that the mantle lithosphere is slightly more dense than underlying asthenosphere by 1–2%, and it is this excess density that powers subduction zones and moves the plates (*Stern*, 2002). However, the basic tenet of plate tectonics have been challenged by recent studies that have raised the possibility that even mature oceanic plates remain buoyant because chemical buoyancy is too high to be overcome by negative thermal buoyancy

(*Korenaga and Korenaga*, 2016).

The potential energy that is released during sinking is used primarily to drive flow in the mantle, to move and deform the tectonic plates, and to deform the slab. Part of this potential energy is also used to overcome resistance at the subduction zone fault plate boundary, where part of the energy is released during interplate subduction zone thrust earthquakes (*Schellart and Rawlinson*, 2013).

Since the advent of plate tectonic theory, it was recognized that subduction zones differ in many aspects that relate to their geometry, geology, physics and chemistry. At different subduction zones around the globe, one might find differences in the age of the downgoing plate, nature of the overriding plate (continental/oceanic), overriding plate topography, overriding plate strain (extension/shortening), trench kinematics, subduction rate, subduction accretion/erosion rate, arc volcanism, slab dip angle, slab length, slab depth and trench curvature (e.g. *Arcay et al*., 2008; *Cerpa et al*., 2015; *Cruciani et al*., 2005; *Gibert et al.,* 2012*; Keppie et al., 2009; Lallemand et al.,* 2005*; van Dinther et al.,* 2010*; Schellart and Rawlinson*, 2013).

Regarding their geometry, subduction zones are strongly asymmetric for the first several hundred kilometres. Their dimensions are defined by deep trenches, lines of volcanoes parallel to the trenches, and by the inclined array of earthquakes known as the "Wadati-Benioff Zone" (after the Japanese and US scientists who independently identified these dipping zones) that dip away from the trench beneath the volcanoes and extend down to the 660 km discontinuity (*Stern*, 2002).

Earthquakes in subduction zones occur at enormously greater depths than elsewhere on Earth, where seismicity is limited to the uppermost 20 km (*Stern*, 2002). The maximum depth of seismicity in a subduction zone can be determined as:

$$\varphi = V \times A$$

where V is the subduction velocity and A the age of the subducted plate (*Lallemand*, 1999). Seismic tomography provides additional details about earthquakes in subduction zones. This technique uses seismic velocity information from many ray paths, crisscrossing Earth between various points near Earth's surface and reaching different depths in its interior, to produce a three-dimensional (3-D) model of relative velocity. Regions of anomalously fast

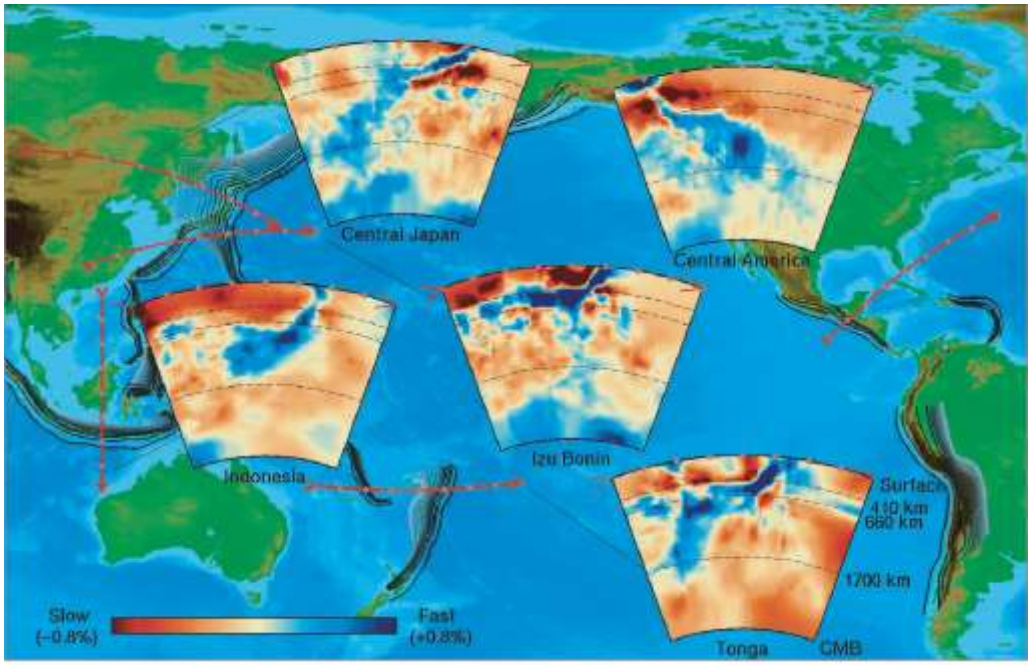

Figure 3.4: Structure of subducted slabs as inferred from mantle tomography (from *Kárason and van der Hilst*, 2000). Red lines show the surface projection of each section. The base of each section is the core-mantle boundary (CMB); dashed lines show the location of mantle discontinuities at 410, 660, and 1700 km. Red and blue colors in each section denote regions where the *P* wave velocities are relatively slow and fast, respectively, compared to average mantle at the same depth.

mantle corresponding to the earthquake plane define the downgoing lithospheric slab (blue color in Figure 3.4), and regions of anomalously slow mantle lie above this (red color in Figure 3.4). Subducted lithosphere sometimes can be traced this way past the 660 km discontinuity into the lower mantle, plunging to the core-mantle boundary, 2900 km beneath the surface (*Stern*, 2002) (Figure 3.4).

3.2 Subduction zone components

Mantle lithosphere, crust and sediments play a key role in controlling the behaviour of subduction zones: mantle lithosphere controls the physics of subduction; sediments control the chemistry of subduction, and the crust exert an important role in both chemistry and physics (*Stern*, 2002).

3.2.1 Mantle lithosphere

As mentioned above, the density excess that characterizes the mantle lithosphere increases as the lithosphere ages and thickens. The age of the subducting lithosphere is one of the parameters that characterizes and differentiates subduction zones. For example, the circum-Pacific subduction zones provide a starting point in understanding their great variability. Seafloor about to descend at convergent margins ranges in age from ~170 Ma (east of Mariana trench) to 0 (spreading ridges being subducted off North and South America) (*Stern*, 2002). Globally, the mean age of the seafloor when it arrives at a trench is ~100 Ma (*Parsons*, 1982), corresponding to a thermal lithosphere thickness of ~100 km. Due to age-dependant thickening, lithosphere becomes negatively buoyant with respect to underlying asthenosphere when it is at least 30 Ma (*Korenaga and Korenaga*, 2016), thus sinking readily when they reach the trench. This old and dense lithosphere results in relatively steep subduction zones with a large amount of gravitational potential energy that drives both the sinking of the lithosphere and plate tectonics (*Stern*, 2002). Nevertheless, a significant proportion of convergent margins subduct when they are younger than 10–30 Ma. This buoyant and young lithosphere resists subduction, resulting in shallow dips and a strong coupling between the plates, generating higher magnitude earthquakes compared to those subducting old lithosphere (*Stern*, 2002; *Lallemand et al*., 2005; *Sen*, 2014). As discussed in *Roda et al*., 2011, *Rodríguez-González et al*., 2012 and *Sharples et al*., 2014, the coupling between the plates is influenced not only by the age of the lithosphere but also by the thickness and the nature of the overriding plate (oceanic or continental).

The very different behaviour of subduction zones involving young (i.e. Chilean) and old (i.e. Mariana) lithosphere is also shown in the strain regime manifested behind the magmatic arc, from highly extensional, characterized by back-arc spreading and typified by the Mariana arc, to highly compressive, characterized by back-arc shortening and typified by the Chilean arc (*Stern*, 2002; *Heuret and Lallemand*, 2005).

It is therefore noticeable that the age of the subducted lithosphere, together with the absolute motion of the overriding plate, is also correlated to the strain regime in the overlying plate, as observed by Jarrard (1986) who subdivided subduction zones into seven strain classes, with class 1 being strongly extensional and class 7 being strongly compressional.

It follows a first-order differentiation of subduction zones recognized by *Uyeda and*

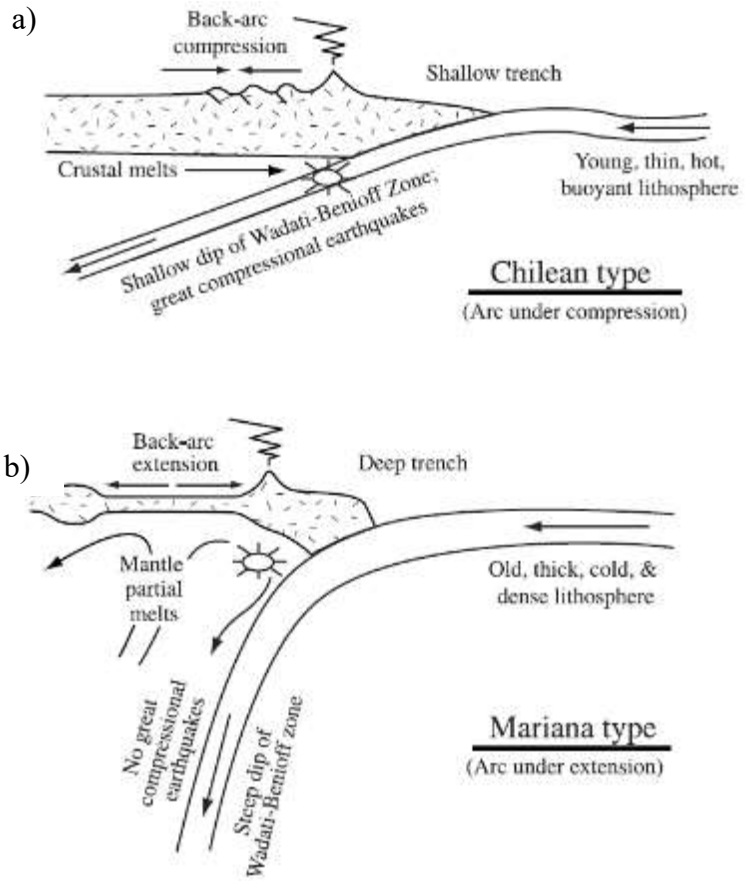

Figure 3.5: Schematic cross-sections of two very different types of subduction zones—Chilean and Mariana type (from *Stern*, 2002).

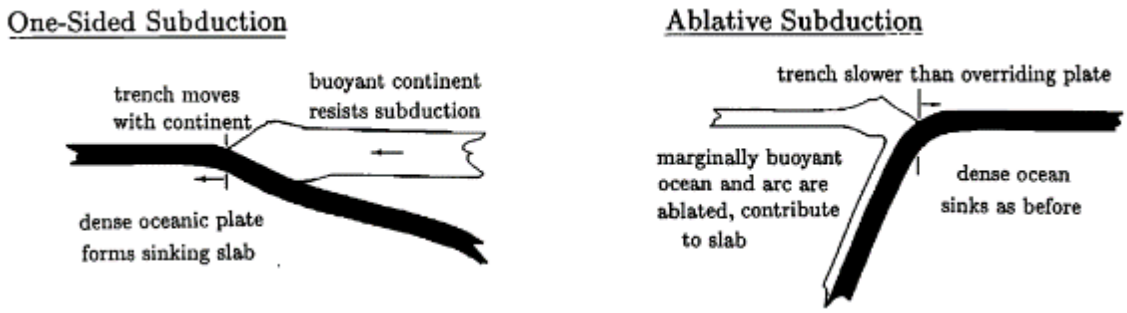

Figure 3.6: One-sided versus two-sided (ablative) subduction models (from *Tao and O'Connell*, 1992).

Kanamori (1979) and *Uyeda* (1987) and controlled by both the age of incoming lithosphere and the strength of mechanical coupling between downgoing and overriding plates:

1. Chilean-type, strongly compressional (strain class 7), characterized by young lithosphere, high seismicity at the interface between the lower and the upper plates, low dip angle of the subducted slab, bulging of the lower plate and well-developed accretionary wedges (Figure 3.5 a);
2. Mariana-type (strain class 1), characterized by old lithosphere and extension in the upper plate with opening of back-arc basins, subsidence in correspondence of the margin, absence of the accretionary wedge, high dip angle of the subducted slab and weak coupling between the two plates (Figure 3.5 b).

In addition to the one-sided subduction characterized by an accretionary wedge (Figure 3.6 a), *Tao and O'Connell* (1992) proposed a model of "ablative subduction" to interpret observations concerning slab profiles, interplate seismicity, back arc tectonics, and complex processes such as double subduction and subduction polarity reversal (Figure 3.6 b) deforms in passive response. This process is potentially double-sided since even a buoyant plate can be dragged downward by a dense, descending neighbor. Thus, an apparent overriding plate may be worn away by a process of viscous ablation, with the rate of ablation that is a function of plate buoyancy (*Tao and O'Connell*, 1992). When ablation is weak, as when a buoyant continent borders the trench, deformable slabs adopt shallow, Chilean-type profiles. These profiles develop over time from an initially steep shape. Differently, for higher ablation rates, as might occur in an ocean-ocean convergence, slabs adopt Mariana-type profiles. Differences between Chilean- and Mariana-type subductions may result from disparities in ablation rate and subduction duration. Furthermore, as shown by numerical experiments conducted by *Gerya et al*., (2008), the subduction configuration is also affected by slab strength and the amount of weak hydrated rocks present above the slab, which contribute to localize deformation at the interface and decouple the strong plates, facilitating asymmetric plate movement. In particular, they demonstrate that two-sided subduction occurs at low slab strength ($\sin[\phi] < 0.15$, where ϕ is effective internal friction angle), regardless of the extent of hydration. In contrast, steady state one-sided subduction requires a weak hydrated slab interface and high slab strength ($\sin[\phi] > 0.15$).

The occurrence of ablation might not be easily detected at depth, because material from subducting and ablating plates adhere closely as a single slab (*Tao and O'Connell*, 1992). Plate deformations associated with ablative subduction are consistent with observed patterns of seismicity. In particular, the relative aseismicity of Marianas-style plate boundaries is consistent with the ablative model, thus explaining how plates can converge aseismically, without requiring that these plates be decoupled (*Tao and O'Connell*, 1992).

3.2.2 Crust

The density and thickness of the crust determine whether the subduction zone operates normally or fails. In fact, if normal oceanic crust is invariably subductable, subduction of continental crust leads to subduction zone failure, which occurs when sufficient buoyant material is introduced into it to disrupt downwelling (*Stern*, 2002). This is called collision or terrane accretion, which is produced by bodies of continental and intraoceanic arc crust greater than ~15 km thick or by oceanic plateaus with a crust greater than ~30 km thick, as revealed by buoyancy analysis (*Stern*, 2002).

The importance of the crust and, in particular, of the oceanic crust, is also linked to the transport of water and of a significant fraction of the chemicals carried into subduction zones. Oceanic crust is ~6 km thick and is composed of MORB and diabase underlain by gabbroic equivalents. Fresh MORB is depleted in incompatible trace elements (i.e., those that preferentially partition into the melt phase) due to repeated episodes of partial melting of the magma source and contains almost no water (*Stern*, 2002; *Wada and King*, 2015). However, the topmost portion of the oceanic crust is relatively porous and permeable due to lava drainage, fissuring, and fractures, promoting pervasive hydrothermal circulation and alteration, resulting in the enrichment of MORB with some incompatible elements (*Wada and King*, 2015). Water, together with CO_2, increases with increasing of hydrothermal alteration, which also leads to formation of amphibolites at greater depth in the crust, and seafloor weathering (*Stern*, 2002). The presence of even small amounts of serpentinite in the oceanic crust is important for water cycling through subduction zones, because equal volumes of serpentinite carry an order of magnitude more water than hydrated mafic crust and because serpentinite is stable to much greater pressures (13% H_2O versus 1-2% in

hydrated mafic crust and 7 GPa or more versus ~3GPa, *Ulmer and Trommsdorf*, 1995; *Stern*, 2002).

3.2.3 Sediments

Subduction zones are our planet's largest recycling system and sediments carried on the subducting plate are crucial for element recycling. Estimates of the mass of sediments subducted annually range from about 1×10^{15} g/yr (*Veizer and Jansen*, 1985; *Hay et al.*, 1988) to $3\text{-}4\times10^{15}$g/yr (*von Huene and Scholl*, 1991).

In contrast to the limited range in compositions present in the mantle lithosphere and oceanic crust, the compositional variety of sedimentary columns being subducted provides potentially distinctive inputs into subduction zones. For example, a few subduction zones are dominated or strongly influenced by carbonate sediments (e.g., Peru-Chile, Central America, and the Aegean) while some subduction zones are dominated or strongly influenced by terrigenous sediments (e.g., the Aleutians, Cascades, and Nankai) or siliceous sediments (e.g., Kamchatka) (*Rea and Ruff*, 1996).

Plank and Langmuir, (1998) have defined the GLOSS (*Global Subducting Sediment*) an approximation of the average composition of subducted sediments. GLOSS is dominated by terrigeneous material (76%) but contains significant proportions of biogenic calcium carbonate (7%) and silica (10%), along with mineral-bound water 7%. Sediments carry 1–2 km^3/yr of interstitial water into subduction zones (*von Huene and Scholl*, 1991; *Moore and Vrolijk*, 1992). Most of this pore water is squeezed out at very shallow depths, and it is estimated that a few cubic meters of water are squeezed out annually for each meter along the trenches (*Rea and Ruff*, 1996).

Sediments accumulate in the forearc region, which lies between the trench and the magmatic front. A first-order distinction can be made between forearcs that broaden by addition and imbrication of material along the trench (accretionary margins) and those that do not (non-accretionary forearc) (Figure 3.7 a and b). This depends on the thickness of sediment being subducted: if greater than 400–1000 m, sediments will be scraped off the downgoing plate and transferred to the overriding plate to form an accretionary prism (*Dahlen*, 1990; *von Huene and Scholl*, 1991; *Le Pichon et al.*, 1993).

Accretionary forearcs (Figure 3.7 a) form where sediment supply is high, typically adjacent to or near continents. They are typically marked by forearc slopes of <3° and form in active margins where the rate of orthogonal convergence is <7.6 cm yr^{-1} and where the trench sediment thickness is >1 km (*Clift and Vannucchi*, 2004). The faster the rate of convergence is, the steeper the forearc slope is, implying that basal friction increases with convergence rate. According to *Clift and Vannucchi* (2004), convergence rate also appears to exercise some control over the thickness of trench sediment because it determines how long any given piece of the oceanic plate resides in the high-sedimentation rate trench zone.

Two models of accretion of the wedge can be identified (*Malavieille*, 2010) (Figure 3.7 c_1, c_2, c_3):

1) models of frontal accretion, for which can be distinguished models with high basal friction and with low basal friction. Models with high basal friction are characterized by a high taper angle and by growth through imbrication of long tectonic units bounded by low-angle thrusts (Figure 3.7 c_1). Backthrusts are minor and develop within the body of the wedge. Wedges with a low basal friction are characterized by a low taper angle and by growth through frontal accretion of new tectonic units involving forward propagation of a basal décollement (Figure 3.7 c_2);
2) models of basal accretion, characterized by multiple décollement décollement (Figure 3.7 c_3). In these models two growth mechanisms act simultaneously: 1) frontal accretion above the upper décollement ("décollement 2" in Figure 3.7 c_3), and 2) deep underplating of thrust slices, with basal accretion at the rear due to duplex formation above a basal lower detachment ("décollement 1" in Figure 3.7 c_3).

   These mechanisms produce a variable taper, which is lower in the frontal part, where there is frontal accretion, and higher in the rear part, where there is basal accretion.

Non-accretionary forearcs form where sediment supply is low, typically distant from continents, and thus they also have poorly developed forearc basins (Figure 3.7 b). Because the accretionary prism and forearc basin are missing, the igneous infrastructure of the forearc is exposed (*Stern*, 2006).

As the accretion act to increase the dimensions of a wedge, the tectonic erosion decreases them. Two processes of tectonic erosion can be distinguished (*Von Huene and Lallemand*, 1990):

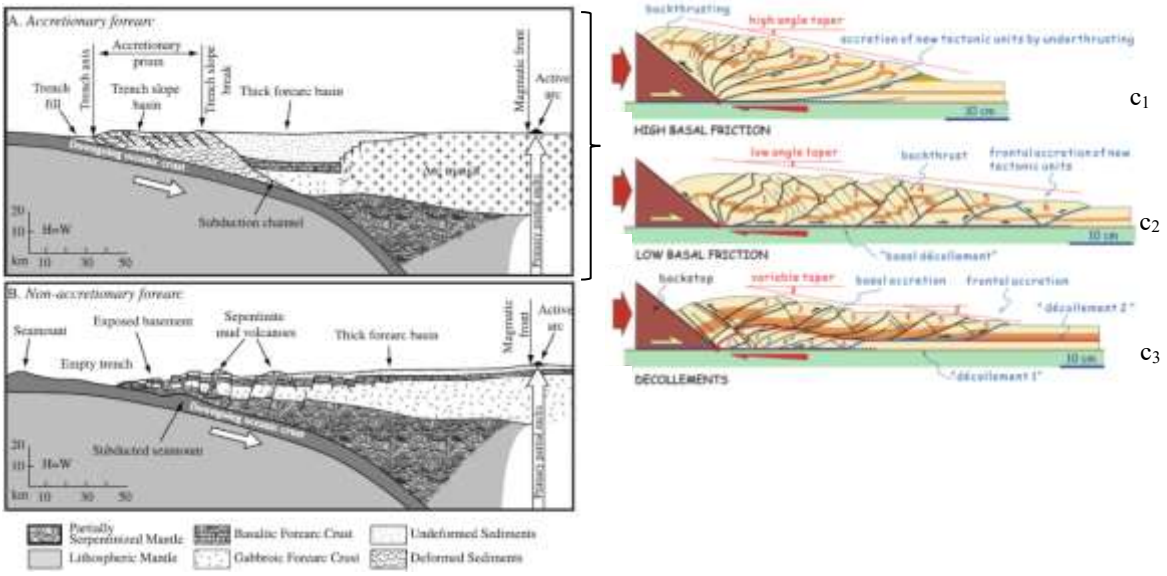

Figure 3.7: Left panels: end-member forearc types: (a) accretionary forearc and (b) non-accretionary forearc (from *Stern*, 2002). Right panels: main mechanisms of wedge accretion and the corresponding critical taper (modified from *Malavieille*, 2010).

- frontal erosion, in which the sediments are removed by the frontal margin of the wedge. This type of erosion is inferred from disrupted topography at the base of the inner trench wall and is most evident in the wake of subducting seamounts (*von Huene and Scholl*, 1991);
- basal erosion, in which the sediments are removed by the lower and rear portion of the wedge.

Tectonic erosion, as demonstrate by *Clift and Vannucchi* (2004) is favored in regions where convergence rates exceed 6 ± 0.1 cm yr^{-1} and where the sedimentary cover is < 1 km.

3.3 Phase transitions and serpentinization

Most of the actions associated with subduction zones happens deep below the surface. Our understanding of these processes is largely inferential, based on geophysics and geochemistry of active systems and on studies of exhumed subduction zones. One of these actions is represented by phase transitions.

As a subducted plate descends, it is progressively heated and squeezed, changing the mineralogy and volatile content of sediments, crust, and mantle lithosphere. One of the most

important transitions is that of the Mg_2SiO_4's polymorphs. Olivine and its high-pressure and hydrated polymorphs make up most of the upper mantle and of the subducted lithosphere. At equilibrium, olivine change into β-spinel structure (wadsleyite) at ~410 km depth. More in depth, wadsleyite should change into γ-spinel structure (ringwoodite) at ~520 km, which then yield perovskite ($MgSiO_3$) plus magnesiowustite (MgO) at 660 km depth. The transition olivine-wadsleyite occurs at the boundary between the upper mantle and the transition zone, while the transition ringwoodite-perowskite + magnesiowustite takes place at the boundary between the transition zone and the lower mantle (*Green et al*., 2010) (Figure 3.8). The wadsleyite-ringwoodite transition involves little change in density, but the olivine-wadsleyite and ringwoodite-perovskite transitions significantly increase the density of the subducted lithosphere (6% and 8% increase, respectively) (*Stern*, 2002; *Billen et al*., 2008). In subducted lithosphere the conversion of olivine to wadsleyite should occur considerably shallower than 410 km, whereas the conversion of ringwoodite to perovskite + magnesiowustite should occur deeper than 660 km (*Irifune*, 1993). This is because the Clapeyron slope (dP/dT) for the olivine-wadsleyite reaction is positive, whereas that for the ringwoodite to perovskite+magnesiowustite transition is negative (*Billen et al*., 2008). Therefore, the shallower nature of the first conversion increases the relative density of the subducting lithosphere, favoring continued sinking, whereas the deeper nature of the second conversion decreases relative slab density *(Stern*, 2002).

Another important reaction in subducted lithospheric mantle is the breakdown of serpentinite to olivine, orthopyroxene, and water, which results in a very large density increase as it releases a lot (13 wt %) of water (*Stern*, 2002). Serpentine (antigorite, $Mg_{48}Si_{34}O_{85}(OH)_{62}$) can contain up to 12.3 wt% H_2O and, together with chlorite (13.0 wt% H_2O), dominates the water budget of hydrous peridotite up to ~150 km depth (Figure 3.9 a). Serpentine forms during low-grade hydration in peridotites and its maximum temperature stability is 720°C (*Schmidt and Poli*, 1998) (invariant point 3 in Figure 3.9 a). The phases with large contributions to the water budget of subducting MOR basalt are lawsonite, chlorite, and amphibole. Lawsonite contains 11.2 wt% H_2O, chlorite in basalt contains about 13 wt% H_2O and amphibole only contains 1 wt.% < H_2O < 3 wt.% depending on the composition and anionic/oxi substitutions in the OH site (*Schmidt and Poli*, 1998; *Faccenda*, 2014) (Figure 3.9 b).

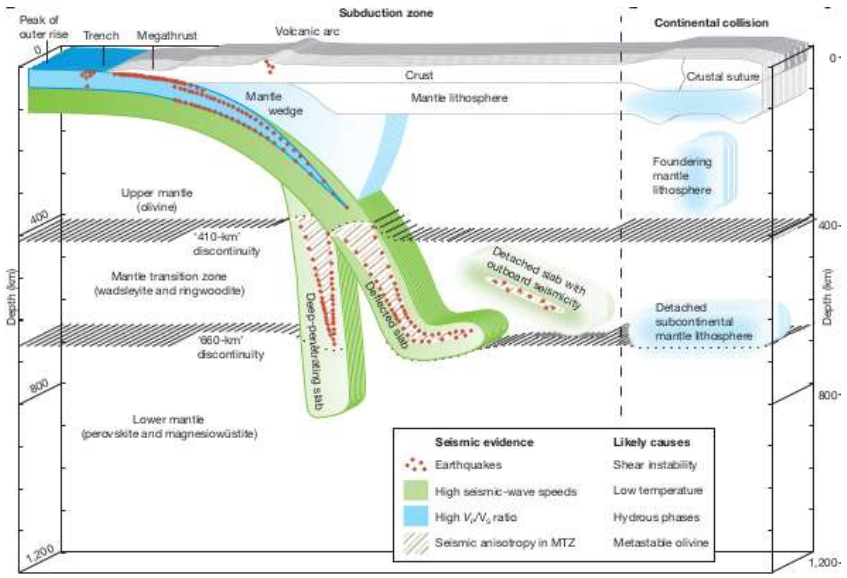

Figure 3.8: Sketches of a subduction zone showing the phases stable through the subduction zone and the behavior of the subducted plate (from *Green et al*., 2010).

Most of the water carried to depth in subduction zones is contained in hydrous minerals in altered and metamorphosed crust and serpentinite. Hydrous basalt and gabbro should convert to blueschist at relatively low pressures (~30 km depth), depending on the thermal regime (Figure 3.10) and kinetics. As hydrous basalt (with up to 5% H_2O) is metamorphosed to blueschist (~3% H_2O) and then amphibolite (~1–2% H_2O), it progressively releases water. Amphibolites in subducted lower crust may persist to ~100 km depth. Blueschist-and amphibolite-facies crust are requilibrated under eclogite-facies conditions as a function of the subduction zone properties. In an ocean-continent subduction zone eclogite-facies conditions are relatively easy to achieve by all rock types (young/old/cold/hot). In a continent-continent subduction it is still possible to achieve eclogite-facies conditions but less easy then in the ocean-continent case (*Regorda et al*., 2021).

Therefore, the subducting plate, due to dehydration and phase transitions, has a higher density than the starting one, while the released fluids penetrate the overlying mantle, hydrating it.

How fluid escapes from the subducted slab is critical for understanding how the overlying mantle melts. *Tatsumi and Eggins*, (1995) argue that pressure-sensitive dehydration reactions release water from the subducted slab at specific depths, forming

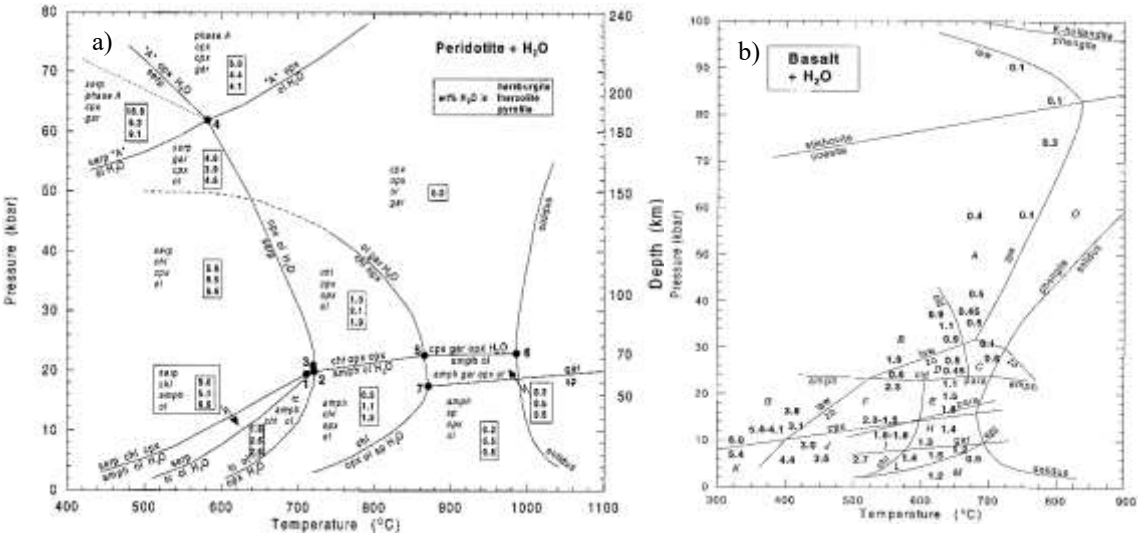

Figure 3.9: a) Phase diagram for H_2O-saturated average mantle peridotite and maximum H_2O contents bound in hydrous phases in average peridotites. Upper value: harzburgite; middle value: lherzolite; lower value: pyrolite. The *italic* labels are assemblages in a given stability field. b) Maximum H_2O contents bound in hydrous phases in H_2O-saturated MOR basalt. '*A*' =phase A, *amph* = amphibole, *chl* =chlorite, cld = chloritoid, *cpx* = clinopyroxene, epi = epidote, *gar* = garnet, law = lawsonite, *ol* = olivine, *opx* = orthopyroxene, para = paragonite, *serp* = serpentine, *sp* = spinel, *tc* = talc, zo = zoisite (from *Schmidt and Poli*, 1998).

"hydrous curtains" where this water rises into the overlying mantle wedge. The line of arc volcanoes in this case might correspond to the surface projection of the controlling dehydration reaction.

In contrast, according to *Schmidt and Poli* (1998) water is released continuously from subducted materials down to a maximum depth of 70 km (for hot slabs) to >300 km (for cold slabs). Furthermore, they also infer that 30–70% of the subducted water will be released below the forearc, where it will likely serpentinize the overlying mantle, and that another 18–37% of the subducted water will persist to depths where it might help generate arc magmas (Figure 3.11).

Excess density of the mantle lithosphere in subduction zones provides most of the power needed to move the plates while inducing convection in the overriding mantle wedge. The mantle wedge is that part of the mantle that lies above the subduction zone and where subducted inputs are mixed with convecting mantle to generate magmas, fluids, and ultimately continental crust.

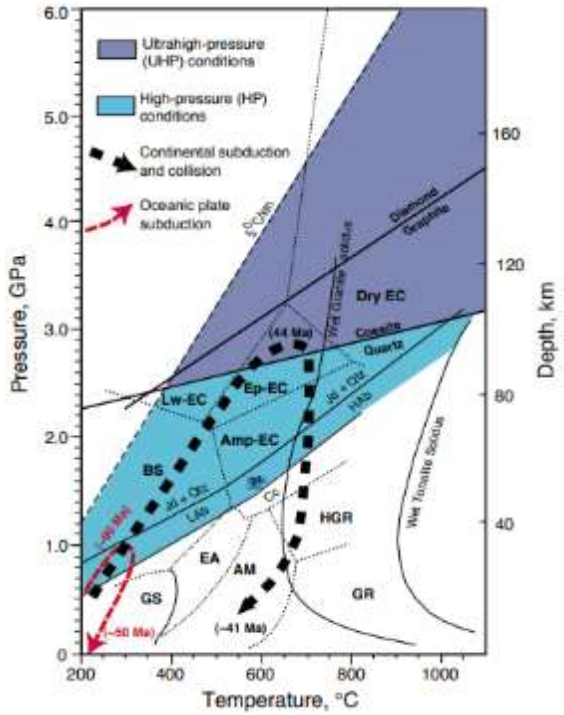

Figure 3.10: Schematic diagrams showing the P–T evolution of common UHP metamorphic rocks in continental subduction zones. UHP and HP metamorphic domains are separated by the P–T boundary for the quartz/coesite equilibrium. A very low subduction-zone geothermal gradient of 5 °C/km is shown for reference. Metamorphic-facies abbreviations: AM = amphibolite; Amp-EC = amphibolite-eclogite; BS = blueschist; EA = epidote amphibolite; EC = eclogite; Ep-EC = epidote-eclogite; GR = sillimanite-granulite; GS = greenschist; HGR = kyanite-granulite; Lw-EC = lawsonite-eclogite; and Px-Hf = pyroxene hornfels (from *Ernst and Liou*, 2008).

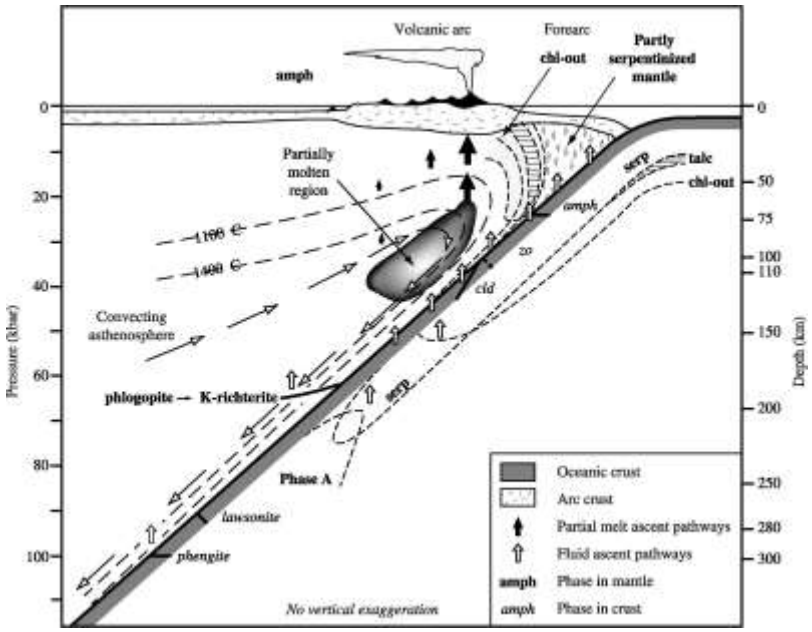

Figure 3.11: Model for dehydration of subducted materials (from *Schmidt and Poli*, 1998).

The thermal gradient produced after the cooling of the asthenosphere in contact with the slab determines the activation of convective flows in the mantle wedge (Figure 3.11). In fact, hotter mantle from the external portion of the wedge moves toward the trench, taking place of the cooled mantle strongly coupled with the slab (*Stern*, 2002). The hydration of the mantle wedge, as a consequence of hydrated mineral breakdown reactions in the descending plate, determines a decrease of the viscosity of at least one order of magnitude *(Billen*, 2008), which in turn facilitates the activation of small convective cells, favouring the exhumation of subducted oceanic and continental material at the base of the crust of the upper plate (*Honda and Saito*, 2003; *Meda et al*., 2010).

The fluids release from subducted sediments, crust, and mantle travel many kilometres through downwelling mantle in order to reach the hot corner, where it is sufficiently hot to melt. Three main mechanisms have been proposed to explain how fluids move through the mantle at great pressure:

1) porous flow: it is a slow process, which maximizes interaction of the fluid with mantle. The release of fluids from subduction zone is continuous, metasomizing the overlying mantle. Migration of fluids away from the slab and toward the hot corner may be accomplished by several cycles of mantle, metasomatism, descent, and breakdown (*Stern*, 2002). Near the surface, fluids move through solids because of their porosity, but in the mantle porosity cannot exist unless there is a melt or fluid phase to hold it open. If a fluid has a dihedral angle θ (which is the angle formed between two mineral/fluid interfaces meeting at a grain boundary) >60°, then the fluid exists as isolated pores and cannot move. If the fluid is a "wetting" fluid (θ <60°), it is interconnected along grain edges and therefore able to move by porous flow (*Stern*, 2002). According to *Navon and Stolper* (1987), porous flow rates could be on the order of meters per year resulting in continued reequilibration of fluid with mantle peridotite;
2) channelized flow: proposed by *Davies* (1999), it is a much more rapid mechanism, which occurs when trapped fluid connect as a result of faulting at intermediate depths, causing a hydrofracture that expels water into the mantle wedge. The fluid in this case would arrive at the zone of melt generation with compositions in equilibrium with the slab;

3) diapiric ascent: this mechanism is produced by serpentinite, which being buoyant and stable to great depth in the mantle, could form diapirs that ascend from the viscous blanket toward the melt zone (*Stern*, 2002).

The role played by water in subduction process has also been tested in different numerical studies (e.g., *Gerya et al*., 2008; *Gerya and Meilick*, 2011; *Liu et al*., 2017; *Regorda et al*., 2017). Numerical studies of hydration of the mantle by slab dehydration have used different simplified numerical approximations for the migration of free water in the mantle, showing differences in the spatial distribution of hydrated material in the mantle wedge as subduction evolves:

1) element-wise vertical migration of free water, occurring independent of the flow of the solid phase (*Arcay et al*., 2005);
2) a vertical migration of free water, coupled with mantle flow, and including a horizontal component. This method has been implemented as an imposed vertical velocity added to the velocity of the solid-phase flow (*Gorczyk et al*., 2007) or as a dehydration front with an imposed horizontal and vertical velocity (*Gerya et al*., 2002);
3) a Darcy velocity, where the free water velocity is a function of the pressure gradient caused by the difference in density between water and the surrounding rocks. In addition, the flow of the solid material field also moves the free water in the imposed vertical velocity and Darcy schemes (*Cagnioncle et al*., 2007).

However, the above water migration schemes use different numerical setup of the subduction models making it difficult to evaluate the possible effects of the numerical implementation of water migration. So in light of this, *Quinquis and Buiter* (2014) have used a linear viscous model of a wet cylinder sinking in a dry mantle and a thermo-mechanical subduction model to investigate the effects of the three numerical water migration schemes described above (schemes 1, 2 and 3) on the dynamics of a subducting slab and its overlying mantle wedge. Keeping simple models, which do not consider melting, shear or adiabatic heating, they find that the bound water distribution is not greatly influenced by the water migration scheme whereas the free water distribution is. Their models also show that a bound water-dependent creep flow law results in a broader area of hydration in the mantle wedge, which feeds back to the dynamics of the system by the associated weakening. Although (de)hydration

processes influence subduction dynamics, *Quinquis and Buiter* (2014) demonstrate that the exact numerical implementation of free water migration does not impact the dynamics in the mantle wedge and, therefore, a simple implementation of water migration could be sufficient for a first-order impression of the effects of water for studies that focus on large-scale features of subduction dynamics.

3.4 Forces acting in the subduction zones

The geometry of the subducting plate is parameterized according to slab dip, maximum depth and length. The dip of subducted slabs can vary greatly. Even for a single subduction zone, the dip can vary with depth, sometimes starting out at a low dip angle at shallow depths and then steepening at greater depths. Typically, slab dip increases gradually from the trench to a depth of 80–150 km (*Lallemand et al*., 2005). Beneath this depth, it remains almost constant down to the limit between upper and lower mantle where it may be deflected (*Lallemand et al*., 2005) (Figure 3.12). The causes of such great variations in dips are controversial but the general idea is that "slab pull" (downward forces that pull the slab toward the core of the earth) must exert a strong overall control. At shallow depths the interaction forces with the overriding plate may be an important factor in controlling the initial dip of the subducting plate (*Sen*, 2014).
According to *Lallemand et al*., (2005), two mean dip angles can be identified (Figure 3.12):

- $\alpha_s = 32° \pm 11°$, the mean dip angle of subducted plate between 0 and 125 km deep;
- $\alpha_d = 58° \pm 14°$, the mean dip angle of subducted slab deeper than 125 km.

After conclusions reached by *Luyendyk* (1970) and *Furlog et al*., (1982), *Lallemand et al*., (2005) have examined the quality of the correlation between the slab dip and plate motions (both relative and absolute) highlighting a tendency for the slab dip to decrease with increasing upper plate velocity, from negative values (in case of a backward movements of the plate) to positive values (in case of forward movements of the plate).
This correlation is better with α_s than α_d, and much better when the slab penetrates into the lower mantle (*Lallemand et al*., 2005).

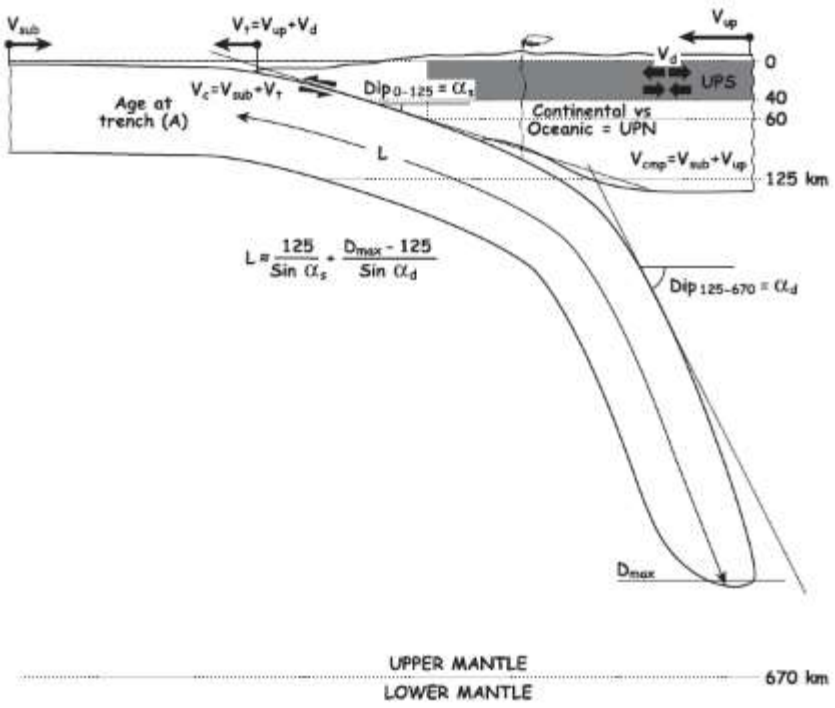

Figure 3.12: Sketch of a subduction zone. It shows the geometric features of the slab, as the length of the slab (L) estimated from its maximum depth and mean dip., maximum depth reached (D_{max}), the velocities of the plates (V_{sup}, V_{up}), the deformation (UPS) and the nature (UPN) of the upper plate (from *Lallemand et al*., 2005).

The upper plate strain, in addition to being influenced by the age of subducting lithosphere (as mentioned in section 3.1), is also related to the slab dip. In fact, the results of *Lallemand et al*., (2005) show an excellent correlation between slab dip and upper plate strain, with back-arc spreading observed for deep dips larger than 51°and back-arc shortening occurring only for deep dips less than 31°.

Another parameter, which influences the dip angle of the subducted plate, is the thermal state of the overriding plate. In particular, for colder thermal states in the upper plate there is a decreasing of the efficiency of the convective cells above the slab, with a consequent decrease of the dip angle *(Lallemand et al*., 2005) as demonstrated also by numerical models (*Roda et al*., 2011), which have shown also a lacking of a relation between the slab dip and both the direction of the subduction and the age of the subducted plate (*Cruciani et al*., 2005; *Lallemand et al*., 2005; *Roda et al*., 2011), in particular for slab with a thickness lower than 100 km (*Roda et al*., 2011; *Hu and Gurnis*, 2020 and reference therein).

There are main forces that influence both the plates kinematics and deformation in a subduction zone (*Heuret and Lallemand*, 2005; *Lallemand et al*., 2005) (Figure 3.13 a):

a. the slab pull force, defined as the mass excess of the slab relative to the surrounding mantle (F_{sp}) (Figure 3.13 a and b);
b. the anchor force F_a (Figure 3.13 a and b) that is the viscous resistance of the mantle during the sinking of the slab as well as the forward or rearward motion of the slab;
c. the viscous shear force during slab penetration;
d. the coupling between the plates along the interplate zone, which includes both the interplate friction and pressure and the bending/unbending of the slab (F_{up}) (Figure 3.13 a and b);
e. the regional mantle flow and the corner flow (F_m) (Figure 3.13 a and b).

The combination of these forces generates stresses in both the subducting and the overriding plates, either deforming the upper plate or determining a migration of the trench.

Heuret and Lallemand (2005) identified three models based on how these forces interact:

1) "upper plate motion controlled model" (Figure 3.14): according to this model, subduction hinge is affected by upper plate motion through two kinds of forces: (1) a suction/push force (F_{up}), which acts on the plate interface, making the upper plate interdependent with the subducting plate, and allowing upper plate motion to be transmitted to the top of the slab; (2) the anchoring-force (F_a), which is the viscous resistance force opposed by the asthenosphere to any lateral migration of the slab and trench that may be induced by F_{up}.

   Following *Scholz and Campos* (1995), the slab anchoring force can be defined as:

$$F_a = -6\pi\mu C V_{up}$$

   where μ is the average mantle viscosity over the depth range of the slab, C is a function of the slab width and length.

   Two end-members cases can be distinguished considering the F_a value:

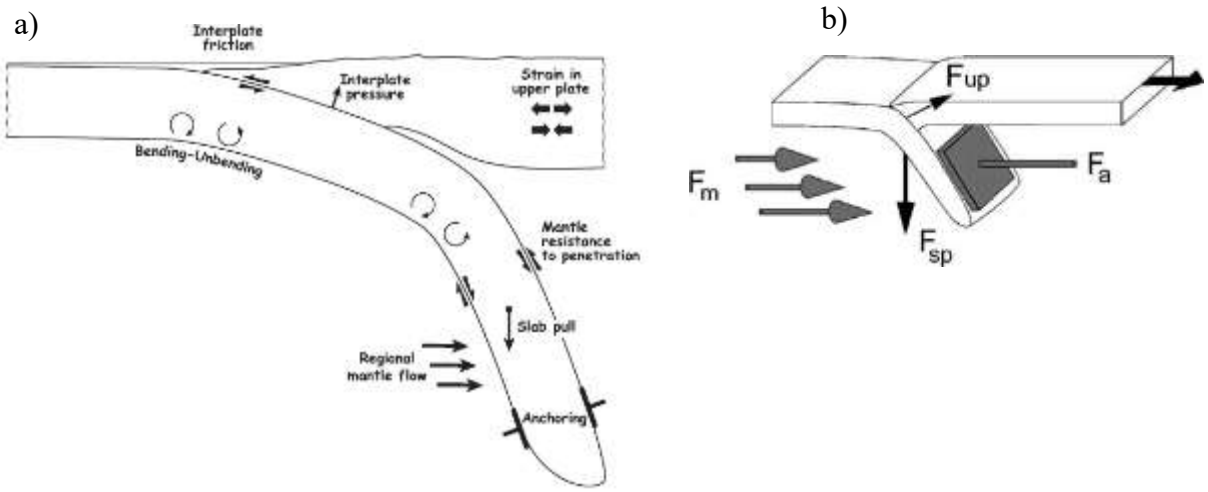

Figure 3.13: a) Major forces acting in a subduction zone. From *Lallemand et al*., 2005. b) Schematic cross section of a subduction zone, showing the main forces that may affect trench migration. F_{sp}: slab pull force, F_{up}: suction/pushing force related to the upper plate absolute motion, and which acts on the plate interface; F_a: slab anchoring force, F_m: pressure force generated by mantle flows on one side of the slab in the trench-normal direction (from *Heuret and Lallemand*, 2005).

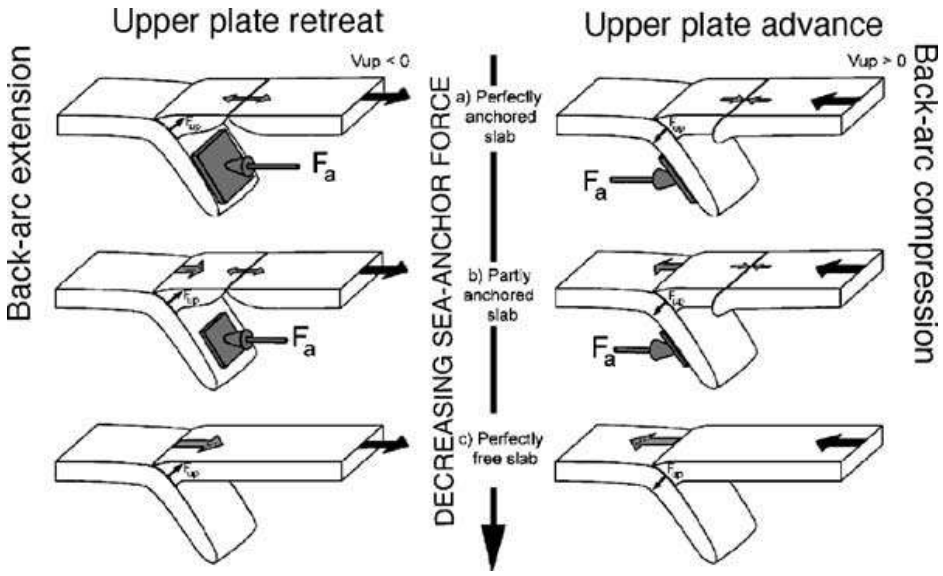

Figure 3.14: The "upper plate motion controlled model". V_d: back-arc deformation rate, V_{up}: upper plate absolute motion, Vt: trench absolute motion, F_{up}: suction/pushing force, F_a: slab anchoring force. a) $F_a \neq 0$; b) Fa = 0 (c) (from *Heuret and Lallemand*, 2005).

- "anchored slabs model" (Figure 3.14) for which the anchoring-force intensity is maximum, all the upper plate motion is converted into back-arc deformation ($V_d = V_{up}$) and the trench is fixed ($V_t = 0$). Therefore, the migration of the trench is inversely proportional to the anchor force, and whole (Figure 3.14 a) or part of the movement (Figure 3.14 b) is converted into back-arc deformation: if the movement is toward the trench there is compression, otherwise there is extension, with a consequent opening of a back-arc basin;
- "perfectly free slabs model" for which there is neither anchoring-force nor back-arc deformation ($V_d = 0$), but a dominant F_{up} force and a trench that strictly follows the upper plate ($V_t = V_{up}$). Consequentially, every movement of the overriding plate is transferred to the subducted plate, determining a migration of the trench without deformation inside the upper plate (Figure 3.14 c);

2) "slab rollback model" (Figure 3.15): the slab pull force F_{sp}, defined as the negative buoyancy of the subducted lithosphere with respect to the surrounding mantle, is thought to be one of the main driving force of the Earth's tectonic plates motion. It is a slab age dependent force according to the following relation:

$$F_{sp} = K \Delta \rho L A^{1/2}$$

where $\Delta\rho$ is the density difference between slab and mantle, L is the slab length, A is the age of the slab and K is a constant.

The slab pull force, together with the bending moment (M_b), produce a retreating of both the trench and the subducted plate (rollback), with a consequent extension in the upper plate. Therefore, this model can be associated to old and cold plates, which sink faster in the asthenosphere with a back-arc extension;

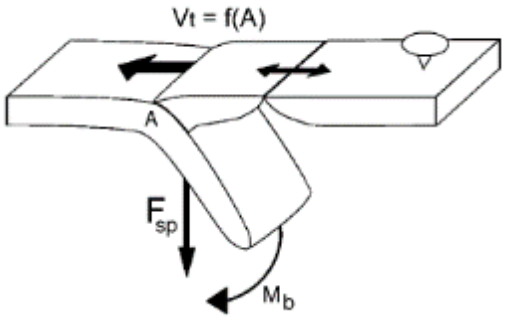

Figure 3.15: The "slab rollback model". V_{up}: upper plate absolute motion, V_t: trench absolute motion, F_{sp}: slab pull force, M_b: bending moment, A: slab age. The upper plate is supposed to be fixed (from *Heuret and Lallemand*, 2005).

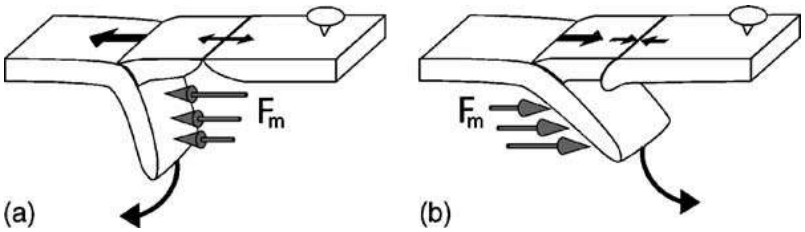

Figure 3.16: Sketch of the "mantle flow induced model". F_m is the pressure force generated by mantle flows on one side of the slab (from *Heuret and Lallemand*, 2005).

3) "mantle flow induced model" (Figure 3.16): the additional pressure force (F_m) generated by mantle flow on one side of the slab generates a slab translation in a directional normal to the trench. If mantle flow and the associated F_m push on the upper plate side of the slab, trench retreat and back-arc extension are generated (figure 3.16 a); conversely, if mantle flow and the associated F_m push on the subducting plate side of the slab, trench advance and back-arc compression are generated (Figure 3.16 b).

3.5 Gravity pattern in subduction zones

In subduction zones, the cool and dense oceanic lithosphere sinks in the mantle due to either tectonic push and/or gravitational instability. This process causes a redistribution of both superficial and deep masses, which in turn is responsible for the establishment of density anomalies with respect to a laterally homogeneous lithosphere-mantle system configuration (Normal Earth). These mass anomalies below the Earth's surface induce gravity anomalies.

The gravitational signal at subduction zones is generally characterized by a low-intensity positive anomaly from the trench towards the ocean, a deep negative anomaly in the vicinity of the trench, and a more intense positive anomaly, often composed of several peaks, towards the upper plate (Figure 3.17).

The positive anomaly towards the ocean, which is extended but not very intense, is called the *Outer Gravity High* (*Watts and Talwani*, 1974) and is due to the external rise of the trench, called *bulge*. This anomaly is generally accompanied by a regional topographical rise of a few hundred meters, and it can be explained by a stress system associated with the convergence of the lithospheric plates at island arcs (*Watt and Talwani*, 1974).

The negative anomaly in the vicinity of the trench, similarly to the first peak identified, is correlated to the topographical depression at the oceanic trench and the presence of light crustal material entrapped within the subduction (*Marotta et al*., 2006, 2020).

The extended positive anomaly above the upper plate is a direct consequence of the thermal cooling of the lithosphere and the underlying mantle. This wide positive anomaly is often superimposed by another narrower (100-150 km) and greater intensity anomaly (>100 mGal) coinciding, in the ocean-ocean context, with the arcs of volcanic islands. This anomaly is ascribed to the combination of the topography and the dynamics of the back-arc area (*Bassett and Watts*, 2015).

In conclusion, as also shown by results obtained by *Marotta et al*., (2020), positive and negative anomalies in the subduction zones are ascribable to several factors.

In particular, positive density anomalies are generally related to:

- the general cooling and thermal contraction of the system far away from the trench;
- the sinking of cold and dense lithospheric mantle into warm and light material;

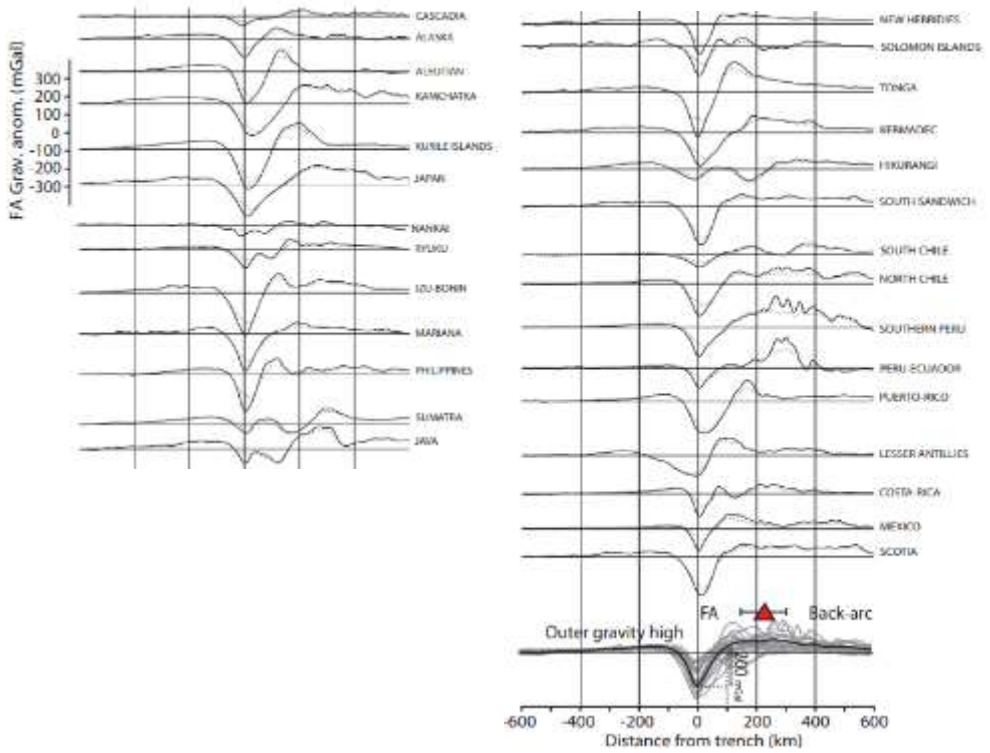

Figure 3.17: Gravitational anomaly profiles of subduction zones stacked on the trench axis and based on EGM2008 global gravity model (*Sandwell and Smith*, 2009). In the last panels on the right side, the global average of these profiles is shown with a black line. FA=Fore arc. Red triangle with bars marks the location of most volcanic arcs (from *Bassett and Watts*, 2015).

- the phase transitions within the subducting plate triggered by the increase in pressure p and temperature T.;
- the mantle that rises and fills the space previously occupied by the crust that has been scraped from the overriding plate.

Negative density anomalies can be attributed to the following:

- negative topography associated with the ocean trench;
- the light material entrapped in the subduction complex, particularly sediments and slices of continental crust scraped by the upper plate;
- the hydration of the mantle wedge leading to the development of serpentine that has a density that is approximately 200 kg m^{-3} lower than that of the non-hydrated mantle.

Therefore, gravitational signature of subductions is a major feature of this dynamic process that involves both the crust and the mantle. Then, new information on the background environment controlling the tectonic loading phase can be disclosed when the traditional analysis of deformation and field stress is combined with the analysis of the perturbation of the gravity field.

As explained in Chapter 1, compared to the last decades, we have now at disposal improved gravity models, both static and time-dependent, thanks to space gravity mission. In particular, GOCE and GRACE allow us to exploit the gravity of our planet to a resolution of about 80 km (static) and 300 km (time-dependent), with the perspective of going further by resolving the time-dependent gravity field at the wavelength of the present-day static component (*Silvestrin et al*., 2012).

Furthermore, the more sophisticated numerical models and the higher computational power now at disposal, allow to account for all the complexities needed to deal with the high resolution of the gravity data.

Chapter 4

Case study: gravity signature of Sumatra and Mariana subduction complexes

4.1 Abstract

In this chapter, I present the results of a comparative analysis between the geodetically retrieved gravitational anomalies, based on the EIGEN-6C4 model, and those predicted by a 2D thermo-chemical mechanical modeling of the Sumatra and Mariana complexes.
The 2D model accounts for a wide range of parameters, such as the convergence velocity, the shallow dip angle, the different degrees of coupling between the facing plates. The *marker in cell* technique is used to compositionally differentiate the system. Phase changes in the crust and in the mantle, and mantle hydration are also allowed. To be compliant with the geodetic EIGEN-6C4 gravity data, we define a *model normal Earth* considering the vertical density distribution at the margins of the model domain, where the masses are not perturbed by the subduction process.
Model prediction are in good agreement with data, both in terms of wavelengths and magnitude of the gravity anomalies measured in the surroundings of the Sumatra and

Mariana subductions. Furthermore, our modeling supports that the differences in the style of the gravity anomaly observed in the two areas is attributable to the different environments – ocean-ocean or ocean-continental subduction – that drives a significantly different dynamic in the wedge area. This work has been published on *Geophysical Journal International.*

4.2 Introduction

In subduction zones, various processes are responsible for the development of density anomalies, whose characteristic lengths, both horizontally and vertically, cover a wide spectrum of wavelengths due to the complexity of the interaction between the subducting and overriding plates. In turn, these density anomalies are responsible for characteristic gravity patterns, representing the fingerprint of the dynamic processes involving the crust and the mantle. The gravitational signal at subduction zones is generally characterized by a low-intensity positive anomaly from the trench towards the ocean, a deep negative anomaly in the vicinity of the trench, and a more intense positive anomaly, often composed of several peaks, towards the upper plate (Figure 4.1).

The positive anomaly towards the ocean, which is extended but not very intense, is called the *outer gravity high* (*Watts and Talwani*, 1974) and is due to the external rise of the trench, called *bulge*. This anomaly is generally accompanied by a regional topographical rise.

Similar to the first positive peak, the negative anomaly in the vicinity of the trench primarily reflects topographical depression at the oceanic trench. An extended positive anomaly is also observed above the upper plate, superimposed by a narrower (100–150 km) and higher positive anomaly (>100 mGal), which in the ocean–ocean context coincides with the island arcs. This anomaly reflects the combination of the topography and dynamics of the backarc area (*Bassett and Watts*, 2015 a,b).

A series of pioneering works (*Hager*, 1984; *Gurnis and Hager*, 1988; *Zhong & Gurnis,* 1992) are the pillars of our understanding of the dynamics of subduction processes and thus of the long-wavelength geoid, gravity and topography anomalies. *Melosh & Raefsky* (1980) demonstrated that positive and negative pressure anomalies are induced beneath the trench and island arc of a viscoelastic subducting plate isolated from the surrounding mantle, thus showing that topography and gravity anomalies are dynamically supported at subduction zones. *Hager et al.,* (1983) and *Gurnis and Hager* (1988), embedding the colliding plates

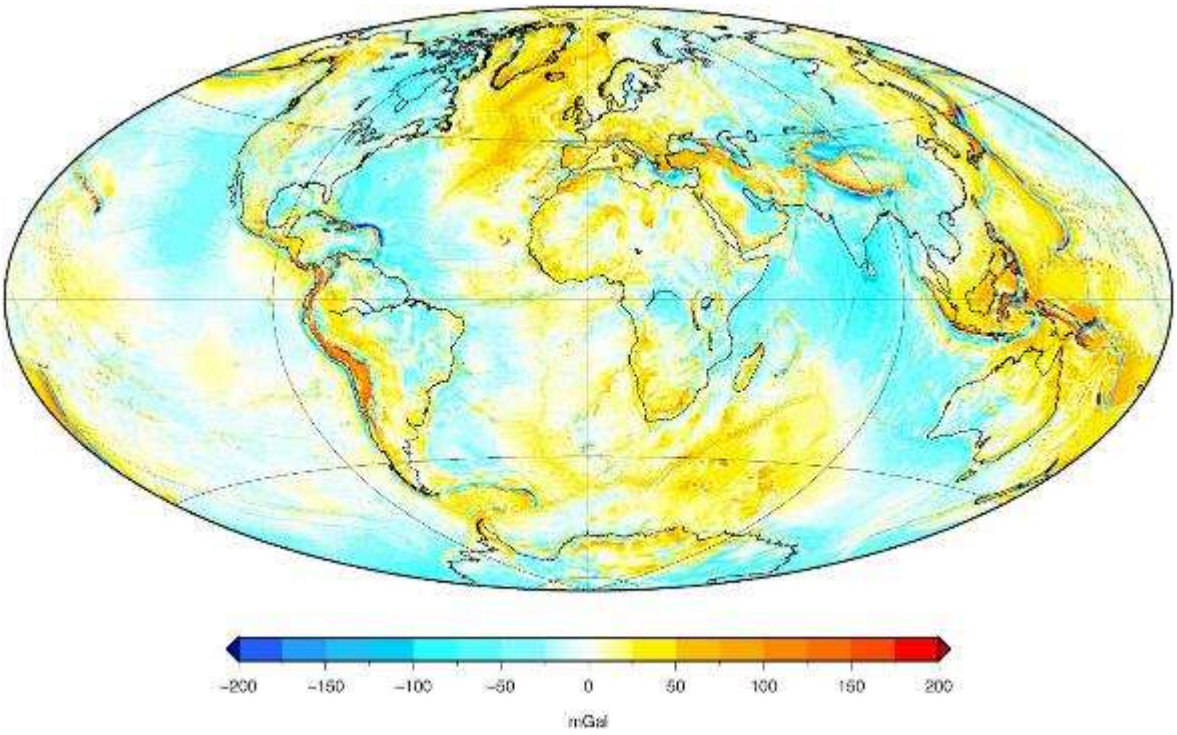

Figure 4.1: Global map of the gravitational disturbance computed at a height h_S =5 km above the ellipsoid based on the EIGEN-6C4 model (the latest combined static global gravity field model including GOCE data up to degree and order 2190*, Förste et al*., 2014).

within a viscous mantle, successfully interpreted the dip angles and the time-evolution of subducting plates. *Zhong and Gurnis* (1992) and *Zhong and Gurnis* (1994) , within the frame of a viscous flow model, highlighted the effects of the subduction fault on the topography and free-air gravity patterns, demonstrating the importance of plate coupling on the trench topography. Compared to the 1980s and 1990s, we now have access to improved gravity models, both static and time-dependent models, thanks to space gravity missions, particularly GOCE (Gravity and steady-state Ocean Circulation Explorer) and GRACE (Gravity Recovery And Climatological Experiment), which allow us to exploit the gravity of our planet to a resolution of approximately 80 km (static) and 300 km (time-dependent), with the perspective of going further by resolving the time-dependent gravity field at the wavelength of the present-day static component (*Silvestrin et al.,* 2012). The present work explores the gravity effects of complexities such as compositional stratification of the crust-lithosphere system, mantle hydration, and degree of plate coupling at ocean–continent and ocean–ocean subduction zones within the frame of dynamic self-consistent viscous modelling, which improves our capability to interpret short-wavelength features of the gravity patterns at

subduction zones, as currently allowed by modern space gravity missions.
Due to the dynamic nature of subduction, we exploit the full time-dependent evolution of the gravity patterns of the subduction processes for both ocean–continent and ocean–ocean subductions, including estimates of their rate of change. The gravity pattern at subduction zones recovered by GOCE, providing homogeneous coverage of the gravity, reflects the present-day density anomaly configuration. The latter is a snapshot taken today of the process that started at the beginning of collision: the present-day density anomaly distribution, made visible by its gravity fingerprint, must thus be coherent with that resulting today from the entire collision process. From this perspective, *Marotta et al.,* (2006) and *Marotta et al.,* (2007), within the frame of a newly developed finite-element numerical model, explored the role of the compositional stratification of light crust and dense lithospheric mantle in shaping the bipolarity of the gravity pattern. They showed that the negative gravity anomalies are correlated with the sinking of light crustal material, belonging to the subducting and overriding plates, while the positive anomalies are due to the thermally contracted subducted slab.

Compared with *Marotta et al.,* (2006), this study introduces new complexities, such as phase changes, hydration of the mantle and plate coupling, allowing us to provide the most realistic density distribution in the crust–mantle system and the corresponding gravity pattern, currently comparable with updated global gravity models, such as EIGEN-6C4 (Figure 4.1). A major issue considered in our analysis is the coupling between the subducting and overriding plates. Although considered in the aforementioned paper by *Zhong and Gurnis* (1992), we consider the effects of the coupling within the frame of our viscous models where all the other effects, from compositional stratification, hydration and phase changes, are included to provide a realistic and detailed picture of the impact of coupling on the density distribution at depth in the collision zone and its gravity signatures. We expect that gravity can provide hints regarding the amount of plate coupling.

4.3 Model setup

The dynamics of the crust and mantle system are governed by the continuity, momentum and energy equations as explained in detail in section 2.1.

The balance equations are numerically integrated via the 2-D finite element (FE)

thermomechanical code *SubMar* (*Marotta et al.,* 2006 and successive upgrading in *Roda et al*., 2010 and *Regorda et al*., 2017) in a 2-D 1000 km wide and 700 km deep rectangular domain (Figure 4.2 a). During the progression of subduction, erosion/sedimentation, mantle hydration/dehydration and phase changes are allowed and implemented as detailed in Appendix A. The domain is discretized by a non-deforming irregular grid composed of 6813 quadratic triangular elements and 13846 nodes, carrying a denser nodal distribution near the contact region between the plates, where the most significant gradients in temperature, pressure and velocity fields are expected. The sizes of the elements vary from 30 to 2.5 km, and the smallest elements are located in proximity to the active margin region to a depth of 300 km.

The marker-in-cell technique has been used to compositionally differentiate different types of materials (e.g. sediment, water, crust and mantle), and at the beginning of the evolution, 455 489 markers are spatially distributed with a density of 1 marker per 0.25 km^2, identifying through a specific index the material particles of air, water, upper and lower oceanic crust, upper and lower continental crust and the mantle belonging to the upper plate. The initial thickness of the oceanic crust is fixed at 10 km, subdivided into a 5-km-thick upper crust and a 5-km-thick lower crust, while the continental crust is 30 km, subdivided into a 20-km-thick upper and a10-km-thick lower crust. To allow for topographic variations a 7.5-km-thick layer of sticky air has been introduced above the crust. Only in the oceanic part of the domain, a sticky water layer of thickness h_w is sandwiched between the sticky air and the crust (Figure 4.2 a). When we refer to topography, we do not mean the upper boundary of the model, which does not deform, but the surface defined through the envelope of the topmost continental and/or oceanic crustal markers. Several comparative studies have demonstrated that, when appropriate low density and low viscosity values are considered (as low as 0–1 kg m^{-3} for density and 10^{18}–10^{20} Pa·s for viscosity), by means of the sticky air method the air/crust interface behaves in a manner that is very similar to that of a true free surface (*Schmeling et al.,* 2008; *Crameri et al.,* 2012; Ruh *et al.,* 2013). In this study we assume a value of 10^{19} Pa·s for the air/water viscosity and values of 1.18 and 1000 kg m^{-3} for the air and water density, respectively.

The model combines a linear viscous rheology for the sublithospheric mantle with a linear viscoplastic rheology for the lithosphere, as detailed in section 2.4 .

The initial global thermal configuration of the system corresponds to a conductive gradient throughout the lithosphere, with a temperature that ranges from 300 K at the surface to 1600 K at its base and a uniform temperature of 1600 K below the lithosphere to the bottom of the model. At the beginning of subduction, the base of the thermal lithosphere is fixed at a depth of 80 km under the lower plate and at 80 or 150 km under the upper plate (red solid and dashed lines in panel a of Figure 4.2). A thickness of 80 km corresponds to either an oceanic lithosphere of approximately 40 Myr (*Turcotte and Schubert*, 2002) or to a thinned continental passive margin extending at a medium-to-slow spreading rate of 2–3 cm yr^{-1} (e.g. *Marotta et al.,* 2018). The 1600 K isotherm defines the base of the thermal lithosphere throughout the evolution of the system.

We use different type of boundary conditions, either Dirichlet or Neumann type, along different boundary of the 2-D domain (Figure 4.2 a), where we prescribe values of velocities and temperatures or their normal derivative.

The thermal boundary conditions correspond to fixed temperatures at the upper (300 K) and lower (1600 K) boundaries of the model and to zero thermal flux through the vertical sidewalls. To minimize the potential effects of an unrealistic motion of the two plates with respect to the deep mantle, our model setup is constructed such that the trench is fixed with respect to the bottom of the 2-D convective cell and trench retreat is not allowed. This assumption, which is also encountered in the perspective of the successive application to the case studies of the Sumatra and Mariana subduction complexes, is consistent with the absolute plate motion by *Wang et al.,* (2018) at these two locations.

Moreover, no-slip conditions are assumed along the upper (top of the air/water layer) and lower boundaries of the 2-D domain and along the right vertical side, with the exception of the uppermost 80 km, where zero normal viscous stress is assumed. Zero normal viscous stress is also assumed along the vertical left-hand side (Figure 4.2 a). To force the subduction of the oceanic lithosphere, a convergence velocity u_s is prescribed along the bottom of the oceanic crust. Velocities of 2, 4, 5 and 8 cm yr^{-1} have been chosen, which are representative of slow, intermediate and fast subductions, respectively. The same velocity is also imposed along a plane that extends from the base of the oceanic lower crust, behind the trench, to a depth of 80 km, with an angle θ_s of 30°, 45° and 60°.

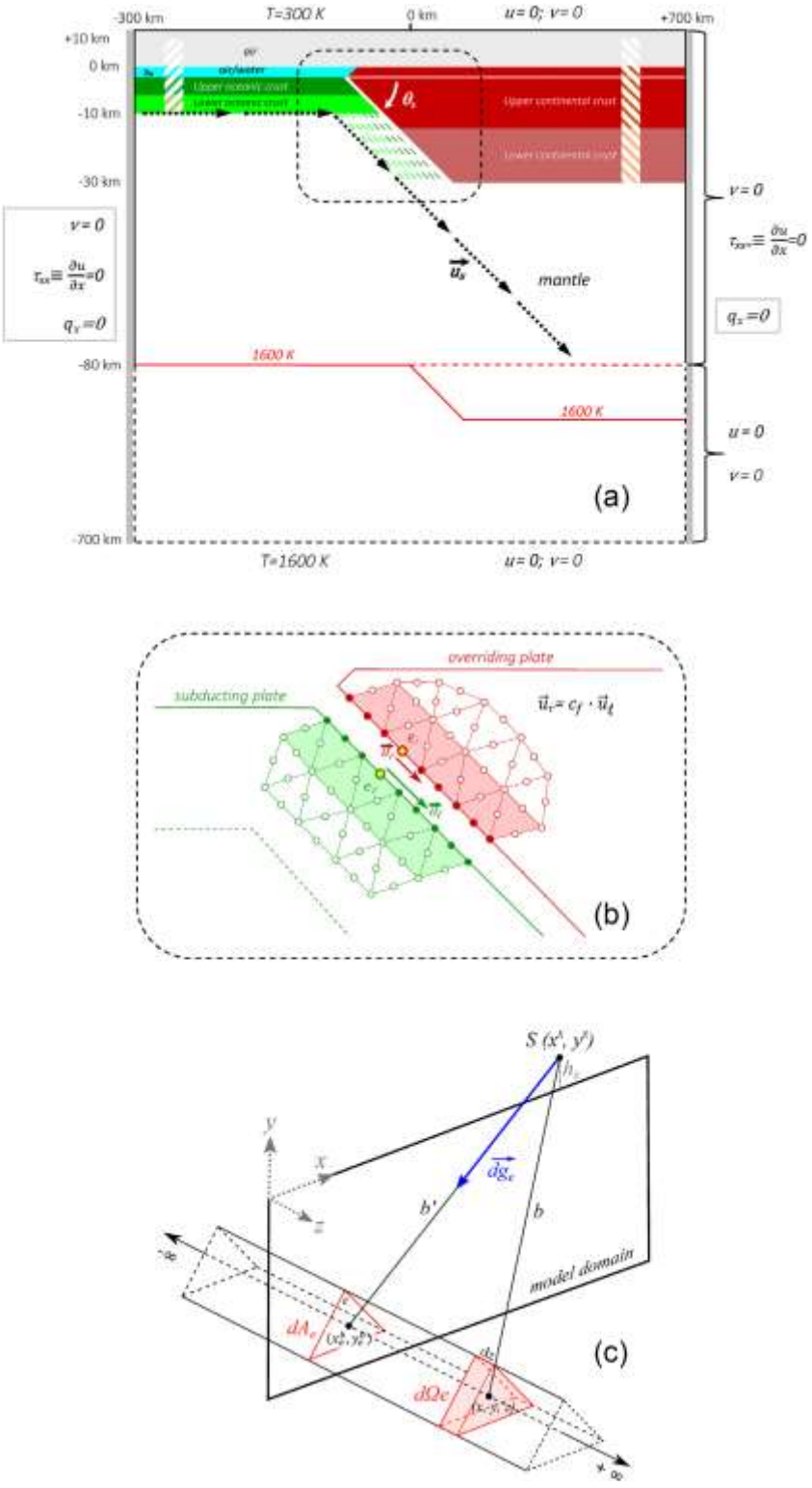

Figure 4.2: (a) Model setup and boundary conditions. Axes, x horizontal and y vertical, are not to scale. (b) Scheme used to implement the plate coupling factor. Triangles are representative of the numerical grid used. Red and green colours are used to graphically differentiate the two sides of the decoupling plane. The empty circles indicate the grid nodes. The solid circles indicate the *slip nodes*. (c) Scheme used to compute the volume integrals of eqs (6) and (7). Distances are not to scale.

Model ID	U_{cc}/L_{cc}	u_s (cm yr^{-1})	θ_s (°)	c_f	L_c (km)	h_t (km)	cf_0
Ocean–continent context							
OC_1	No	5	45	1	80	2.5	1
OC_2	Yes	5	45	1	80	2.5	1
OC_3	Yes	5	45	0.5	80	2.5	1
OC_4	Yes	5	45	0.5	80	2.5	0
OC_5	Yes	5	45	0.25	80	2.5	1
OC_6	Yes	8	45	0.5	80	2.5	1
OC_7	Yes	5	60	0.5	80	2.5	1
OC_8	No	5	45	1	150	2.5	1
OC_9	No	5	45	0.5	150	2.5	1
OC_{10}	Yes	5	45	0.5	150	2.5	1
OC_{11}	Yes	5	30	1	80	2.5	1
OC_{12}	Yes	2	45	1	80	2.5	1
OC_{13}	Yes	2	45	0.25	80	2.5	1
OC_{14}	Yes	2	45	0.5	80	2.5	1
Ocean–ocean context							
OO_1	–	5	45	1	80	0.0	1
OO_2	–	5	45	1	80	2.5_{ms}	1
OO_3	–	5	45	1	80	0.0	0
OO_4	–	5	45	0.5	80	0.0	1
OO_5	–	5	45	0.5	80	2.5_{ms}	1
OO_6	–	5	45	0.5	80	0.0	0
OO_7	–	5	45	0.25	80	0.0	1
OO_8	–	5	45	0.25	80	0.0	0
OO_9	–	4	45	0.25	80	0.0	0
OO_{10}	–	4	60	0.5	80	0.0_{ms}	1
OO_{11}	–	4	60	0.5	80	0.0_{ms}	0
OO_{12}	–	5	60	0.5	80	0.0_{ms}	0
OO_{13}	–	2	60	0.5	80	0.0_{ms}	1
OO_{14}	–	5	60	0.5	80	2.5_{ms}	1
OO_{15}	–	5	60	1	80	0.0_{ms}	1
OO_{16}	–	2	60	1	80	0.25_{ms}	1

Table 4.1: List of the models implemented for the present analysis. *Ucc*/*Lcc*: stratified (yes) or homogeneous (no) continental crust of the upper plate; *us*: prescribed subduction velocity; *θs*: prescribed subduction dip angle; c_f: degree of plate coupling; *Lc*: initial thickness of the upper plate; h_t: maximum topographic height before the activation of erosion; *cfo* : degree of coupling between the subducting plate and the sticky air layer. *ms*: modified sedimentation algorithm.

These dip values allow the development of low-, medium-, high-dip subductions and are based on the compilation by *Syracuse and Abers* (2006) who averaged the slab dips between 50 and 250 km depth, for all the known subductions. Flow is allowed across the left edge to guarantee that the total mass is conserved in the cell.

Finally, a different plate coupling along the contact plane between the lower and upper plates is implemented, modifying the classical split-node technique (*Jungels*, 1973; *Jungels and Frazier*, 1973) by introducing a plate *coupling factor* c_f that varies from 0 to 1 to indicate a shear-free or a fully coupled contact surface, respectively (Figure 4.2 b). The details about the implementation of the plate *coupling factor* c_f are presented in Appendix A.

The assumption of a total degree of coupling (c_f = 1) corresponds to a condition of continuity in the velocity field through the contact surface between the two interacting plates, that is commonly used in similar studies, even when a low viscosity channel or a weak zone are implemented to ensure the separation between the two plates (e.g. *Billen and Hirth*, 2007; *Duretz et al.,* 2011) intrinsically contains the condition of continuity. In our study, instead, we simulate a varying degree of coupling in terms of a discrete structural discontinuity. We assume a reference model that simulates a fully coupled subduction in order to enlighten its effects on the gravitational signature of subduction.

Table 4.1 lists the models implemented in this study and their main characteristics.

Because we are interested in estimating the perturbation induced on the gravity field only by subduction, for each element *e* of the numerical grid, at each time we calculate the density anomaly as follows:

$$\Delta\rho_e(t) = \rho_e(t) - \rho_e(t_0), \tag{4.1}$$

where $\rho_e(t)$ is the density within element *e* at time *t* and $\rho_e(t_0)$ is the density within the same element at the beginning of subduction. The elemental density anomaly $\Delta\rho_e(t)$ computed by Equation (4.1) are then used to calculate the corresponding gravitational contributions at the observational point *S*, $\Delta g(S, t)$, as follows:

$$\Delta g(S,t) = \sum_{e=1}^{nelem} dg_e\,(S,t) \tag{4.2}$$

$$dg_e(S,t) = G \iiint_{\Omega_e} \frac{\Delta\rho_e(t)}{b^2}\, d\Omega_{e,} \tag{4.3}$$

where *G* is the universal gravitational constant, 6.67×10^{-11} $m^3kg^{-1}s^{-2}$; *b* is the distance between the observational point *S* and the centre of the volume element $d\Omega_{e,}$ inside grid element *e*; $\Omega_{e,}$ is the volume of the prism, infinitely extended along the direction perpendicular to the model, whose section coincides with the grid element (Figure 4.2 c); *nelem* is the total number of the grid elements. After few mathematical steps Equation (4.3) becomes

$$dg_e(S,t) = 2\pi G \iint_{A_e} \frac{\Delta\rho_e(t)}{\left(x^S - x_e^b\right)^2 + \left(y^S - y_e^b\right)^2}\, dA_e \tag{4.4}$$

where A_e is the area of the grid element, x_e^b and y_e^b are the coordinate of its barycenter and x^S and y^S are the coordinates of the observational point *S*.

4.4 Model results and discussion

The description of the results concerns the general thermal state of the system and the dynamics in the wedge area, the density distribution and the gravity changes induced by subduction. First, we illustrate the results of a reference model (OC_2 model in Table 4.1) (Section 4.4.1). This model simulates a fully coupled ocean–continent subduction (c_f = 1), with a subduction velocity u_s = 5 cm yr^{-1}, a subduction dip angle θ_S= 45°. Secondly, we compare the results of models characterized by different parameters in order to enlighten the effects of a variation of the degree of coupling *cf* (1, 0.5, 0.25), the subduction dip angle θ_S (45° and 60°), the subduction velocity u_s (2, 4, 5 and 8 cm yr^{-1}) and the environment (ocean–ocean and ocean–continent) (Section 4.4.2).

4.4.1 Reference model OC_2

4.4.1.1 General thermomechanics

The general thermomechanical behavior of the crust–mantle system during subduction has already been extensively described in the literature (e.g. *Marotta et al.,* 2007; *Billen,* 2008; *Afonso and Zlotnik,* 2011; Roda *et al.,* 2012; *Gerya,* 2015; *Regorda et al.,* 2017; *Dai et al.,* 2018; *Stern and Gerya,* 2018; *Wang et al.,* 2019). Here, we will focus on those aspects tha we consider to be related to the gravitational signature and its changes in time, which are the objectives of this work. Figure 3.3 shows the temperature and velocity fields predicted by the reference model OC_2 at different times after the beginning of subduction.

The system is characterized by the following:

(i) The sinking of the cold lithosphere into the hot mantle and its progressive steepening at great depths (Figure 4.3 d);

(ii) A convective flow that is activated above the lower plate during the early stages of subduction (Figures 4.3 a and b) and progressively enlarges with the sinking of the slab (Figures 4.3 c and d);
(iii) The large-scale flow that favours the rising of hot mantle in the wedge area, producing a progressive, but local, thermal thinning of the overriding plate (Figure 4.3 c and d).
Focusing on the mass redistribution shown in Figure 4.4, it is also worth highlighting the following:

(i) The subducted crustal material originates either from the lower plate or from the upper plate, from which it is scraped (Figure 4.4 a);
(ii)The scraping effect is maximum within the first 5 Ma (Figures 4.4 a and b);
(iii) During the early stages of subduction, crustal erosion and thinning are controlled by the mechanical coupling between the interacting plates (Figures 4.4 a and b);
(iv) In the advanced stages of subduction, however, the main role of crustal erosion and thinning is played by the local mantle convective flow in the wedge area (Figure 4.4 c);
(v) Since the beginning of subduction, a widening of the trench trough occurs until a stationary configuration is reached after a few million years (cyan colour in Figure 4.4 a);
(vi) After a few million years, the erosion/sedimentation mechanism is activated, with a vast amount of sediments that, with water, contributes to filling the trench and that sinks to great depths (black dots in Figures 4.4 a–c);
(vii) The *p–T* conditions become favourable for activating mantle hydration and serpentinization in the wedge area within the first 2 Myr from the beginning of subduction (yellow area in Figures 4.4 a–c).

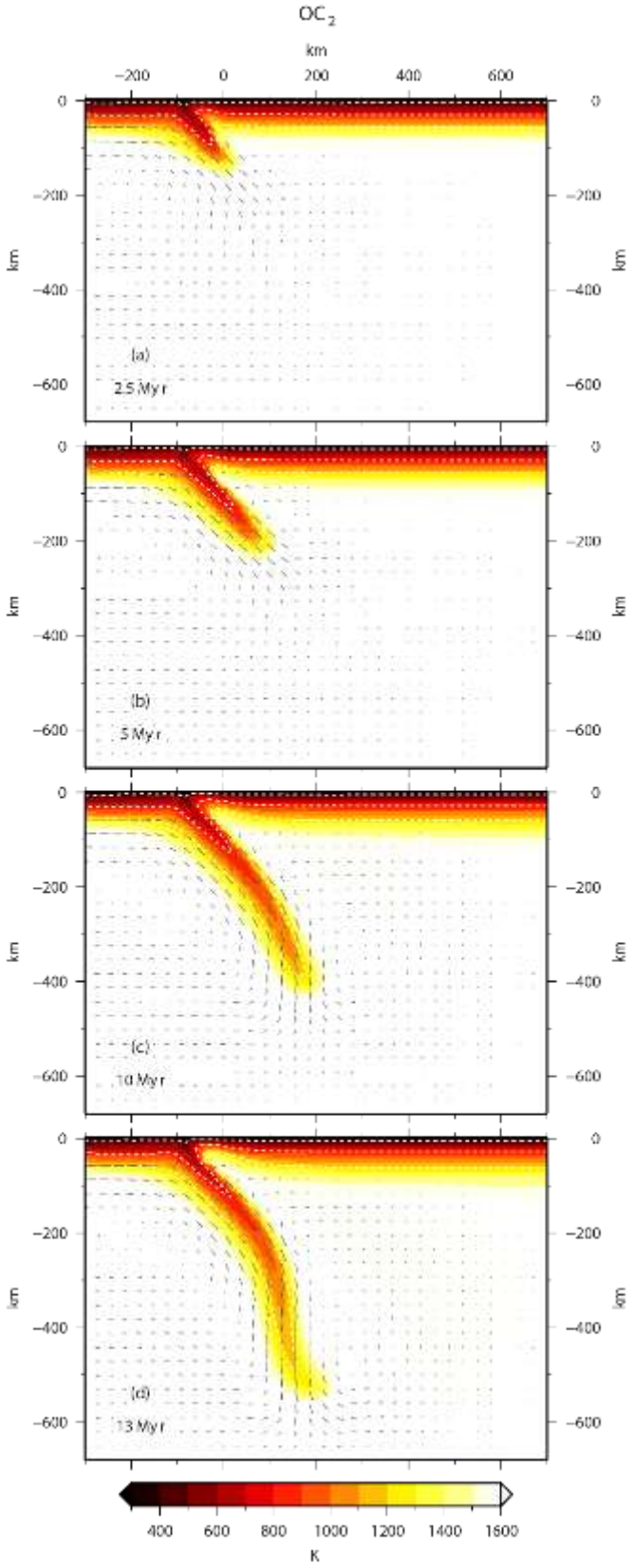

Figure 4.3: Large-scale thermal (colour) and velocity (black arrows) fields predicted by the OC_2 model after 2.5 (a), 5 (b), 10 (c) and 13 Myr (d) since the beginning of subduction. The white dashed lines indicate the 400, 800 and 1200 K isotherms. OC_2; u_s = 5 cm yr^{-1}; θ_s = 45°; c_f = 1.

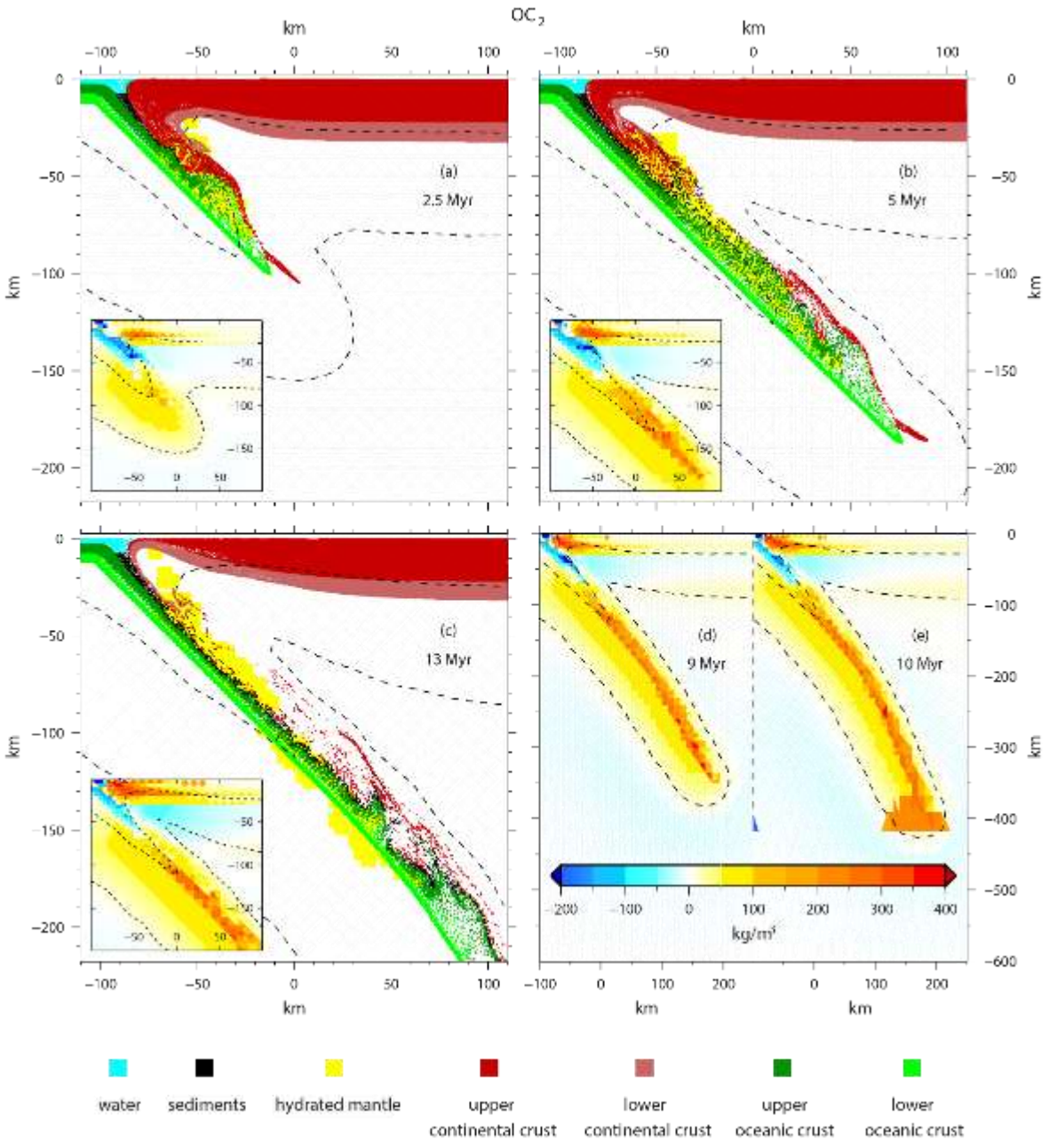

Figure 4.4: Marker distribution predicted by the OC_2 model after 2.5 (a), 5 (b) and 13 Myr (c) since the beginning of subduction. The insets show the density anomalies at the same times. Panels (d) and (e) show the large-scale density anomaly after 9 (d) and 10 Myr (e). The dashed black lines indicate the 800 and 1500 K isotherms. OC_2: $u_s = 5$ cm yr^{-1}; $\theta_s = 45°$; $c_f = 1$.

4.4.1.2 Density anomalies

The density anomalies predicted by the OC_2 model at different times after the initiation of subduction are shown in the insets of Figure 4.4.

Alternating regions of negative (blue colour) and positive (yellow to red colours) density anomalies are localized at shallow depths around the arc-trench region during the whole evolution (insets in Figures 4.4 a–c); a dominant positive density anomaly, increasing in time, characterizes the core of the subducting lithosphere to great depths (Figures 4.4 d and e). Both the extension and the magnitude of the density contrasts are sensitive to the age of subduction.

The negative density anomalies can be attributed to the following:

(i) The negative topography associated with the oceanic trench. The depression that constitutes the oceanic trench is filled with water and sediments and produces the most intense (and shallowest) negative anomalies (insets of Figures 4.4 a–c);
(ii) The light material entrapped in the subduction complex, particularly sediments and slices of continental crust scraped by the upper plate. The sediments and the continental material play a peculiar role: if their presence is initially important (Figure 4.4 a), then at longer times, their concentration decreases because they are transported at depth by the flow generated by the descent of the subducted plate (Figures 4.4 b and c);
(iii) The hydration of the mantle wedge leading to the development of serpentine (yellow colour in Figures 4.4 a–c) that has a density that is approximately 200 kg m^{-3} lower than that of the non-hydrated mantle;
(iv) The general warming of the system at the mantle levels of the wedge area (see the deflection of the isotherms 800 and 1600 K in Figures 4.4 b and c).

The positive density anomalies can in turn be attributed to the following:

(i) The sinking of cold and dense lithospheric mantle into warm and light material;
(ii) The phase transitions within the subducting plate triggered by the increase in pressure p and temperature T. In fact, mineralogical phases that are stable at lower depths are replaced by denser phases that are stable at higher p–T conditions. The effect of phase transitions adds to the thermal contraction;
(iii) The mantle that rises and fills the space previously occupied by the crust that has been

scraped from the overriding plate (Figures 4.4 a–c);
(iv) The general cooling and thermal contraction of the system far away from the trench.

4.4.1.3 Gravitational contribution

The profiles of the gravitational contributions, calculated for the OC_2 model using Equations (4.2) and (4.3), at time intervals of 1 Myr since the beginning of subduction and along the top boundary of the model domain are shown in panel a of Figure 4.5. Each profile is characterized by two maxima and a minimum within a distance of 200 km (Figure 4.5 a). The most intense maximum is located on the upper plate, while the secondary one is located behind the trench. The local minimum is positioned approximatively above the trench. The gravity anomalies decrease progressively outwards, assuming an almost constant value in the far field. With the progression of the subduction, the intensity of the gravity anomalies increases globally, accompanied by a coeval increase in the difference between the absolute maximum and the minimum. For the OC_2 model, the positions of the two maxima and of the minimum remain almost unchanged for the entire evolution.

The analysis of the separate contributions of the positive and negative density anomalies (Figures 4.5 b and c, respectively) allows us to clarify the origin of the peculiar style of the gravitational contribution and its variation in time and space. The bulk of the gravity change due to the negative anomalies in the surrounding of the trench occurs within the first two million years (Figure 4.5 c) and is attributable to the formation of the trench trough, to the subduction of crust and sediments and to the mantle wedge hydration. Subsequently, the most significant changes occur far from the subduction complex, and these changes can be associated with the progressive but widespread cooling of the system. Conversely, the progressive growth of the positive density anomalies (Figure 4.4) induces an equally continuous increase in their gravitational contribution, although with different rates (Figure 4.5 b). The following four phases in the time variation of the gravity contribution can be distinguished:
(i) A first phase, from the beginning of subduction to approximately 5 Myr. This phase is characterized by the highest rate of growth in the surroundings of the trench, with a total variation of approximately 200 mGal (blue lines in Figure 4.5 a). During this first period, the

subducted slab reaches a depth of more than 200 km (Figure 4.3 b), and most of the negative and positive density anomalies are localized at shallow/intermediate depths around the trench (inset of Figure 4.4 b);

(ii) A second phase, from 5 to 9 Myr (cyan to yellow lines in Figure 4.5 a). During this phase, the gravitational contribution continues to increase, but at a lower rate, and the positive density anomalies still grow but at great depths (Figure 4 c, and inset of Figure 4.4 c);

(iii) A third phase, from 9 to approximately 11 Myr (yellow to dark orange lines in Figure 4.5 a). This phase is characterized by a gravity change of approximately 60 mGal within just 2 Myr. Note that this effect occurs when the subducted slab crosses the *olivine – spinel* transition at a depth of 410 km (Figure 4.4 d and e), where a density change of approximately 100 kgm^{-3} occurs. The great depth at which the density variation occurs makes the corresponding perturbation induced on the gravity field have a regional character;

(iv) A fourth phase, from 11 Myr onwards (dark orange to pink lines in Figure 4.5 a), during which the growth rate is stabilized everywhere at low values of the far field.

Figure 4.6 shows the rate of change of the gravitational contribution of the density anomalies predicted by the OC_2 model. The plotted rate of change corresponds to the average value calculated over a time span of 0.5 Myr, which confirms that during the first phase, the gravitational contribution of the negative density anomalies increases rapidly at a rate as high as 0.05 μGal yr^{-1} (Figure 4.6 c). Afterwards, the rate of change remains smaller than 0.01 μGal yr^{-1}. Regarding the gravitational contribution of the positive density anomalies (Figure 4.6 b) during the first phase, the corresponding rate of change is comparable to that associated with the negative density anomalies and is reduced by almost a factor of two during the second phase. The discontinuity observed at approximately 9 Myr from the beginning of subduction (yellow lines in Figures 4.6 a and b) is evident here in terms of a rate of change varying from approximately 0.02–0.03 μGal yr^{-1}, moving from the lower to the upper plates; values close to 0.04 μGal yr^{-1} characterize the surroundings of the trench (Figures 4.6 a and b). The low values of the rate of change characterizing the mature phases indicate that, at long times, the contribution from the positive density anomalies becomes quasi-stationary.

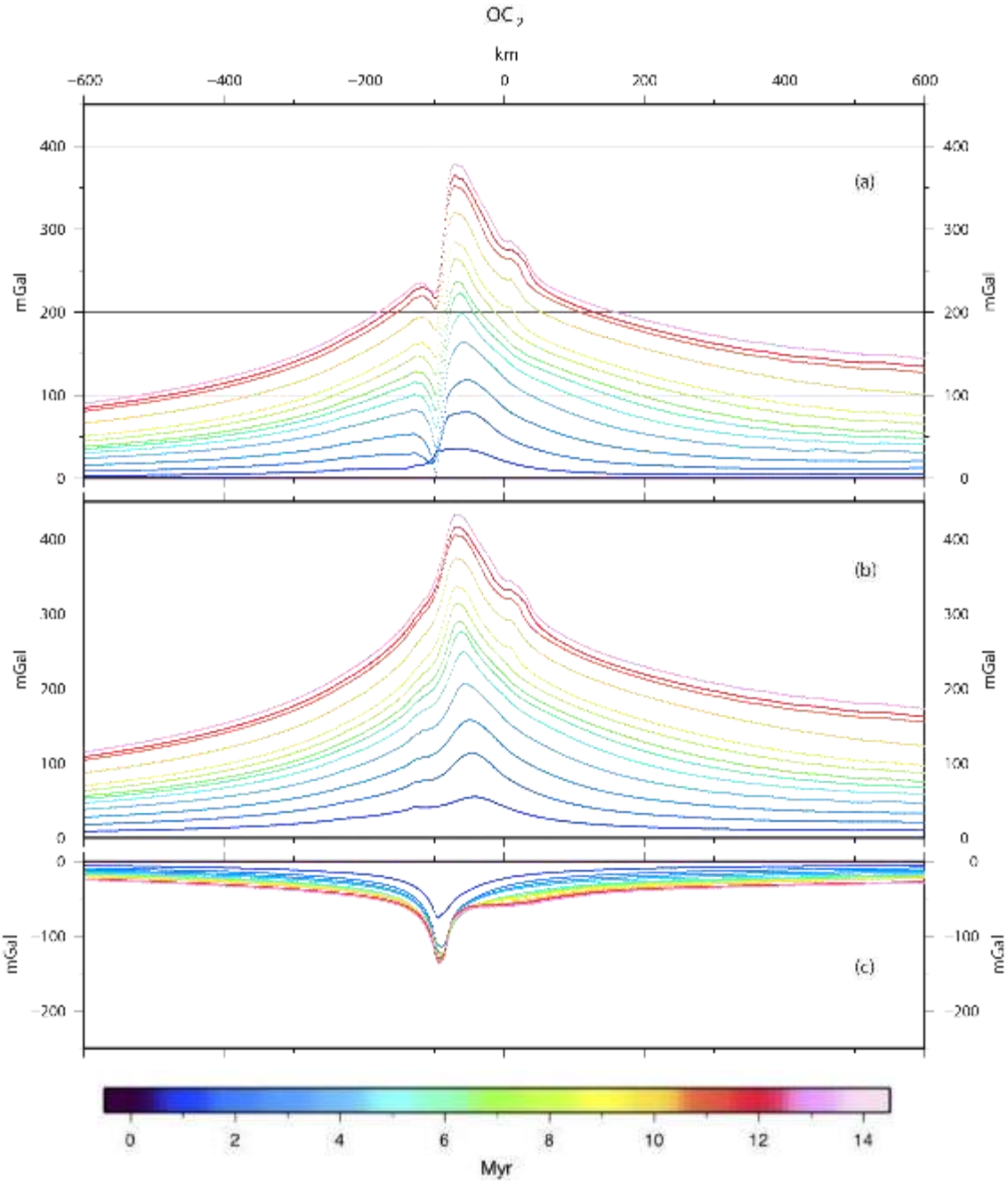

Figure 4.5: (a) Gravitational contribution of the density anomalies predicted by the OC_2 model after different time intervals since the beginning of subduction.(b) Gravitational contribution of the sole positive density anomalies. (c) Gravitational contribution of the sole negative density anomalies. The profiles are plotted at 1 Myr time intervals. Colours indicate the age of subduction. OC_2: $u_s = 5\,\mathrm{cm\,yr^{-1}}$; $\theta_s = 45°$; $c_f = 1$.

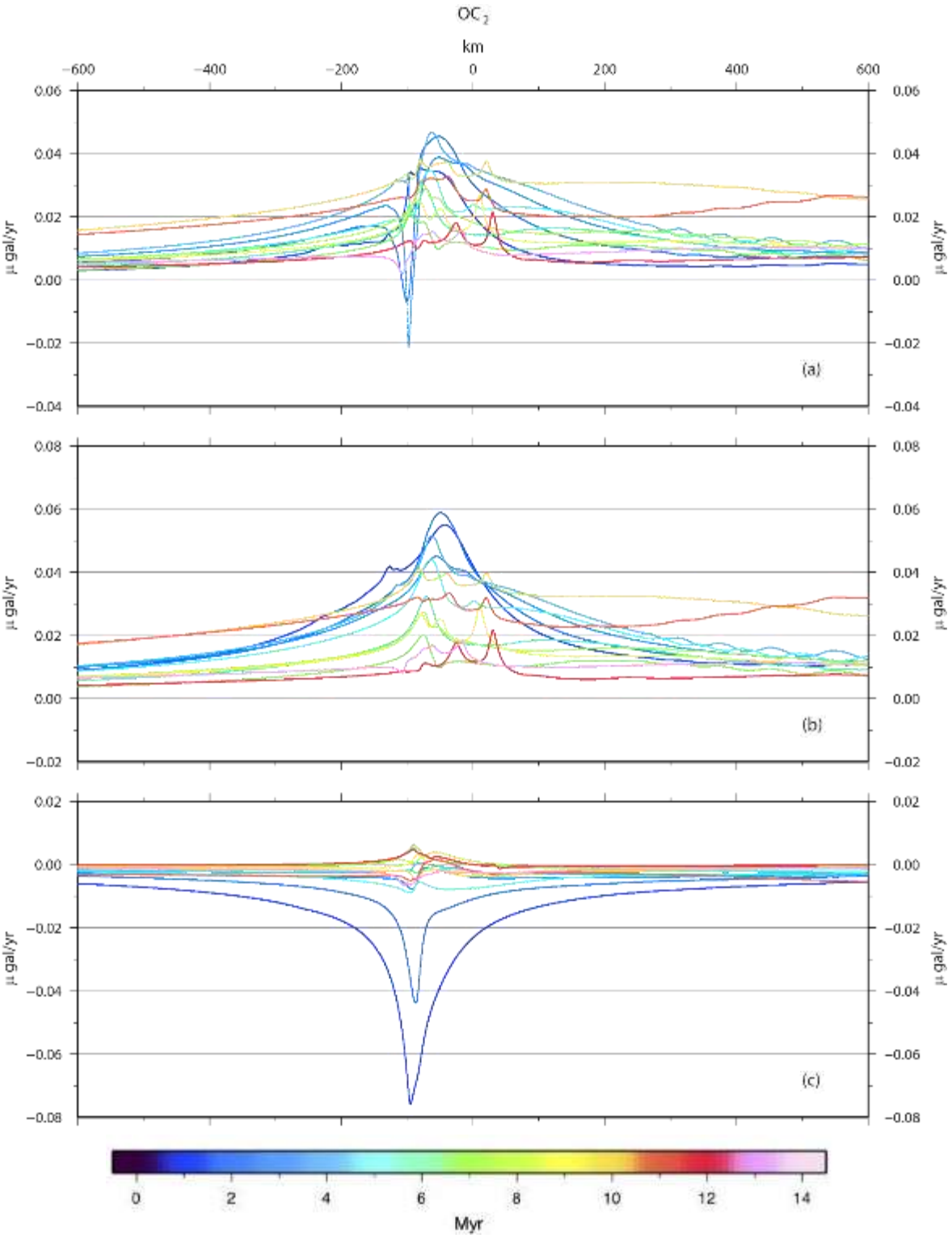

Figure 4.6: (a) Rate of change of the gravitational contribution of the density anomalies predicted by the OC_2 model after different time intervals since the beginning of subduction. (b) Rate of change of the gravitational contribution of the sole positive density anomalies. (c) Rate of change of the gravitational contribution of the sole negative density anomalies. The profiles are plotted at 1 Myr time intervals. Colours indicate the age of subduction. OC_2: $u_s = 5\,\mathrm{cm\,yr^{-1}}$; $\theta_s = 45°$; $c_f = 1$.

4.4.2 Effects of a varying c_f, θ_S, u_s and of a OO environment

4.4.2.1 Coupling factor c_f

To investigate the effects of a different degree of plate coupling on the gravitational field, we implemented a different set of models with the same values for all the characteristic parameters, with the exception of the value of the coupling factor c_f, set equal to 1 (total coupled system), 0.5 and 0.25 (almost completely decoupled system). Figure 4.7 shows how a different plate coupling degree along the contact between the subducting and overriding plates impacts the global thermomechanics of the subduction complex, with panels a and b corresponding to the fully coupled OC_2 model and panels c and d corresponding to the OC_5 model, characterized by a c_f = 0.25. During the early stages of subduction, no significant differences in the global thermal field are evident, with the exception of the slightly lower temperatures in the wedge area occurring as the plate coupling decreases (compare panel c to panel a of Figure 4.7). Over time, the difference in the thermal state is intensified and, as the plate coupling decreases, the cooling of the wedge area progressively increases (compare panel d to panel b of Figure 4.7) while, at great depths, the subducted slab remains warmer (compare panels e and f of Figure 4.7, corresponding to c_f = 0.25, to panels c and d of Figure 4.3, corresponding to c_f = 1). The thermomechanics remain unchanged at great distances from the trench.

The explanation of the enlightened changes in the thermal field stands on the more vigorous small-scale convection when the plate coupling is higher in the corner region between the subducting and overriding plate, which enhances the entering of cold material into the mantle due to the active subduction, making the fully coupled OC_2 model colder at depth compared to the decoupled OC_5 model. At the same time, as already stated in Section 4.4.1.1, the large-scale flow favours the rising of hot mantle in the wedge area, producing a progressive local thermal thinning of the overriding plate (Figures 4.3 c and d). The concomitance of these two factors makes the OC_2 system warmer at shallow depths and colder at deep depths. For low coupling (Figures 4.7 c–f) the two plates are partially or totally mechanically disjoined and the low intensity convective cornel flow is not able to perturb the thermal field in the wedge area, where the thermal state becomes increasingly depressed over time. At the same time, the progressive cooling of the wedge area further inhibits the

convective flow in the wedge which in turn disfavors the subduction of cold material for the lower plate coupling model, which thus remains warmer at great depths.

The role of plate coupling appears to be even more evident from the distribution of the markers in the wedge area (Figure 4.8). At the early stages of subduction, the scraping of the crustal material belonging to the upper plate is increasingly less effective as the plate coupling decreases (Figures 3.8 a and b, compared to Figure 4.4 a). A smaller amount of the scraped crust is subducted at great depths over time compared to the OC_2 model (Figure 4.4 c), and over long times, the recycling flow of crustal material inside the hydrated mantle wedge is more intense (Figures 4.8 c and d). Focusing on this last aspect, the maximum depth of the hydrated area is greater for strong plate coupling (Figure 4.4 with respect to Figure 4.8); conversely, the horizontal extension of the hydrated area increases as the coupling decreases, favoured by the low temperatures that characterize the wedge area.

The differences in the density anomalies predicted by models characterized by different couplings (insets of Figure 4.8) increase with the age of subduction. The main differences occur at low depths, where the less effective mantle wedging occurring for low plate coupling causes a shallow positive density anomaly of smaller intensity (insets of Figure 3.8 compared to insets of Figure 4.4). The positive density anomaly is instead mainly due to the ascent to low depths of the lower crust, which is heavier than the upper crust. The negative density anomaly, associated with the trench trough, the subducted crust and sediments and the mantle hydration, increases and widens laterally as the plate coupling decreases (Figures 4.8 c and d, compared to Figure. 4.4 c). Finally, the diffuse negative density anomaly associated with the warming of the mantle in the wedge area disappears for low values of plate coupling.

Figure 4.9 shows the gravitational contribution predicted by the OC_3 and OC_5 models, accounting for plate couplings of $c_f = 0.5$ and $c_f = 0.25$, respectively. The decrease in the maximum value of the positive contribution accompanying the decrease in plate coupling is due to both the warming of the internal part of the subducted plate, which is lighter for low plate coupling with respect to the strong coupling (Figures 4.7 e and f), and to the missing wedging mantle flow (Figures 4.8 b and d). In contrast, the gravitational contribution due to negative density anomalies increases both in magnitude and in width as the plate coupling decreases, reflecting the differences in the negative density anomaly distribution discussed above and particularly the progressive enlargement of the hydrated mantle area where a very intense recirculation of crustal material occurs (Figures 4.8 b and d).

Note that with the progression of the subduction, the amplitude of the gravity trough increases as the plate coupling decreases. Although the degree of plate coupling does not affect the position of the local minimum that remains localized above the trench throughout the evolution, the position of the absolute maximum moves forward over the upper plate as the degree of plate coupling decreases (Figure 4.9), which is correlated with the main role played by the heavy subducted slab in localizing the bulk of the positive density anomaly further away from the trench, below the upper plate, as subduction progresses.

4.4.2.2 Subduction dip θ_S

Figure 4.10 shows the temperature and velocity fields (panels a and b), the marker distribution (panels c and d) and the density anomalies (insets of panels c and d) predicted after 2.5 and 13 Myr from the beginning of subduction by the OC_7 model that is characterized by a subduction velocity u_s = 5 cm yr^{-1}, a coupling factor c_f = 0.5 and a subduction dip θ_s = 60°. With respect to the homologous 45° OC_3 model, a higher subduction dip angle allows the development of a more intense mantle wedge flow, responsible for a stronger erosion and thinning of the upper plate, with a larger amount of light material (both crust and sediments) dragged at great depths (compare panels c and d of Figure 4.10 to panels a and c of Figure 4.8). The local thermal warming occurring at mantle levels in the wedge area also generates unfavorable *p–T* conditions for mantle hydration, which in turn limits the recirculation of light material. All these factors generate intense and localized negative and positive density anomalies, as shown in the insets of panels (c) and (d) of Figure 4.10. The substitution of the scraped crust and the rising of cold mantle is responsible for shallow positive density anomalies that are considerably more intense than that predicted by the homologous 45° OC_3 model (compare panel d of Figure 4.10 to panel c of Figure 4.8). Conversely, at greater depths, the positive density anomalies are less intense for the 60° OC_7 model, mainly because the interior of the subducted slab remains warmer than in the 45° OC_3 model (compare panel d of Figure 4.10 to panel c of Figure 4.8). Regarding the negative density anomalies, the component associated with the trench trough, the subducted crust and sediments and the mantle hydration remains almost unchanged in magnitude but assumes a thinner shape along the subduction plane. Furthermore, a diffuse negative anomaly appears at the mantle level

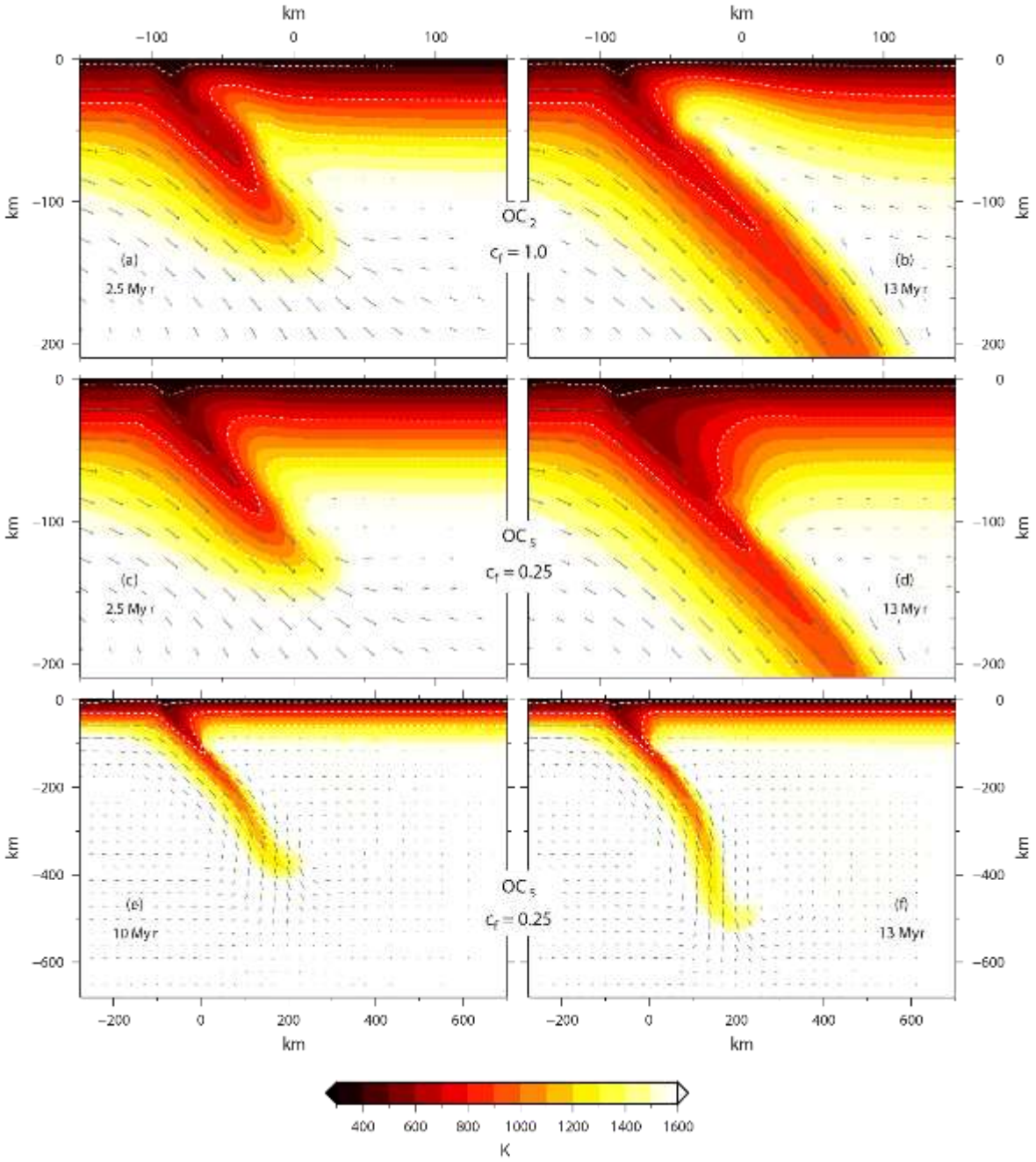

Figure 4.7: Thermal (colour) and velocity (black arrows) fields predicted by the OC_2 (panels a and b) and OC_5 (panels c and d) models after 2.5 (panels a and c) and 13 Myr (panels b and d) since the beginning of subduction. Panels (e) and (f) show, at the large scale, the thermal and velocity fields predicted by model OC_5 after 10 (e) and 13 Myr (f) since the beginning of subduction. The white dashed lines indicate the 400, 800 and 1200 K isotherms. OC_2: u_s = 5 cm yr^{-1}; θ_s = 45°; c_f = 1; OC_5: u_s = 5 cm yr^{-1}; θ_s = 45°; c_f = 0.25.

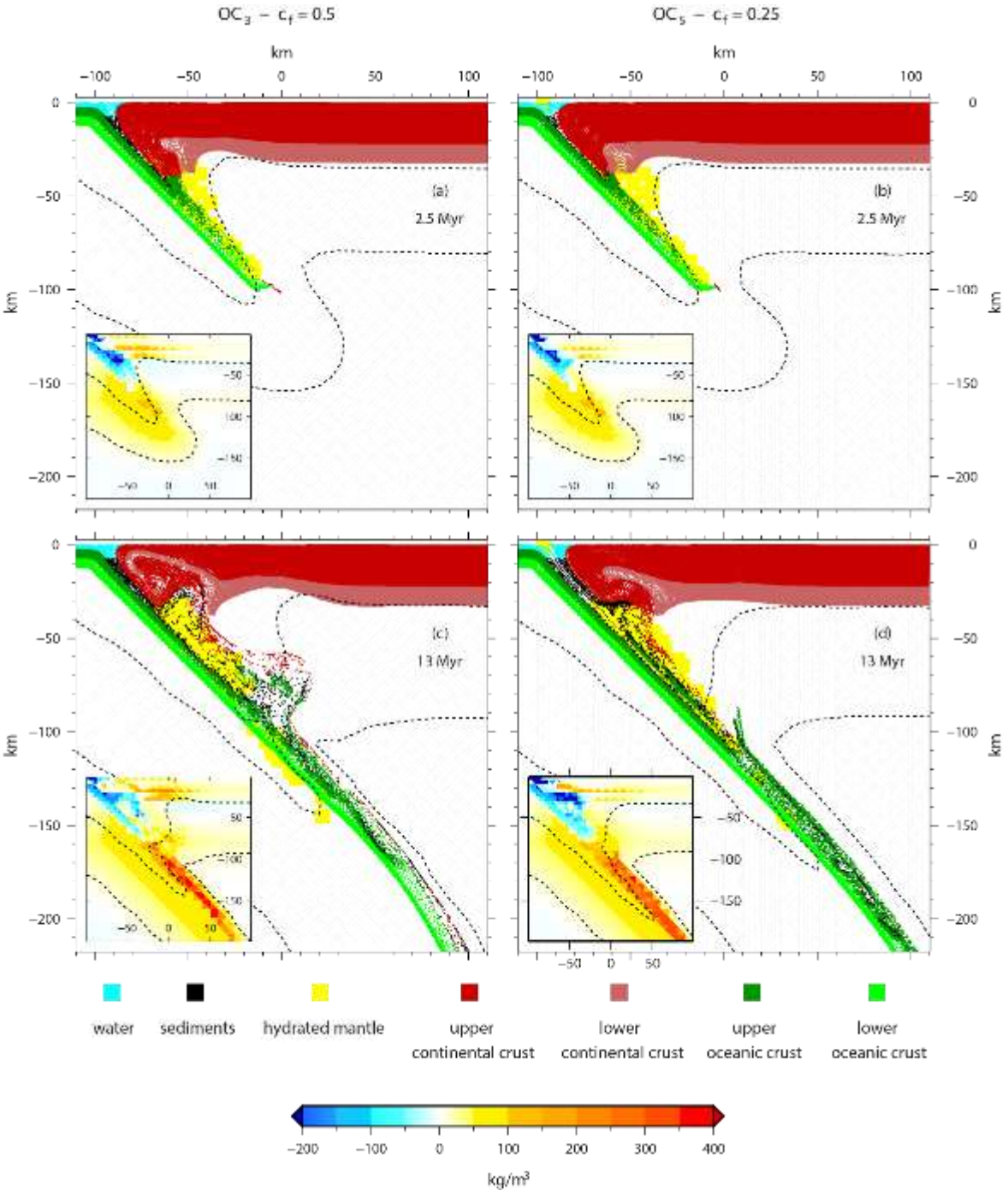

Figure 4.8: Marker distribution predicted by the OC_3 (panels a and c) and OC_5 (panels b and d) models after 2.5 (panels a and b) and 10 Myr (panels c and d) since the beginning of subduction. The insets in the same panels show the density anomalies at the same times. The dashed black lines indicate the 800 and 1500 K isotherms. OC_3: $u_s = 5$ cm yr $^{-1}$; $\theta_s = 45°$; $c_f = 0.5$; OC_5: $u_s = 5$ cm yr^{-1}; $\theta_s = 45°$; $c_f = 0.25$.

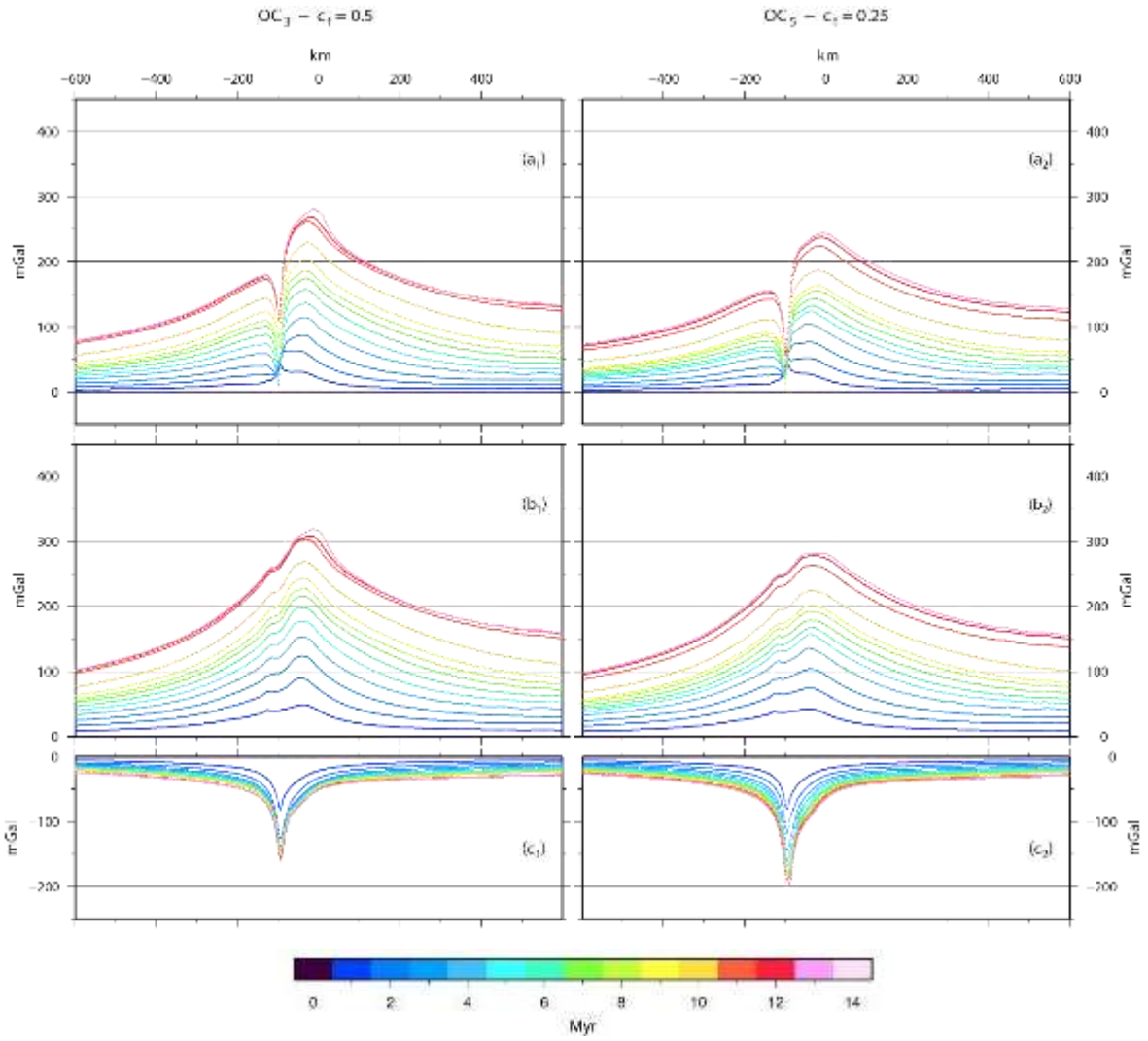

Figure 4.9: Gravitational contribution of the density anomalies predicted by the OC_3 (a1) and OC_5 (a2)models after different time intervals since the beginning of subduction. The Gravitational contribution of the sole positive density anomalies predicted by the OC_3 (b1) and OC_5 (b2) models. (c) Gravitational contribution of the sole negative density anomalies predicted by the OC_3 (c1) and $OC5$ (c2) models. The profiles are plotted at 1 Myr time intervals. Colors indicate the age of subduction. OC_3: $u_s = 5$ cm yr $^{-1}$; $\theta_s = 45°$; $c_f = 0.5$; OC_5: $u_s = 5$ cm yr^{-1}; $\theta_s = 45°$; $c_f = 0.25$.

of the wedge area, similar to that predicted by the fully coupled OC_2 model (Figure 4.4 c). However, it is now less intense because the lower plate coupling makes the local crustal erosion due to the mantle wedging flow not accompanied by coeval and equally effective local heating (compare isotherms 800 and 1500 K in Figure 4.10 d, and Figure 4.4 c).

Figure 4.11 shows the gravitational perturbation due to the density anomaly shown in Figure 4.10. A decrease of approximately 20 mGal in the magnitude of the gravitational contribution due to the negative density anomalies occurs with respect to the 45° OC_3 model

during the whole evolution (compare panel c of Figure 4.11 to panel c_1 of Figure 4.9); an increase in the gravitational contribution due to the positive density anomalies also occurs, up to more than 50 mGal in the mature stages of subduction. In addition, during evolution, the lateral extension of the gravity trough decreases with time because the absolute maximum moves towards the trench as a consequence of the intensification and localization of the shallow positive density anomaly (insets of Figures 4.10 c and d). This behaviour is opposite of that occurring with the 45° OC_3 model.

Finally, because the subducted plate reaches the olivine-spinel transition in a more vertical way, the jump in the gravitational contribution occurs earlier and more rapidly (compare Figure 4.11 b, to Figure 4.9 b_1).

4.4.2.3 Subduction velocity u_s

To identify the effects induced by a different subduction velocity on the gravitational field, we compare the predictions from three models characterized by the average values of all the characteristic parameters, with the exception of the assumed subduction velocity, set equal to 8 cmyr–1 (OC_6 model), 5 cm yr^{-1} (OC_3 model) and 2 cm yr–1 (OC_{14} model) (panels a_i, b_i and c_i of Figure 3.12, respectively). In this case, the comparison is not performed after the same time span since the beginning of the subduction but rather after a different time span for each model, when the same amount of ocean is consumed, specifically 200 and 600 km, corresponding to approximately 2.5 and 7.5 Myr for u_s =8 cm yr^{-1}, 4 and 12 Myr for u_s = 5 cm yr^{-1}, and 10 and 32 Myr for u_s = 2 cm yr^{-1}. The depth of 200 km is chosen because the subducted slab is well developed but still unaffected by the olivine-spinel phase boundary, while the depth of 600 km is chosen because it is comparable with the maximum length of the Benioff planes.

The major effects of a change in subduction velocity are in the thermal field of the wedge area and of the subducted slab (Figure 4.12). From the general thermomechanical perspective, the more efficient advection characterizing the high-velocity model OC_6 of panels a1 and a_2 is responsible for a thinner and colder slab that favours maintaining the prescribed subduction dip angle at great depths (panel a_2 of Figure 4.12, compared to b_2 and c_2).

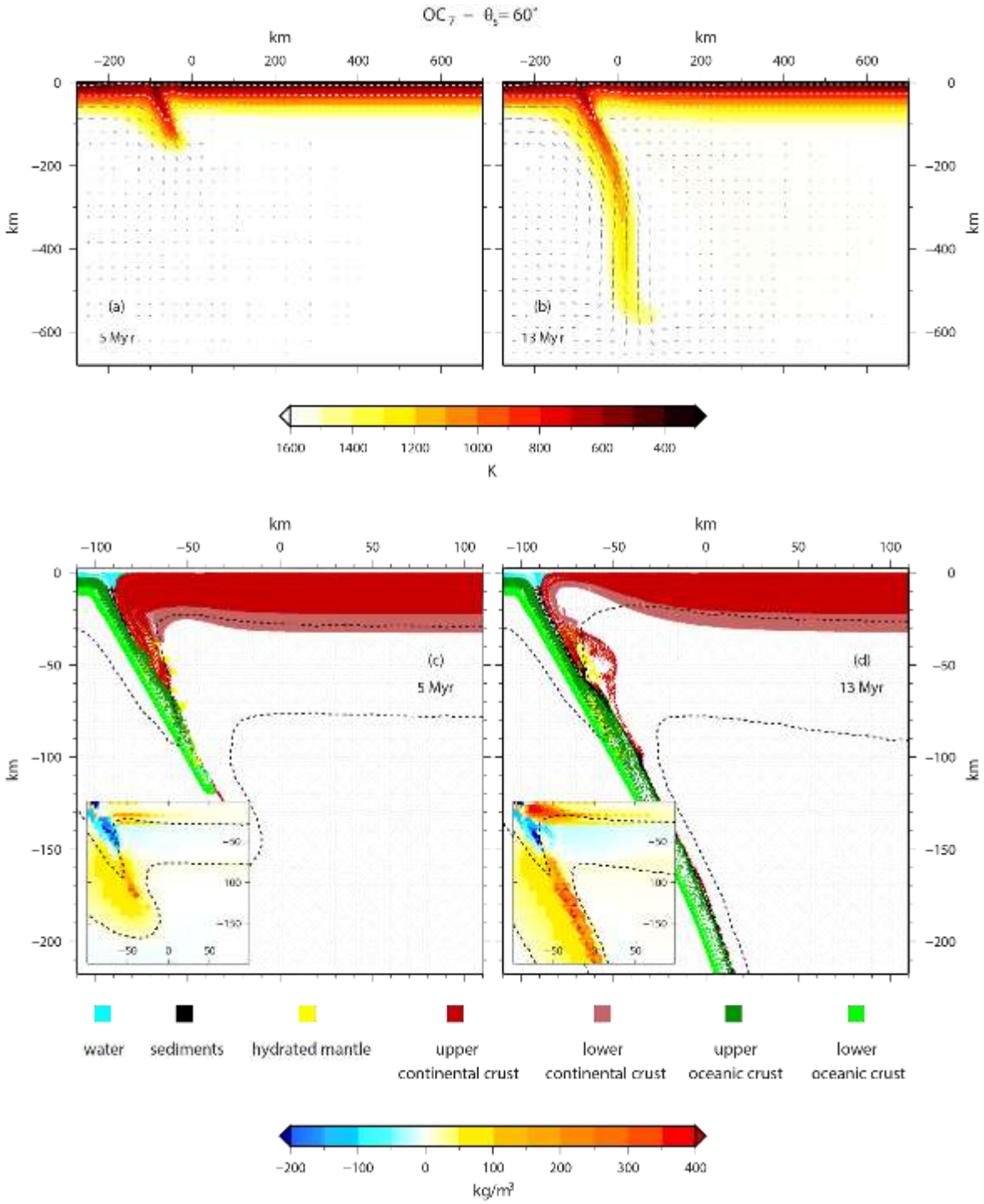

Figure 4.10: (a and b) Large-scale thermal (color) and velocity field (black arrows) predicted by the *OC*$_7$ model after 5 (a) and 13 Myr (b) since the beginning of subduction. The white dashed lines indicate the 400, 800, 1200 and 1500 K isotherms. (c and d) Marker distribution predicted by the same model after 5 (c) and 13 Myr (d) since the beginning of subduction. The insets show the density anomalies at the same times. The dashed black lines indicate the 800 and 1500 K isotherms. OC$_7$: u_s = 5 cm yr^{-1}; θ_s = 60°; c_f = 0.5.

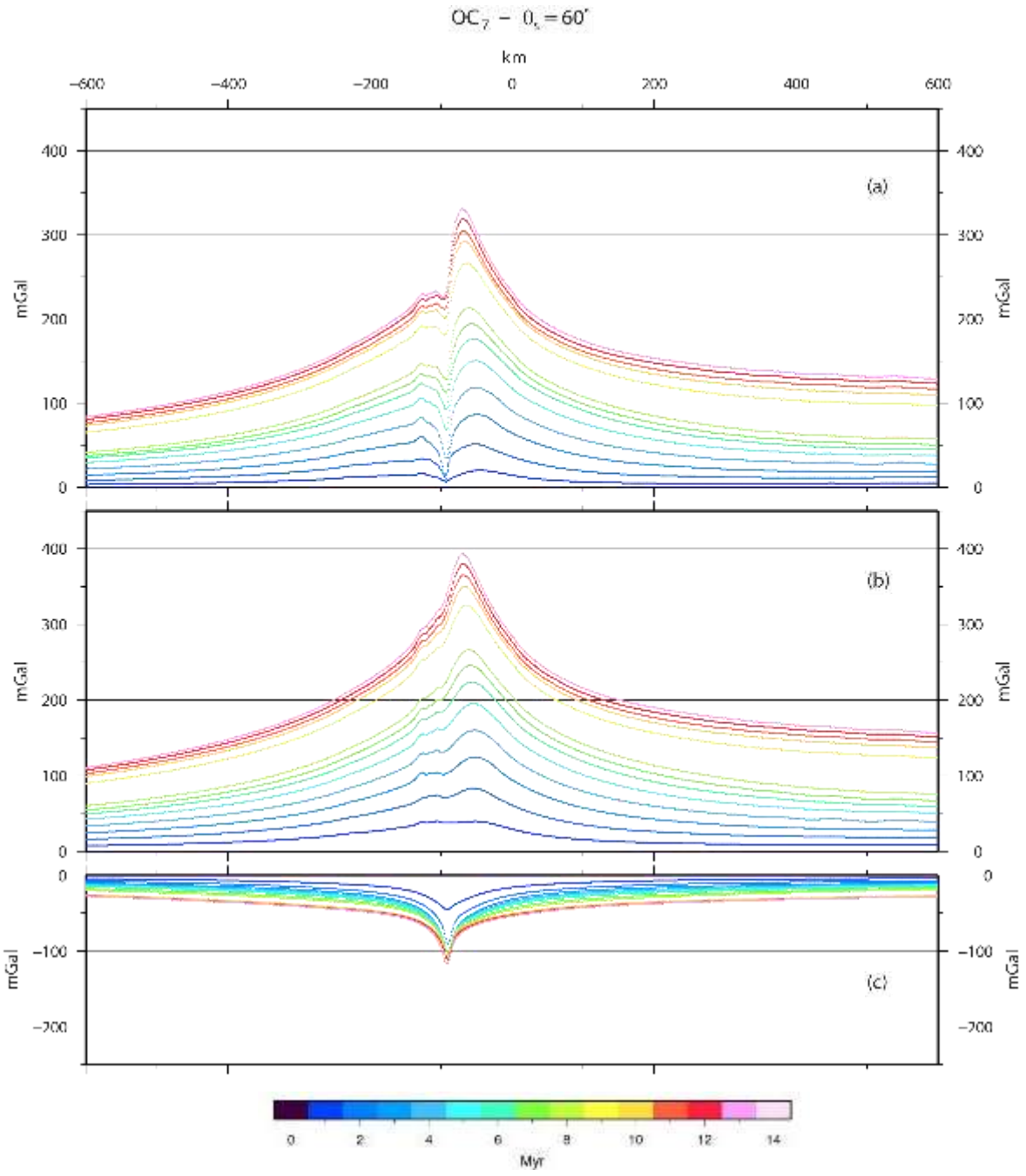

Figure 4.11: (a) Gravitational contribution of the density anomalies predicted by the OC_7 model after different time intervals since the beginning of subduction. (b) Gravitational contribution of the sole positive density anomalies. (c) Gravitational contribution of the sole negative density anomalies. The profiles areplotted at 1 Myr time intervals. Colors indicate the age of subduction. OC_7: u_s = 5 cm yr^{-1}; θ_s = 60°; c_f = 0.5.

In addition, the thermal field remains almost unchanged far from the trench (Figure 4.12). A decrease in the subduction velocity results in a thermal thickening of the subducted slab at shallow depths, in a more effective thermal erosion at high depths, in a significant variation of the deep dip and in a thermal thickening of the upper plate (Figure 4.12, panels b_1, b_2, c1 and c_2).

If we focus on the wedge area and on the distribution of the material particles (Figure 4.13, with the fast *OC*6 model in panels a and c and the slow OC_{14} model in panels b and d), it is evident that the thermal differences are not accompanied by equally significant differences in the distribution of material particles and by significant differences in the shallow density anomalies (compare panels c and d of Figure 4.13 to panel c of Figure 4.8).

Instead, at the deep lithosphere mantle level and at great depths, the thermal thickening characterizing the slowest subduction velocity model OC_{14} induces a widespread positive density anomaly close to the lithosphere base and a positive anomaly associated with the subducted slab with a thickness of almost one and a half times (compare panels e and f of Figure 4.13). Figure 4.14 shows the gravitational perturbation at times when the subducted slabs reach depths of 200 km (panels a_1, b_1 and c_1) and 600 km (panels a_2, b_2 and c_2) from the fastest to the slowest models, from top to bottom. Although the contribution of the negative density anomalies (dotted black lines) is not significantly influenced by the subduction velocity, the contribution from the positive density anomalies (dashed black lines) increases as the subduction velocity decreases due to the thermal thickening of the subducted plate and to the anomaly of the positive density that develops near the base of the lithosphere (also see the insets of panels e and f of Figure 4.13). The latter, due to its widespread nature, also intensifies the asymmetry in the gravity profile, increasing the difference between the minimum value of the gravitational contribution and its far field value as the subduction velocity decreases. Finally, note that at any time, the width of the gravity trough increases as the subduction velocity decreases.

It is certainly interesting to compare the rate of change of the gravity anomalies for different subduction velocities. Based on the considerations made in the previous paragraphs regarding the variations in time of the areal distribution and of the magnitude of the density anomalies obtained for different subduction velocities, we expect that the rate of change of the gravity anomalies varies significantly as the subduction velocity varies. This is in fact,

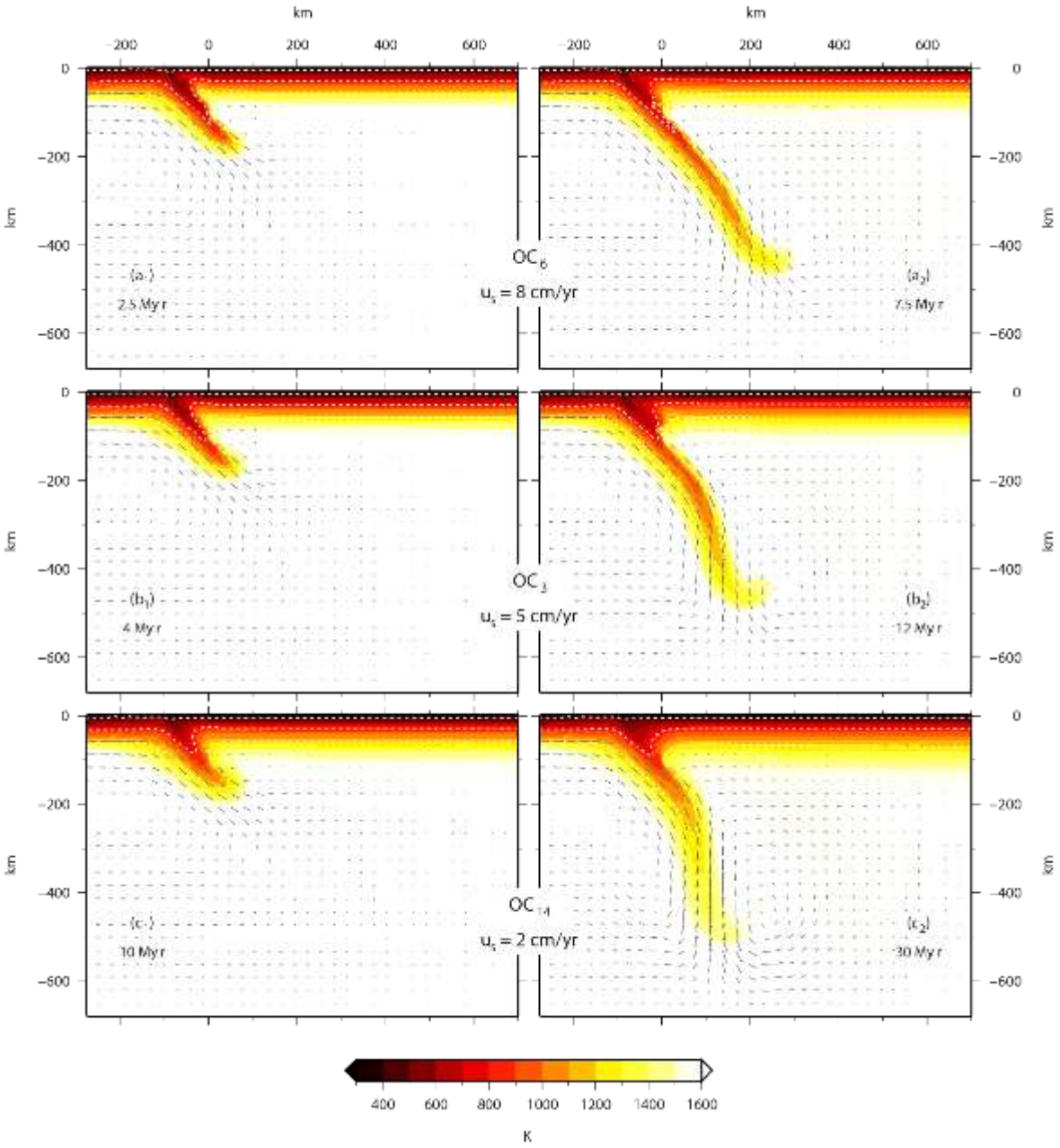

Figure 4.12: Large-scale thermal (color) and velocity (black arrows) fields predicted by OC_6 (panels a_1 and $a2$), OC_3 (panels b_1 and b_2) and OC_{14} (panels $c1$ and $c2$) when the same extent of ocean is consumed, specifically 200 km (2.5 Myr for the $OC6$ model, panel $a1$, 4 Myr for the OC_3 model, panel $b1$ and 10 Myr for the OC_{14} model, panel c_1) and 600 km (7.5 Myr for the OC_6 model, panel a_2, 12 Myr for OC_3 model, panel b_2 and 30 Myr for the OC_{14} model, panel c_2). The white dashed lines indicate the 400, 800 and 1200 K isotherms. OC_3: $u_s = 5$ cm yr^{-1}; $\theta_s = 45°$; $c_f = 0.5$; OC_6: $u_s = 8$ cm yr^{-1}; $\theta_s = 45°$; $c_f = 0.5$; OC_{14}: $u_s = 2$ cm yr^{-1}; $\theta_s = 45°$; $c_f = 0.5$.

what occurs in Figure 4.15, where the rates of change for the OC_6 (us = 8 cm yr^{-1}) and OC_{14} (u_s = 2 cm yr^{-1}) models are presented.

As expected, the differences can be significant and the rate of change decreases to one third when the subduction velocity decreases from 8 to 2 cm yr^{-1} (Figure 4.15), making slow subduction appear to be a quasi-static process even from the gravitational perspective. However, note that when the rates of change are normalised with respect to the corresponding subduction velocity, the graphs, with the exception of some differences due to local-scale features, become comparable (Figure 4.16), making it possible to estimate a maximum rate of change equal to 0.008 μGal yr^{-1} for each cm/yr of subduction velocity.

4.4.2.4 Ocean–ocean context

Here, we illustrate only the major differences between predictions from ocean–ocean models and the corresponding ocean–continent models.

Figure 4.17 shows the marker distribution and the density anomalies (in the insets) predicted by the OO_1, OO_4 and OO_7 models, with the coupling factor decreasing from top to bottom, from 1, 0.5 and 0.25, after 2.5 and 13 Myr from the beginning of subduction, at a velocity of 5 cm yr^{-1}, with a subduction dip angle of 45°. With respect to the corresponding ocean–continent-type models (models OC_2 - Figure 3.4, OC_3 and OC_5 - Figure 4.8), a generally larger amount of light material (both crust and sediments) recirculates in the wedge where a wider hydrated area is further developed. A significant erosion of the crust belonging to the upper plate occurs, allowing the exhumation of the recirculated light material.

This peculiar mass redistribution is at the origin of the very intense and shallow negative density anomalies that develop over an area wider than 60 km.

Figure 4.18 shows the gravitational contribution at 4 and 12 Myr from the initiation of subduction for the same models shown in Figure 3.17, with the coupling factor decreasing from top to bottom, from 1, 0.5 and 0.25. Unlike the ocean–continent context, plate decoupling does not significantly affect the shape of the gravitational contribution pattern. The aspects that deserve to be noticed are a slight increase in the positive contribution accompanying the decrease in the coupling of the plates and a slightly more significant increase in the negative contribution with the increase in the coupling (compare panels a and c of Figure 4.18). The most important characteristic is instead the greater width of the gravity

trough, on the order of more than 200 km, that occurs in the ocean–ocean environments compared to 100 km in the ocean–continental environment (Figure 4.14, panel b_2) due to the peculiar wider distribution of the recycled material (Figure 4.17).

4.5 Case studies: the Sumatra and Mariana complexes

4.5.1 Tectonic setting

The Sumatran and Mariana subductions are considered to be two classical tectonic settings representative of an ocean–continent subduction and an ocean–ocean subduction. The Indonesian Island of Sumatra represents an interesting natural laboratory for geodynamic and geophysical investigations because it is one of the most active regions in the world. In fact, numerous large earthquakes have occurred in the Sumatra subduction zone within the last two centuries, including the magnitude 9.3 Sumatra-Andaman earthquake on 26 December 2004 (*Gamage*, 2017). The subduction zone of Sumatra results from the underthrusting of the Indo-Australian Plate subducting beneath the Sunda plate, Andaman and Burma microplate (*Shapiro et al.,* 2008; *Gamage*, 2017) along three main trenches, Java, Sunda and Andaman–Nicobar *(Nielsen et al.,* 2004), with a convergence velocity that decreases northward, from 7.23 cm yr^{-1} off Java to 4.3 cm yr^{-1} in Andaman and approximately 5.5 cm yr^{-1} in the northern Sumatra (*Moeremans et al.,* 2014). The Andaman-Sumatra section of subduction represents an example of oblique subduction resulting in slip partitioning into a trench-normal component at the plate interface (*Moeremans et al.,* 2014) and a strike-slip component along the Great Sumatra Fault (GSF, *Moeremans et al.,* 2014; *Bradley et al.*, 2017) and possibly the West Andaman Fault (WAF, *Moeremans et al.,* 2014).

The convergence is nearly orthogonal along the Java trench and subparallel along the Andaman Islands trench (*Moeremans et al.,* 2014). The transition between the two subduction regimes occurs south of the Sunda Strait (*Malod and Kemal*, 1996). Here, where the plate boundary geometry changes abruptly, tomography and seismic studies show slab tearing, with a distinct gap in seismicity between depths of 300 and 500 km beneath the central Sunda (Java) block *(Kundu and Gahalaut,* 2011).

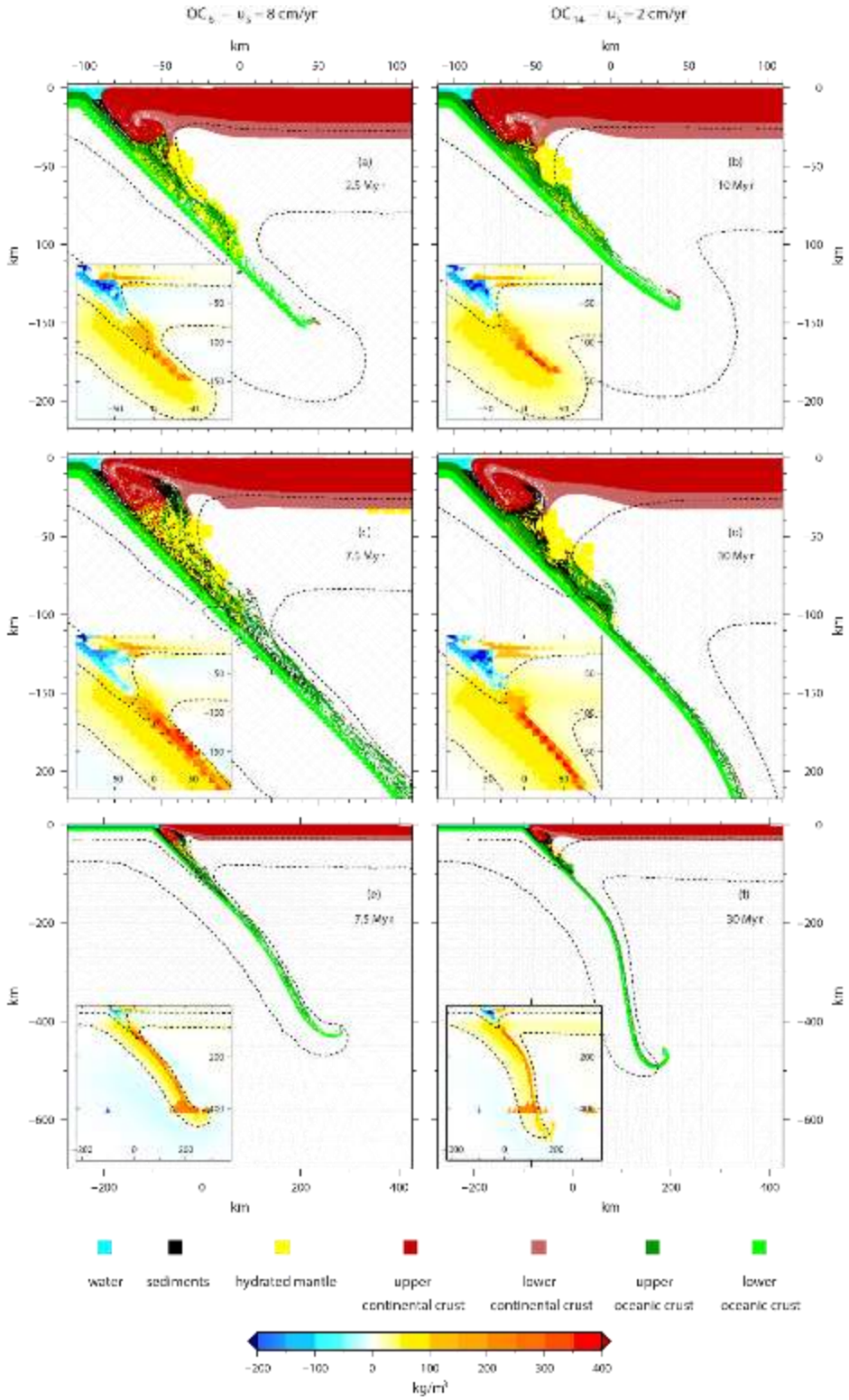

Figure 4.13: Marker distributions predicted by OC_6 (panels a and c) and OC_{14} (panels b and d) when the same extent of ocean is consumed, specifically 200 km (2.5 Myr for the OC_6 model, panel a, and 10 Myr for the OC_{14} model, panel b) and 600 km (7.5 Myr for the OC_6 model, panel c, and 30 Ma for OC_{14} model, panel d). Panels e and f show the large-scale marker distributions predicted by OC_6 after 7.5 Myr (e) and OC_{14} after 30 Myr (f) since the beginning of subduction. The insets in all panels show the density anomalies at the same times. The dashed black lines indicate the 800 and 1500 K isotherms. OC6: $u_s = 8$ cm yr^{-1}; $\theta_s = 45°$; $c_f = 0.5$; OC_{14}: $u_s = 2$ cm yr^{-1}; $\theta_s = 45°$; $c_f = 0.5$.

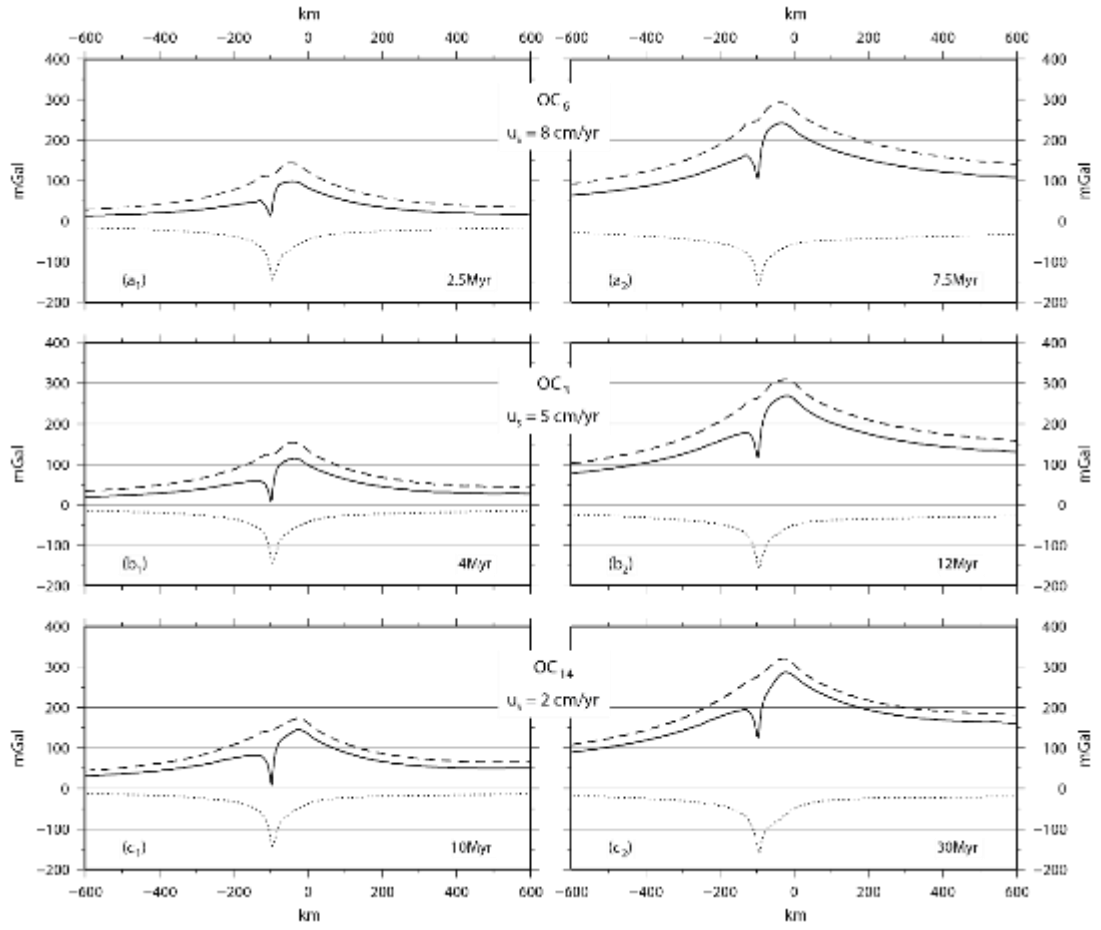

Figure 4.14: Solid lines indicate the gravitational contribution of the density anomalies predicted by OC_6 (panels a_1 and a_2), OC_3 (panels $b1$ and $b2$) and OC14 (panels $c1$ and $c2$) when 200 km (panels $a1$, b_1 and c_1) and 600 km (panels a_1, b_2 and c_2) of ocean is consumed. Dashed and dotted lines indicate the gravitational contribution of the sole positive and negative density anomalies, respectively, for the same models in the same configuration. OC_3: $u_s = 5$ cm yr^{-1}; $\theta_s = 45°$; $c_f = 0.5$; OC_6: $u_s = 8$ cm yr^{-1}; $\theta_s = 45°$; $c_f = 0.5$; OC_{14}: $u_s = 2$ cm yr^{-1}; $\theta_s = 45°$; $c_f = 0.5$.

In addition to strong strain partitioning, the area presents other peculiar tectonic settings, such as active spreading in the backarc beneath the Andaman Sea and lateral age variability of the incoming Indian Plate. Beneath Sumatra, a young oceanic lithosphere of approximately 40–60 Myr is subducting (*Schluter et al.,* 2002; *Shapiro et al.*, 2008), corresponding to a thickness of 80–100 km (*Turcotte and Schubert*, 2002). In contrast, off Java and Andaman Islands, the age of the oceanic lithosphere varies from 70 to 120 Myr and from 70 to 90 Myr (*Moeremans et al.,* 2014). This aspect influences the style of deformation and seismicity along the entire arc.

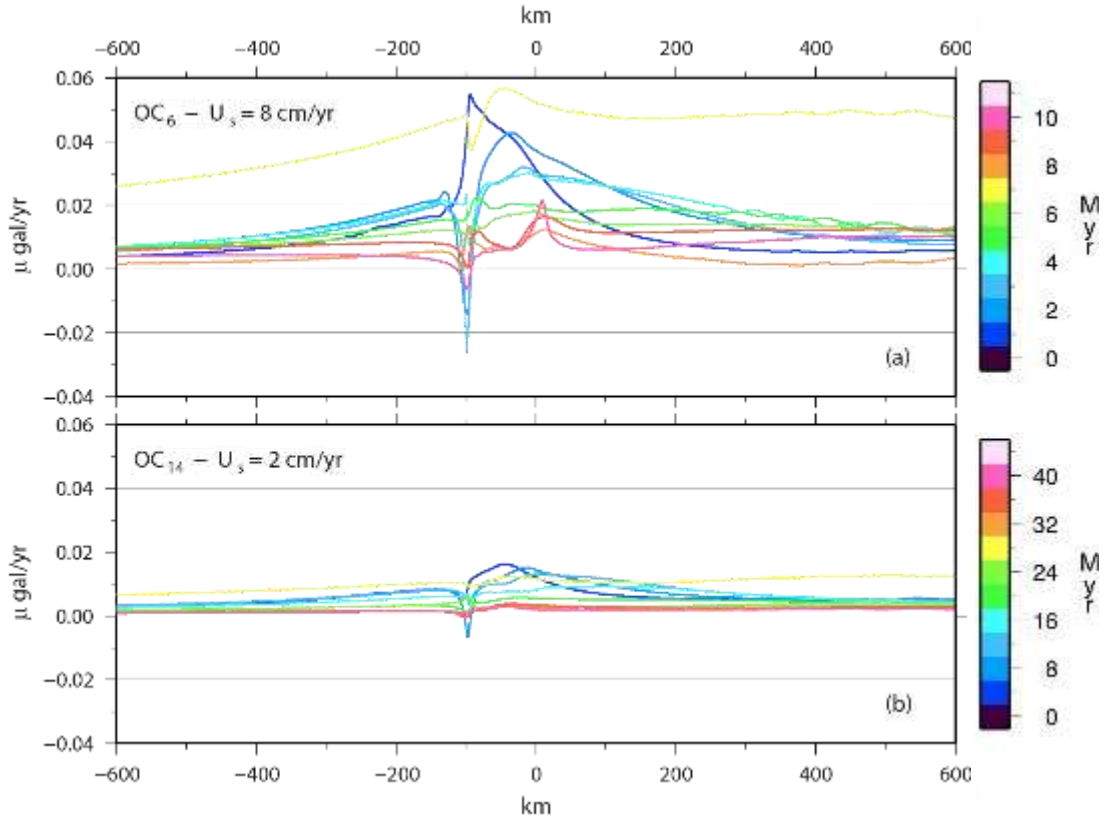

Figure 4.15: Rate of change of the gravitational contribution of the density anomalies predicted by OC_6 (panel a) and OC_{14} (panel b) after different time intervals since the beginning of subduction. The profiles are plotted at 1 and 4 Myr time intervals for OC_6 (panel a) and OC_{14} (panel b). OC_6: $u_s = 8$ cm yr^{-1}; $\theta_s = 45°$; $c_f = 0.5$; OC_{14}: $u_s = 2$ cm yr^{-1}; $\theta_s = 45°$; $c_f = 0.5$.

Where the lithosphere is younger and consequently warmer and more buoyant, the subducting plate and the mantle wedge appear to be strongly coupled with a Wadati-Benioff zone of approximately 30–45° (*Shapiro et al.,* 2008; *Kundu and Gahalaut*, 2011). In contrast, in adjacent areas to the north and south, the seismic zones have higher dip angles (*Shapiro et al.*, 2008; *Kundu and Gahalaut*, 2011).

The variability in the convergence velocity, particularly in the component perpendicular to the trench, as well as in the dip angles, from 30° to −45° to higher angles, indicates that the appropriate velocity values of 8, 5 and 2 cm yr^{-1} (with 5 cm yr^{-1} as the most representative value) and the three dip angles of 30°, 45° and 60° (with 45° the most representative one) are appropriate for the modelling of the EIGEN-6C4 gravitational disturbance characterized by a 2-D dipolar pattern perpendicular to the trench, first requiring a 2-D modelling approach as performed herein to capture the characteristics of the gravity pattern.

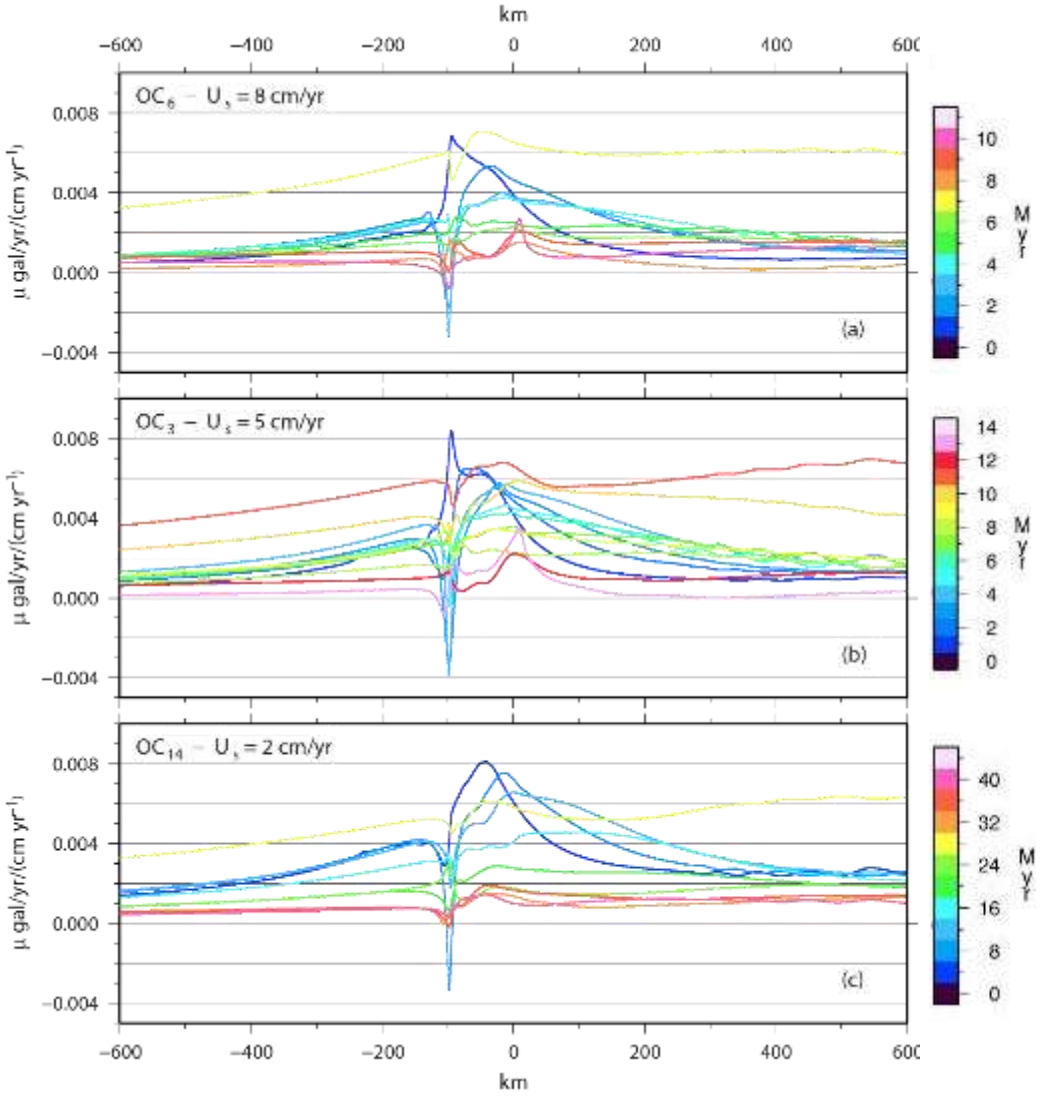

Figure 4.16: Rate of change, normalized with respect to the corresponding prescribed subduction velocity, of the gravitational contribution of the density anomalies predicted by *OC*6 (panel a), *OC*3 (panel b) and OC14 (panel c), after different time intervals since the beginning of subduction. The profiles are plotted at 1Myr for *OC*6 (panel a) and *OC*3 (panel b) and at 4 Myr time interval for OC14 (panel c). OC_3: $u_s = 5$ cm yr^{-1}; $\theta_s = 45°$; $c_f = 0.5$; OC_6: $u_s = 8$ cm yr^{-1}; $\theta_s = 45°$; $c_f = 0.5$; OC_{14}: $u_s = 2$ cm yr^{-1}; $\theta_s = 45°$; $c_f = 0.5$.

Regarding the age of subduction, for these case studies, we take as a reference the youngest age of the Sumatra oceanic lithosphere of 40 Myr.

Taken collectively, within the frame of a 2-D approach used to model the 2-D pattern of the EIGEN-6C4 gravitational disturbance, similar features can be found in the Izu-Bonin-Mariana (IBM) trench. Stretching for 2800 km (*Pearce et al.,* 2015) accommodates the oblique west-dipping subduction (*Faccenna et al.,* 2018; *Kong et al.,* 2018) of the Pacific beneath the Philippine Sea Plate at a velocity of approximately 9 cmyr^{-1} along the Izu–Bonin arc and 5 cm yr^{-1} along the Mariana arc (*Kong et al.*, 2018). Since the Eocene, the plate-

tectonic history of this region has been affected both by multiple clockwise rotation events of the Philippine Sea Plate, as evidenced by paleomagnetic data (*Hall et al.*, 1995; *Sdrolias et al.*, 2004), and by the northeast migration of the triple junction between the Eurasian, Philippine Sea, and Pacific Plates from 30 to 17 Myr (*Castle and Creager*, 1999). Along with the triple junction motion, the northern Izu-Bonin trench retreated over 1000 km to the northeast, producing the opening of the Shikoku basin (between 25 and 15 Myr, *Hall et al.*, 1995; *Anderson et al.*, 2017), while the Mariana trench retreated 400 km to the northeast (*Castle and Creager*, 1999; *Anderson et al.*, 2017) accompanied by the opening of the Parece Vela basin (Anderson *et al.*, 2017). The age of the subducting lithosphere varies along the arc system from approximately 135 Myr at the northern Izu-Bonin trench to over 150 Myr at the Mariana trench (*van der Hilst and Seno*, 1993), corresponding to a thickness of 160 km (*Turcotte and Schubert*, 2002). Several studies of seismic tomography and seismicity have clearly defined the geometry of the subducting slab in depth. The variation in the geometry of the subducted slab along the arc is a peculiar aspect of the region. *van der Hilst and Seno* (1993) proposed that, during the fast Oligocene-Middle Miocene, beneath the Izu-Bonin arc the combination of young oceanic lithosphere and rapid trench migration produced a shallow subduction angle, with the slab deflecting horizontally at the 670 km discontinuity (*van der Hilst and Seno*, 1993; *Miller et al.*, 2005; *Anderson et al.*, 2017; *Kong et al.,* 2018). In contrast, southward, below the Mariana trench, the slab plunges steeply into the lower mantle (*Faccenna et al.*, 2018; *Holt et al.,* 2018). The abrupt change from a horizontal to a vertical slab is accommodated by tearing at the junction of the Izu-Bonin and Mariana arcs at ∼26°N, where the Ogasawara Plateau occurs at the junction *(Anderson et al.,* 2017). In fact, tomographic and seismic the images reveal a distinct change in the seismic property of the subducted Pacific plate beneath Izu-Bonin arc, with a seismic gap at approximately 300–400 km, interpreted as a probable slab tear (*Kong et al.,* 2018). A N–S trending slab tear is also suggested at the southern end of the Mariana arc, known as the Challenger Deep (*Miller et al.,* 2006).

Due to the similarities in convergence velocity, dip angles and age, as well as their variability along the trench, we consider the Sumatra values for these parameters to also be appropriate for the Mariana case study, focusing on the effects of the most important difference between these two types of subduction, namely, the nature of the overriding plate, oceanic versus continental.

4.5.2 Regional gravity pattern

Figure 4.19 shows a regional map of the gravity disturbance in the surroundings of the Sumatra and Mariana subduction complexes based on the static global combined gravity field model EIGEN-6C4 (*Förste et al.,* 2014) and evaluated in the spherical approximation at a height h_S=5 km above the spheroid of radius R = 6378.137 km. We consider this altitude to smooth slightly the geodetic signal and make it more suitable to be compared with the modelled one. The geodetic functional gravity disturbance is defined as the difference between the magnitude of the gravity g and the magnitude of the normal gravity γ :

$$\delta g\,(h,\,\lambda,\,\varphi) = g\,(h,\,\lambda,\,\varphi) - \gamma\,(h,\,\varphi)\,, \tag{4.5}$$

where λ is the ellipsoidal longitude, φ is the ellipsoidal latitude and h is its height above the sea level. Among others, this functional is the most suitable for a direct comparison with our model predictions, because both normal gravity and actual gravity are calculated in the same point, without introducing any other reference point.

Figure 4.19 includes for each subduction complex three profiles perpendicular to the trench, along which the observed gravity disturbance will be compared to the modelled gravity disturbance. These profiles are chosen in order to sample three different regions of the subduction complex, taken collectively as representatives of the whole arc, being each of them perpendicular to a different sector of the arc itself.

The two settings portray similar gravity features away from the trench region over the upper plate, characterized by a widespread positive gravity disturbance up to 200 mGal in both the continental and oceanic domains. Differences are instead visible over the lower plates, with gravity disturbances very low, close to zero, over the oceanic plate at Sumatra and higher gravity positive values characterizing the upper oceanic plate of the Mariana subduction. In the proximity of the trench, the map shows the bipolar trend typical of the subduction complexes, and beyond the variability depending on the position along each arc, there are some features that are peculiar of each subduction context: ocean–ocean and ocean–continent.

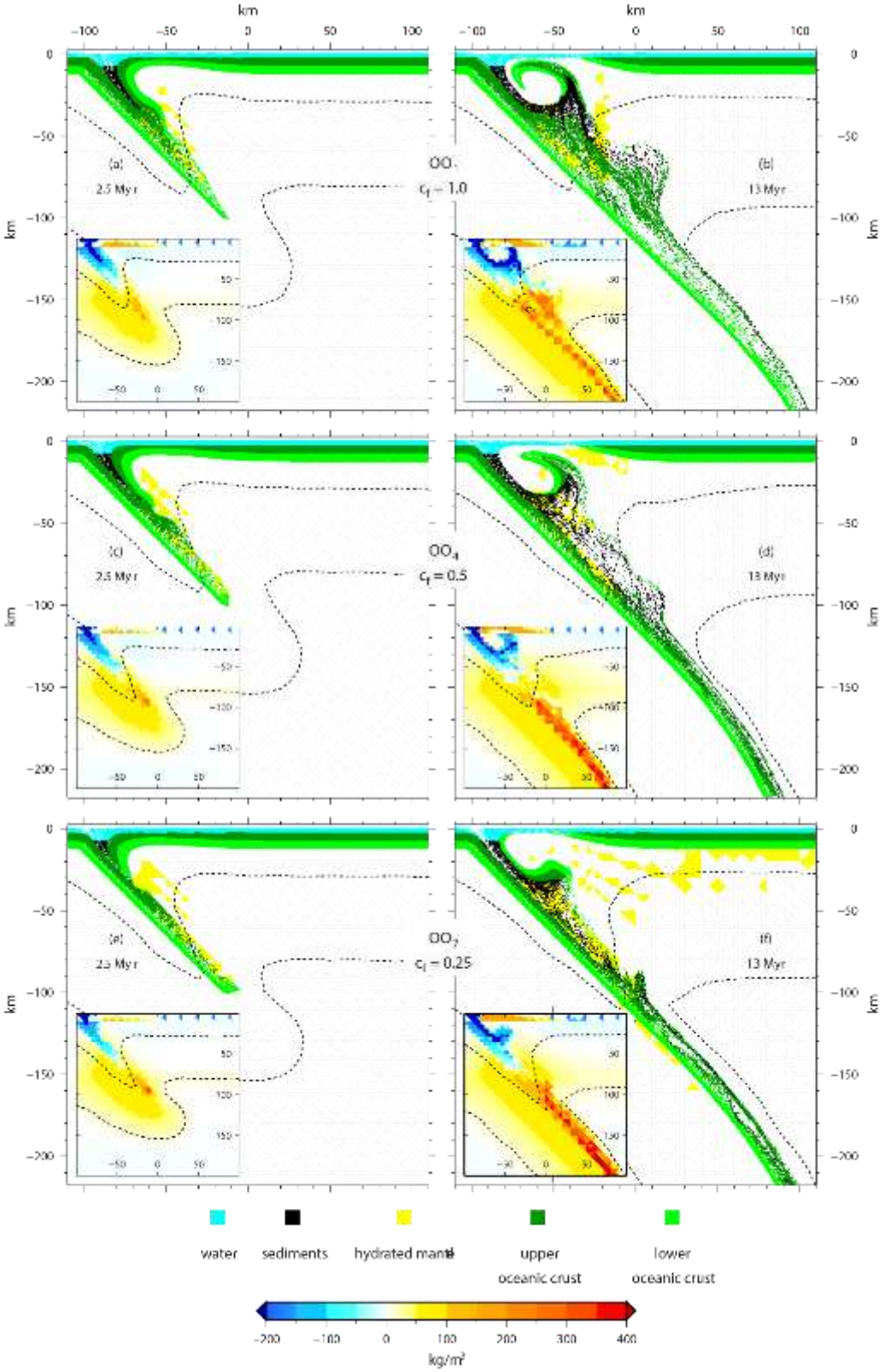

Figure 4.17: Marker distribution predicted by *OO*1 (panels a and b), *OO*4 (panels c and d) and *OO*7 (panels e and f) after 2.5 (panels a, c and e) and 13 Myr (panels b, d and f) since the beginning of subduction. The insets in the same panels show the density anomalies at the same times. The dashed black lines indicate the 800 and 1500 K isotherms. OO_1: u_s = 5 cm yr^{-1}; θ_s = 45°; c_f = 1; OO_4: u_s = 8 cm yr^{-1}; θ_s = 45°; c_f = 0.5; OO_7: u_s = 2 cm yr^{-1}; θ_s = 45°; c_f = 0.25.

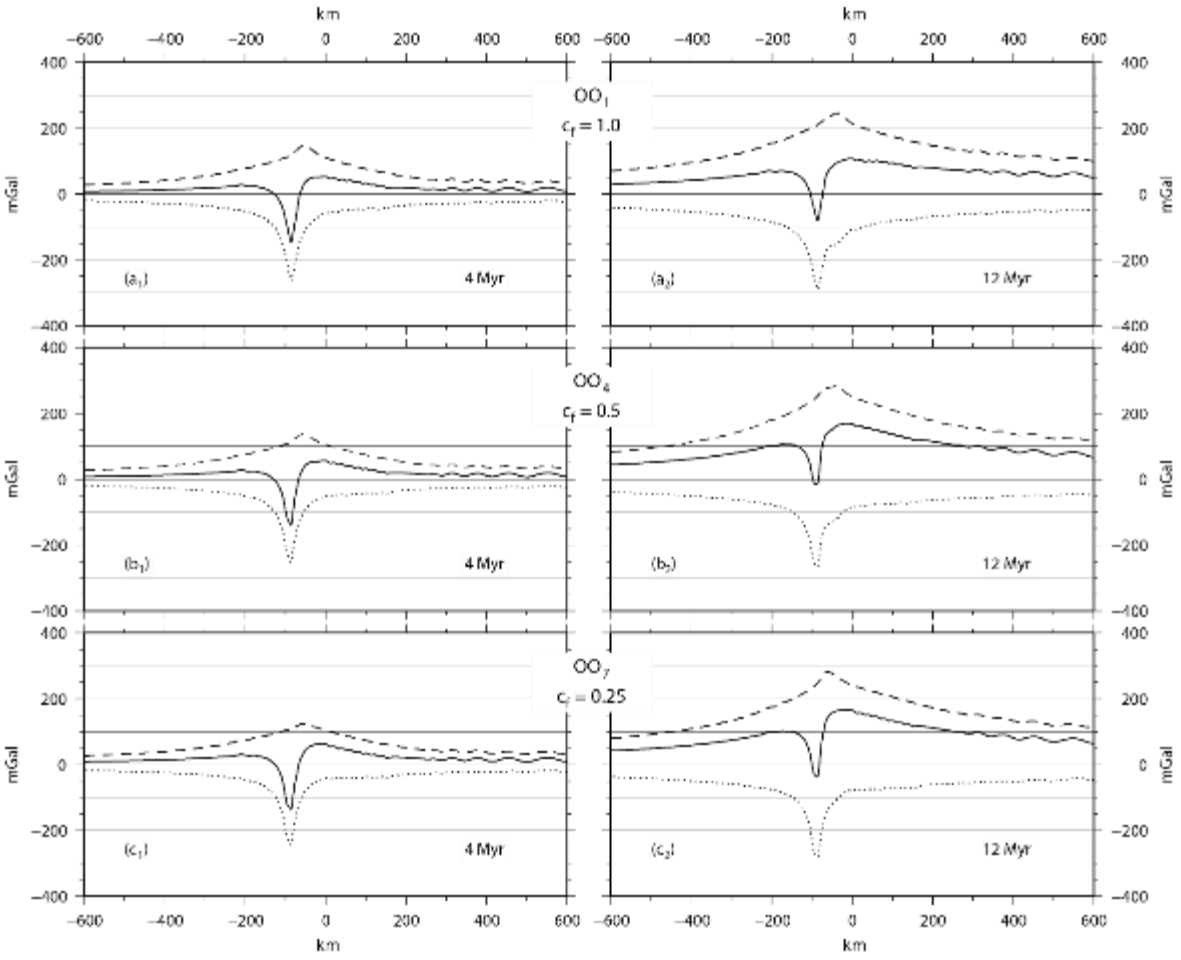

Figure 4.18: Solid lines indicate the gravitational contribution of the density anomalies predicted by OO_1 (panels $a1$ and $a2$), OO_4 (panels b_1 and b_2) and OO7 (panels c_1 and c_2) after 4 (panels a_1, b_1 and c_1) and 12 Myr (panels a_2, b_2 and c_2) since the beginning of subduction. Dashed and dotted lines indicate the gravitational contribution of the sole positive and negative density anomalies, respectively, for the same models in the same configuration. OO_1: $u_s = 5$ cm yr^{-1}; $\theta_s = 45°$; $c_f = 1$; OO_4: $u_s = 8$ cm yr^{-1}; $\theta_s = 45°$; $c_f = 0.5$; OO_7: $u_s = 2$ cm yr^{-1}; $\theta_s = 45°$; $c_f = 0.25$.

For the ocean–continent subduction, the peak-to-peak gravity disturbance varies from approximately 240 mGal in the southern part to 280 mGal in the central portion and to 140 mGal to the north. For the ocean–ocean subduction, the peak-to-peak gravity disturbance is generally higher, approximately 30 per cent, varying from 310 mGal in the south, 270 mGal in the centre and 200 mGal to the north. In addition, for ocean–ocean subduction, the gravity disturbance across the trench is characterized by a well-developed single minimum as low as -220 mGal, and for the ocean–continent subduction, a single minimum is not well defined, and a negative value that is approximately a factor two smaller, at most -120 mGal, is observed. Finally, the lateral extent of the gravitational contribution trough is smaller across

the Sumatra (smaller than 200 km) than across the Mariana (larger than 300 km) subduction complex.

4.5.3 Modelled gravity disturbance

In the previous section, we considered the density distribution at the beginning of subduction as the reference density configuration, because the target of the analysis was the perturbation induced by subduction on the gravity field. To properly compare model prediction to the EIGEN-6C4 gravity data, based on a geodetic normal Earth characterized by a uniformly thick continental crust and whose gravity is $\gamma\,(h,\varphi)$ in Equation (4.5), we here define a 1-D *model normal Earth* such that it is possible to calculate a *modelled gravitational disturbance*, which is compliant with the geodetic definition of gravity disturbance given by Equation (4.5).

Since the *normal Earth* of the EIGEN6C4 model is based on a continental lithosphere, in order to construct the *model normal Earth*, we consider the vertical density distribution at a great distance from the trench, on the side of the continent, for all the ocean–continent models.

Furthermore, since the *normal Earth* must represent the present-day reference density distribution, it is built at each time the comparison is made. Figure 4.20 shows the density distribution of the model normal Earth obtained after 40 Myr from the beginning of subduction for model OC_3 that will prove to be the best-fitting model for Sumatra.

We thus calculate the *modelled gravitational disturbance* as the difference between the magnitude of the modelled gravitational contribution of the perturbed masses at a given time t, $g$model, and the magnitude of the gravitational contribution from the *model normal Earth* at the same time t, γ model, both calculated at the same point:

$$\Delta g^{\text{model}}(h, x, t) = g^{\text{model}}(h, x, t) - \gamma^{\text{model}}(h, x, t), \tag{4.6}$$

where x indicates the position of the observational point with respect to the trench and h is its height above sea level. $g$model is calculated as expressed in Equations (4.2) and (4.3), but with ρ_e instead of $\Delta\rho_e$.

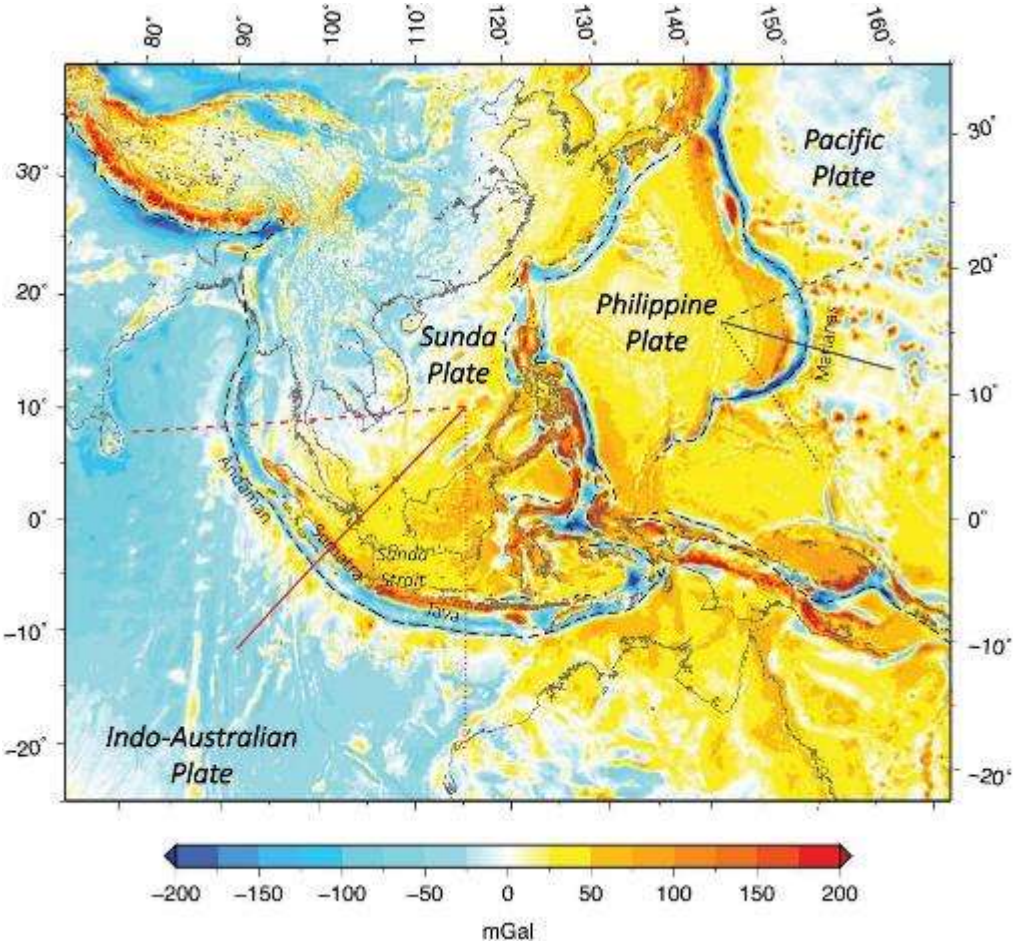

Figure 4.19: Gravity disturbance in the surroundings of the Sumatra and Mariana subduction complexes, computed at a height h_S=5 km above the ellipsoid and based on the EIGEN-6C4 model (*Förste et al.,* 2014). Dashed light blue lines indicate the plate boundaries in the area.

Among all the gravity functionals, the gravity disturbance is the most suitable one for a direct comparison with our model prediction, because it is based on the difference between the normal gravity and the actual gravity computed in the same point, without introducing any other reference point.

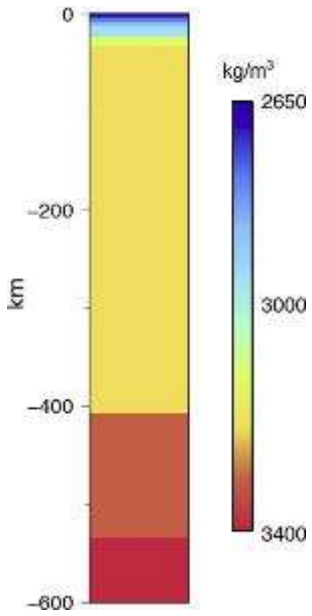

Figure 4.20: 1-D density distribution of the *model normal Earth* based on predictions from the OC_3 model at 40 Myr since the beginning of subduction.

4.5.4 Comparative analysis

4.5.4.1 Sumatra subduction

For the Sumatra subduction, we consider all the ocean–continent models with a subduction velocity of 5 cm yr^{-1}, compatible with the tectonic information of Section 4.5.1, and we calculate the gravitational contribution of the mass distribution predicted after approximately 40 Myr from the beginning of the subduction, accounting for a 4-km-thick ocean overlying the subducting plate. Below the discussion will be limited to the only model that shows the best agreement with the data, namely, model OC_3.

Panel a of Figure 4.21 compares the gravity disturbance predicted by model OC_3 and the gravity disturbance based on EIGEN-6C4, extracted along three sections perpendicularly crossing the Sumatra trench in the north (dashed red line), in the centre (solid red line) and in the south (dotted red line). The model (solid black curve) based on a coupling factor of c_f=0.5 and on the bathymetry of the southern profile (Figure 4.21 b) fits the envelope of the profiles well in terms of positioning and height of the maxima of 30 and 200 mGal (solid red curve), with a depth of the trough or gravitational disturbance minimum of –120 mGal (dashed red

curve) and with the asymptotic average values of a few tens of mGal over the subducting and overriding plates, negative and positive, respectively. As expected for a model that does not account for processes except subduction, the series of local maxima are not reproduced. Instead, the model does reproduce the narrowest trough of approximately 175–180 km of the red solid curve, evaluated from the distance between the two positive peaks surrounding the trough, to be compared in the following with that of the ocean–ocean subduction.

Panel (c) of Figure 4.21 depicting the marker distribution and the density anomalies after 40 Myr since the beginning of subduction, provides the explanation for this gravitational disturbance pattern due to the narrow region of negative density contrast, as large as 80 km at most, to a depth of approximately 80 km, embedded between the subduction cold plate and the upwelled lithospheric mantle. This mantle substitutes the less dense continental crust, as indicated by the white region below the thinned crust, dark and light red in panel c of the marker distribution between 20 and 40 km, thus producing a positive density contrast, portrayed by the shallow red zone in the inset of panel (c). This shallow positive density contrast is thus effective in the thinning of the trough in the ocean–continent subduction. Furthermore, this positive density contrast has the effect of increasing the positive gravitational peak located on the continental side. This positive density contrast at depths of 20–50 km originating from the indentation of dense upper mantle material within the continental crust in this ocean–continent case to some extent shields the deeper negative density contrasts, whose contribution to the formation of the trough is thus inhibited.

4.5.4.2 Mariana subduction

For the Mariana subduction, we consider all the ocean–ocean models with the same value of subduction velocity of 5 cm yr^{-1} as for Sumatra, and we calculate the gravitational contribution of the mass distribution after 45 Myr, compatible with Sumatra, accounting for 5-km-thick ocean overlying the subducting plate and a 4-km-thick ocean overlying the overriding plate. Below the discussion will be limited to the only model that shows the best agreement with the data, namely, model OO_1. Figure 4.22 shows the same information as Figure 4.21 but for the Mariana subduction. A wider trough with respect to the ocean–continent subduction characterizes this region and is well reproduced by the OO_1 model.

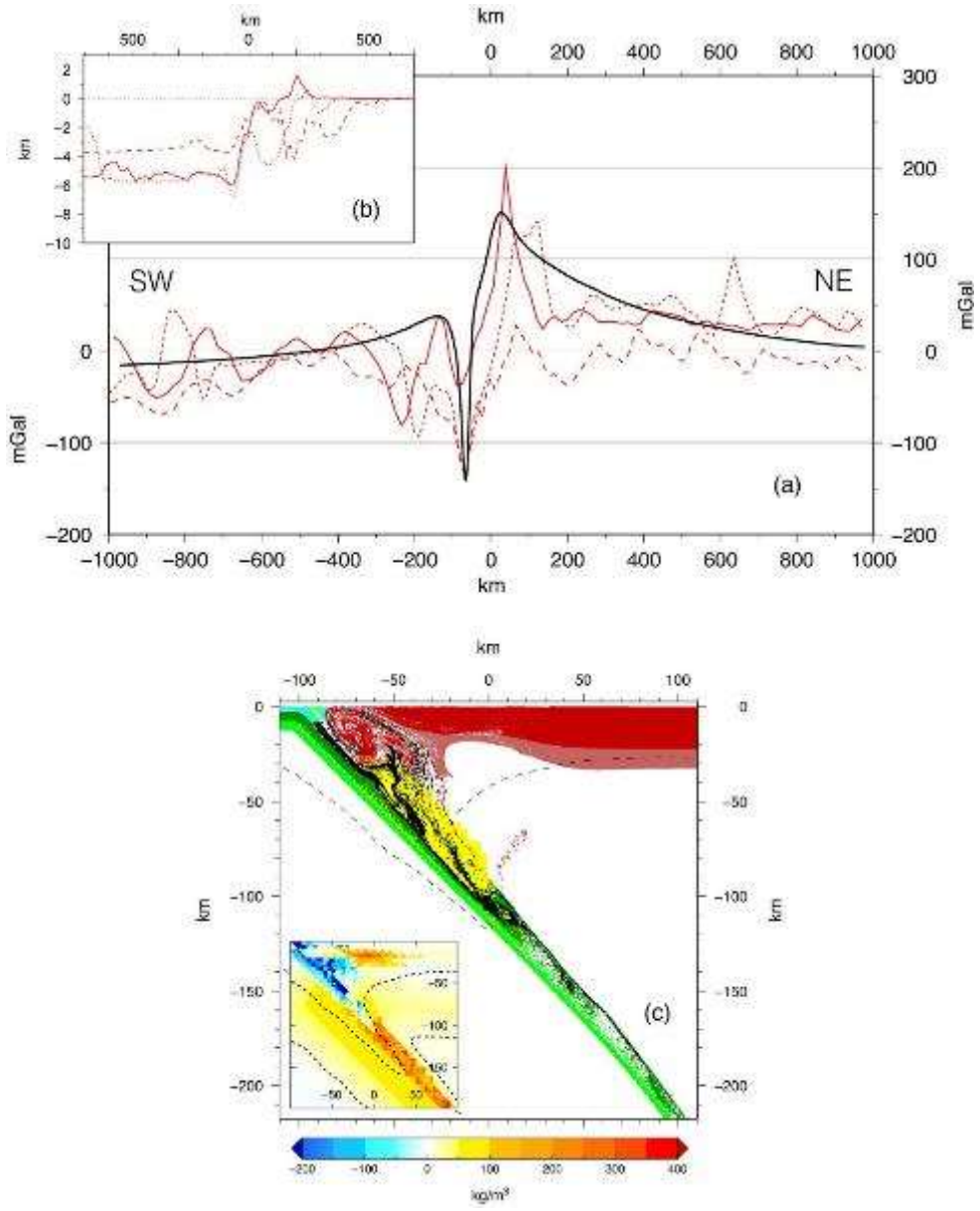

Figure 4.21: (a) Comparison between the gravity disturbance predicted by the OC_3 model (solid black curve) and the gravity disturbance based on the EIGEN- 6C4 model, extracted along three sections crossing the Sumatra trench in the north (dashed red line), in the centre (solid red line) and in the south (dotted red line). (b) Bathymetry along the same sections as in panel a, based on the ETOPO1 1 Arc-Minute global relief model (*Amante and Eakins*, 2009). (c) Marker distribution predicted by the OC_3 model after 40 Myr since the beginning of subduction. The insets in the panels show the density anomalies at the same times. The dashed black lines indicate the 800 and 1500 K isotherms. OC_3: u_s = 5 cm yr^{-1}; θ_s = 45°; c_f = 0.5.

This model accounts for a coupling factor of c_f=1 and builds on the bathymetry of the southern profile (Figure 4.22, panel b). With respect to the ocean– continent subduction, the ocean–ocean subduction is also characterized by a large recirculation of light material

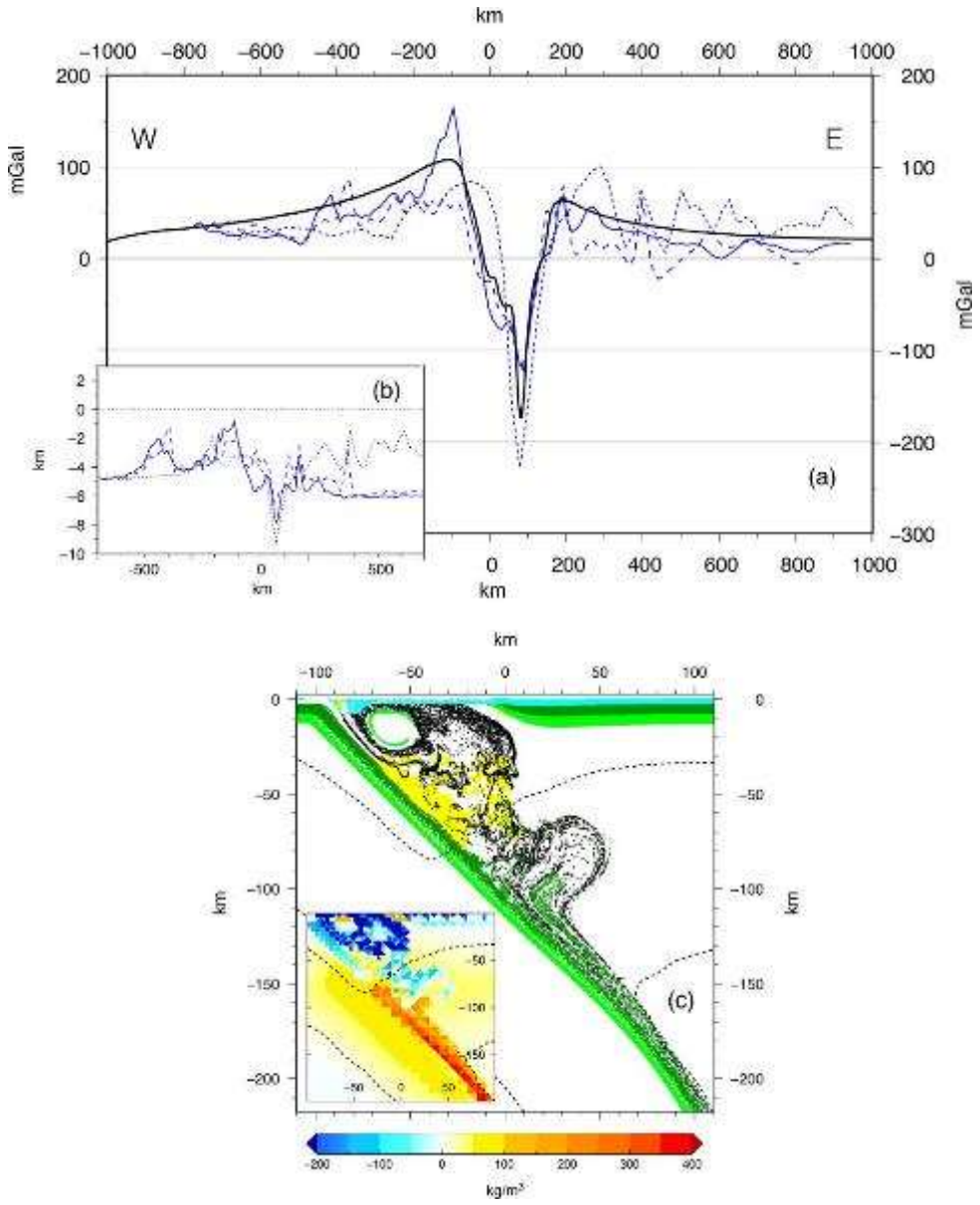

Figure 4.22: (a) Comparison between the gravity disturbance predicted by the OO_1 model (solid black curve) and the gravity disturbance based on the EIGEN- 6C4 model, extracted along three sections crossing the Sumatra trench in the north (dashed red line), in the centre (solid red line) and in the south (dotted redline). (b) Bathymetry along the same sections as in panel a, based on the ETOPO1 1 Arc-Minute global relief model (*Amante and Eakins*, 2009). (c) Marker distribution predicted by the OO_1 model after 45 Myr since the beginning of subduction. The insets in the panels show the density anomalies at the same times. The dashed black lines indicate the 800 and 1500 K isotherms. OO_1: u_s = 5 cm yr^{-1}; θ_s = 45°; c_f = 1.

in the mantle wedge, which is responsible for the wide region of negative density contrasts in blue in the inset of panel (c) of Figure 4.22, encompassing a region in the horizontal direction as large as approximately 150 km and leading to the prediction of a large gravity

trough in agreement with the data (Figure 4.22 a). Another major difference that makes the distribution of light material more effective in the ocean–ocean subduction in the formation of a pronounced and wide gravitational trough relies on the fact that in this type of subduction, in contrast to the ocean–continent one, the dense mantle does not substitute the lighter continental crust, which causes the formation of the positive density contrast observed above, contributing to the narrowness of the trough in the OC_3 modelshown in Figure 4.21. Panel (c) of Figure 4.22 provides another perspective on this issue regarding the width of the trough, showing the markers of light material well distributed along both the dip of the slab and the horizontal direction away from the trench. Thanks to the picture provided by this figure, we can provide an explanation for other characteristics of the ocean–ocean case, namely, the second-order maxima characterizing the gravitational signature within the trough on the side of the overriding plate, both along two data profiles and along the model black curve. The recirculation of light crustal material and sediments indicated by the markers in panel (c) of Figure 4.22 is characterized by a core of small-scale positive density contrast originating from the dense oceanic subducting crust, carried at shallow depth by the vigorous convective circulation occurring in the mantle wedge once out-scraped from the top of the slab. Our results allow us to provide a physical explanation for the occurrence of the small-scale local maxima in the gravitational disturbance on the side of the subducting slab due to localized dense material from the out-scraping of the slab.

4.6 Conclusion

We have developed a thermomechanical model that contains most of the complexities, such as compositional and phase changes, hydration, sedimentation and the degree of plate coupling, within the frame of a convective viscoplastic model, to analyse the static and time -dependent particularly in the trench region, when a self-consistent comparison with EIGEN-6C4 model is also performed. The effects on the gravity pattern due to a variation of several parameters (such as the degree of plate coupling, the subduction velocity, the subduction dip and the ocean–ocean or ocean–continent environment) have been also exploited. The model results indicate that:

(i) As the plate coupling decreases, (a) the cooling of the wedge area intensifies while, at great depths, the subducted slab remains warmer; (b) the horizontal extension of the hydrated wedge area increases as the plate coupling decreases, while the maximum depth decreases; (c) the shallow negative density anomaly, associated with the trench trough, the subducted and recycled crust and sediments and the mantle hydration, increases and widens; (d) the gravitational contribution from the negative density anomalies increases as well as the amplitude of the gravity trough;

(ii) As the subduction dip angle increases: (a) the *p–T* condition becomes unfavorable for mantle hydration and recirculation of light material; (b) intense but localized shallow negative and positive density anomalies develop; (c) more intense shallow positive density anomalies while less intense deep positive density anomalies develop; (d) the gravitational contribution from the negative density anomalies decreases as well as the amplitude of the gravity trough; (e) the gravitational contribution from the positive density anomalies increases;

(iii) As the subduction velocity decreases (a) a thermal thickening of the subducted slab is enhanced at shallow depths; (b) a widespread positive density anomaly develops at the base of the upper plate and along the subducted slab; (c) the negative density anomaly is not affected by changes in the subduction velocity; (d) the gravitational contribution due to the positive density anomalies increases as well as the width of the gravity trough. When the rate of changes are normalized with respect to the corresponding subduction velocity, non-significant differences are detectable and it is possible to estimate a common rate of change of 0.008 μGal yr^{-1} (cm yr^{-1})$^{-1}$;

(iv) The differences between ocean–ocean and ocean–continent environments are due to the different dynamics within the wedge embedded between the subducting and overriding plates for the two types of subduction, affecting in particular the amount of low-density material and thus the gravity low characterizing the trough. The gravity trough is generated by the negative topography and by the low-density material that overcomes, in proximity to the trench, the global positive gravitational disturbance caused by the cold subducted lithosphere, which remains unaffected by the nature of the overriding plate, being a continent or an ocean;

(v) A gravity change of approximately 60 mGal occurs within about 2 Myr when the subducted slab crosses the *olivine-spinel* transition.

The study of the EIGEN-6C4 gravitational disturbance patterns of the Sumatra and Mariana subductions have allowed us to strengthen the analysis of the gravitational signature in ocean–continent and ocean–ocean subductions in terms of the physics of the processes occurring during the convergence of the plates. Although both types of subduction show the classical 2-D dipolar profile perpendicular to the trench, they can be distinguished in terms of some fundamental features.

Our modelling is able to reproduce the gravity disturbance difference of 250–300 mGal well between the maximum and the minimum, characterizing both types of subduction. In the same way it reproduces the fundamental differences highlighted by the EIGEN-6C4 data: (a) the width of the trough (larger for the ocean–ocean subduction than for the ocean–continent one); (b) the symmetry, in terms of the different amplitudes of the two positive gravity peaks facing the trench.

Although focused on the analysis of the different gravitational disturbance patterns of the two types of subduction, our study provides a physical explanation for the broadness of the negative gravitational contribution for mature subductions (as the Mariana) compared to immature ones, as highlighted by *Kim et al.,* (2009). Serpentinization, partial melt due to frictional heating in the mantle wedge and differences in the density structure between the overriding and subducting plates were in fact proposed by *Kim et al.,* (2009) to explain the broad gravitational contribution in the trench region for mature ocean–ocean subductions.

Finally, our results show that gravity patterns and their rate of change in subduction zones provide important information not only on their anomalous density structure but also on the dynamics of the subduction process, complementing those studies in which density anomalies are obtained from seismic tomography or petrological information (e.g. *Kim et al.,* 2009; *Simmons et al.,* 2010; *Moulik and Ekström*, 2016).

Chapter 5

Continental rift zones

5.1 General features of continental rift zones

The continuous process from continental rifting to seafloor spreading is a key step in Wilson's cycle (*Wilson*, 1966) and an important stage that controls the growth and evolution of continents and the birth of ocean basins.

Rifting is described as a thinning process of the lithosphere ultimately leading to the rupture of the continent and the formation of a mid-oceanic ridge and sea-floor spreading. The lengthening and flattening of the continental lithosphere can be quantified by dividing the initial thickness of the lithosphere by its thickness when flattened a ratio known as the β factor (*McKenzie*, 1978). The rifting process, however, does not always continue to completion and many rifts become inactive before the point, at which new oceanic crust is formed.

Rifting initiates when the joint contribution of lithospheric buoyancy forces, mantle tractions, and subduction-related forces (Figure 5.1) overcome the lithospheric strength. Subsequently, rifting is facilitated by softening mechanisms, such as frictional weakening, diking and surface processes and by inherited rheological weaknesses (*Brune et al*., 2022). These forces may be counter-balanced by dynamic processes resisting deformation such as

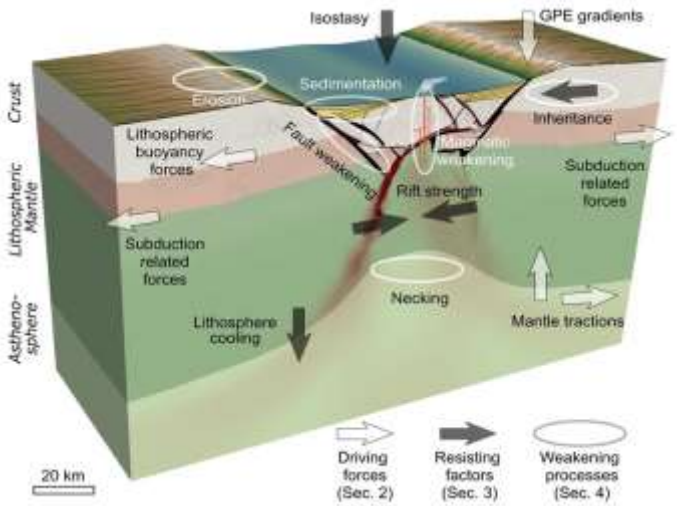

Figure 5.1: Model showing key processes and forces controlling rift dynamic (from *Brune et al*., 2022)

isostatic force or lithospheric cooling, which in turn may led to the abandonment of a rift. A rift-system goes through several phases before it enters the post-rift phase and either stops extending (resulting in a failed rift) or becomes a successful spreading centre:

1. rift initiation: rifts localize when tensional stresses exceed the strength of the continental lithosphere and the resulting deformation, often facilitate and guided by structures inherited from previous deformation episodes, can be accommodated by brittle faults, ductile shear zones and magmatic dikes (*Brune et al*; 2022);
2. basin evolution: neighbouring faults coalesce into an array of dominant faults. The strike-perpendicular extent of a rift can vary from less than hundred kilometres in narrow rifts (e.g. the Main Ethiopian Rift in East Africa), to several hundred kilometres in wide rifts, like in the Basin and Range region of North America. Slip along major faults and ductile thinning of the lower lithosphere causes hanging wall subsidence with the formation of sedimentary basins. In response to lithospheric thinning, asthenosphere rises causing decompression melting, which migrate rapidly through the lithosphere generating dikes, sills, and volcanoes (*Brune et al*., 2022);
3. oceanization: when the crust is thinned sufficiently, deformation progressively focusses migrating towards the location of future break-up. Enhanced decompression melting at a successively larger depth range intensifies magmatic emplacement in the rift centre.

When the continental lithosphere is separated and replaced by upwelling mantle and basaltic melt intrusions, the transition to mid-ocean spreading takes place (*Brune et al*., 2022);

4. post rift: once the newly formed mid-ocean ridge accommodates all plate divergence, the former rift turns into a rifted continental margin. This margin, however, continues to deform: proximal and distal parts of the margin cool at different rates, causing the distal part to subside slightly faster, leading to margin tilting. On the other hand, sediments transported by onshore river networks may load the proximal margin inducing subsidence (*Brune et al*., 2022).

5.2 Classifying extension systems

The evolution of extensional basins is controlled by multiple internal and external forcing factors and parameters, such as variable plate divergent rates, surface processes, coupled or decoupled crustal and lithospheric configurations, evolution of asthenospheric thermal anomalies and associated mantle dynamics (e.g *Huismans and Beaumont*, 2003; *Burov and Poliakov*, 2003; *Burov*, 2007; *Liao and Gerya*, 2014; *Wang et al*., 2015).

The various combination of these factors forms rifts as diverse as (1) narrow rifts (e.g. the East African Rift or the Cenozoic European Rift) versus wide rifts (e.g. The Basin and Range province or the Aegean extensional area): the first category is characterized by a strong continental lower crust, extension concentrated in the mantle of the lithosphere and a low thermal gradient while wide rifts are rifts whose width is greater than the lithospheric thickness resulting in a weak continental lower crust, thinning that is uniformly distributed over the mantle and lithosphere and an intermediate thermal gradient (e.g. *Brun*, 1999; *Buck*, 1991); (2) asymmetric versus symmetric extension on a crustal or lithospheric scale (e.g. *Keen et al*., 1987; *Morgan and Baker*, 1983; *Wernicke*, 1981) or (3) magmatic rifts versus exceptionally non-magmatic rifts (*Perez-Gussinye and Reston*, 2001).

A natural distinction can be made between tectonically active and inactive rifts and rifts that evolved in continental and oceanic lithosphere (*Ziegler and Cloetingh*, 2004). Tectonically active intracontinental (intraplate) rifts, such as the Rhine Graben, the East African Rift, the Baikal Rift and the Shanxi Rift of China, correspond to important earthquake and volcanic

hazard zones (*Ziegler and Cloetingh*, 2004). Rifts that are tectonically no longer active are referred to as palaeo-rifts, aulacogens, inactive or aborted rifts and failed arms, in the sense that they did not proceed to crustal separation. Conversely, the evolution of successful rifts culminated in the breakup of continents, the opening of new oceanic basins and the development of conjugate pairs of passive margins (*Ziegler and Cloetingh*, 2004).

A dynamic classification based upon forces that initiate rifting was introduced by *Sengör and Burke* (1978), distinguishing "active" and "passive" rifting (Figure 5.2 a and d).

In the "active" scenario (Figure 5.2 a), ascent of a large-scale hot/buoyant plume from the deep mantle initially results in symmetrical domal topographic uplift of the order of a few km. This is followed by a phase of widespread magmatism related to decompressional melting of the hot plume material spreading below the lithosphere (*Merle*, 2001; *Koptev et al*., 2021). Subsequently, the gravity effect of dynamic topography in combination with a horizontal drag at the base of the lithosphere imparted by radial flow of the plume head induces an "active" extension of the overlying lithosphere (*Koptev et al*., 2021). Therefore, the main criterion of the "active" (plume-induced) mechanism is the presence of plume related magmatic events preceding the onset of the deformation associated with rifting (*Koptev et al*., 2021).

"Passive" rifts develop in response to lithospheric extension driven by stresses located within or at the boundaries of the lithosphere (Figure 5.2 d) and the space created by lithosphere thinning is passively filled by the asthenosphere (*Huismans et al*., 2001). The "passive" scenario assumes neither (1) topographic uplift and widespread magmatism predating onset of rifting nor (2) large amounts of syn-break-up volcanism, a purely "passive" rifting to-break-up system that evolves into non-volcanic passive margins (*Koptev et al*., 2021).

Despite this classification is useful and widely used, it has limitations. In fact, "active rifting" has been shown to be rare on Earth and only in East Africa is the Rift recognized to fall into this category, although some authors suggest that this process played an important role in opening of the Atlantic Ocean (e.g. *Morgan*, 1983; *Wilson and Guiraud*, 1992).
Another reason is that this classification is far from being clear-cut: numerous rifts display a tectonic evolution that combines "passive" and "active" mechanisms (*Michon and Merle*, 2001; *Ruppel*, 1995; *Wilson*, 1993; *Ziegler and Cloetingh*, 2004), making it difficult to place them unambiguously into one of these two categories (*Merle*, 2001).

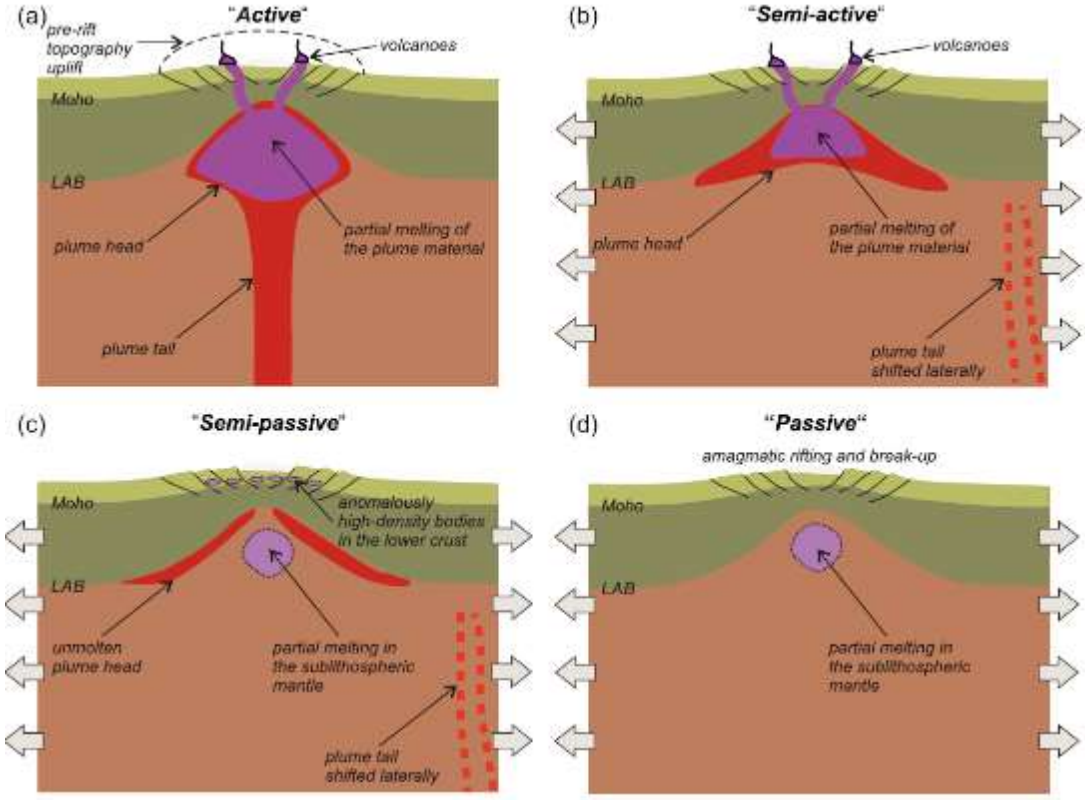

Figure 5.2: Four types of continental rifting and break-up according to a new classification proposed by *Kopotev et al*., (2021): (a) 'active'; (b) 'semi-active'; (c) 'semi-passive' and (d) 'passive' (from *Koptev et al*., 2021).

As shown by *Huismans et al*., (2001) during "passive" rifting, stretching of the lithosphere may trigger a destabilization of the underlying asthenosphere and generate a small-scale convective upwelling whose effect mimics that of "active" rifting. This "active" component in "passive" rifting may also result from the formation of a mantle lithospheric root following continental collision (*Channel and Mareschal*, 1989; *Merle and Michon*, 2001). In the same way, for mechanical reasons, some authors (e.g. *Mulugeta*, 1985) think that "active" rifting is not able to produce complete rupture of the lithosphere (i.e. to the point of oceanic crust formation) and that a component of "passive" rifting is needed, which would provide by deviatoric stresses resulting from lateral gradients of gravitational potential energy due to the doming created by the underlying mantle plume (*Merle*, 2001; *Stamps et al*., 2010). Therefore, such combinations of "active" and "passive" components make it difficult to distinguish the appropriate model when studying a natural case.

Moreover, *Corti et al*., (2003) and *Morley*, (1994) demonstrate that the difference in tectonic evolution between "active" and "passive" rifting disappears during the final stage of

deformation when the asthenosphere reaches shallow levels of the plate and triggers abundant partial melting and magmatic intrusions.

In this controversy, *Koptev et al*., (2021) have proposed a new classification for the modes of continental rifting, completing the old classification separating "passive" rifting from "active" rifting. In particular, they have introduced two principally new modes of rifting and break-up: "semi-active" and "semi-passive" (Figure 5.2 b and c) where extension and rupture of the continental lithosphere is mainly produced by far-field tectonic forces but in presence of "secondary" mantle plume(s) of moderate temperature and size, seeded below passively extended lithosphere (*Koptev et al*., 2021). In fact, mantle plumes are not restricted to whole-mantle ("primary") plumes emanating from the mantle-core boundary but also include "secondary" plumes originating from the upper mantle transition zone or shallower with horizontal diameters of only ~100–200 km and, therefore, called "baby" plumes (*Koptev et al*., 2021). *Koptev et al*., (2021) have carried out a systematic parametrical analysis focused on the life-cycle of small-scale thermal upper mantle anomalies and their impact on the style of lithosphere rifting and continental break-up. In this study, they have tested four controlling parameters including: (1) temperature and (2) diameter of the plume, (3) rheological structure of the overlying lithospheric plate and (4) style of intraplate tectonics. Their findings have important implications for the styles of rifting induced by small thermal anomalies, leading to the recognition of two novel intermediate modes of rifting and break-up. The "semi-active" assumes extension and rupture of the plate produced by far-field tectonic stresses but in the presence of mantle plume(s) of modest size and temperature seeded below passively stretched lithosphere. This mode is characterized by syn-break-up volcanism carrying geochemical signatures of the deep mantle with deformation localized above the plume head not anymore connected by its tail to the original source of hot material. On the contrary, lithospheric rupture operated by a 'semi-passive' mechanism occurs without aerial flood basalt eruptions but might be assisted by magmatic intrusions/underplating at the level of the lower crust.

There are two end-member extremes of passive rifted margins: (1) non-volcanic rifted margins (NVRM, Figure 5.3 a) and (2) volcanic rifted margins (VRM, Figure 5.3 b) (e.g. *Mutter et al*., 1988; *White and McKenzie*, 1989; *Boillot and Coulon*, 1998). However, used in the strictest sense, this classification became somewhat binary and confusing implying

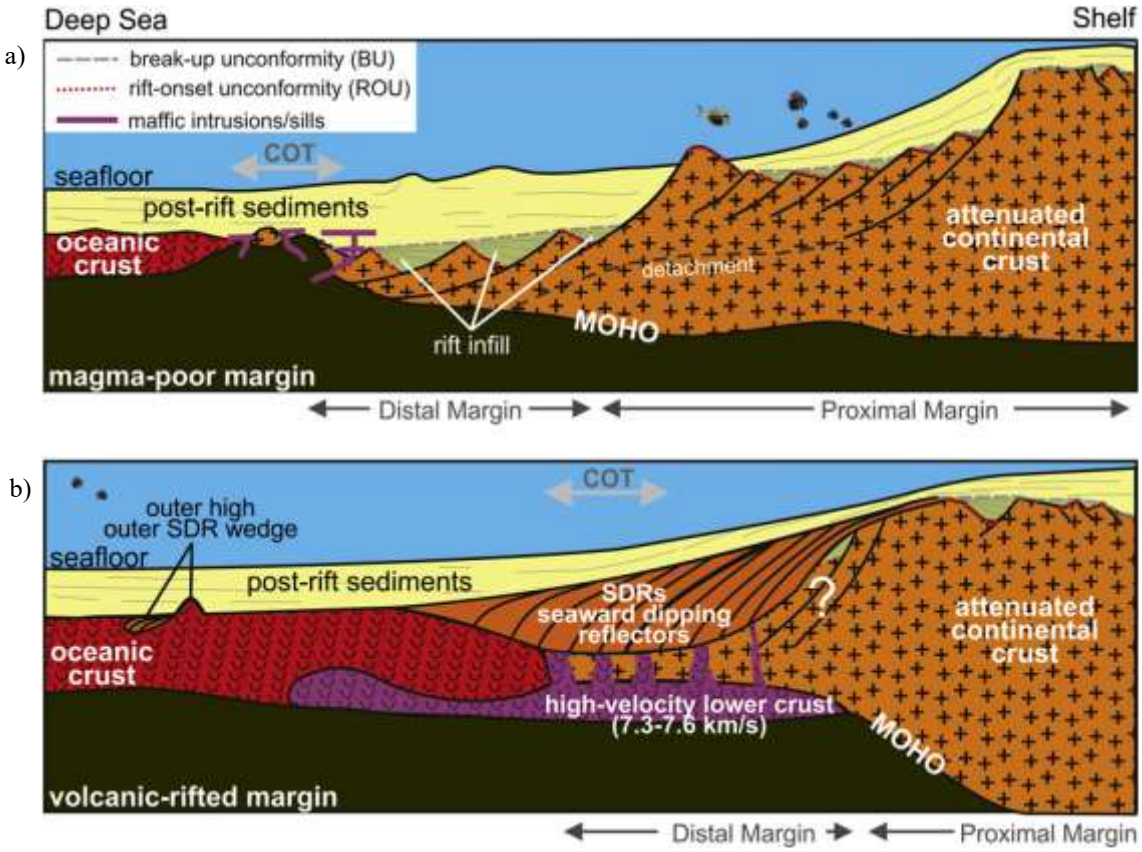

Figure 5.3: Schematic sketch of the end-member extremes of passive continental margins: magma-poor margin (top panel) and volcanic- rifted margin (lower panel). ROU is the rift onset unconformity; BU the breakup unconformity (from *Franke*, 2013).

different mechanisms for lithospheric thinning and breakup. Since magmatism is observed even in settings initially considered as non-volcanic, this terminology has been later adjusted to "magma-poor" ("magma-starved") or "magma-rich" ("magma-dominated") rifted margins (*Reston and Manatschal*, 2011; *Doré and Lundin*, 2015; *Tugend et al*., 2020), distinction that is basically drawn on the basis of timing and degree of mantle melting in relation to lithosphere extension, break-up and plate separation (*Geoffroy et al*., 2015). In particular, this terminology leads to assumptions on the magmatic budget: magma-rich rifted margins have a high magmatic budget during rifting and at lithospheric breakup, with an excess decompression melting, often associated with elevated asthenosphere temperatures, compared with steady-state seafloor spreading, while magma-poor margins have a very low magmatic budget, with an inhibited decompression melting (*Tugend et al*., 2020).

A breakup of the entire crust preceding breakup of the lithospheric mantle is a prerequisite for the exhumation of the mantle, one of the key findings at magma-poor

margins. On the contrary, the lithospheric mantle breaks before or at the same time with respect to the crust at volcanic-rifted margins, producing large volumes of syn-rift igneous rocks (*Franke*, 2013).

Volcanic rifted margins evolve by extension accompanied by extensive extrusive magmatism over short time periods during breakup. They are characterized by thick sequences of subaerial lava flows (up to 15 km) in the ocean-continent transition (OCT) zone, manifested in seismic reflection data as seaward dipping reflectors (SDRs) (*Bowling and Harry*, 2001) and high-velocity (V_p>7.3 km/s) lower crust seaward of the continental rifted margin (*Franke*, 2013) (Figure 4.4 b). Because crustal thinning typically occurs over a comparably short distance (50-100 km), the OCT is abrupt and located in the vicinity of the SDRs (*Franke*, 2013) (Figure 5.3 b). Furthermore, characteristics of volcanic rifted margins include the common presence of extrusive and intrusive rocks distributed throughout the region of extended continental crust and unusually thick oceanic crust adjacent to the margin (*Bowling and Harry*, 2001).

In contrast, on non-volcanic rifted margin (NVRMs) seaward-dipping seismic reflector sequences and high-velocity layers are lacking (5.3 a), syn-rift magmatic rocks are rare and of comparatively small volume, and the oldest oceanic crust adjacent to the margin is often anomalously thin (*Bowling and Harry*, 2001) (~5 km thick). They also show the exhumation and exposure, or near exposure, of serpentinized continental mantle lithosphere in the transition between continental and oceanic crust (*Huismans and Beaumont*, 2014). Furthermore, lithosphere necking is accommodated by an early system of upward-concave conjugate detachment faults dipping “oceanward”(Figure 5.4 a). A major trans-lithospheric detachment developing seaward would finally exhume the upper lithospheric mantle through a rolling-hinge deformation of the footwall (*Geoffroy et al*., 2015) (Figure 4.4 b).

Another way of grouping extensional systems was designed in the 80’s when rift geometries were linked according to shear settings (Figure 5.5):

1. in “pure shear” setting the lithosphere thins instantaneously and symmetrically. It is characterized by listric faults, extensive horst and graben structures, and is largely influenced by the thermal state of the system (*McKenzie*, 1978) (Figure 5.5 a). A modification to the pure-shear model is the ‘‘continuous depth-dependent’’ stretching model, which assumes that stretching of the mantle–lithosphere affects a broader area than the zone of crustal extension (*Rowley and Sahagian*, 1986; *Ziegler*

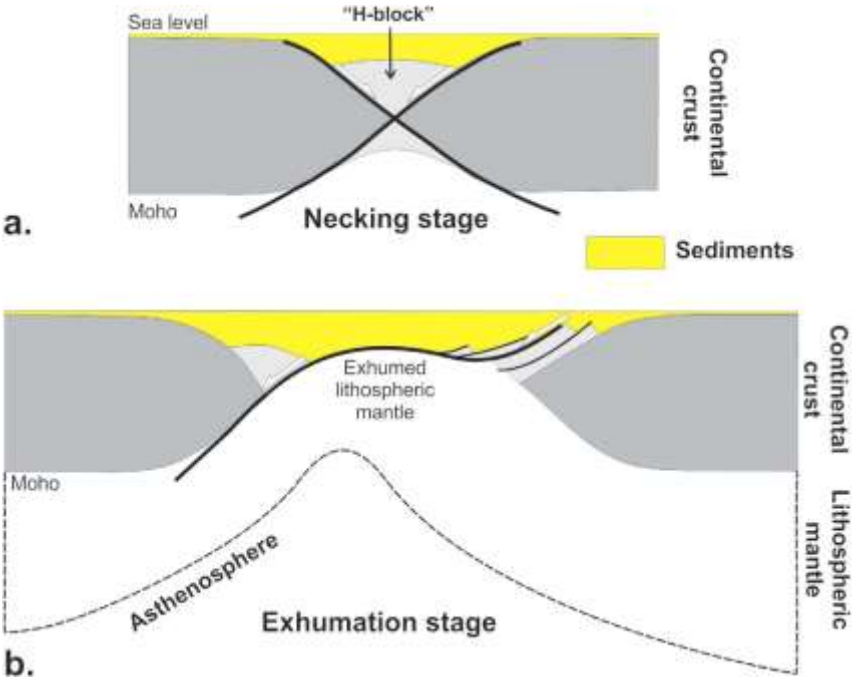

Figure 5.4: Necking (a) and mantle exhumation (b) stages at non-volcanic passive margins (from *Geoffroy et al*., 2015).

and Cloetingh, 2004);

2. the "simple shear" setting is marked by basin development bounded by low angle detachment faults, asymmetry and a lower thermal regime. It can be also observed with one plate overlying and another underlying the extension, giving the rift a strongly asymmetrical component (*Wernicke*, 1985) (Figure 5.5 b);
3. other models combine the two described above (*Buck et al*., 1988), or involve detachment (Lister *et al*., 1986) where the shear zone presents decollements between the brittle upper crust and the ductile lower crust, and between the latter and the lithospheric mantle (Figure 5.5 c).

A further categorization of extensional systems was based on the tectonic setting, e.g. extension vs. contraction:

1. the category "Atlantic"-type of system points to rift-to-break-up systems that form in an extensional setting: during early phases of rifting, large areas around future zones of crustal separation can be affected by tensional stresses, giving rise to the

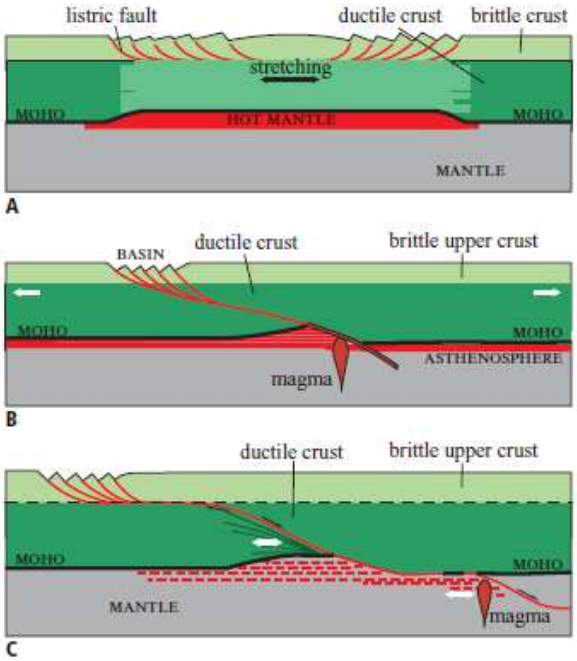

Figure 5.5: End-member lithosphere stretching models: (A) pure shear (*McKenzie*, 1978); (B) simple shear (*Wernicke*, 1985); (C) detachment (*Lister et al*., 1986).

development of complex graben systems (*Ziegler and Cloetingh*, 2004). In time, rifting activity concentrates on the zone of future crustal separation, with tectonic activity decreasing and ultimately ceasing in lateral graben systems. As a consequence of progressive lithospheric attenuation and ensuing crustal doming, local deviatoric tensional stresses play an important secondary role in the evolution of such rift system (*Ziegler and Cloetingh*, 2004);

2. subduction-related rifts: the classic relationship between subduction and rifts is the formation of back-arc basins, which result from the roll-back of the subducting slab (*Merle*, 2011). This type of rifting develops in an overarching contractional regime (e.g. the Aegean Sea) in response to a decrease in convergence rate and/or even a temporary divergence of colliding plates, ensuing steepening of the subduction slab and development of a secondary upwelling system in the upper plate mantle wedge above the subducted lower plate lithospheric slab (*Ziegler and Cloetingh*, 2004; *Beniest*, 2017). Back-arc rifting can progress to crustal separation and the opening of limited oceanic basins (e.g. Sea of Japan, South China Sea, Black Sea) (*Ziegler and Cloetingh*, 2004). Subduction-related rifts may also exhibit extensional terrains,

which are different to those of classic back-arc basins, for example the Basin and Range Province in the USA. Here, the primary cause of the continental extension is the subduction of the Farralon and Pacific plates under the North-American continent. The Eo–Oligocene magmatism bears a subduction zone signature and thus the Basin and Range Province is classified as a subduction-related rift. However, it was not until the East Pacific Rise descended beneath the North American plate that extension within the continent began (*Merle*, 2011), since this event deeply modified the kinematic and thermomechanical state of the overlying continent. Moreover, the detachment of the Farallon slab, which sank into the mantle (*Jones et al*., 1992), generated "active" upwelling of the asthenosphere. Thus, the Basin and Range Province exhibits many characteristics of "active" rifting during its main Mio–Pliocene stage. As a result, the US Cordillera collapsed and there was rapid extension over a very wide zone (1500×1500 km) leading to the formation of metamorphic cores complexes, together with abundant vulcanicity (*Merle*, 2011; *Wernicke et al*., 1987)

In "subduction-related" rifts, distinct tectonic evolutions can be distinguished (Figure 5.6):

- the classic case is slab retreat (i.e. roll-back process), which causes the formation of a back-arc basin in the continent. This evolution does not cause any destabilization of the asthenosphere and extension results from regional stresses located at the lateral boundary of the continental lithosphere (*Merle*, 2011) (Figure 5.6 A);
- in contrast, when a portion of the slab breaks off and sinks into the asthenosphere, the latter is destabilized and active upwelling occurs (*Merle*, 2011) (Figure 5.6 B). This evolution has been recently questioned by *Freeburn et al*., (2017). By using numerical models to quantify any melting processes during post collisional slab breakoff, they show that the classical style of slab breakoff related magmatism may not commonly occur, since breakoff depths are typically deeper that the overriding plate thickness, and may not induce a significant thermal perturbation in the overriding lithosphere. Even if slab breakoff is very shallow, the hot mantle inflow into the slab window is not sustained long enough to sufficiently heat the hydrated overriding plate to cause significant magmatism.

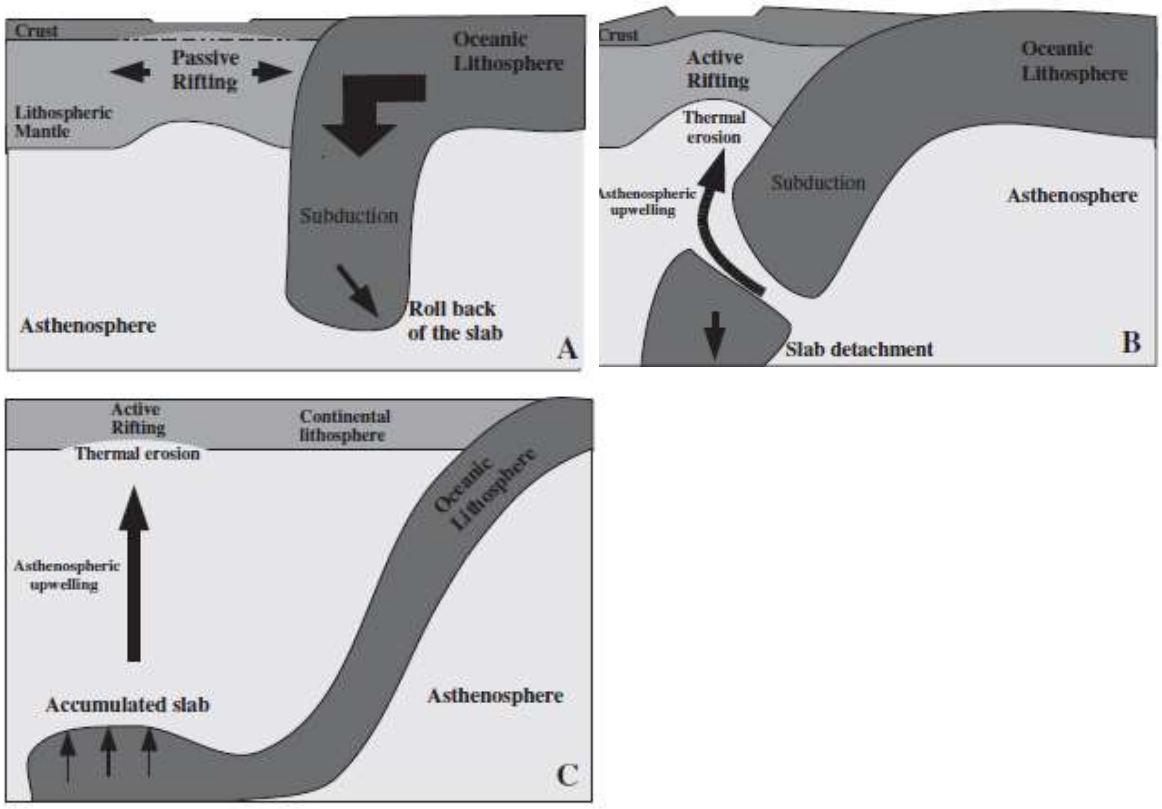

Figure 5.6: Tectonic evolutions in subduction-related rifts. Slab roll-back process (A), slab detachment (B) and stagnant slab (C) (from *Merle*, 2011).

Therefore, they suggest that melting is also generated through mechanisms that are not directly resulting from slab breakoff. In fact, numerical results show that small amounts of decompression melting of the continental crust can occur during exhumation, which is not necessarily initiated by slab breakoff as well as larger amounts of melting can be generated at the base of the continental crust from heating by upwelling asthenosphere during post-collisional extension (*Freeburn et al*., 2017);

- in the case of accumulation and thickening of a stagnant slab at the mantle transition zone (i.e. 660 km depth), active rise of the asthenosphere may also happen (*Merle*, 2011) (Figure 5.6 C).

3. plume-related rifts: as mentioned above, the notation of "active" rifting is associated with the ascent of a mantle plume to the base of the lithosphere. Mantle plumes rise diapirically from the core–mantle boundary through the lower mantle and, upon

reaching a density equilibrium, spread out variably at the 670- and 410-km discontinuities. Plume heads spreading out at these discontinuities act as major heat sources and can trigger partial melting of the upper mantle and upwelling of a system of secondary plumes (*Ziegler and Cloetingh*, 2004). On Earth, the only potential example of a plume-related rift is the East African Rift whose evolution includes two stages of "active" rifting: the first tectono-magmatic event was a voluminous episode of flood basalts and the formation of the Ethiopian and Somalian Plateaus (i.e. uplift) at about 30 Ma. The phase of rifting itself started later, during the Mio–Pliocene, with the activation of large border faults, the formation of the Ethiopian Rift Valley and a diffuse magmatic event (*Merle*, 2011).

5.3 Driving forces

Rifting activity, resulting in the breakup of continents, is governed by forces controlling the movement and interaction of lithospheric plates, as shown in Figure 5.1.

Far-field forces are transmitted through the plates and may combine the classical plate driving forces of slab pull, slab suction, basal drag, and ridge push (*Forsyth and Uyeda*, 1975). Rift suction is a local force arising from the thinning of the lithosphere, which generates a relative pressure gradient at depth that causes subvertical inflow of asthenospheric mantle (*Brune*, 2018). The thermal buoyancy of these upwelling hot mantle rocks constitutes another local force within the rift (*Huismans et al*., 2001) that may impact the entire region if a mantle plume exists, such as under East Africa (*Bagley and Nyblade*, 2013). Flow dynamics of the sublithospheric mantle have a twofold impact on rifting:

1) the upward flow component generates dynamic topography, which increases the gravitational potential energy and hence produces a tensional body force (*Brune*, 2018);
2) the divergent mantle flow component viscously couples to the lithosphere, generating shear stresses (*Brune*, 2018).

Lithospheric cooling plays a major role during slow rifting (*van Wijk and Cloetingh*, 2002; *Burov*, 2007) and in the post-rift phase (*Petersen et al*., 2015) by imposing a downward-

directed body force via negative thermal buoyancy. This may ultimately lead to Rayleigh-Taylor instabilities where parts of the lithosphere are removed (*Göğüş*, 2015). In fact, if a denser layer (mantle lithosphere) is located on top of a lighter layer (asthenosphere), then the system is gravitationally unstable and may develop negative Rayleigh–Taylor instabilities. This possibility specifically refers to rifting, passive or active, where hot light asthenosphere ascends to the surface and replaces colder denser lithosphere (*Burov*, 2007). Isostatic adjustment is the major control on topography, where thinning crust generates characteristic depressions within the rift (*Brune*, 2018). Surface processes distribute material, and thus generate negative or positive vertical loads in erosional areas and depocenters, respectively (*Burov and Poliakov*, 2001; *Brune*, 2018).

5.4 Magma source and composition

The generation of magma within the asthenosphere and deep lithosphere of continental rifts can be caused by different processes (*Brune et al*., 2022):

1. decompression melting can be induced by the adiabatic ascent of mantle rocks due to the thinning of continental lithosphere, with the production of higher melt volumes at greater stretching factors (β) (*Mckenzie and Bickle*, 1988);
2. melts can also be generated due to elevated mantle potential temperatures that are caused by the impingement of mantle plumes on the lithosphere (*Koppers et al*., 2021), by broad asthenospheric upwelling associated with lithospheric thinning or by small-scale convection at lithospheric edge (*King and Anderson*, 1998);
3. melting can be further enhanced by the presence of fusible metasomes in the lithospheric mantle (*Rooney et al*., 2014).

Volcanic rocks associated with intracontinental rifts display a typically alkaline, mafic–felsic bimodal composition, with mafic melts that appear to be generally derived from an incompatible element-enriched mantle source, residing presumably either in the lithospheric mantle, in the depleted asthenosphere or within mantle plumes (*Wilson*, 1989; *Ziegler and Cloetingh*, 2004). Initial magma generation in intracontinental rifts generally occurs in the 100–200 km depth range, corresponding to the lower parts of the lithosphere and the upper

asthenosphere (*Wilson*, 1989). During the evolution of some rifts, as the lithosphere is progressively thinned, it can be recognized an increase in the contribution of melts from the asthenosphere. This is responsible both of a decrease in alkalinity of the extruded mafic magmas and of an increase in contribution of MORB-source melts in time, generally towards the rift axis (*Ziegler and Cloetingh*, 2004).

The amount of melt generated during rifting in intraoceanic and intracontinental domains depends to a large extent on the potential temperature of the asthenosphere with enhanced melt production reflecting above ambient temperatures. Such domains correspond either to areas where deep mantle plumes have impinged on the lithosphere or that are underlain by an upwelling branch of the deep mantle convection systems, possibly activating less vigorous plumes rising from the 670-km discontinuity (e.g. Africa*, Nikishin et al*., 1996; *Ziegler and Cloetingh*, 2004).

As mentioned above, rift-related mechanical stretching of the lithosphere can cause, by adiabatic decompression of the lower lithosphere and upper asthenosphere, their partial melting and the diapiric rise of melts along fractures in the zone of lithospheric thinning. The volume and composition of melts generated is a function of the amount of lithospheric extension, the thermal state of both the asthenosphere and the lithosphere at the onset of extension, the presence of volatiles and the thickness of the lithosphere *(McKenzie and Bickle*, 1988; *White and McKenzie*, 1989; *Wilson*, 1989; *Ziegler and Cloetingh*, 2004).

Lithospheric stretching factors play an important role by controlling the degree of adiabatic decompression of the lower lithosphere and the asthenosphere and the upwelling of the latter. Partial melting occurs when the upwelling material crosses the mantle solidus line, the position of which in P-T (Pressure-Temperature) space is a function of its composition (*Ziegler and Cloetingh*, 2004). It can be deduced that stress-induced extension of the lithosphere is likely to cause in areas underlain by anomalously hot asthenosphere (upwelling, plume-input) a greater degree of partial melting (e.g. East African rift, South Atlantic rift, Baikal rift) than in areas underlain by an asthenosphere characterized by ambient or even below ambient (down welling) temperatures (e.g. Late Palaeozoic and Mesozoic Norwegian–Greenland Sea rift) (*Ziegler and Cloetingh*, 2004). Furthermore, the extension of a very thick (150 km) and cold lithosphere, little magmatism can be expected unless a very high degree of extension has occurred. Under such conditions, melts generated are expected to be derived mainly by partial melting from the lower lithosphere (*Ziegler and*

Cloetingh, 2004). Conversely, considering a 100 km thick lithosphere stretched by a β factor of 1.2–1.3, significant volumes of melts can be generated that are rapidly dominated by an asthenospheric source (*Wilson*, 1993; *Ziegler and Cloetingh*, 2004). In addition, strain rates appear to play an important role in the volume of melts generated: at low strain rates, conductive and convective heat diffusion probably plays an important role in suppressing partial melting. As rifting progresses, when strain is concentrated on the zone of future crustal separation, large volumes of melts can be generated, particularly in the presence of an asthenosphere characterized by above ambient temperatures (*Ziegler and Cloetingh*, 2004). Finally, in the presence of volatiles, the solidus is significantly lowered and partial melting can start at much smaller stretching factors than under anhydrous conditions (*Ziegler and Cloetingh*, 2004).

Chapter 6

Case study: From Rifting to Oceanization in the Gulf of Aden: Insights from 2D Numerical Models

6.1 Abstract

The breakup of continents to form oceans is a first order tectonic process and the start of the plate tectonic cycle of plate creation and destruction. However, the extensional evolution going from early rifting through breakup to seafloor spreading remains the subject of considerable discussion.

In this chapter, I analyze the evolution from rifting to ocean spreading of Gulf of Aden, a young oceanic basin that offers an excellent opportunity to understand breakup processes during extension. Regional stress field or thermal upwelling of the asthenosphere, inherited zones of weakness and the rheological structure of the lithosphere are the factors contributing to the initiation of rifting and deformation of lithosphere. 2D thermo-mechanical models are used to simulate the formation of oceanic crust and serpentinite due to the hydration of upwelling mantle peridotite. In addition to highliths four main tectonic phases developing

during rifting each one characterized by particular distributions of velocity gradients and strain rates inside divergent crustal blocks, which allow us to determine when breakup occurs, numerical results show that: a) the timing of mantle serpentinization is not affected by the initial thermal configuration of the system but is related to crustal thickness; b) the timing of mantle partial melting strongly depends on the thermal conditions in both lithospheric plates.

Finally, the results obtained so far support the hypothesis that the Gulf of Aden developed as a slow passive rift in a thin lithosphere with thick crust and that the variations in features along the passive margins could be related to lateral variations in the amount of H_2O in the mantle, which determines the different times of mantle melting. Further analyzes are underway in order to confirm these preliminary conclusions. This work has been published on *Tectonophysic.*

6.2 Introduction

Discriminating the driving forces that control the complex tectonic context in the Gulf of Aden and surrounding areas is one of the most recent and intriguing topics for researchers who study the evolution of the area surrounding the Afar Depression. The main mechanisms proposed to date are a) far-field tensile tectonic forces due to the subduction of the Tethyan slab below the Zagros suture zone (e.g., *Bellahsen et al*., 2003), b) emplacement of the African plume that may have caused diffuse lithospheric weakening (e.g., *Bellahsen et al*., 2003) and c) a combination of these mechanisms (e.g., *Petrunin et al*., 2020).

Several analogue and numerical models have been developed in recent years that focus on different aspects, such as the role of the subduction-collision process on Arabia-Africa separation and on intraplate stresses, which generated the Red Sea-Gulf of Aden rift system (*Bellahsen et al*., 2003); the effect of oblique rifting on the fault geometry (*Autin et al*., 2010, 2013); the reactivation of preexisting faults and rift localization (*Bellahsen et al*., 2006) and their roles in controlling the geometry and the kinematics of rifts (*Autin et al*., 2013); interactions between local and far-field tectonic stresses in an evolving rift system (*Brune and Autin*, 2013); the importance of mantle strength (*Gueydan et al*., 2008), rheology and composition on the formation of passive margins, ocean-continent transition zones and oceanic basins (*Watremez et al*., 2013); the structural consequences of crustal necking

processes and of the degree of mechanical decoupling during a relatively continuous extensional event (*Chenin et al*., 2018); the influence of erosion/sedimentation on the rifting process (*Beucher and Huismans*, 2020); and the overall effect of inherited obliquity and changes in relative plate motions along continent-ocean transform margins (*Farangitakis et al*., 2020). However, many questions remain debated, such as the timing and nature of the rifting and why the ocean-continent transition zone did not develop along the entire oceanic margins.

To shed light on these issues, we implemented a set of numerical models that simulate the passive rifting of lithosphere with varying crustal thickness and initial thermal configuration, whose predictions in terms of timing and petrological characteristics of the phases of rifting make it possible to discriminate among different tectonic hypotheses. Models are founded on integrated modeling of elevation, geoid data and thermal analysis and account for the present-day kinematics observed between the Arabian plate and Africa (Nubia) and Somalia. Rather than being interested on ridge propagation mode as a function of ridge parallel inflow or obliquity, requiring a 3D modeling formulation as for *Jourdon et al*., (2020) or on the effects of a 3D weak zone in the lower crust as for *Liao and Gerya* (2015), we are herein interested on the timing of occurrence of oceanization and serpentinization, which makes a 2D formulation the preferred one. This 2D formulation allows us to focus on the basic physics of the rifting processes along transects perpendicular to the ridge, focusing the analysis on the central portion of the Gulf of Aden, encompassed between the Shukra-el-Sheik fracture zone and Alula-Fartak fracture zone, which is in fact a 2D structure. Furthermore, within our 2D formulation we implement the formation of oceanic crust by partial melting and magma crystallization, generally not considered in 3D formulations.

6.3 Tectonic setting

The Gulf of Aden is a young oceanic basin situated between southern Arabia and the Horn of Africa that links the Ethiopian rift and the Red Sea with the Carlsberg Ridge in the NW Indian Ocean.

The rifting started at approximately 40-35 Ma (*Watchorn et al*., 1998; *Watremez et al*., 2011), followed by oceanic spreading at approximately 19-18 Ma at the Sheba Ridge, in the eastern part of the Gulf (*Bosworth et al*., 2005; *Watremez et al*., 2011; *Shuler and Nettles*,

2012; *Bosworth*, 2015). Later, the ridge propagated westward into the central Gulf of Aden by 16 Ma and, at 10 Ma, over 300 km from the central Gulf of Aden to the Shukra al Sheik discontinuity (*Bosworth et al*., 2005; *Bosworth*, 2015). Rifting stalled there and propagated west of the Shukra-el-Sheik discontinuity only during the last 2–3 Ma (*Shuler and Nettles*, 2012). The age of the oceanic crust thus becomes progressively younger westward. The spreading rate increases from 13 mm/yr in the west to ~23 mm/yr in the east (*ArRajehi et al*., 2010; *Autin et al*., 2010).

The general trend of the Gulf of Aden is WSW–ENE (N70°E) while the present-day spreading direction ranges between N25°E to the east and N35°E to the west, indicating an oblique rifting (*Huchon and Khanbari*, 2003).

The oceanic domain of the gulf may be divided into three sectors (western, central and eastern sectors, Figure 5.1) by the Shukra-el–Sheik Fracture Zone (SSFZ), the Alula-Fartak Fracture Zone (AFFZ) and the Socotra-Hadbeen Fracture Zone (SHFZ) (*Leroy et al*., 2010). The eastern sector (light red area in Figure 6.1) extends from the Alula-Fartak transform fault to the eastern border of the African craton (*Leroy et al*., 2012) and shows an extremely thin transitional crust at the Ocean-Continent Transition (OCT), which most likely involves exhumed serpentinized mantle rocks indicating a magma-poor setting (*Leroy et al*., 2012).

The central sector (light yellow area in Figure 6.1) of the Gulf lies between the SSFZ and the AFFZ (*Leroy et al*., 2012) and, as in the eastern sector, the margins here are thought to be either magma-poor, or of intermediate-type, as no magmatic structures, such as seaward-dipping reflectors have been recognized in the OCT. In fact, *Nonn et al*. (2019) propose that the central Gulf of Aden is composed of hybrid margins (or intermediate-type, Larsen et al., 2018), transitional between magma-rich and magma-poor margins, in the western and eastern parts of the central sector, respectively. Their analysis of marine geophysical and geological data reveals that at the western boundary of central sector, near the XAMFZ, magmatic processes are predominant and the higher thermal regime is associated with the development of SDRs wedges from the late phase of the thinning of the continental crust (early Miocene ~21 Ma) up to the exhumation phase (Burdigalian ~18 Ma) that lead to the OCT development. East of BHFZ, the Bosaso-Sayhut margins segment is characterized by magma-poor margins, for which the exhumation stage is characterized by the unroofing of mantle along multiple detachment faults in the OCT and shortly followed by diachronous volcanism (~18 Ma) (*Nonn et al*., 2019). The OCT on the northern margin of the central

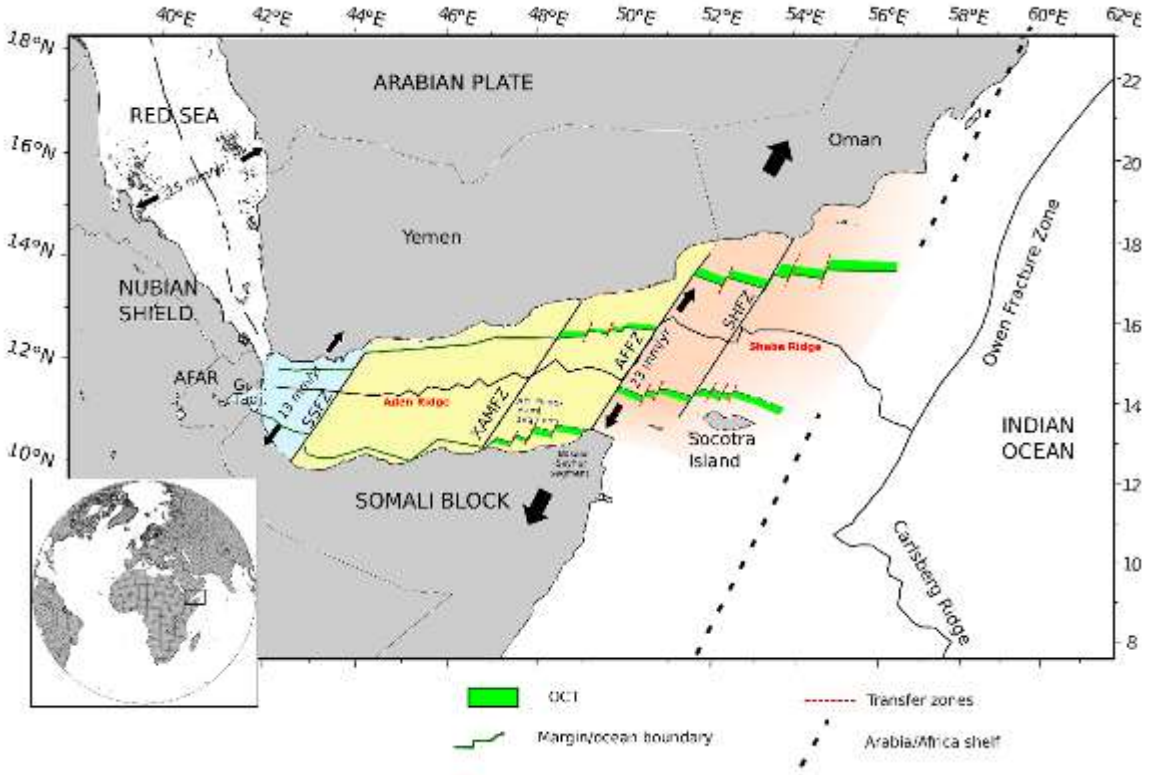

Figure 6.1: Overview map showing the main tectonic features of the Gulf of Aden and surrounding areas using published data (*Leroy et al*., 2012; *Nonn et al*., 2019). Large black arrows indicate the directions of plate motion in the region. SSFZ: Shukra-el-Sheik fracture zone. XAMFZ: Al Mukalla fracture zone. AFFZ: Alula-Fartak fracture zone. SHFZ: Socotra-Hadbeen fracture zone. Cyan, light yellow and light red colors indicate the western, central and eastern sectors, respectively.

sector is wider in the eastern segment (~23–45 km) than in the western segment (~17–33 km), and on the southern margin, it is wider in the Bosaso-Sayhut segment (~23 km) than in the Ahl-Medo-Hami segment (~10–20 km) (*Nonn et al*., 2019). The difference in width of the conjugate OCT highlights the asymmetry of the Yemeni and Somalian margins (*Nonn et al*., 2019).

The western sector (cyan area in Figure 6.1) extends from the active rift of the Gulf of Tadjoura to the SSFZ (*Leroy et al*., 2012). West of the SSFZ, the system was heated up by the strong influence of the Afar plume, which led to breakup with much less extension, inducing the development of volcanic rifted margins in the western part of the Gulf of Aden (*Leroy et al*., 2012). In fact, the major discontinuity of Shukra-el-Sheik (Figure 6.1) may indicate the limit of the Afar plume influence and corresponds to a major change in the rheology of the lithosphere (*Basuyau et al.*, 2010).

6.4 Model setup

The physics of the crust–mantle system during the transition from rifting to seafloor spreading is described by the equations of conservation of mass, momentum and energy for incompressible fluids as detailed in section 2.1.

The balance Equations are integrated using the 2D finite element code SubMar (*Marotta et al*., 2006) in a 1400 km-wide and 700 km-deep rectangular domain (Figure 6.2). The domain is discretized by a non-deforming irregular grid composed of 5836 quadratic triangular elements and 11889 nodes. The sizes of the elements vary, with the highest nodal density localized near the future rifting zone, where the most significant gradients in temperature and velocity fields are expected.

The marker in-cell technique (e.g., *Christensen*, 1992) is used to compositionally differentiate the different types of materials with 514009 markers spatially distributed with a density of 1 marker per 0.25 km^2, identifying through a specific index the material particles of air/water, continental crust, non-serpentinized and serpentinized mantle. Mantle markers have been distributed only along a 200 km-wide vertical column centered at the future ridge position (yellow zone in Figure 6.2 a). This permitted to assure a high marker concentration and, at same time, to limit the total number of markers and optimize the time consuming. Such marker distribution resulted appropriate to identify those markers involved in the processes under study.

In order to limit the maximum effective viscosity and to minimize the hardening effects of temperature and strain, we introduce a cut-off value of 10^{25} Pa·s, in agreement with other authors (e.g., *Gerya and Yuen*, 2003, *Marotta et al*., 2009) (Figure 5.2 c). Neither stress hardening nor stress softening is considered. This simple rheological model is appropriate in reproducing the average continuum properties of a discontinuous medium and makes the analyses of gross mechanical behavior during the geodynamic evolution of the study area possible, allowing the formation of localized shear zones that can be interpreted as faults in continuum mechanics (see section 6.5.1).

The numerous models developed to analyze the dynamics of rifting (e.g., *Huismans and Beaumont*, 2002, 2003; *Richter et al*., 2021) show that a use of a more complex elasto-visco-plastic rheology affects mainly the initial stages of rifting, when the mode of small-scale localization of deformation structures is important for the successive breakup development.

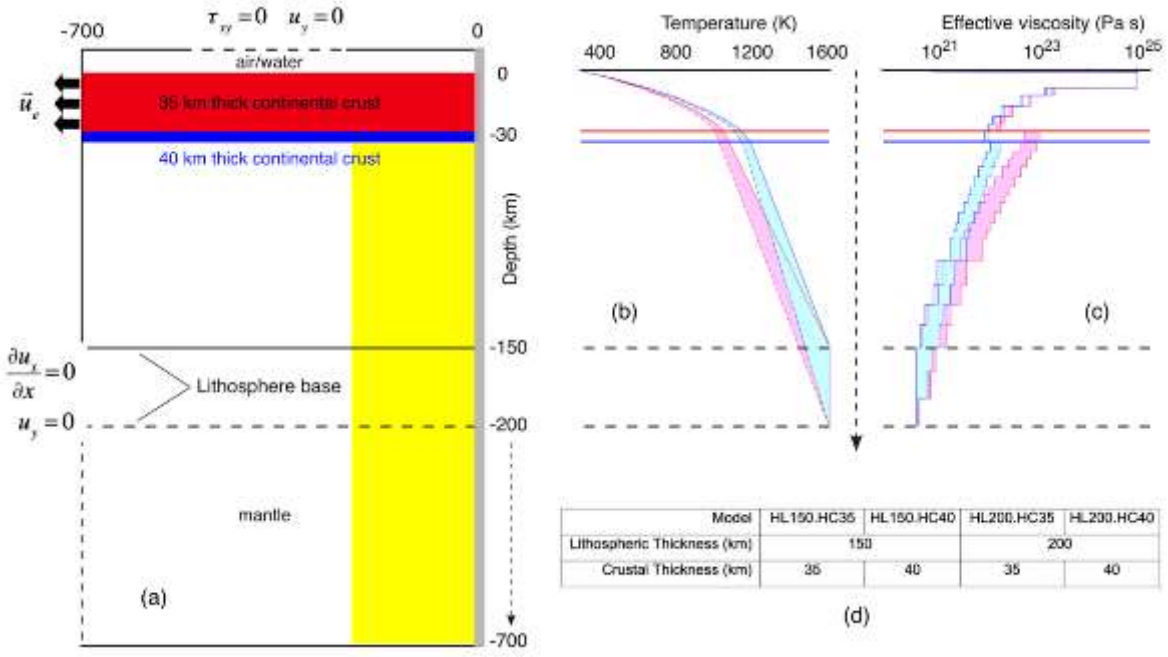

Figure 6.2: (a) 2D geometry and numerical setup of the numerical model. Crustal markers are colored red and blue. Mantle markers are colored yellow. Green area indicates the assumed low viscosity weak zone. Thermal (b) and rheological (c) profiles at the beginning of evolution for the models listed in panel d. Blue and red colors in panels (b) and (c) refer to a 40km and 35 km thick crust, respectively. The thin red and blue lines refer to the geotherms (panel b) and the effective viscosities (panel c) for the 35 km and the 40 km -thick crust models, respectively. Continuous and dashed lines indicate geotherms and effective viscosities for a 150 km and 200 km -thick lithosphere, respectively. The horizontal black dashed lines indicate the base of the 150 and 200 km lithosphere. The horizontal thick solid lines indicate the base of the 35 km (red) and 40 km (blue) -thick crust.

However, this is beyond the scope of the present study, in which we assume an a-priori weakness point where breakup will develop. In particular, we introduced a 10 km wide x 15 km deep weak zone in the center of the model, from surface downward (green area in Figure 5.2 a), and characterized by a viscosities of 10^{19} Pa·s to localize the deformation and allow the development of the rifting since a continuous medium necessitates a heterogeneity in the mechanical properties as a seed for initiating the process of rifting (*Huisman and Beaumont*, 2003; *Liao and Gerya*, 2015; *Wenker and Beaumont*, 2018).

We account for the brittle behavior of the crust only to define the rheological condition for mantle serpentinization during continental rifting and the transition to oceanic spreading. Table 2.1 lists the material and rheological parameters used in the analysis.

In agreement with studies on the lithospheric structure in the Gulf of Aden and its surroundings, four model sets have been developed changing the initial thickness of the continental crust (fixed at 35 and 40 km) and the initial thickness of the lithosphere (fixed at 150 and 200 km), in order to match the lower and upper bounds of the estimates of the present-day crustal and lithospheric thickness in the internal part of the Arabian plate suggested by integrated modeling of elevation, geoid data and thermal analysis (e.g. *Hansen et al*., 2007; *Leroy et al*., 2010; *Globig et al*., 2016). We list the acronyms and setup of the models in Figure 6.2 d where HL stands for lithospheric thickness and HC stands for crustal thickness.

To allow for topographic variations, a 10 km-thick layer of sticky air is present above the crust, characterized by a viscosity of 10^{20} Pa·s and a density of 1.18 kg m^{-3} (e.g., *Crameri et al*., 2012; *Marotta et al*., 2020). Our topography is thus the surface defined through the envelope of the topmost markers.

We are aware that the limited height of the sticky air could affect to some extent the detailed estimate of the topography, that is not in any case the focus of the present work.

Boundary conditions are fixed in terms of temperature and velocity. The temperature is fixed to 300 K at the top of the crust and through the air layer. A temperature of 1600 K is fixed at the bottom of the model; zero thermal flux occurs through the vertical sidewalls. The initial thermal configuration corresponds to a steady-state conductive thermal profile, from 300 K at the surface to 1600 K at the base of the lithosphere and considering a radiogenic heat production in the continental crust (Table 6.1); an initial uniform temperature of 1600 K is assumed through the sublithospheric mantle (Figure 6.2 b). The 1600 K isotherm defines the base of the thermal lithosphere throughout the evolution of the system.

To simulate the northeastward relative motion between the Arabian plate and the African (Nubian) and Somalian plates, we apply an extension rate of 11.5 mm/yr on both sides of the domain, from depths of 0 to 100 km, resulting in symmetric passive rifting with a total extension rate of 23 mm/yr that is compatible with the highest velocities suggested for the eastern part of the Gulf of Aden (*ArRajehi et al*., 2010; *Reilinger et al*., 2015). No-slip conditions are prescribed along the top and the bottom of the model domain. Along the vertical sides, from the base of the lithosphere (-100km) below, we fix to zero the vertical component of velocity and the horizontal gradient of the horizontal component of velocity, according to eq. 1 (Figure 5.2 a). We ran the simulation for 40 Ma to cover the entire time

span (approximately 35-40 Ma) from the beginning of continental rifting to the present (*Bosworth et al*., 2005; *Bellahsen et al*., 2006; *Leroy et al*., 2012; *Bosworth et al*., 2015; *Rasul et al*., 2015; *Brune and Autin*, 2013). A constant time step of 50 kyr is used that always satisfies the Courant-Friedrichs-Lewy condition.

6.4.1 Mantle serpentinization and Oceanization

The role of serpentinization of the lithospheric mantle during continental rifting and the transition to oceanic spreading have been extensively discussed in the literature (e.g., *Pérez-Gussinyé et al*., 2006; *Marotta et al*., 2018). In the present work, we implement mantle serpentinization and the associated compositional and rheological changes following *Marotta et al*., (2018)'s approach. At each time step, we check whether a) the pressure and the temperature of each mantle-type marker match the stability field of serpentine and b) the overlying crustal layer is under brittle conditions.

In our model the partial melting of asthenospheric mantle allows the growth of the oceanic crust at the ridge, assuming an instantaneous transfer of mantle melt to shallow depths, as commonly implemented (e.g. *Gerya*, 2013, *Nikolaeva et al*., 2008, *Gulcher et al*., 2019). This is also in agreement with estimates of the magma ascent rate across the continental and oceanic crust (*Clague*, 1987; *Turner et al*., 2000).

To verify whether the predicted thermal state can result in partial melting of the mantle and the formation of oceanic crust, we estimate the melting percentage of lithospheric mantle following the melting model by *Katz et al*., (2003) at each time step, as discussed in *Roda et al*., (2018). *Basuyau et al*., (2010) have combined seismological data with existing gravity data in a joint inversion scheme to estimate both *P* wave velocity and density structure beneath the northeastern margin of the Gulf of Aden, reaching depths of 250 km with a spatial resolution of about 50 km. Their analysis highlights the presence of two low-velocity anomalies along the continuation of Socotra-Hadbeen and Alula-Fartak fracture zones between 60 and 200 km depth with evidence for partial melting (3–6 per cent) within these two negative anomalies. In the partial melting implementation, we estimate the melting percentage of lithospheric mantle and we use the value of 3% of partial melting as the minimum value at which the oceanic crust begins to form. This value is also in agreement

with melt extraction threshold by *Nikolaeva et al*., (2008). After the melt fraction reach the threshold the melt is extracted and it migrates instantaneously creating new oceanic crust (*Gerya*, 2013).

Some authors (*Nichols et al*., 2002; *Thompson et al*., 2015) have proposed that the percentage of water near an oceanic ridge tends to increase as the ridge approaches a plume. In proximity to plumes, mid-ocean ridge basalts (MORB) can have H_2O percentages up to 0.03-0.1%, similar to those observed in oceanic island basalts (OIB) (*Dixon et al*., 2002; *Hirschmann*, 2006). This feature can also be observed in the central and eastern parts of the Gulf of Aden, where basalts show the geochemical signature of normal MORB (N-MORB) (*Rooney et al*., 2014; *Shinjo et al*., 2015) incorporating a component from a plume-associated source. Therefore, we considered the solidus of a wet lherzolite with a bulk of H_2O between 0.05 and 0.1%. We calculate the areas where partial melting occurs at the post-processing stage and the rate of the partial melting is determined following *Katz et al*., (2003). Within this work, we refer to crustal breakup when the two continental crusts are compositionally separated, although crust can still deform, being still subjected to the shear stresses exerted by the underlying lithospheric mantle, which has not yet broken. We assume that lithosphere breakup is instead achieved when the effective strain rate decreases below the threshold value of 10^{-16} s^{-1} through the whole crustal thickness. The analysis of variations with time in the horizontal velocity and in the strain rate at crustal levels will thus allow to identify the times when crustal and lithospheric breakup occur.

The domain between the thinned continental crust and the oceanic crust, composed of denuded mantle that has been serpentinized before the occurrence of the gabbros, will be henceforth referred to as the Ocean Continent Transition zone (OCT). The width changes of the OCT and of the oceanic lithosphere in the study domain will be estimated considering the structural configuration of the system at the time of partial melting and at the time when the two continents are separated by a distance of 350-400 km (as observed in the Gulf of Aden).

6.5 Model results

6.5.1 Thermomechanical evolution and deformation

During the first few million years from the beginning of extension, for all models, the predicted velocity field is controlled mainly by the far-field traction that induces predominantly horizontal velocities throughout the lithosphere. During this stage, the intensity of upwelling mantle flow below the future ridge is lower than the far-field intensity (panels a_2 and b_2 of Figures 6.3 to 6.6), especially for the colder and thus stiffer models HL200.HC35 (Figure 6.5) and HL200.HC40 (Figure 5.6). With the progression of the forced extension, all models undergo continuous warming that is localized around the position of the future ridge, as revealed by the rising of the 800 K and 1500 K isotherms (Figures 6.3 to 6.6). Thermal thinning is accompanied by progressive crustal thinning, which results in crustal breakup over a period ranging from 6 Ma for model HL150.HC35 to 20 Ma for model HL150.HC40.

The analysis of variations with time in the horizontal velocity and in the strain rate at crustal levels allows us to identify the times when crustal breakup occurs. To aid this analysis, Figure 6.7 shows the horizontal crustal velocity, averaged over the crustal thickness, as a function of distance from the future ridge and at different times of evolution. Four main phases can be distinguished in the thermomechanical evolution of the crust. The first phase (phase I) lasts a few million years from the beginning of extension. During this phase, the horizontal crustal velocities predicted by all models slowly decrease from the external borders to approximately 100 km from the future ridge, while in the central part of the domain the velocities rapidly decrease to 0 mm yr^{-1} (Figures 6.3 a_2, 6.4 a_2, 6.5 a_2 and 6.6 a_2 and green area in Figure 6.7). This velocity pattern induces low strain rates within the crust away from the ridge (ranging from 1 to 3 $\cdot 10^{-16}$ s^{-1}), while the highest values of strain rate (higher than 10^{-14} s^{-1}) characterize the surroundings of the future ridge (Figure 6.3 a_1, 6.4 a_1, 6.5 a_1 and 6.6 a_1). This phase lasts 5.9 Ma for model HL150.HC35 (Figure 6.3 c_1), 2.9 Ma for model HL150.HC40 (Figure 6.4 b_1), 4.9 Ma for model HL200.HC35 (Figure 6.5 b_1) and 3.9 Ma for model HL200.HC40 (Figure 6.6 b_1), indicating a longer duration of phase I for thinnest crust and thinnest lithosphere.

During the second phase (phase II), a significant change occurs in the horizontal crustal velocities, which linearly decrease in intensity from the borders to the future ridge (Figure

5.7), resulting in more intense strain rates, higher than 10^{-15} s^{-1}, throughout the crust. The duration of the second phase is different for the different models. It lasts approximately 17 Ma for model HL150.HC40, 8.5 Ma for models HL200.HC35 and 9.5 Ma for model HL200.HC40 (Figure 5.4 c, 5.5 c and 5.6 c, respectively), while the HL150.HC35 model does not show a phase II.

The crustal horizontal velocities remain stable until the end of phase II when continental crust breakup occurs. For all models, crustal breakup can be recognized in Figure 6.7 by the interrupted dotted black line localized around the future ridge and the immediately preceding velocity profile (black thick solid line). Crustal breakup occurs between 5.9 and 6.4 Ma for model HL150.HC35, between 19.9 and 20.4 Ma for model HL150.HC40, and between 13.4 and 13.9 Ma for models HL200.HC35 and HL200.HC40. Crustal strain rates and horizontal velocity patterns at these two times are shown in Figure 6.3 c_1-d_1, 6.4 c_1-d_1, 6.5 c_1-d_1 and 6.6 c_1-d_1 for models HL150.HC35, HL150.HC40, HL200.HC35 and HL200.HC40, respectively. The thermomechanical evolution of model HL150.HC35 is faster than those of the other models, and continental crustal breakup occurs at the end of phase I (black solid lines in Figure 6.7 a).

After crustal breakup (beginning of phase III) the magnitude of the crustal horizontal velocity progressively increases in all models both in space (towards the passive margin) and in time with the progression of model evolution (panels d_2 of Figure 6.3-6.6). These changes are compatible with the variation in time of the oceanic spreading rate. Consequently, the effective strain rate decreases over time until the crust starts moving as a rigid block, with the same velocities as those imposed at the marginal sides of the model.

Figure 6.7 shows that local horizontal contraction may occur at crustal level after crustal breakup, evident in terms of a value of the horizontal velocity that increases moving toward the axial zone. It could be correlated to the coeval intensification of the uprising mantle flow in the central part of the model, as evidenced by the arrows represented in Figures 6.3-6.6. A deeper investigation would be necessary to confirm this hypothesis but it is out of the scope of the present paper.

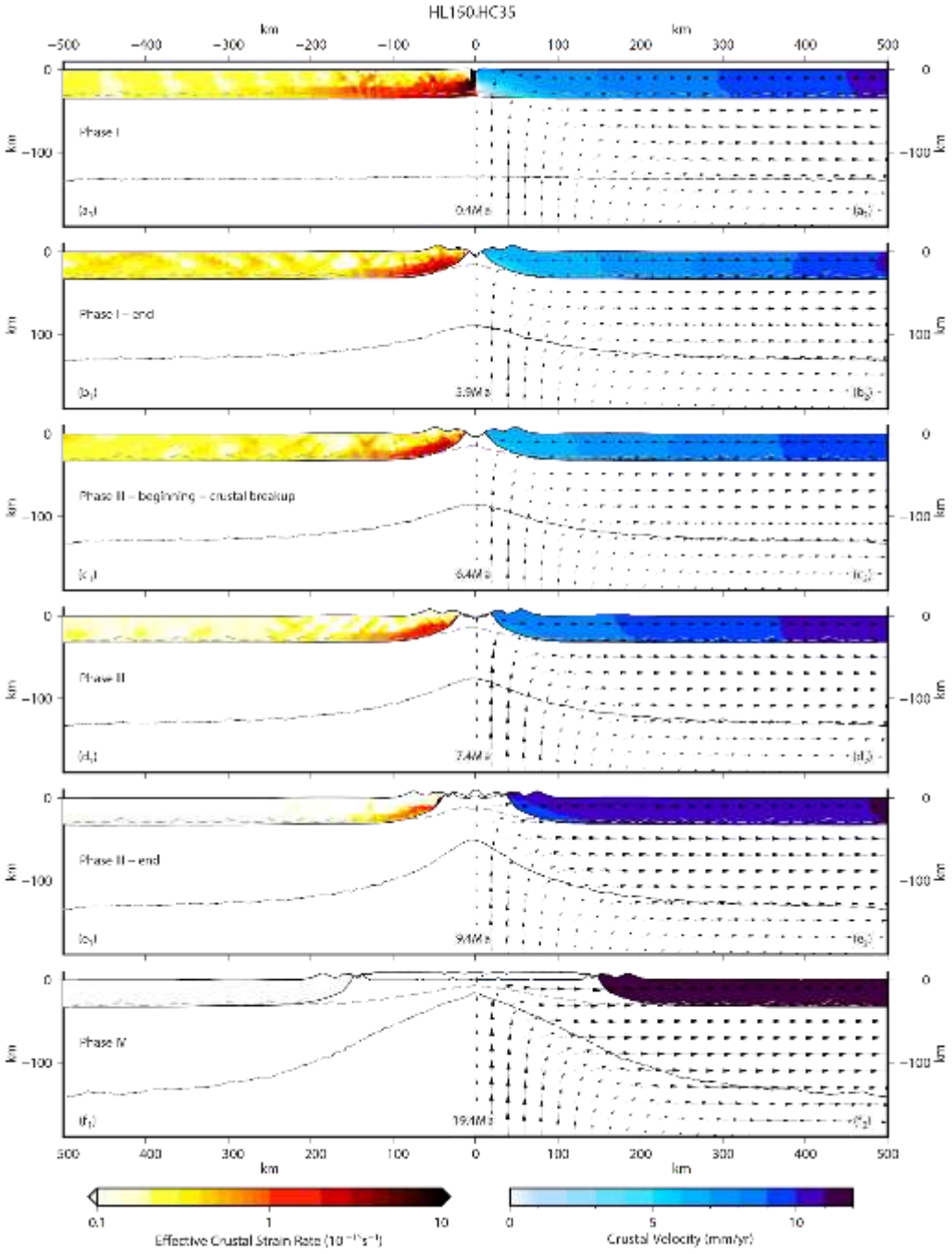

Figure 6.3: Effective crustal strain rate (left side) and intensity of crustal horizontal velocity and velocity fields (right side) predicted by model HL150.HC35 at different times after the beginning of forced extension. Gray dashed lines correspond to the 800 K and 1500 K isotherms. Solid black lines represent the envelopes of crustal- and mantle-type markers.

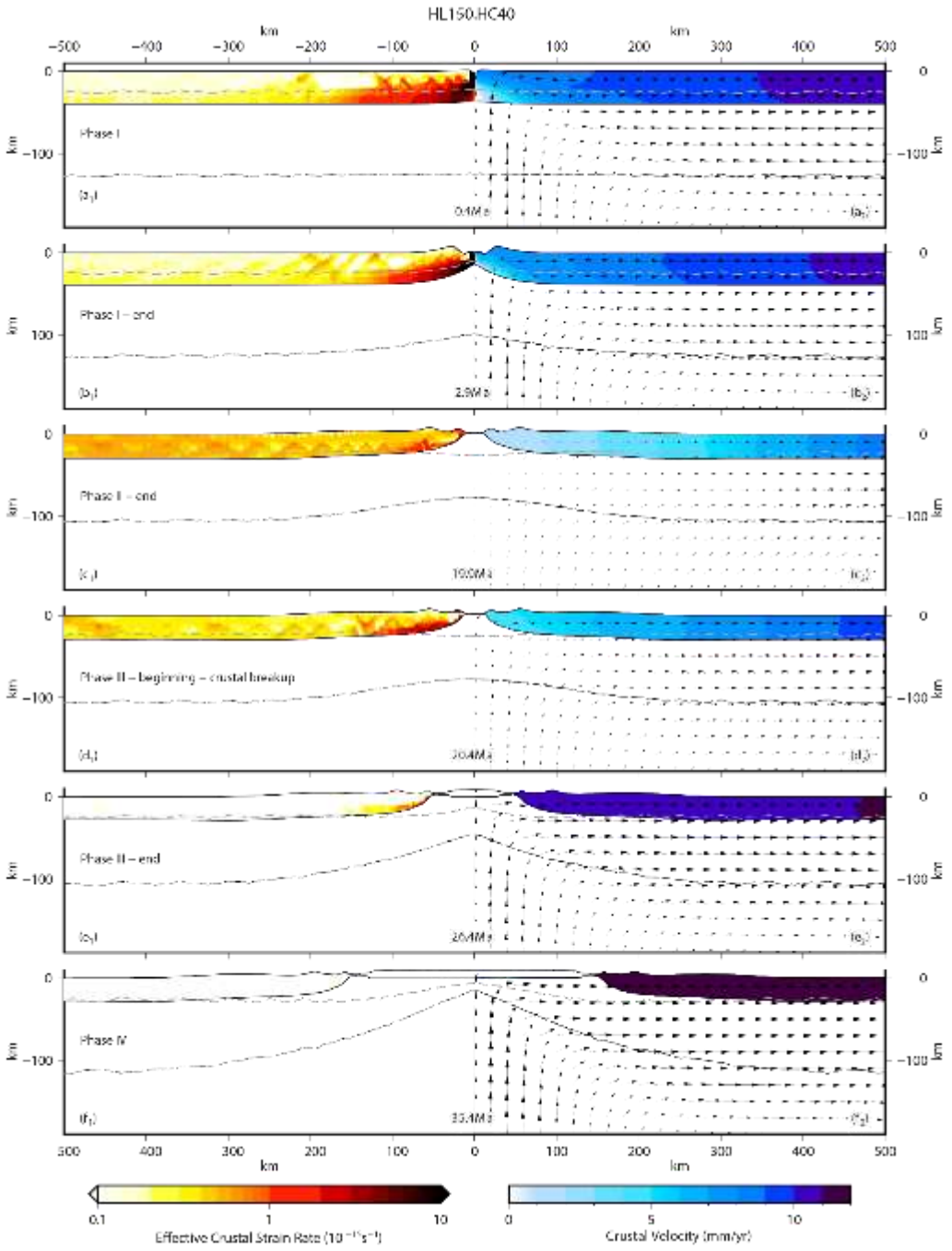

Figure 6.4: Effective crustal strain rate (left side) and intensity of crustal horizontal velocity and velocity fields (right side) predicted by model HL150.HC40 at different times after the beginning of forced extension. Gray dashed lines correspond to the 800 K and 1500 K isotherms. Solid black lines represent the envelopes of crustal- and mantle-type markers.

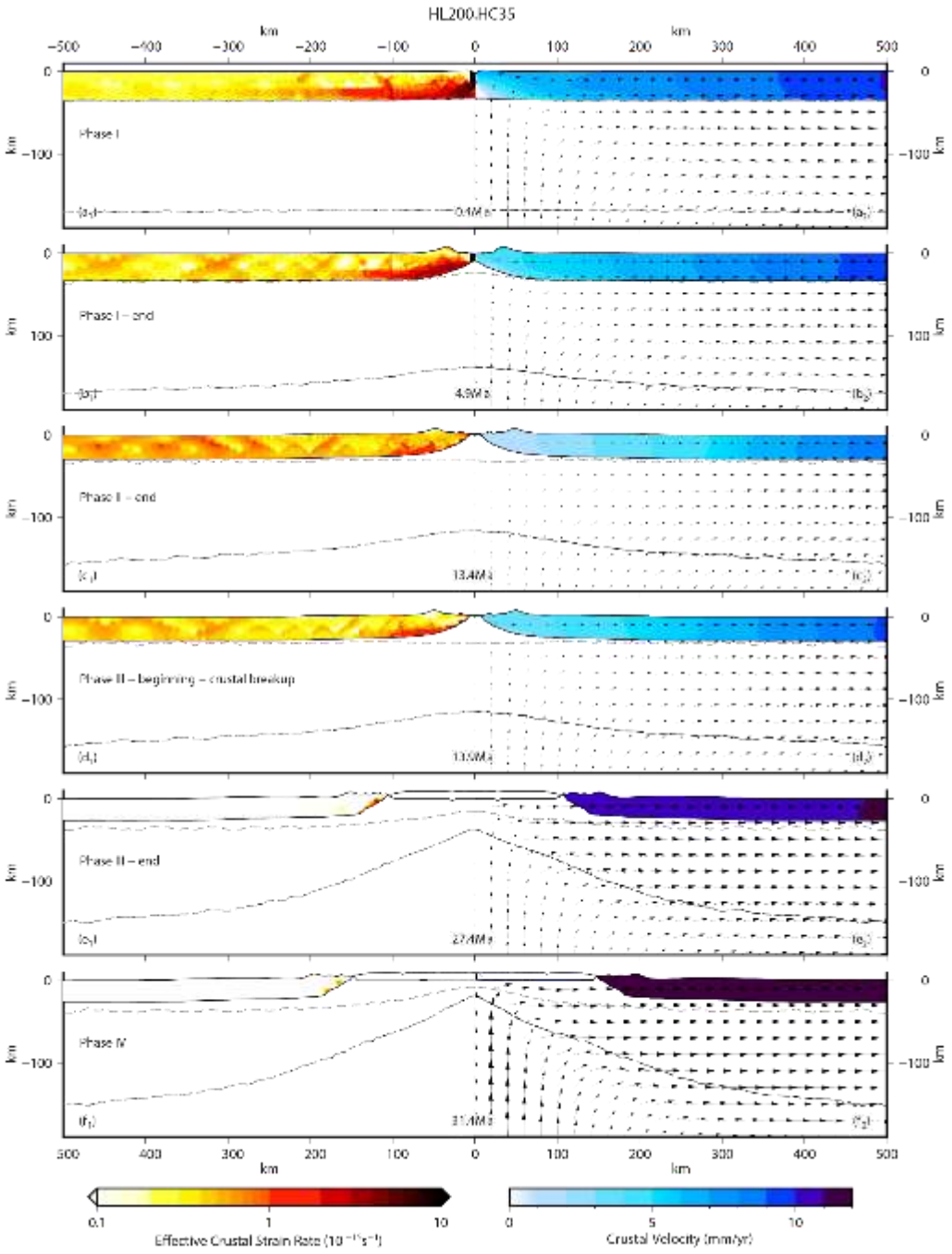

Figure 6.5: Effective crustal strain rate (left side) and intensity of crustal horizontal velocity and velocity fields (right side) predicted by model HL200.HC35 at different times after the beginning of forced extension. Gray dashed lines correspond to the 800 K and 1500 K isotherms. Solid black lines represent the envelopes of crustal- and mantle-type markers.

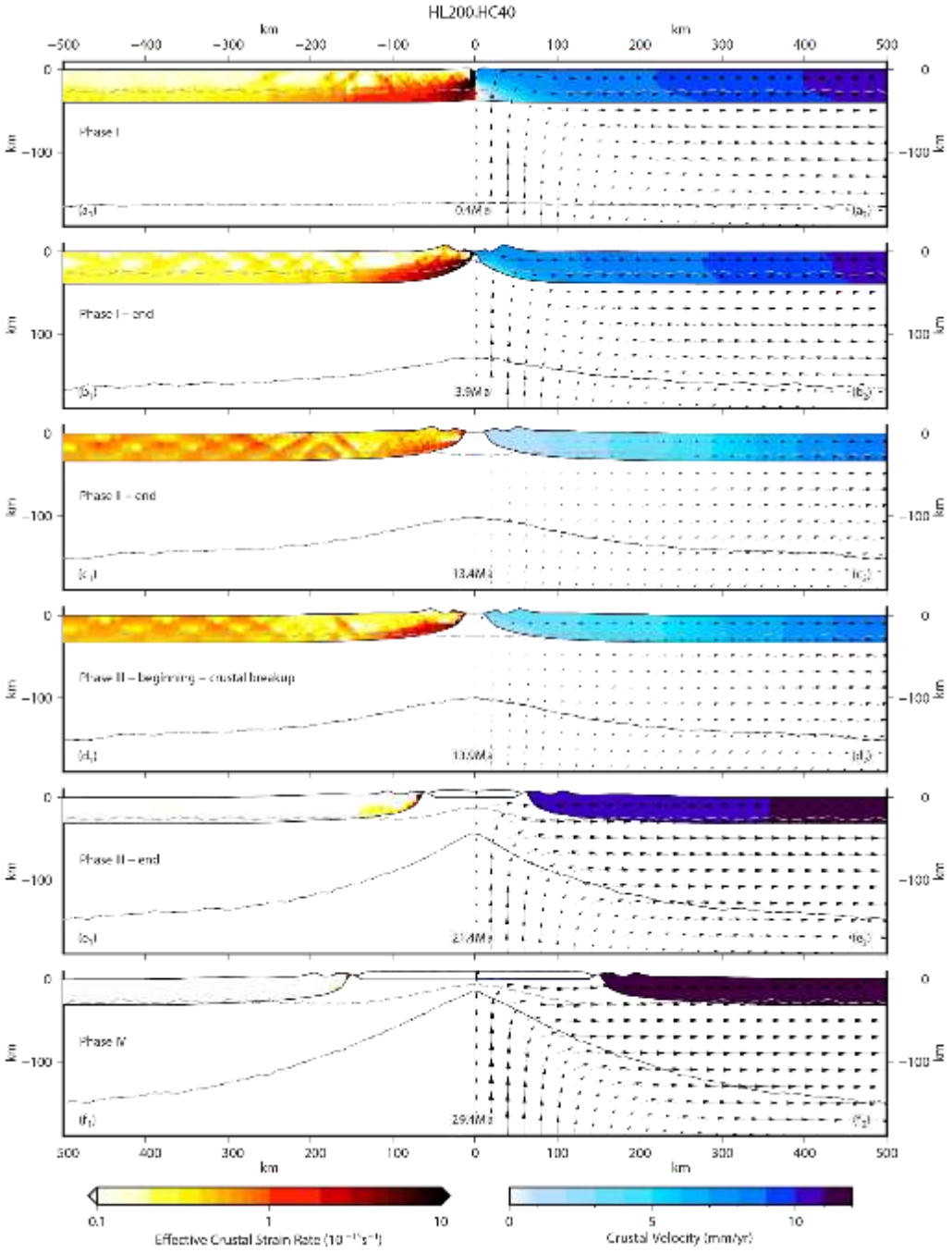

Figure 6.6: Effective crustal strain rate (left side) and intensity of crustal horizontal velocity and velocity fields (right side) predicted by model HL200.HC40 at different times after the beginning of forced extension. Gray dashed lines correspond to the 800 K and 1500 K isotherms. Solid black lines represent the envelopes of crustal- and mantle-type markers.

We assume that phase III ends when the crustal horizontal velocities differ by less than 10% from the maximum value prescribed at the marginal sides of the model (i.e., they are greater than 10.35 mm/year) and the effective strain rate is decreased anywhere well below 10^{-16} s^{-1}, as shown in panels e Figure 6.3 (HL150.HC35 model, at 9.4 Ma), 6.4 (HL150.HC40 model, at 26.4 Ma), 6.5 (HL200.HC35 model, at 27.4 Ma) and 6.6 (HL200.HC40 model, at 21.4 Ma). The sole exception occurs near the passive margin, where values of the effective strain rate higher than 10^{-15} s^{-1} are still induced at the Moho level by basal shear due to the rising mantle. Based on the definition given in Section 6.4, at the end of phase III lithospheric breakup is accomplished.

Finally, the last phase (IV) is characterized by two sections of crust that move as rigid blocks, with a velocity that, within a tolerance of 10%, is equal to that prescribed at the marginal sides. During this phase the extension of the central part of the model domain is driven by the upwelling mantle flow only and is accommodated by seafloor spreading (panel f of Figures 6.3-6.6). As mentioned in Section 6.3, continental extension in the Gulf of Aden culminated in crustal rupture at approximately 16 Ma, and the accretion of new oceanic lithosphere in the central portion of the study area led to the formation of a 300 km-wide ocean. Our results agree with the analysis of the dragged samples along the mid-ocean ridge axis, which confirm that the basin is actually floored with basalts, as stated in *Leroy et al*., 2010 and *Gass*, 1970.

We stop the simulations when the two continental blocks are 400 km apart, which occurs at 24.4 Ma for model HL150.HC35, 40.4 Ma for model HL150.HC40, 35.4 Ma for model HL200.HC35 and 34.4 Ma for model HL200.HC40 (Figures 6.3f, 6.4f, 6.5f and 6.6f, respectively). The long simulation time span also allows us to simulate the formation of the OCT zone, if this should develop.

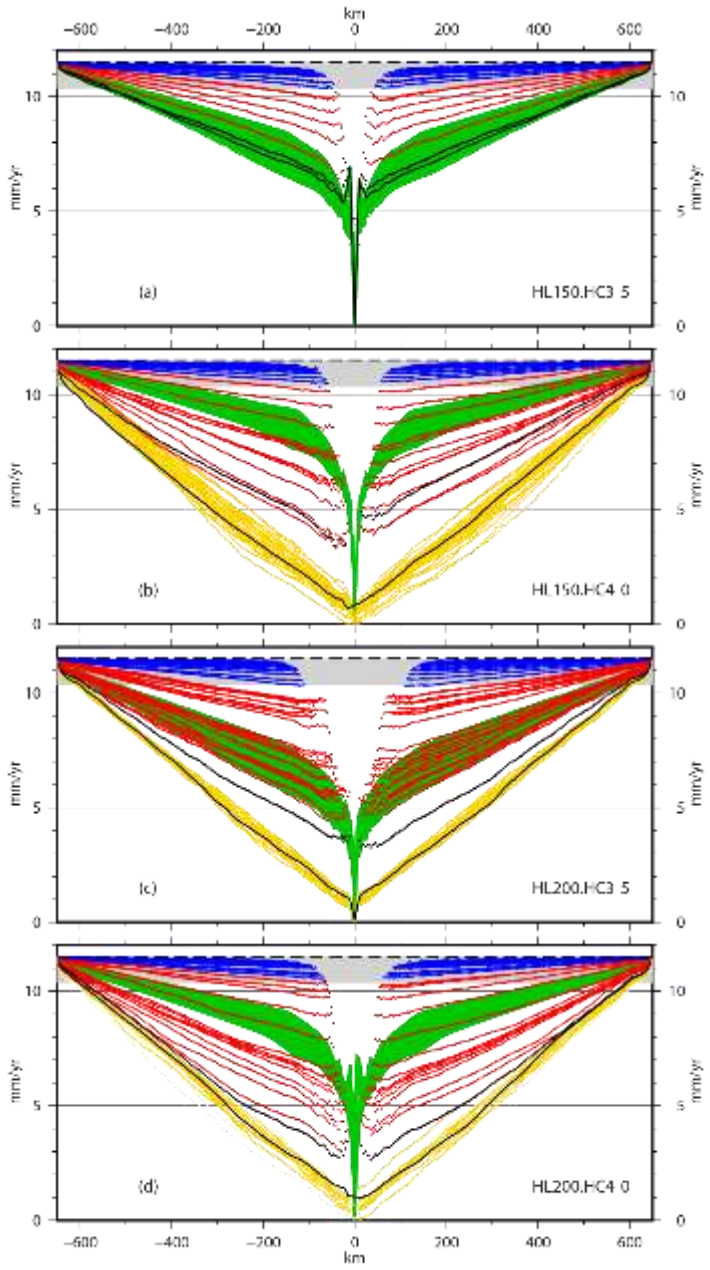

MODEL

	HL150.HC35	HL150.HC40	HL200.HC35	HL200.HC40
PHASE 1	0Ma ÷ 5.9Ma	0Ma ÷ 2.9Ma	0Ma ÷ 4.9Ma	0Ma ÷ 3.9Ma
PHASE 2	---	3.4Ma ÷ 19.9Ma	5.4Ma ÷ 13.4Ma	4.4Ma ÷ 13.4Ma
PHASE 3	6.4Ma ÷ 9.4Ma	20.4Ma ÷ 26.4Ma	13.9Ma ÷ 27.4Ma	13.9Ma ÷ 21.4Ma
PHASE 4	9.9Ma ÷ 24.4Ma	26.9Ma ÷ 40.4Ma	27.9Ma ÷ 35.4Ma	21.9Ma ÷ 34.4Ma

Figure 6.7: Horizontal velocities vertically averaged on crustal thickness, predicted by models HL150.HC35 (a), HL150.HC40 (b), HL200.HC35 (c) and HL200.HC40 (d) at different distances from the ridge along the model during the different evolutionary phases (colors). The time step between lines is 0.5Ma. Solid and dotted black lines indicate the average horizontal crustal velocity just before (end of phase II) and just after (beginning of phase III) crustal separation. Gray areas indicate the 10% tolerance in velocity used to define phase IV.

6.5.2 Partial melting and Oceanization

In all models, mantle serpentinization occurs during the early stages of evolution at the base of the thinned continental crust whose thickness is lower than 10 km in agreement with *Pérez-Gussinyé and Reston* (2001). In particular, 4.4 Ma after the beginning of forced extension, mantle serpentinization is observed below the ridge axis in models HL150.HC35 (Figure 6.8 a) and HL150.HC40 (Figure 6.9 b), at 5.4 Ma in model HL200.HC35 (Figure 6.10 a) and at 3.9 Ma in model HL200.HC40 (Figure 6.11 a). Mantle serpentinization causes a local decrease in the viscosity and consequently an increase in the local velocity.

Our results on the depth of the serpentinized zone with a thinned continental crust in magma-poor rifted margins are consistent with *Pinto et al*., (2015) who, from field work, obtain for proximal rift domains the possibility of highly extended (thinned) continental crust, lower than 10 km, which agrees with our modeling approach that does not contain faults or structural discontinuities, (Figures 6.8 a, 6.9 b, 6.10 a, 6.11 a).

As already stated in Section 6.4.2, we assume that the oceanic crust forms after the beginning of mantle partial melting. Considering wet peridotite with a total amount of H_2O equal to 0.05%, pressure and temperature conditions at the base of the lithosphere are favorable for the formation of oceanic lithosphere after a relatively short time from crustal breakup for models HL150.HC35 (3 Ma, Figure 6.8 c) and HL150.HC40 (4 Ma, Figure 6.9 d). In contrast, for models HL200.HC35 and HL200.HC40, favorable pressure and temperature conditions are reached 10 Ma and 6.5 Ma after the occurrence of crustal breakup (Figures 6.10 d and 6.11 d, respectively).

Considering wet peridotite with a total amount of H_2O equal to 0.1%, in models HL150.HC35 and HL150.HC40, favorable pressure and temperature conditions are reached 2 Ma and 17 Ma before the occurrence of crustal breakup (Figures 6.8 a and 6.9 a, respectively).

Similarly, in models HL200.HC35 and HL200.HC40, the formation of oceanic crust still starts after crustal breakup, namely, 4.5 and 2.5 Ma (Figures. 6.10 c and 6.11 c, respectively).

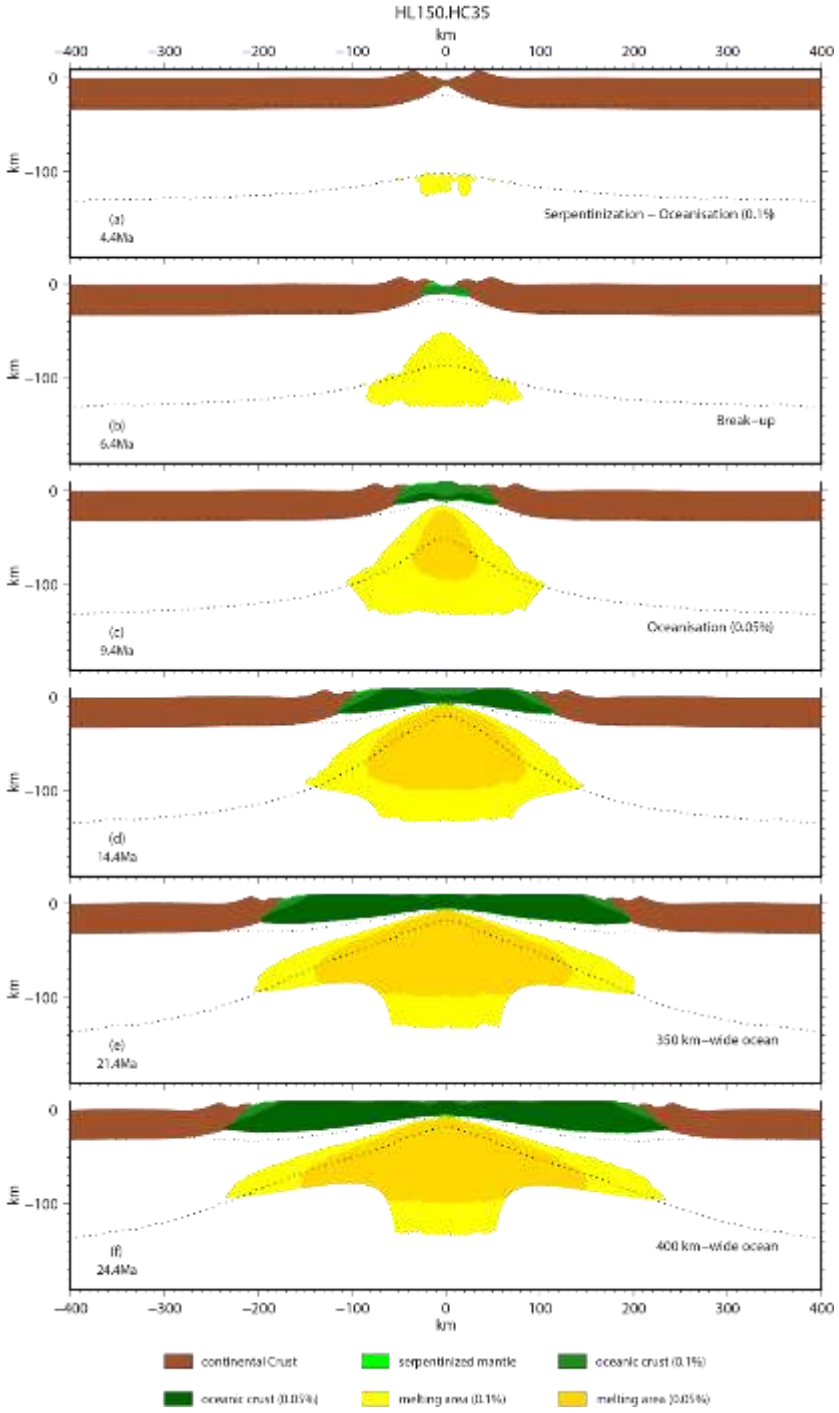

Figure 6.8: Marker distributions predicted by model HL150.HC35 at different times from the beginning of forced extension. Different colors indicate different material types as specified in the legend. See text for more details. Black dotted lines correspond to the 800 K and 1500 K isotherms.

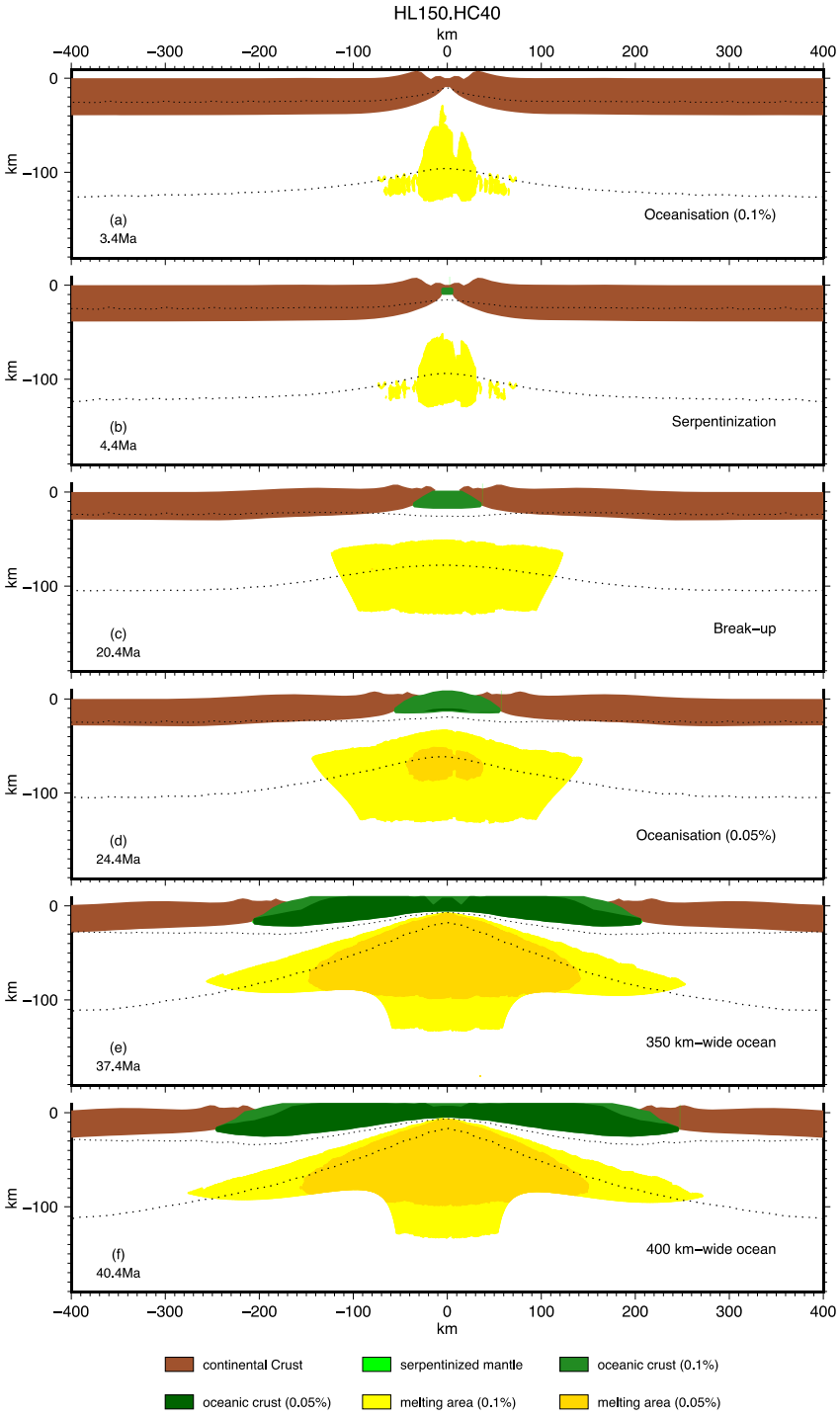

Figure 6.9: Marker distributions predicted by model HL150.HC40 at different times from the beginning of forced extension. Different colors indicate different material types as specified in the legend. See text for more details. Black dotted lines correspond to the 800 K and 1500 K isotherms.

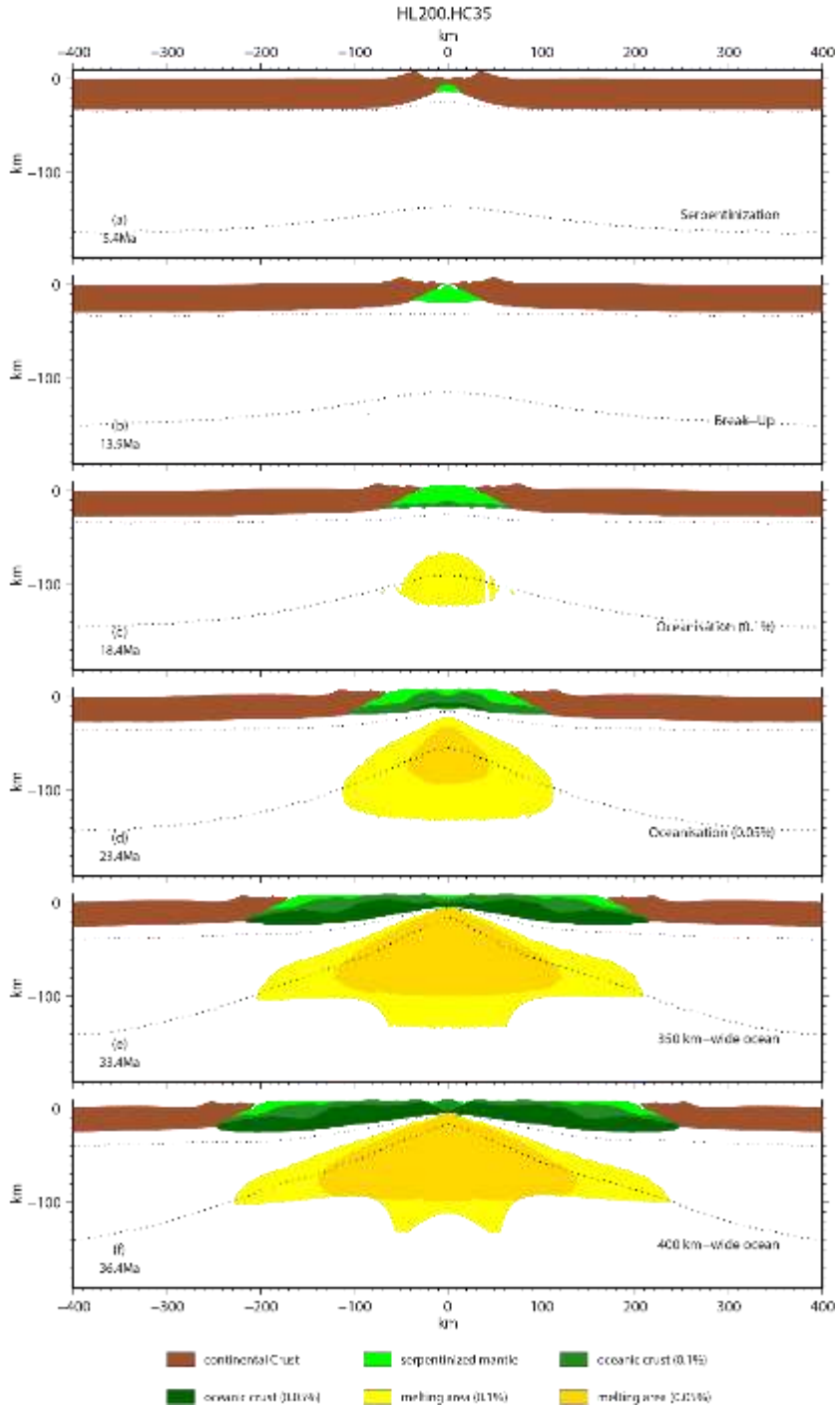

Figure 6.10: Marker distributions predicted by model HL200.HC35 at different times from the beginning of forced extension. Different colors indicate different material types as specified in the legend. See text for more details. Black dotted lines correspond to the 800 K and 1500 K isotherms.

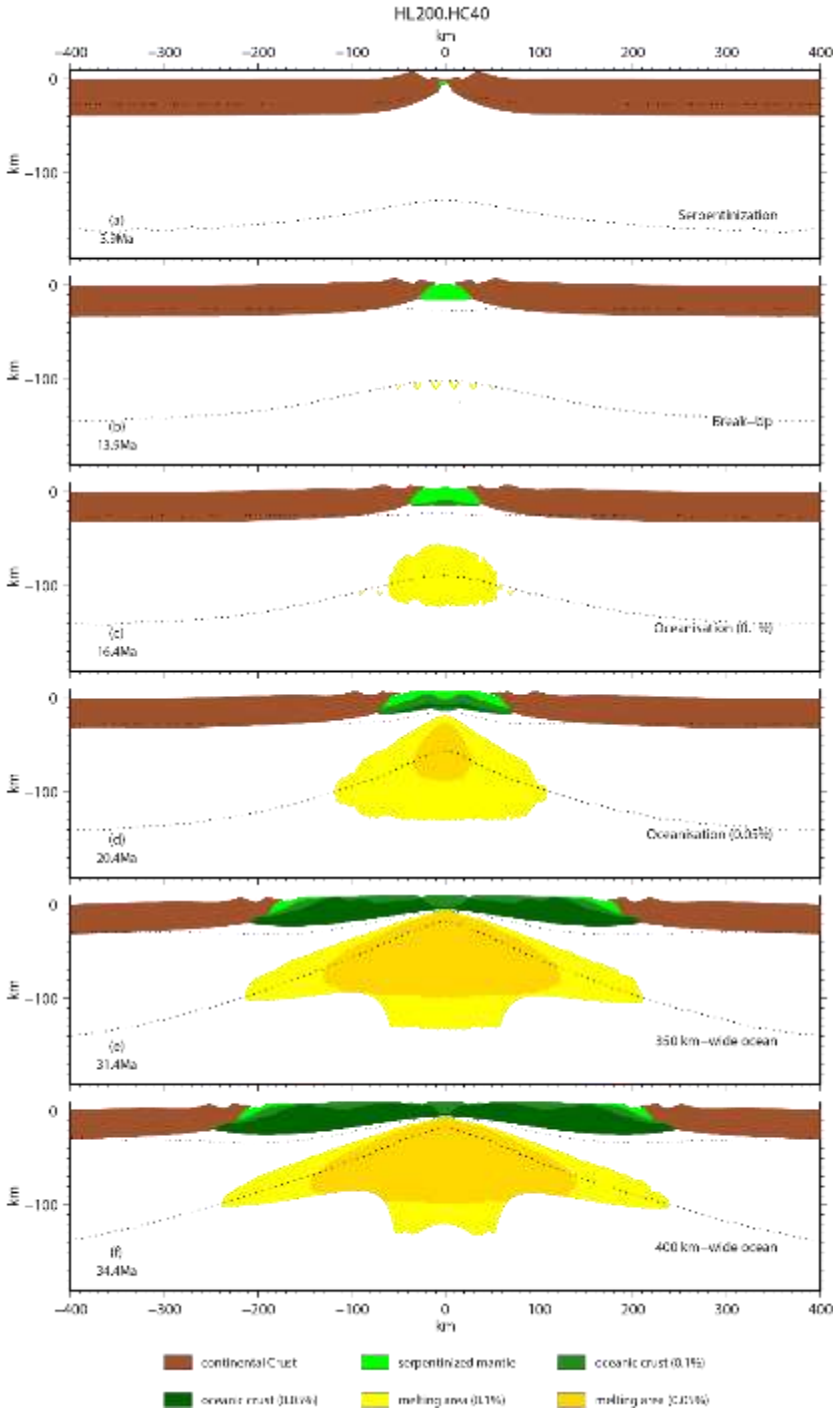

Figure 6.11: Marker distributions predicted by model HL200.HC40 at different times from the beginning of forced extension. Different colors indicate different material types as specified in the legend. See text for more details. Black dotted lines correspond to the 800 K and 1500 K isotherms.

As stated in Section 6.4, for the formation of the OCT, partial melting must occur after mantle serpentinization and our results show that this condition is satisfied in all models considering wet peridotite with a total amount of H_2O equal to 0.05%. In this case, at the time when the two continents are separated by a distance of 400 km, the denuded serpentinized mantle covers an area of variable width, from approximately 30 km at both continental margins in model HL150.HC35 (light and medium green color in Figure 6.8 f) to 50 km in model HL150.HC40 (Figure 6.9 f) and 70 km in model HL200.HC40 (Figure 6.11 f). In the HL200.HC35 model, the OCT zone lies below the oceanic crust; therefore, oceanization does not occur (Figure 6.10 f).

Considering peridotite with a total amount of H_2O equal to 0.1%, the conditions for OCT formation are predicted only by models HL200.HC35 and HL200.HC40, and OCT domain widths ranging from 80 km to 60 km develop (light green in Figures 6.10 f and 6.11 f, respectively). In the case of 0.1% hydrated peridotite, models HL150.HC35 and HL150.HC40 predict partial melting before crustal breakup, thus preventing the development of an OCT.

Our model results indicate that partial melting can occur before breakup (panel a of Figure 6.9), and the oceanic crust could underplate the lithosphere, in agreement with observation in continental rifts of the northernmost part of the Central Red Sea *(Ligi et al*., 2015).

Figure 6.12 synthesizes the main stages of the deformation history predicted by the implemented models in terms of the timing of crustal breakup, serpentinization and melting with respect to the four thermomechanical phases. Our results show that a thicker lithosphere makes less important the variation in crustal thickness on the breakup timing, which in fact is the same for the two models characterized by a 200 km thick lithosphere. The reduction of lithospheric thickness allows to emphasizes the effect of crustal variation on the crustal break up timing, which occurs earlier for a thinner crust.

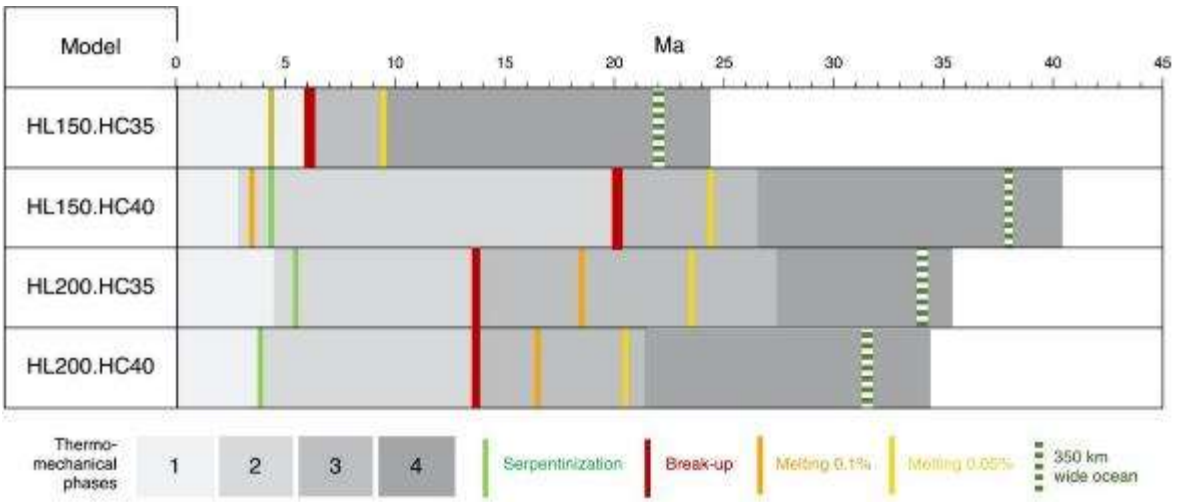

Figure 6.12: Synthetic representation of the main stages of the deformation history predicted by the models implemented in this study.

6.6 Discussion

In this study, we simulate the transition from continental rifting to oceanic spreading in the Gulf of Aden by means of a 2D numerical model based on the results of geodynamic studies and integrated modeling of elevation, geoid data and thermal analysis. A prescribed velocity of 11.5 mm/yr is applied at both sides of the domain to fit the present-day kinematics of the study area. Furthermore, we adopt initial thicknesses of 35 and 40 km for the continental crust and 150 and 200 km for the lithosphere.

A main result is that the thermomechanical evolution of the system can be separated into four phases with various durations for the different models:

a) phase I is characterized by horizontal crustal velocities that slowly decrease from the boundary of the model to approximately 100 km from the ridge and by rapid decreases in velocities in the central portion of the domain; as a consequence, low strain rates characterize the crust away from the ridge, while very high strain rates characterize the surroundings of the future ridge, as also shown in the modeled strain rate pattern in *Brune and Autin* (2013), *Brune* (2014) and *Schettino et al*., (2019);

b) phase II has a crust characterized by velocities that are almost constant in time but decrease linearly in space from the lateral sides to the future ridge. During this phase,

the highest velocity gradients and strain rates are observed (e.g., *Brune and Autin*, 2013; *Watremez et al*., 2013; *Brune*, 2014;). Phase II ends when continental crustal breakup occurs after 19.9 Ma from the beginning of rifting in model HL150.HC40 and after 13.4 Ma in models HL200.HC35 and HL200.HC40. This phase is not recorded by model HL150.HC35, which exhibits crustal breakup after 5.9 Ma, i.e., at the end of phase I;

c) phase III characterizes the post crustal breakup evolution in all models. During this phase, there are fast increases in both horizontal velocities in the crust and vertical velocities corresponding to the ridge. Compared to phase II, the lateral velocity gradients are less intense and even decrease over time, resulting in strain rates that are lower than those predicted for phase II. This phase lasts 3 Ma for model HL150.HC35, 6 Ma for models HL150.HC40, 13.5 Ma for model HL200.HC35 and 7.5 Ma for HL200.HC40. At the end of phase III, when the lithospheric breakup occurs, the horizontal velocities in the crustal blocks are constant, with values higher than 10 mm/yr in all models, and strain rates are very low (well below 10^{-16} s^{-1}) compared to those predicted during previous phases;

d) phase IV is marked by two sections of crust that move as rigid blocks with a velocity that, within a tolerance of 10%, is equal to that prescribed at the marginal sides, comparable with the velocity trend shown in *Marotta et al*., (2018). This phase ends when the two continental blocks are 400 km apart, that is after 24.4, 40.4, 35.4 and 34.4 Ma from the beginning of evolution, for models HL150.HC35, HL150.HC40, HL200.HC35 and HL200.HC40, respectively.

The Gulf of Aden is characterized by different velocities of oceanic spreading, which increase from west to east. In particular, west of the SSFZ, where magnetic anomalies date the formation of the oceanic floor at 2-3 Ma (*Bellahsen et al*., 2003; *Bellahsen et al*., 2006; *Fournier et al*., 2010; *Leroy et al*., 2010; *Bonatti et al*., 2015), velocities are approximately 13 mm/yr, while in the east, in proximity to the AFFZ, where magnetic anomalies date the formation of the oceanic floor at 16-17 Ma (*Bellahsen et al*., 2003; *Bellahsen et al*., 2006; *Fournier et al*., 2010; *Leroy et al*., 2010; *Bonatti et al*., 2015), velocities are approximately 20 mm/yr. The variation velocities predicted near the passive margin at different times of the evolution may contribute to explain the different velocities observed in the Gulf of Aden

along different transects characterised by different ages of spreading. In fact, models HL150.HC40, HL200.HC35 and HL200.HC40 predict a total spreading rate of 12-13 mm/yr 3 Ma after the breakup at approximately 100 km from the ridge, which is compatible with the velocity observed at present in proximity to the SSFZ; the sole exception occurs for model HL150.HC35. Furthermore, all models predict a total spreading rate of 21-22 mm/yr 15-16 Ma after the breakup, at approximately 150 km from the ridge, as observed at present in proximity to the AFFZ.

Our results show that mantle serpentinization does not depend strictly on the initial thickness of crust and lithosphere: for almost all models it starts at 4.4 Ma after the beginning of rifting and only in model HL200.HC35 serpentinization occurs one million years later. In contrast, the timing of mantle partial melting strongly depends on the thickness and thus on the initial thermal state of the lithosphere (*Mckenzie and Bickle*, 1988; *Schmeling*, 2000; *Furlong and Chapman*, 2013) (compare Figures 6.8 and 6.9 and Figures 6.10 and 6.11). In particular, considering wet peridotite with a total amount of H_2O equal to 0.1%, partial melting occurs very early for models with thinner lithosphere (Figures 6.8 a and 6.9 a, for models HL150.HC35 and HL150.HC40, respectively) and even before the occurrence of serpentinization when a thicker initial crust is considered (model HL150.HC40). This result is caused by the higher thermal conditions of thinner lithosphere (models HL150.HC35 and HL150.HC40) and, in the same way, by the thicker continental crust of model HL150.HC40, which generates higher temperatures at the Moho level due to the higher production of radiogenic energy. Since the initial thermal conditions of the thin models are not very different from those required for melting in 0.1% hydrated mantle, mantle melting occurs very quickly in these models. In contrast, in colder models, a long time is required to increase the thermal state to pressure–temperature conditions that are suitable for mantle melting.
When peridotite with a total amount of H_2O equal to 0.05% is assumed, mantle partial melting needs a higher thermal state (temperatures approximately 100°C higher than those required for hydrated mantle with 0.1% water content). Consequently, models take more time to reach melting for 0.05% hydrated mantle. For all models, melting of 0.05% hydrated mantle occurs after breakup and 4 to 5 Ma after melting of 0.1% hydrated mantle. The sole exception occurs for model HL150.HC40, which predicts melting of 0.05% hydrated mantle only 20 Ma later than that of wetter mantle. The highest temperatures and the lowest stiffness characterizing this model make the stress transmission less effective, and the localization of

thinning that drives the local increase in temperature occurs very late.

As mentioned in Section 6.3, the Gulf of Aden is a juvenile ocean that began rifting during the late Eocene between 42 and 35 Ma (*Watchorn et al*., 1998; *Basuyau et al*., 2010; *Leroy et al*., 2010). Magnetic data indicate that the emplacement of the oceanic floor can be dated at 19.7 Ma in the easternmost part of the Sheba Ridge, at 17.6 Ma up to the AFFZ and at approximately 16 Ma between the AFFZ and the SSFZ (*Bellahsen et al*., 2003; *Bellahsen et al*., 2006; *Fournier et al*., 2010; *Leroy et al*., 2010; *Bonatti et al*., 2015). These results suggest a period of 20 Ma characterized by extensional tectonics before the occurrence of continental breakup, and subsequently an oceanic/OCT domain forms, with width from approximately 350-400 km in proximity to the Sheba Ridge, where the opening rate is 23 mm/yr, to approximately 200 km near the SSFZ, where the opening rate is 16 mm/yr.
West of the SSFZ (Figure 5.1), which marks the limit of the Afar plume influence, the Gulf of Aden exhibits volcanic margins without the formation of an OCT; partial melting possibly occurs before crustal breakup, and oceanic crust is created as soon as the continental crust is broken apart by dikes (*Watremez et al*., 2003). East of the SSFZ, the Gulf is characterized by magma-poor rifted margins where partial melting occurs after crustal breakup, and a narrow OCT (15-50 km) forms between the last continental crust and the first oceanic crust (*Bauer et al*., 2000; *Watremez et al*., 2003), which presents strong along-margin variations with serpentinization and little volcanism (*Watremez et al*., 2013). In particular, in the eastern part, oceanic crust begins to form approximately 1 Ma after continental breakup, with the consequent formation of an approximately 25-40 km-wide OCT (*Nonn et al*., 2019).

The comparison between numerical models and the natural Gulf of Aden mainly focuses on the central sector of the Gulf between the SSFZ and the AFFZ, where the emplacement of the oceanic floor was a continuous process *(Fournier et al*., 2010). Therefore, considering an extensional period lasting 20 Ma before the breakup, the HL150.HC35 model is not compatible with the geodynamic reconstructions because of its early breakup, which is predicted to occur approximately 7 Ma after the beginning of forced extension (Figure 6.7 a). In addition, model HL150.HC35, when a percentage of H_2O equal to 0.1% is accounted for in the mantle, predicts mantle serpentinization that is coeval with mantle partial melting, thus not satisfying the conditions for OCT formation (Figure 6.8 a). Similarly, models characterized by a 200 km-thick lithosphere predict breakup approximately 14 Ma after the start of rifting (Figure 6.7 c-d). Further, considering peridotite

with a total amount of H_2O equal to 0.05%, models HL200.HC35 and HL200.HC40 show delays between crustal breakup and mantle melting ranging from 6.5 to 10 Ma (Figures 6.8 d and 6.9 d), with the development of an OCT larger than that observed in the Gulf of Aden.

Considering 0.05% hydrated mantle, model HL150.HC40 is the most appropriate to reproduce the geodynamic evolution of the study area; this model is also in agreement with crustal and lithospheric thicknesses based on geoid data and thermal analysis (*Globig et al*., 2016) that show a thinned continental crust (passive margin), an OCT zone and an oceanic lithosphere, which characterize the final structure of the system. In fact, model HL150.HC40 predicts the onset of mantle serpentinization under the continental crust before the occurrence of mantle partial melting (Figure 6.9 a), which occurs 4 Ma after crustal breakup. This sequence of events allows the formation of an approximately 40-50 km-wide OCT (Figure 6.9 f). In addition, the oceanic domain in this model reaches an extension of 350-400 km by 37-40 Ma after the beginning of forced extension, in agreement with the ages of the first extensional structures observed in the area.

The westernmost part of the area, near the SSFZ, is characterized by a transition between magma-rich and magma-poor margins, moving from west to east (Figure 6.1) and by the absence of an OCT. Therefore, models that predict dynamics compatible with the evolution of the margins of this area are models HL150.HC35 and HL150.HC40 with 0.1% hydrated mantle because mantle serpentinization occurs synchronously with mantle partial melting and the OCT does not form. However, model HL150.HC35 does not show a timing compatible with the geodynamic reconstruction of the area, as revealed previously. In addition, model HL150.HC40 fits the westernmost part of the area characterized by volcanic margins since melting occurs before continental breakup. Geochemical studies of MORB that incorporate a component from a plume-associated source suggest H_2O concentrations in plume sources ranging from 0.03 to 0.1% (300–1000 ppm; *Hirschmann*, 2006), compatible with the peridotite water content used in our simulations.

Our results show that model HL150.HC40 describes the evolution of the central sector of the Gulf of Aden well, and the variations in the features along the passive margins could be related to lateral variations in the amount of H_2O in the mantle, which determine different times of mantle melting. In fact, melting in the case of 0.05% hydrated mantle leads to the formation of a magma-poor margin and a narrow OCT, while increasing the water content

up to 0.1% causes melting to occur before continental breakup, with a consequent volcanic margin and the absence of an OCT. The increase in mantle water storage can be associated with the presence of the Afar plume in the westernmost portion of the Gulf of Aden; a similar situation is also observed in proximity to a mantle plume along the Reykjanes Ridge in the North Atlantic (*Nichols et al*., 2002).

The dependence of mantle hydration on mantle melting and of the timing of breakup on the thickness of the crust and lithosphere, allow us to further constrain the latter compared with previous analyses. In particular, our results define an upper bound for crustal thickness of 40 km, in agreement with the findings obtained from the integration of elevation and geoid data and thermal analysis of north Africa by *Globig et al*., (2016).

Our results for model characterized by 150 km -thick lithosphere show melting production before continental breakup, in agreement with numerical models by *Pérez-Gussinyé et al*., (2006) accounting for an extensional velocity of 1 cm/yr.

6.7 Conclusion

We developed 2D thermomechanical numerical models of passive rifting to investigate the evolution of the lithosphere in the Gulf of Aden. The models are founded on integrated modeling of elevation, geoid data and thermal analysis and account for the present-day kinematics observed between the Arabian plate and Africa (Nubia) and Somalia. For the combination of parameters assumed in the present analysis, our results indicate that, in addition to support a deformation history that develops in 4 different phases, the timing of mantle serpentinization is not affected by the initial thermal configuration of the system, and mantle serpentinization starts a few million years (4-5 Ma) after the onset of rifting for all models, well before crustal breakup.

Furthermore, our results show that the OCT always develops when the rifting to oceanization transition occurs in case of a thick lithosphere. In contrast, with a thin lithosphere, wet peridotite with a total amount of H_2O equal to 0.05% is required to drive the development of an OCT zone. Model predictions, in terms of the times of different deformation phases and sizes of the oceanic domain and the OCT zone, are compared with information based on magnetic data analysis and on the observed distribution of volcanic

margins in the region between the SSFZ and the AFFZ, where emplacement of the oceanic floor was a continuous process. Model results confirm that the model with an initial 150 km-thick lithosphere and a 40 km-thick crust is the most appropriate to reproduce the geodynamic evolution of the study area when 0.05% hydrated mantle is considered. This model is also in agreement with the crust and lithosphere thicknesses based on thermal analysis and geoid data, which imply that the central part of the Gulf of Aden started to rift at approximately 37-40 Ma in its easternmost sector and is characterized by the sequence of a thinned passive margin, an OCT zone and an oceanic domain.

The best-fit model predicts a 40-50 km-wide OCT zone and a 350-400 km-wide oceanic domain in the eastern sector, while a 100 km-wide oceanic domain with no OCT zone is predicted in the western sector of the Gulf of Aden. The variations in features along the passive margins from west to east are ascribable to lateral variations in the amount of H_2O in the mantle, which determines the different times of mantle melting. In particular, an increase from 0.05% to 0.1% hydrated mantle associated with the Afar plume might have preceded mantle melting and thus precluded the development of an OCT zone in the western sector of the Gulf of Aden. Our approach allows us to obtain a robust estimate of the crustal thickness of 40 km, thus definitively choosing the upper bound in previous estimates of this parameter for the crust surrounding the Gulf of Aden.

6.8 Regional gravity pattern of Gulf of Aden

Figure 6.13 shows a regional map of the gravity disturbance in the surroundings of the Gulf of Aden based on the static gravitational model GO_CONS_GCF_2_TIM_R6 (*Brockmann et al*., 2019) that is the 6th release of the GOCE gravity field model by means of the time-wise approach.

The gravity disturbance is evaluated in the spherical approximation at a height h_S=5 km above the spheroid of radius R = 6378.137 km. We consider this altitude to smooth the geodetic signal and make it more suitable to be compared with the modelled one. The geodetic functional gravity disturbance is defined as the difference between the magnitude of the gravity g and the magnitude of the normal gravity γ :

$$\delta g\,(h,\,\lambda,\,\varphi) = g\,(h,\,\lambda,\,\varphi) - \gamma\,(h,\,\varphi)\,,$$

where λ is the ellipsoidal longitude, φ is the ellipsoidal latitude and h is its height above the sea level.

The observed gravity disturbance will be compared to the modelled gravity disturbance across the six profiles drawn perpendicularly to the ridge axis (Figure 6.13), crossing the eastern (red lines) and the central (blue lines) part of the study area.

The map of the gravity disturbance (Figure 6.13) shows a large regional EW trend dominates the gravity disturbance pattern and ranges from approximately -40 mGal in the west to 30-35 mGal in the east. This trend is mainly related to the continent-ocean transition: the positive gravity disturbance values along the ridge axis reflect a thinner crust, compatible with the presence of oceanic crust. The maximum values (30-35 mGal) are located over the central section of the Sheba Ridge where the identification of Chron 5d yields an age of at least 17.6 Ma for the inception of seafloor spreading (*Leroy et al*., 2010). Moving west from AFFZ, the zone of oceanic crust accretion becomes limited to a narrow axial strip while, west of ~44°E, the lack of positive gravity values suggests the presence of thick, possibly stretched crust in the Gulf od Tadjoura (*Hébert et al*., 2001). This indicates that the axial emplacement of oceanic crust may have just started, as confirmed by the non-detection of regular magnetic stripes (*Bonatti et al*., 2015).

The positive gravity disturbances values can be also attributed to the presence of hot mantle under the Gulf of Aden. In fact, low electrical resistivity values of the mantle as well as the existence of very low seismic velocity in the zone between Alula–Fartak Fracture zone (AFFZ) and Socotra–Hadbeen Fracture zone (SHFZ) coincide with active off-axis volcanism on the ridge flanks, which can be related to anomalous presence of melt beneath the lithosphere (*Leroy et al*., 2010).

According to the channelized along-axis plume flow model proposed in *Leroy et al*. (2010) to give a possible explanation for the existence of a regional melting anomaly in the Gulf of Aden, partial melt may channelled from Afar plume along the corridor formed by the Aden-Sheba ridge system as far eastwards as Yemen, Somalia and Oman, implying an influence of the Afar Plume, which extends toward the eastern Gulf of Aden (*Leroy et al*., 2010; *Corbeau et al*., 2014).

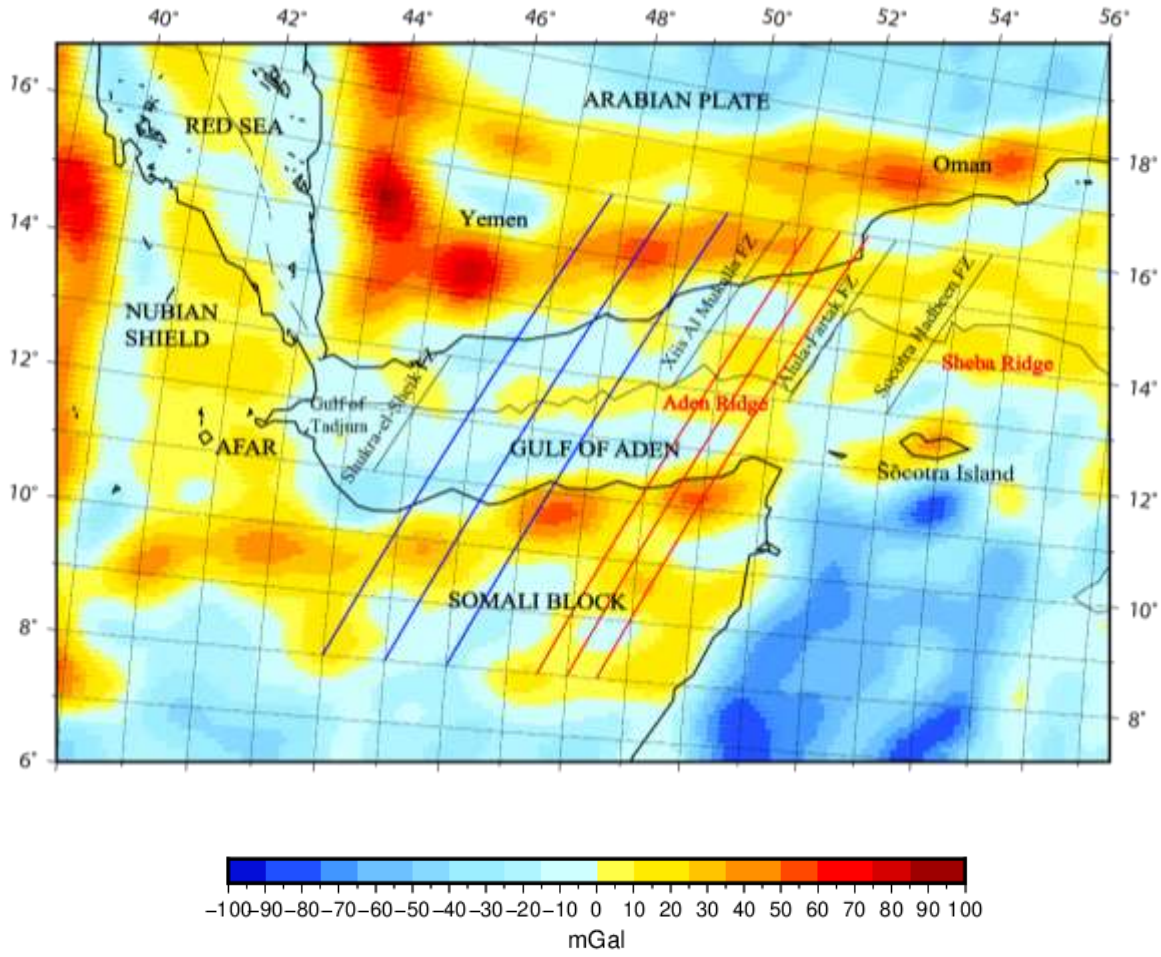

Figure 6.13: Gravity disturbance in the surroundings of the Gulf of Aden, computed at a height h_S=5 km above the ellipsoid and based on the static gravitational model GO_CONS_GCF_2_TIM_R6 *(Brockmann et al.,* 2019).

The configuration and structure of this young ocean basin plays and important role in channeling material away from the Afar plume. In the westernmost oceanic domain, the number of ridge offsets is low whereas the Aden Ridge in central domain is more highly segmented with several transform faults that shift the ridge northward and that act as rheological barriers, diverting flow toward the site of active volcanism, away from the ridge (*Leroy et al*., 2010; *Corbeau et al*., 2014).

Another important structural aspect lies in the fact that the Gulf of Aden is a narrow oceanic basin flanked by blocks of relatively thick continental lithosphere and such lithospheric thickness variations with distance from the ridge axis, crates a sloping rheological boundary layer that focuses plume material along the ridge axis and inhibits its flow away from the

spreading axis itself (*Leroy et al*., 2010). The combination of this factors may enhance the along-axis flow and favour channeling of plume material, which flows along the Aden-Sheba ridge, without encountering large offset, until it arrives at the AFTF (*Leroy et al*., 2010). Near the middle of the transform, the almost homogeneous lithospheric thickness on the either side of AFTF, ensure that mantle plume is able to cross the AFTF without a complete damming, thus being redirected along the transform towards the next ridge segment and feeding the volcanoes located in the ocean-continent transition domain (i.e. Yemen, Somalia and Oman) *(Leroy et al*., 2010).

The comparative analysis between modelled and observed gravity disturbance is still ongoing.

Chapter 7

Conclusions

This work aims to investigate the gravitational signatures of the mechanisms that regulate slow rate tectonic deformation in areas where the earthquakes enucleate by using 2D thermo-mechanical numerical models to simulate the crust-mantle dynamics. The original code (Marotta *et al*., 2006) has been modified to include new processes such as phase changes, hydration of the mantle (*Roda et al*., 2010; *Regorda et al*., 2017), and plate coupling that improve the density distribution in the crust, lithosphere, and mantle system and, consequently, the gravity signature, to be compared to the most nowadays updated global gravity models, such as EIGEN 6c4 one *(Förste et al*., 2014).

During my first Ph.D. year, I focused on Sumatra and Mariana complexes, representative of the two major types of subductions: ocean–continent and ocean–ocean, respectively.

In particular, research activity focused on the following points:

- coupling between the interacting plate, which gives information about the accumulation of strain during the interseismic loading phase;
- background crustal deformation and stress;
- shallow and deep density distribution, considering the role of mantle wedge hydration, stratification of the crust-lithosphere system and both shallow and deep

phase transitions;

- gravity pattern due to subduction and its time variation exploited in terms of gravity anomalies, gravity gradients and rates of changes of these observables.

In a first phase, a set of numerical tests has been developed, varying three main parameters: prescribed subduction velocity (u_s), prescribed subduction dip angle (θ_S) and degree of plate coupling (c_f). Subsequently, with the aim of better understanding the processes that are responsible for the characteristic bipolar gravity pattern of subduction, a comparative analysis between the geodetically retrieved gravitational anomalies, based on the EIGEN-6C4 model, and those predicted by a 2D thermo-mechanical modeling has been carried out.

For the Sumatra subduction, all the ocean-continent models with a subduction velocity of 5 cm/yr have been considered and the gravitational contribution of the mass distribution predicted after approximately 40 Myr from the beginning of the subduction has been calculated, accounting for a 4 km thick ocean overlying the subducting plate. The only model that shows the best agreement with the data is namely model $OC3$, characterized by a c_f=0.5. The results show that the gravity disturbance predicted by OC_3 model fits the envelope of the gravity disturbance based on EIGEN-6C4, extracted along three sections perpendicularly crossing the Sumatra trench. In particular, the model fits the envelope of the profiles well in terms of positioning and height of the maxima of 30 and 200 mGal, with a depth of the trough or gravitational disturbance minimum of –120 mGal. The comparison highlights a narrow region of negative density contrast embedded between the subducted cold plate and the upwelled lithospheric mantle, as large as 80 km to a depth of approximately 80 km, that generates the gravity trough. Furthermore, the upwelled lithospheric mantle, which substitutes the less dense continental crust between 20 and 40 km produces a positive density contrast. This shallow positive density contrast is thus effective in the thinning of the trough in the ocean–continent subduction. Furthermore, this positive density contrast has the effect of increasing the positive gravitational peak located on the continental side. This positive density contrast at depths of 20–50 km originating from the indentation of dense upper mantle material within the continental crust shields the deeper negative density contrasts, whose contribution to the formation of the trough is thus inhibited.

For the Mariana subduction, all the ocean–ocean models with the same value of subduction velocity of 5 cm/yr as for Sumatra have been considered, and the gravitational

contribution of the mass distribution after 45 Myr, compatible with Sumatra, accounting for 5-km-thick ocean overlying the subducting plate and a 4-km-thick ocean overlying the overriding plate has been calculated The only model that shows the best agreement with the data is namely model OO_1, characterised by a c_f=1. The comparative analysis shows a wider gravity trough with respect to the ocean-continent subduction, generated by a vigorous convective circulation of light material in the mantle wedge, which in turn is responsible for the wide region of negative density contrasts.

Another major difference that makes the distribution of light material more effective in the ocean–ocean subduction in the formation of a pronounced and wide gravitational trough relies on the fact that in this type of subduction, in contrast to the ocean–continent one, the dense mantle does not substitute the lighter continental crust, which causes the formation of the positive density contrast observed above, contributing to the narrowness of the trough in the OC_3 model.

In conclusion, the study of the EIGEN-6C4 gravitational disturbance patterns of the Sumatra and Mariana subductions have allowed to strengthen the analysis of the gravitational signature in ocean–continent and ocean–ocean subductions in terms of the physics of the processes occurring during the convergence of the plates. Although both types of subduction show the classical 2-D dipolar profile perpendicular to the trench, they can be distinguished in terms of some fundamental features. In particular, the modelling is able to reproduce the gravity disturbance difference of 250-300 mGal well between the maximum and the minimum, characterising both types of subductions. In the same way it reproduces the fundamental differences highlighted by the EIGEN-6C4 data:

- the width of the trough (larger for the ocean-ocean subduction than for the ocean-continent one);

- the symmetry, in terms of the different amplitudes of the two positive gravity peaks facing the trench.

Further, this study provides a physical explanation for the broadness of the negative gravitational contribution for mature subductions (as the Mariana) compared to immature ones.

Finally, the results have allowed to strengthen the analysis of the gravitational signature in ocean-continent and ocean-ocean subductions, providing important information not only on their anomalous density structure but also on the dynamics of the subduction process.

A second study has been carried out developing a set of numerical models, varying the crustal thickness and the initial thermal configuration, and in which the formation of oceanic crust and serpentinite due to the hydration of upwelling mantle peridotite is implemented, to simulate the evolution of the Gulf of Aden from the rift initiation to the development of an active oceanic spreading center.

A main result is that the thermomechanical evolution of the system can be separated into four phases with various durations for the different models:

1) phase I is characterized by horizontal crustal velocities that slowly decrease from the boundary of the model to approximately 100 km from the ridge and by rapid decreases in velocities in the central portion of the domain; as a consequence, low strain rates characterize the crust away from the ridge, while very high strain rates characterize the surroundings of the future ridge, as also shown in the modelled strain rate pattern in *Brune and Autin* (2013), *Brune* (2014) and *Schettino et al*. (2019);

2) phase II has a crust characterized by velocities that are almost constant in time but decrease linearly in space from the lateral sides to the future ridge. During this phase, the highest velocity gradients and strain rates are observed (e.g., *Brune and Autin*, 2013; *Watremez et al*., 2013; *Brune*, 2014;). Phase II ends when continental crustal breakup occurs after 19.9 Ma from the beginning of rifting in model HL150.HC40 and after 13.4 Ma in models HL200.HC35 and HL200.HC40. This phase is not recorded by model HL150.HC35, which exhibits crustal breakup after 5.9 Ma, i.e., at the end of phase I;

3) phase III characterizes the post crustal breakup evolution in all models. During this phase, there are fast increases in both horizontal velocities in the crust and vertical velocities corresponding to the ridge. Compared to phase II, the lateral velocity gradients are less intense and even decrease over time, resulting in strain rates that are lower than those predicted for phase II. At the end of phase III, when the lithospheric breakup occurs, the horizontal velocities in the crustal blocks are constant, with values higher than 10 mm/yr in all models, and strain rates are very low (well below 10^{-16} s^{-1}) compared to those predicted during previous phases;

4) phase IV is marked by two sections of crust that move as rigid blocks with a velocity that, within a tolerance of 10%, is equal to that prescribed at the marginal sides, comparable with the velocity trend shown in *Marotta et al*. (2018). This phase ends when the two continental blocks are 400 km apart, that is after 24.4, 40.4, 35.4 and 34.4 Ma from the beginning of evolution, for models HL150.HC35, HL150.HC40, HL200.HC35 and HL200.HC40, respectively.

Model results show that the timing of mantle serpentinization is not affected by the initial thermal configuration of the system, and mantle serpentinization starts a few million years (4-5 Ma) after the onset of rifting for all models, well before crustal breakup.
Furthermore, the results show that the OCT always develops when the rifting to oceanization transition occurs in case of a thick lithosphere. In contrast, with a thin lithosphere, wet peridotite with a total amount of H2O equal to 0.05% is required to drive the development of an OCT zone.

The comparison between numerical models and the natural Gulf of Aden mainly focuses on the central sector of the Gulf between the SSFZ and the AFFZ, where the emplacement of the oceanic floor was a continuous process. Therefore, considering an extensional period lasting 20 Ma before the breakup and considering 0.05% hydrated mantle the results confirm that the model with an initial 150 km-thick lithosphere and a 40 km-thick crust is the most appropriate to reproduce the geodynamic evolution of the study area when 0.05% hydrated mantle is considered. This model is also in agreement with the crust and lithosphere thicknesses based on thermal analysis and geoid data, which imply that the central part of the Gulf of Aden started to rift at approximately 37-40 Ma in its easternmost sector and is characterized by the sequence of a thinned passive margin, an OCT zone and an oceanic domain.

The best-fit model predicts a 40-50 km-wide OCT zone and a 350-400 km-wide oceanic domain in the eastern sector, while a 100 km-wide oceanic domain with no OCT zone is predicted in the western sector of the Gulf of Aden. The variations in features along the passive margins from west to east are ascribable to lateral variations in the amount of H2O in the mantle, which determines the different times of mantle melting. In particular, an increase from 0.05% to 0.1% hydrated mantle associated with the Afar plume might have preceded mantle melting and thus precluded the development of an OCT zone in the western sector of the Gulf of Aden.

An important aspect is that this approach allows us to obtain a robust estimate of the crustal thickness of 40 km, thus definitively choosing the upper bound in previous estimates of this parameter for the crust surrounding the Gulf of Aden.

Appendix A

Mathematical formulation of the *SubMar* Code

A.1 Finite element method

The finite element (FE) method is a computational technique for obtaining approximate solutions to the partial differential equations in scientific and engineering applications and it is used widely in geodynamic modelling (see *Christensen*, 1984, 1992; *Moresi and Solomatov*, 1995; *Moresi et al*., 2003; *Ismail-Zadeh et al*., 2007). The FE method uses a variational problem that involves an integral of the differential equation over the model domain. This domain is divided into a number of sub-domains called finite elements, interconnected by a discrete number of nodal point and the behavior of each element is defined by a finite number of nodal parameters that are the variables of the problem. The elements are called *linears* if the nodal points are only at the vertexes of each element, or *quadratics* if there are nodal points also at the middle of each side. Higher-order elements can have nodal points also in the interior.

The solution of the partial differential equation is approximated by a simple polynomial function on each element. These polynomials have to be pieced together so that the approximate solution has an appropriate degree of smoothness over the entire domain. Once this has been done, the variational integral is evaluated as a sum of contributions from each finite element. The result is a set of algebraic equations for the approximate solution having a finite size rather than the original
infinite-dimensional partial differential equation. Therefore, the FE process discretises the partial differential equation and the approximate solution is known throughout the domain as a piecewise polynomial function.

Considering a two-dimensional structure assembled from individual components and interconnected by a variable number of nodes (numbered from 1 to 6) for each element (Figure A.1), a typical element labelled (1) and associated with nodes 1, 2, 3 is analyzed. As a starting point it will be assumed that the characteristics of each element are precisely known. The forces acting at the nodes are uniquely defined by the displacement of these nodes, the distributed loading acting on the element (p), and its possible initial strain, which may be due to temperature or shrinkage.
The forces and the corresponding displacements are defined by appropriate components (U, V and u, v) in a common coordinate system (*Zienkiewicz and Taylor*, 2000).

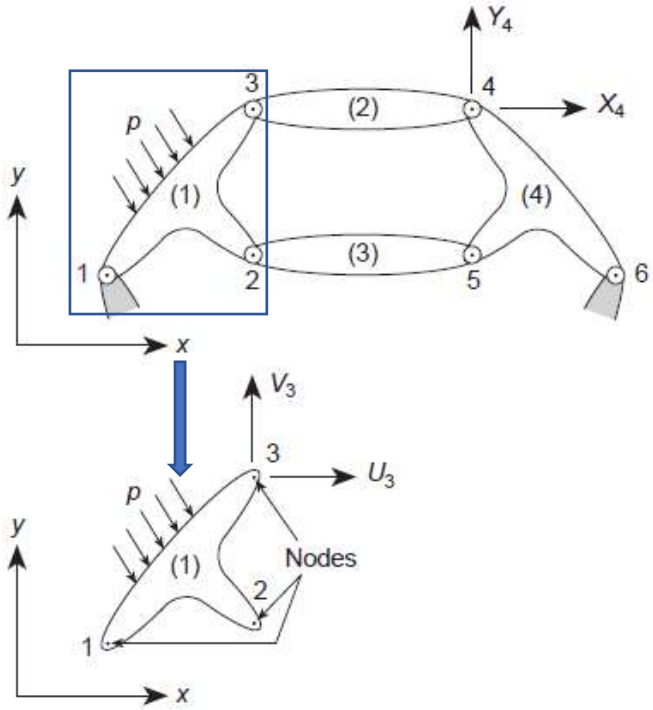

Figure A.1: A 2D structure built up from elements interconnected by nodes (modified from *Zienkiewicz and Taylor*, 2000).

Listing the forces acting on all the nodes of the element (three nodes for the element (1) in the case illustrated in Figure A.1) as a matrix we have:

$$q^1 = \begin{Bmatrix} q_1^1 \\ q_2^1 \\ q_3^1 \end{Bmatrix} \quad \text{where} \quad q_1^1 = \begin{Bmatrix} U_1^1 \\ V_1^1 \end{Bmatrix}, \quad q_2^1 = \begin{Bmatrix} U_2^1 \\ V_2^1 \end{Bmatrix}, \quad q_3^1 = \begin{Bmatrix} U_3^1 \\ V_3^1 \end{Bmatrix} \tag{A.1}$$

and the corresponding nodal displacements is:

$$a^1 = \begin{Bmatrix} a_1 \\ a_2 \\ a_3 \end{Bmatrix} \quad \text{where} \quad a_1^1 = \begin{Bmatrix} u_1^1 \\ v_1^1 \end{Bmatrix}, \quad a_2^1 = \begin{Bmatrix} u_2^1 \\ v_2^1 \end{Bmatrix}, \quad a_3^1 = \begin{Bmatrix} u_3^1 \\ v_3^1 \end{Bmatrix} \tag{A.2}$$

Assuming linear elastic behavior of the element, the characteristic relationship will be in the form:

$$q^1 = K^1 \cdot a^1 + f_p^1 + f_{\epsilon_0}^1 \tag{A.3}$$

where f_p^1 represents the nodal forces required to balance any distributed loads acting on the element, $f_{\epsilon_0}^1$ represents the nodal forces associated to the initial deformation and $\mathbf{K}^1 \cdot a^1$ represents the nodal forces associated to nodal displacements. **K** is called *stiffness matrix*.

For a generic element *e* with *m* nodal points, the vectors of the nodal forces q^e and of the nodal displacements a^e can be represented as:

$$q^e = \begin{Bmatrix} q_1^e \\ q_2^e \\ \vdots \\ q_m^e \end{Bmatrix} \text{ and } \quad a^e = \begin{Bmatrix} a_1 \\ a_2 \\ \vdots \\ a_{\boldsymbol{m}} \end{Bmatrix} \tag{A.4}$$

with each q_i^e and a_i^e have the same number *n* of components (or *degree of freedom*). Therefore, the stiffness matrices of the element will always be square and of the form:

$$K^e = \begin{bmatrix} K_{ij}^e & \cdots & K_{im}^e \\ \vdots & \ddots & \vdots \\ K_{mj}^e & \cdots & K_{mm}^e \end{bmatrix} \tag{A.5}$$

in which *j* is the nodal points influencing *i-esim* node.

Considering the *i-esim* node of the *e-esim* element, the Equation 6.19 can be written as:

$$q_i^e = K_{i,1}^e \cdot a_1^e + K_{i,2}^e \cdot a_2^e + \cdots + K_{i,nnode}^e \cdot a_{nnode}^e + f_{p_i}^e + f_{\epsilon_{0_i}}^e = \\ = \sum_{inode=1}^{nnode} K_{i,inode}^e \cdot a_{inode}^e + f_{p_i}^e + f_{\epsilon_{0_i}}^e \tag{A.6}$$

in which *nnode* is the number of nodes in the *j-esim* element. The numbering of the local nodes, or rather of each element, must follow the same criteria (for example clockwise).
If *m* elements have a node *i* in common the resulting force is:

$$q_i = q_i^1 + q_i^2 + \cdots + q_i^m = \sum_{e=1}^{m} q_i^e = \sum_{e=1}^{m} \left[\underbrace{\sum_{inode=1}^{nnode} K_{i,inode}^e \cdot a_{inode}^e}_{\text{Stiffness matrix in local coordinates}} + f_{p_i}^e + f_{\epsilon_{0_i}}^e \right] \tag{A.7}$$

The first summation can be done on all the elements (*nelem*) instead that only on the elements with the node in common (*m*), because only the elements, which include point i will contribute non-zero forces. Considering the number of nodes of all the system (*npoin*) instead of the number of nodes of the element (*nnode*), the stiffness matrix can be written in global coordinates. Therefore, for each element the stiffness matrix has null values except for the nodes belonging to the own element, and the Equation 6.23 can be written as:

$$q_i = \sum_{e=1}^{nelem} \left[\underbrace{\sum_{inode=1}^{npoin} K^e_{i,inode} \cdot a^i_{inode}}_{\text{Stiffness matrix in local coordinates}} + f_i^e \right] \tag{A.8}$$

where:

$$f^e = f_p^e + f_{\epsilon_0}^j$$

In order to have the equilibrium condition of the *i-esim* node, the resulting of the forces q_i must either have a zero value or be or equal to the sum of the component forces contributed by the elements meeting at the node. Thus, considering all the force components, we have:

$$r_i = \sum_{e=1}^{nelem} q_i^e \tag{A.9}$$

Therefore, Equation A.8 can be written as:

$$K \cdot a = r - f \tag{A.10}$$

in which the submatrices are:

$$K_{i,inode} = \sum_{e=1}^{nelem} K^e_{i,inode} \quad and \quad f_i = \sum_{e=1}^{nelem} f_i^e \tag{A.11}$$

This simple rule for assembly is very convenient because as soon as a coefficient for a particular element is found it can be put immediately into the appropriate location specified in the computer, additioning all the coefficients in that location (*Zienkiewicz and Taylor*, 2000).

An important step in the FE method is the choice of functions (*displacement functions*) to define uniquely the state of displacement within each element and on its boundaries in terms of its nodal displacement. A typical finite element, *e*, is defined by nodes *i*, *j*, *m*, etc. and the displacement **u** at any point within the element can be approximated as a column vector, $\widehat{\boldsymbol{u}}$:

$$\boldsymbol{u}(x,y) \approx \widehat{\boldsymbol{u}}(x,y) = \sum_{\boldsymbol{k}} \mathbf{N}_{\mathrm{k}} \cdot \mathbf{a}_k^{\boldsymbol{e}} = \begin{bmatrix} \boldsymbol{N}_i & \boldsymbol{N}_j & \boldsymbol{N}_m \end{bmatrix} \cdot \begin{bmatrix} \mathbf{a}_i \\ \mathbf{a}_j \\ \mathbf{a}_m \end{bmatrix} = \boldsymbol{N} \cdot \mathbf{a}^{\boldsymbol{e}} \tag{A.12}$$

in which **N** is the vector of the displacement functions and **a** represents a listing of the nodal displacements for a particular element. In this way, the displacement for all points of the element is approximated as linear function of the nodal displacement. The functions $\mathbf{N}_i, \mathbf{N}_j, \mathbf{N}_m$ are arbitrary functions, known as *displacement functions* or *shape functions*, which link the field of internal displacements of the element to the vector of nodal displacements. The shape of the displacement field inside the element depends on them so they have to be chosen to reflect the nodal displacement if the values of the coordinates are changed. For example, for the node *i*:

$$\begin{aligned} \widehat{\boldsymbol{u}}(x_i, y_i) &= \sum_{i=1}^{nnode} N_i \cdot a_i^e \\ &= \boldsymbol{N}_i(x_i, y_i) a_i + \boldsymbol{N}_j(x_i, y_i) a_j + \boldsymbol{N}_m(x_i, y_i) a_m a_i \end{aligned} \tag{A.13}$$

where:

$N_j(x_i, y_i) = N_m(x_i, y_i) = 0$

$N_i(x_i, y_i) = 1 = N_i \mathbf{I}$ (identity matrix)

The same holds for the other nodal points of the element. In all the other points inside the element $0 < N < 1$.

The displacement functions define uniquely the state of deformation within each element. These deformations with an eventual pre-existed deformation ε_0 and the rheological proprieties define the state of stresses of the system. With displacements known at all points within the element the strains at any point can be determined. These will always result in a relationship that, using Equation A.13, can be written in matrix notation as:

$$\varepsilon \approx \hat{\varepsilon} = \begin{bmatrix} \varepsilon_{xx} \\ \varepsilon_{yy} \\ \varepsilon_{xy} \end{bmatrix} = \begin{bmatrix} \frac{\partial u}{\partial x} \\ \frac{\partial v}{\partial x} \\ \frac{1}{2}\left(\frac{\partial u}{\partial y} + \frac{\partial v}{\partial x}\right) \end{bmatrix} = \begin{bmatrix} \frac{\partial}{\partial x} & 0 \\ 0 & \frac{\partial}{\partial y} \\ \frac{1}{2}\frac{\partial}{\partial y} & \frac{1}{2}\frac{\partial}{\partial x} \end{bmatrix} \cdot \begin{bmatrix} u \\ v \end{bmatrix} = \boldsymbol{S} \cdot \mathbf{u}(x, y) = \boldsymbol{S} \cdot \mathbf{a} \tag{A.14}$$

In the Equation A.14 the vector of the displacement **a** can be written as:

$$\begin{bmatrix} u \\ v \end{bmatrix} \approx \begin{bmatrix} \hat{u} \\ \hat{v} \end{bmatrix} = \begin{bmatrix} N_i\mathbf{I} & N_j\mathbf{I} & N_m\mathbf{I} \end{bmatrix} \cdot \begin{bmatrix} a_i \\ a_j \\ a_m \end{bmatrix} =$$

$$= \begin{bmatrix} N_i & 0 & N_j & 0 & N_m & 0 \\ 0 & N_i & 0 & N_j & 0 & N_m \end{bmatrix} \cdot \begin{bmatrix} u_i \\ \mathrm{v}_i \\ u_j \\ v_j \\ u_m \\ v_m \end{bmatrix} = \begin{bmatrix} N_i u_i + & N_j u_j + & N_m u_m \\ N_i v_i + & N_j v_j + & N_m v_m \end{bmatrix} \tag{A.15}$$

and integrating the Equation A.15 in the Equation A.14 it is obtained that:

$$\varepsilon = \begin{bmatrix} \frac{\partial}{\partial \mathrm{y}} & 0 \\ 0 & \frac{\partial}{\partial \mathrm{x}} \\ \frac{1}{2}\frac{\partial}{\partial \mathrm{y}} & \frac{1}{2}\frac{\partial}{\partial \mathrm{x}} \end{bmatrix} \cdot \begin{bmatrix} N_i u_i + & N_j u_j + & N_m u_m \\ N_i v_i + & N_j v_j + & N_m v_m \end{bmatrix} =$$

$$= \begin{bmatrix} \frac{\partial N_i}{\partial x} u_i + \frac{\partial N_j}{\partial x} u_j + \frac{\partial N_m}{\partial x} u_m \\ \frac{\partial N_i}{\partial y} v_i + \frac{\partial N_j}{\partial x} v_j + \frac{\partial N_m}{\partial x} v_m \\ \frac{1}{2}\left(\frac{\partial N_i}{\partial y} u_i + \frac{\partial N_j}{\partial y} u_j + \frac{\partial N_m}{\partial y} u_m + \frac{\partial N_i}{\partial x} v_i + \frac{\partial N_j}{\partial x} v_j + \frac{\partial N_m}{\partial x} v_m\right) \end{bmatrix} \tag{A.16}$$

in which the components *u* and *v* do not depend by *x* and *y* because they are the displacement in the nodes. Eventually, they can depend by the time if the problem is not stationary. Therefore, the Equation A.16 can be written as:

$$\varepsilon = \begin{bmatrix} \frac{\partial N_i}{\partial x} & 0 & \frac{\partial N_j}{\partial x} & 0 & \frac{\partial N_m}{\partial x} & 0 \\ 0 & \frac{\partial N_i}{\partial x} & 0 & \frac{\partial N_i}{\partial x} & 0 & \frac{\partial N_i}{\partial x} \\ \frac{1}{2}\frac{\partial N_i}{\partial y} & \frac{1}{2}\frac{\partial N_i}{\partial x} & \frac{1}{2}\frac{\partial N_j}{\partial y} & \frac{1}{2}\frac{\partial N_j}{\partial x} & \frac{1}{2}\frac{\partial N_m}{\partial y} & \frac{1}{2}\frac{\partial N_m}{\partial x} \end{bmatrix} \cdot \begin{bmatrix} u_i \\ v_i \\ u_j \\ v_j \\ u_m \\ v_m \end{bmatrix} = \boldsymbol{B} \cdot \mathbf{a} \tag{A.17}$$

with the shape functions N_i, N_j, and N_m already determined, the matrix **B** can be obtained.

Knowing the deformation and the rheological properties of the material, the stress for each point inside the element can be expressed as:

$$\sigma = \sigma_0 + \mathbf{D}(\varepsilon - \varepsilon_0) \quad \rightarrow \quad \begin{bmatrix} \sigma_{xx} \\ \sigma_{yy} \\ \sigma_{xy} \end{bmatrix} = \begin{bmatrix} \sigma_{0xx} \\ \sigma_{0yy} \\ \sigma_{0xy} \end{bmatrix} + \mathbf{D} \begin{bmatrix} \varepsilon_{xx} - & \varepsilon_{0xx} \\ \varepsilon_{yy} - & \varepsilon_{0yy} \\ \varepsilon_{xy} - & \varepsilon_{0xy} \end{bmatrix} \tag{A.18}$$

where **D** is the matrix containing the rheological properties of the material and σ_0 and ε_0 are stresses and deformations pre-existing. Under plane stress conditions, from the Hooke's law:

$$\begin{cases} \varepsilon_{xx} - \varepsilon_{0xx} = \dfrac{\sigma_{xx}}{E} - \dfrac{v}{E}\sigma_{yy} \\ \varepsilon_{yy} - \varepsilon_{0yy} = -\dfrac{v}{E}\sigma_{xx} + \dfrac{\sigma_{yy}}{E} \\ \varepsilon_{xy} - \varepsilon_{0xy} = \dfrac{(1+v)}{E}\sigma_{xy}\dfrac{1}{2_\mu}\sigma_{xy} \end{cases}$$

from which the components of the stress can be written as:

$$\begin{cases} \sigma_{xx} = \dfrac{E}{1-v^2}(\varepsilon_{xx} - \varepsilon_{0xx}) - \dfrac{E_v}{1-v^2}(\varepsilon_{yy} - \varepsilon_{0yy}) \\ \sigma_{yy} = \dfrac{E_v}{1-v^2}(\varepsilon_{xx} - \varepsilon_{0xx}) - \dfrac{E_v}{1-v^2}(\varepsilon_{yy} - \varepsilon_{0yy}) \\ \sigma_{yy} = \dfrac{E(1-v)}{1-v^2}(\varepsilon_{xy} - \varepsilon_{0xy}) \end{cases} \tag{A.19}$$

Substituting the Equation A.19 in the Equation A.18 it is obtained that:

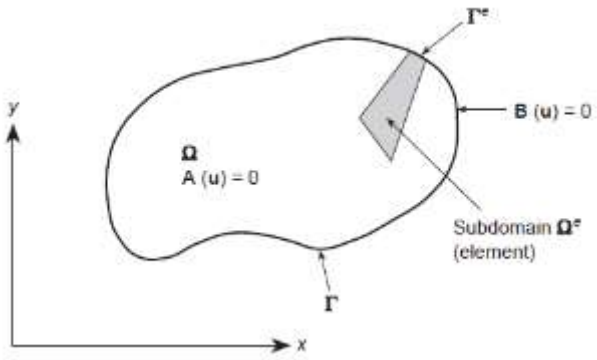

Figure A.2: Example of domain Ω with boundary Γ, in which to satisfy the system of differential equations **A**(**u**) with boundary conditions **B**(**u**) (from *Zienkiewicz and Taylor*, 2000).

$$\begin{bmatrix}\sigma_{xx}\\ \sigma_{yy}\\ \sigma_{xy}\end{bmatrix} = \frac{E}{1-v^2}\begin{bmatrix}1 & v & 0\\ v & 1 & 0\\ 0 & 0 & 1-v\end{bmatrix}\cdot\begin{bmatrix}\varepsilon_{xx} - & \varepsilon_{0xx}\\ \varepsilon_{yy} - & \varepsilon_{0yy}\\ \varepsilon_{xy} - & \varepsilon_{0xy}\end{bmatrix} = \mathbf{D}\cdot\begin{bmatrix}\varepsilon_{xx} - & \varepsilon_{0xx}\\ \varepsilon_{yy} - & \varepsilon_{0yy}\\ \varepsilon_{xy} - & \varepsilon_{0xy}\end{bmatrix}$$

$$\Downarrow$$

$$\boldsymbol{\sigma} = \boldsymbol{D}\cdot\varepsilon = \boldsymbol{D}\cdot\varepsilon_{tot} - \boldsymbol{D}\cdot\varepsilon_0 \tag{A.20}$$

The Equation A.4 define the nodal forces, which are statically equivalent to the boundary stress and distributed body forces on the element. To do this, the simplest procedure is to impose an arbitrary nodal displacement and to equate the work expended by the stresses and the distributed forces during the displacement.

Considering a virtual nodal displacement δa^e for the element *e*, the work due to the nodal forces is:

$$L^e_{ext} = \sum_{inode=1}^{nnode} q^e_{inode}\cdot\delta a^e_{inode} = \delta a^{e^T}\cdot q^e \tag{A.21}$$

The distributed body forces $\mathbf{b}=\begin{Bmatrix}b_x\\ b_y\end{Bmatrix}$ are defined as those acting on a unit volume of material within the element and with the directions corresponding to those of the displacement **u** at that point.

The work of a unit volume is:

$$L_b = \boldsymbol{b} \cdot \delta \boldsymbol{u} = \delta \boldsymbol{u}^T \cdot \boldsymbol{b} \tag{A.22}$$

while for the stresses $\sigma = \begin{bmatrix} \sigma_{xx} & \sigma_{xy} \\ \sigma_{yx} & \sigma_{yy} \end{bmatrix}$ the work is:

$$L_\sigma = \delta \varepsilon^T \cdot \sigma \tag{A.23}$$

Considering that $\delta \varepsilon = \mathbf{B} \cdot \delta \mathbf{a}^e$ and $\delta \mathbf{u}(x, y) = N \cdot \delta \mathbf{a}$, adding Equations A.22 and A.23 and integrating on the volume of the element the internal work of the element is:

$$\boldsymbol{L}_{int}^e = \int_{Ve} \delta \mathbf{a}^{\boldsymbol{T}} \cdot (\mathbf{B}^{\boldsymbol{T}} \cdot \boldsymbol{\sigma} - \boldsymbol{N}^{\boldsymbol{T}} \cdot \boldsymbol{b}) dV \tag{A.24}$$

As the Equations A.21 and A.24 must be equal:

$$\boldsymbol{q}^e = \int_{V_e} (\mathbf{B}^T \cdot \boldsymbol{\sigma}) - \int_{V_e} (\mathbf{N}^T \cdot \mathbf{b})\, dV \tag{A.25}$$

with the linear law expressed in the Equation A.3, the Equation A.25 can be written as:

$$\boldsymbol{q}^e = \boldsymbol{K}^e \mathbf{a}^e + \mathbf{f}^e \tag{A.26}$$

where:

$$\mathbf{K}^e = \int_{V_e} \mathbf{B}^T \cdot \mathbf{D} \cdot \mathbf{B} dV \tag{A.27}$$

and

$$f^e = -\int_{V_e} (\mathbf{N}^T \cdot \mathbf{b})\, dV - \int_{V_e} (\mathbf{B}^T \cdot \mathbf{D} \cdot \varepsilon_0)\, dV + \int_{V_e} (\boldsymbol{B}^T \cdot \boldsymbol{\sigma}_0) dV \tag{A.28}$$

In the last Equation, the three terms represent forces due to body forces, initial strain and initial stress, respectively.

A.2 Galerkin method

The solution of the problems with the finite element method results in finding an unknown function **u** that satisfies a given set of differential equations:

$$\mathbf{A}(\mathbf{u}) = \begin{Bmatrix} A_1(\mathbf{u}) \\ A_2(\mathbf{u}) \\ \vdots \\ A_n(\mathbf{u}) \end{Bmatrix} = 0 \tag{A.29}$$

in a domain (volume, area, etc.) Ω (Figure A.2) together with appropriate boundary conditions:

$$\mathbf{B}(\mathbf{u}) = \begin{Bmatrix} B_1(\mathbf{u}) \\ B_2(\mathbf{u}) \\ \vdots \\ B_n(\mathbf{u}) \end{Bmatrix} = 0 \tag{A.30}$$

defined on the boundaries Γ of the domain Ω (*Zienkiewicz and Taylor*, 2000) (Figure A.2). The finite element process, being one of approximation, will seek the solution in the approximate form of the Equation A.12 where $\boldsymbol{N}_i$ are shape functions prescribed in terms of independent variables and all or most of the parameters $\mathbf{a}_i$ are unknown.
To obtain the unknown parameters $\mathbf{a}_i$ in the integral from, the Equation is:

$$\int_{\Omega} \mathbf{G}_j\,(\hat{\mathbf{u}})d\Omega + \int_{\Gamma} \mathbf{g}_j(\hat{\mathbf{u}})d\Gamma = 0 \tag{A.31}$$

in which $\mathbf{G}_j$ and $\mathbf{g}_j$ prescribe known functions or operators. To obtain the approximation in such integral forms the method of *weighted residuals* (the Galerkin method) can be used.

The differential equations (A.29) have to be zero at each point of the domain Ω. Therefore:

$$\int_{\Omega} \mathbf{v}^T\,\mathbf{A}(\mathbf{u})d\Omega \equiv \int_{\Omega} [v_1 A_1(\mathbf{u}) + v_2 A_2(\mathbf{u}) + \cdots]\,d\Omega \equiv 0 \tag{A.32}$$

Where:

$$v = \begin{Bmatrix} v_1 \\ v_2 \\ \vdots \\ v_n \end{Bmatrix} \tag{A.33}$$

is a set of arbitrary functions equal in number to the number of equations **A**(**u**) involved.
For any set of functions $\bar{\mathbf{v}}$ the boundary conditions are to be simultaneously satisfied, requiring that:

$$\int_{\Omega} \bar{v}^T \mathbf{B}(\mathbf{u}) = 0 \rightarrow \int_{\Omega} [\bar{v}_1 B_1(\mathbf{u}) + \bar{v}_2 B_2(\mathbf{u}) + \cdots + \bar{v}_n B_n(\mathbf{u})] d\Omega = 0 \tag{A.34}$$

Therefore, the integral statement that

$$\int_{\Omega} \mathbf{v}^T \mathbf{A}(\mathbf{u}) d\Omega + \int_{\Gamma} \bar{\mathbf{v}}^T \mathbf{B}(\mathbf{u}) d\Omega = 0 \tag{A.35}$$

is satisfied for all **v** and and $\bar{\mathbf{v}}$ it is equivalent to the satisfaction of the differential Equations A.29 and their boundary conditions A.30.

In some cases, it is possible to perform an integration by parts on Equation A.35 and replace it by an alternative statement of the form

$$\int_{\Omega} \mathbf{C}(\mathbf{v}) \cdot \mathbf{D}(\mathbf{u}) d\Omega + \int_{\Gamma} \mathbf{E}(\bar{\mathbf{v}})^{\ T} \mathbf{F}(\mathbf{u}) d\Gamma = 0 \tag{A.36}$$

where the operators **C** to **F** usually contain lower order derivatives than those occurring in operators **A** or **B** thus requiring a lower order of continuity in the choice of the **u** function and a higher continuity for **v** and $\bar{\mathbf{v}}$.
The Equation A.36 is now more permissive than the original problem posed by Equations A.29, A.30 and A.36 and it is called a *weak form* of these equations.
The integral statement (A.35) allows an approximation to be made if, in place of any function **v**, we put a finite set of approximate functions:

$$\mathbf{v} = \sum_{j=1}^{n} \mathbf{w}_j \, \delta \mathbf{a}_j \qquad \bar{\mathbf{v}} = \sum_{j=1}^{n} \bar{\mathbf{w}}_j \, \delta \mathbf{a}_j \tag{A.37}$$

in which $\delta \mathbf{a}_j$ are arbitrary parameters and *n* is the number of unknowns entering the problem.

Inserting the approximation A.36 into the Equation A.35, it can be obtained that:

$$\delta \mathbf{a}_j^T \left[\int_\Omega \mathbf{w}_j^T \, \mathbf{A} \left(\sum_i \mathbf{N}_i \cdot \mathbf{a}_i \right) d\Omega + \int_\Omega \bar{\mathbf{w}}_j^T \, \mathbf{B} \left(\sum_i \mathbf{N}_i \cdot \mathbf{a}_i \right) d\Omega \right] = 0 \qquad \text{(A.38)}$$

and since $\delta \mathbf{a}_j$ is arbitrary, there is a set of equations, which is sufficient to determine the parameters $\mathbf{a}_j$ as:

$$\int_\Omega \mathbf{w}_j^T \, \mathbf{A} \left(\sum_i \mathbf{N}_i \cdot \mathbf{a}_i \right) d\Omega + \int_\Omega \bar{\mathbf{w}}_j^T \, \mathbf{B} \left(\sum_i \mathbf{N}_i \cdot \mathbf{a}_i \right) d\Omega = 0 \qquad with\ 1, n \qquad \text{(A.39)}$$

$\mathbf{A}(\sum_i \mathbf{N}_i \cdot \mathbf{a}_i)$ represents the residual or error obtained by substitution of the approximation into the differential equation and $\mathbf{B}(\sum_i \mathbf{N}_i \cdot \mathbf{a}_i)$ the residual of the boundary conditions. So, the Equation A.38 is a weighted integral of such residuals. The approximation may thus be called the *method of weighted residuals* (*Zienkiewicz and Taylor*, 2000). In the Galerkin method v≡ $\mathbf{N}_i$ and $\bar{v} = -\mathbf{N}_i$ obtaining symmetric Stiffness matrices, and the Equation A.38 can be written as:

$$\int_\Omega \mathbf{N}_j \, \mathbf{A} \left(\sum_i \mathbf{N}_i \cdot \mathbf{a}_i \right) d\Omega + \int_\Omega \mathbf{N}_j \, \mathbf{B} \left(\sum_i \mathbf{N}_i \cdot \mathbf{a}_i \right) d\Omega = 0 \qquad \text{(A.40)}$$

These integral form permits the approximation to be determined element by element, and dividing the system in *nelem* elements, it can be written as:

$$\sum_{ielem=1}^{nelem} \left[\int_\Omega \mathbf{N}_j \, \mathbf{A} \left(\sum_i \mathbf{N}_i \cdot \mathbf{a}_i \right) d\Omega + \int_\Omega \mathbf{N}_j \, \mathbf{B} \left(\sum_i \mathbf{N}_i \cdot \mathbf{a}_i \right) d\Omega \right] = 0 \qquad \text{(A.41)}$$

A.3 From local to global coordinates

If the elements have an irregular shape, it is not possible to determine the integral exactly. In this case it is necessary to develop the method in the local coordinates of the element (s, t) and come back to the global coordinates (x, y) (Figure A.3) at the end of the calculation, by using the *Jacobian Matrix*. In local coordinates:

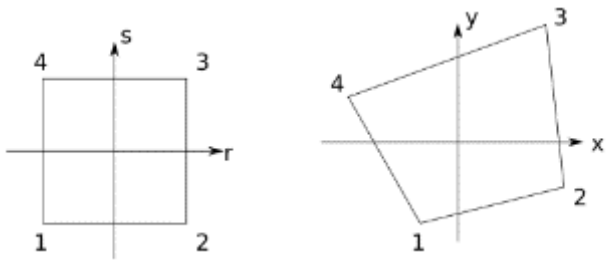

Figure A.3: Bilinear mapping on a linear quadrilateral.

$$\frac{\partial N_i}{\partial s} = \frac{\partial N_i}{\partial x}\frac{\partial x}{\partial s} + \frac{\partial N_i}{\partial y}\frac{\partial y}{\partial s}$$
$$\frac{\partial N_i}{\partial t} = \frac{\partial N_i}{\partial x}\frac{\partial x}{\partial t} + \frac{\partial N_i}{\partial y}\frac{\partial y}{\partial t} \tag{A.42}$$

or in the matrix form:

$$\begin{bmatrix} \frac{\partial N_i}{\partial s} \\ \frac{\partial N_i}{\partial t} \end{bmatrix} = \underbrace{\begin{bmatrix} \frac{\partial x}{\partial s} & \frac{\partial y}{\partial s} \\ \frac{\partial x}{\partial t} & \frac{\partial y}{\partial t} \end{bmatrix}}_{\mathbf{J}=\text{Jacobiano}} \cdot \begin{bmatrix} \frac{\partial N_i}{\partial x} & \frac{\partial N_i}{\partial y} \end{bmatrix} \tag{A.43}$$

where **J** is called the Jacobian of the transformation. By inverting the Jacobian matrix, the desired derivatives with respect to *x* and *y* can be obtained:

$$\begin{bmatrix} \frac{\partial N_i}{\partial x} & \frac{\partial N_i}{\partial y} \end{bmatrix} = [\mathbf{J}]^{-1} \cdot \begin{bmatrix} \frac{\partial N_i}{\partial s} & \frac{\partial N_i}{\partial t} \end{bmatrix} \tag{A.44}$$

The Jacobian matrix can be evaluated knowing the relation between system of global coordinates and that of the local coordinates. For every point has to be valid the relation:

$$x = \sum_{i=1}^{nnode} N_i x_i \tag{A.45}$$

which introduced in the Jacobian matrix gives:

$$\boldsymbol{J} = \begin{bmatrix} \frac{\partial}{\partial s}\left(\sum_{i=1}^{nnode} N_i x_i\right) & \frac{\partial}{\partial s}\left(\sum_{i=1}^{nnode} N_i y_i\right) \\ \frac{\partial}{\partial t}\left(\sum_{i=1}^{nnode} N_i x_i\right) & \frac{\partial}{\partial t}\left(\sum_{i=1}^{nnode} N_i y_i\right) \end{bmatrix} = \begin{bmatrix} \sum_{i=1}^{nnode} x_i \frac{\partial N_i}{\partial s} & \sum_{i=1}^{nnode} y_i \frac{\partial N_i}{\partial s} \\ \sum_{i=1}^{nnode} x_i \frac{\partial N_i}{\partial t} & \sum_{i=1}^{nnode} y_i \frac{\partial N_i}{\partial t} \end{bmatrix} =$$

$$= \begin{bmatrix} \frac{\partial N_1}{\partial s} & \frac{\partial N_2}{\partial s} & \cdots & \frac{\partial N_{nnode}}{\partial s} \\ \frac{\partial N_1}{\partial t} & \frac{\partial N_2}{\partial t} & \cdots & \frac{\partial N_{nnode}}{\partial t} \end{bmatrix} \cdot \begin{bmatrix} x_1 & y_1 \\ x_2 & y_2 \\ \vdots & \vdots \\ x_{nnode} & y_{nnode} \end{bmatrix} \tag{A.46}$$

For what concern *dΩ*, it is also depends on *dx* and *dy*, with:

$$dx = \frac{\partial x}{\partial t} ds + \frac{\partial x}{\partial t} dt \quad and \quad dy = \frac{\partial y}{\partial s} ds + \frac{\partial y}{\partial t} dt$$

which in matrix form is:

$$\begin{bmatrix} d_x \\ d_y \end{bmatrix} = \begin{bmatrix} \frac{\partial x}{\partial s} & \frac{\partial x}{\partial t} \\ \frac{\partial y}{\partial s} & \frac{\partial y}{\partial t} \end{bmatrix} \cdot \begin{bmatrix} d_s \\ d_t \end{bmatrix} \tag{A.47}$$

obtaining

$$d\Omega = dxdy = det\, \boldsymbol{J} \cdot dsdt \tag{A.48}$$

A.4 Gauss quadrature

Dealing with complex problem, numerical integration with numerical methods is essential to return an approximate value of the integral. In 1D, the numerical calculation of the integral is called *quadrature*; for integration orders greater than 1 the numerical calculation is called *cubature* although the term quadrature is often used to refer to any order of integration.

In most procedures, like the Newton-Cotes integration (Figure A.4a), points at which the function is to be found are determined *a priori*, usually at equal intervals, and a polynomial

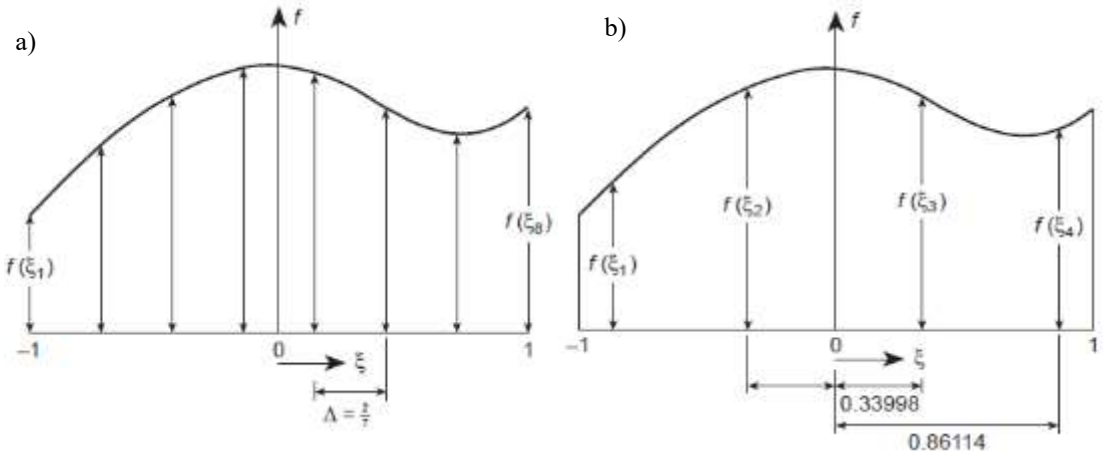

Figure A.4: a) Newton-Cotes and b) Gauss quadrature (from *Zienkiewicz and Taylor, 2000*).

passed through the values of the function at these points and exactly integrated. Conversely, with the Gauss quadrature, in place of specifying the position of a given number of sampling points *a priori*, the points of integration can be determined to aim an increase of the accuracy (Figure A.4b). Considering:

$$\int_a^b f(\xi)d\xi = \sum_{i=1}^{N} H_i f(\xi_i) \tag{A.49}$$

where H_i is the weight in every point and N, which are the Gauss points, depends on both the order of the partial derivative and the accuracy of the quadrature. The function is approximated by a polynomial of order $(N-1)$. For example, in case of a 2-dimensional system:

$$K_{ij} = \int_{-1}^{1}\int_{-1}^{1} K(s,t)dsdt = \int_{-1}^{1}\left(\sum_{i=1}^{N} H_i K(s_i)\right)dt = \sum_{j=1}^{N}\sum_{i=1}^{N} H_j H_i K(s_i, t_j) \tag{A.50}$$

with K determined in the Gauss points of coordinates (s, t).

A.5 Implementation of the *SubMar* code

A.5.1 Hydration and serpentinization of the mantle wedge

The distribution of water in the Earth's interior and its transportation from the surface to the deep mantle play an important role in the evolution of the planet (e.g., *Faccenda*, 2014; *Li*, 2020). During subduction, oceanic lithosphere, capped by variably hydrated uppermost mantle, oceanic crust and sediments, undergoes progressive metamorphism and devolatilization. In fact, subducting sediments and altered oceanic crust progressively release water, first during the porosity collapse at shallow depths and later due to dehydration reactions (*Guillot et al*., 2001). Such fluids may hydrate the overlying mantle wedge altering the rheology of mantle rocks and decreasing significantly mantle rocks strength thus enhancing the corner flow in the wedge. Slab dehydration process also promotes a viscosity e pressure reduction that in turn suck in more fluids, and serpentinites formed in the mantle wedge may act as a lubricant for the exhumation of eclogites (*Guillot et al*., 2001; *Arcay et al*., 2003; *Meda et al*., 2010).

Therefore, this subduction-induced water cycling is most likely responsible for triggering mantle wedge melting and is involved in the arc volcanism as highlighted by geochemistry of arc lavas and by geophysical observations, which attribute the decrease of the electrical resistivity and low seismic velocities in the mantle wedge to the partially molten or hydrated mantle wedge (*Magni et al*., 2014).

As already described in section 2.3, the oceanic crust can contain a certain amount of water in the hydrous minerals, which could be carried into the mantle by subduction and then liberate during the heating of sinking slab. Slab dehydration during subduction starts with the breakdown of serpentine and chlorite in mantle rocks, and of amphibole and lawsonite in the oceanic crust *(Schmidt and Poli*, 1998; *Meda et al*., 2014) and it takes place according to the plate thermal regime function of the slab age and sinking velocity (*Arcay et al*., 2003; *Faccenda et al*., 2014).

As mentioned above, the phases with large contributions to the water budget of subducting MORB are lawsonite, chlorite and amphibole; however, at pressures higher than 3–4 GPa, lawsonite constitutes the only hydrous phase. At pressures above the zoisite stability field, the lawsonite breakdown reaction has a positive dp/dT slope in the coesite

stability field, while it has a negative dp/dT slope in the stishovite stability field, above 8 GPa (*Schmidt and Poli*, 1998).

In the *SubMar* code the hydration / dehydration process has been implemented as described in *Roda et al*. (2010) and *Regorda et al*. (2017), determining the maximum dehydration depth of the oceanic crust Y_{dehydr}, below, which the water content in hydrous phases in H_2O-saturated MORB basalt is negligible, using the stability field of lawsonite (*Schmidt and Poli*, 1998; *Roda et al*., 2010) as follows:

$$Y_{dehydr} = -0.8755 \cdot T_{imarc} + 714.35 \tag{A.51}$$

where Y_{dehydr} is calculated for each oceanic crustal marker with temperature T_{imarc} up to a depth of 300 km. In fact, though *Schmidt and Poli* (1998) indicate that a significant water budget should be available until a depth of about 150–200 km, the exhumation of subducted continental rocks show evidence of stishovite that induce to consider the transport of water up to 250-300 km deep (Liu *et al*., 2007). The water released by the slab hydrates the mantle wedge and can lead to its serpentinization, with a consequent decrease in viscosity and density (*Gerya et al.,* 2002; *Arcay et al.,* 2005). The rheological weakening of the mantle wedge has been simulated by assuming a constant viscosity of 10^{19} Pa · s and a density of 3000 kg m^{-3} for the serpentinized mantle (*Arcay et al.,* 2005; *Gerya and Stockhert*, 2006; *Roda et al.,* 2010).

The stability field of serpentine is calculated for each element by using the following two equations (*Roda et al*., 2010):

$$\begin{aligned} Y_{hydr} &= -0.3394 \cdot T_{elem} + 268.09 \quad \text{above 66 km depth} \\ Y_{hydr} &= -0.9540 \cdot T_{elem} + 993.28 \quad \text{below 66 km depth} \end{aligned} \tag{A.52}$$

where Y_{hydr} represents the maximum hydration depth, and T_{elem} is the elemental temperature. Each element with an average depth and temperature (Y_{elem}, T_{elem}) is considered to be hydrated if $Y_{hydr} < Y_{elem} < Y_{dehydr}$ where Y_{hydr} is calculated from Equation A.52. The hydrated area is limited from below by the oceanic subducting plate. Specifically, to better delineate the geometry of the lower border of the hydrated area, the subducted plate is subdivided into segments of equal length, and the deepest dehydrated oceanic crust marker

for each segment is identified at each time during the system's dynamic evolution. The line that connects these markers defines the lower limit of the hydrated area.

Furthermore, a free-water migration mechanism has been implemented at a constant velocity of 20 cm yr^{-1}, in accordance with the velocities obtained by *Quinquis and Buiter* (2014) for different water migration schemes (10–70 cm yr^{-1}). Further, *Quinquis and Buiter* (2014) demonstrated that the exact manner of water migration does not impact the dynamics in the mantle wedge. In *SubMar* code, a time step (50 000 yr) is used, sufficient to have a complete serpentinization of the hydrated areas (*Arcay et al.,* 2005).

A.5.2 Erosion and sedimentation process

The erosion and sedimentation process has been implemented as described in *Roda et al*., (2010). To implement this process, it is necessary to introduce a low viscosity and low-density layer that simulates the atmosphere/water. Thus, the topographic surface is treated as a free surface between the crust and this new layer. Erosion and sedimentation processes are simulated by evaluating, at each time step, the size of the accretionary prism, which in turn is generated by the combined effects of oceanic plate bending and the ablation of the overriding plate. The instantaneous erosion of continental crust and the total or partial filling of the accretionary prism is simulated by using a substitution technique, in which all the crustal particles lying above 2 km are replaced with air particles, and an equal number of sediment particles are introduced into the trench region, thus respecting global mass conservation. This procedure reproduces the erosion and sedimentation rates variable in time, as function of the system dynamics.

A.5.3 Phase changes

With respect to the original *SubMar* of *Marotta et al*., (2006), the code has been implemented taking into account phase transitions both for the mantle and for all the lithologies considered for the crust.

Phase changes have a dual effect, determining a variation in density and release or absorption of latent heat. Since *Afonso and Zlotnik* (2011) demonstrated that the impact of the crustal metamorphic reactions on the local thermal state is on the order of 5–10 °C, and then, the latent heat produced by phase changes of the crust can be ignored in large-scale models, the *SubMar* code did not include in Equation 6.3 the latent heat produced by phase changes occurring in the continental and oceanic crust, by phase changes related to hydration of the mantle wedge and by phase changes regarding the transformation of the olivine in the deep mantle. Regarding the phase changes in the mantle wedge, the latent heat of serpentinization can be neglected because it is balanced at large scales by the latent heat produced by de-serpentinization (*Perez-Gussinye and Reston*, 2001; *Rupke et al.,* 2004, 2013).

The following olivine $(Mg, Fe)_2SiO4$ transformations occurring in the mantle has been introduced in the *SubMar* code:

- from the $\alpha - phase$ to the high-pressure polymorphs wadsleyite ($\beta - phase$) at a depth of 410 km;
- from the wadsleyite ($\beta - phase$) to ringwoodite ($\gamma - phase$) at a depth of 520 km;
- from ringwoodite ($\gamma - phase$) to perovskite + periclase at a depth of 670 km.

Figure A.5 shows the assumed stability fields for minerals mentioned above. Considering a temperature of ∼1600 K for the upper mantle, olivine is expected to transform into wadsleyite at a pressure of ∼13 GPa, while the wadsleyite → ringwoodite transformation is expected to occur at ∼17.5 GPa (*Katsura and Ito*, 1989; *Kerschhofer et al.,* 1998), both with a positive Clapeyron slope. For the olivine it has been considered a density of 3200 kg m^{-3} (*Deer et al.,* 1992), while the $\alpha \rightarrow \beta$ and $\beta \rightarrow \gamma$ phase transformations result in increases in density of 6 and 2 per cent (*Kerschhofer et al.,* 1998), respectively, obtaining densities of 3392 and 3460 kg m^{-3} for the wadsleyite and ringwoodite, respectively. At the bottom of the upper mantle, ringwoodite transforms into perovskite + periclase ($MgSiO3+MgO$).

At a temperature of 1600 K, this transformation occurs at ∼22 GPa (corresponding to the 660-km seismic velocity discontinuity in the mantle), with a negative Clapeyron slope (*Fei et al.,* 2004 and refs. therein) and produces an additional increase in density. In particular, considering densities of ∼4000 and ∼3600 kg m^{-3} for the perovskite and the periclase (*Deer et al.* 1992), respectively, a density of 3800 kg m^{-3} for the lower mantle has been considered.

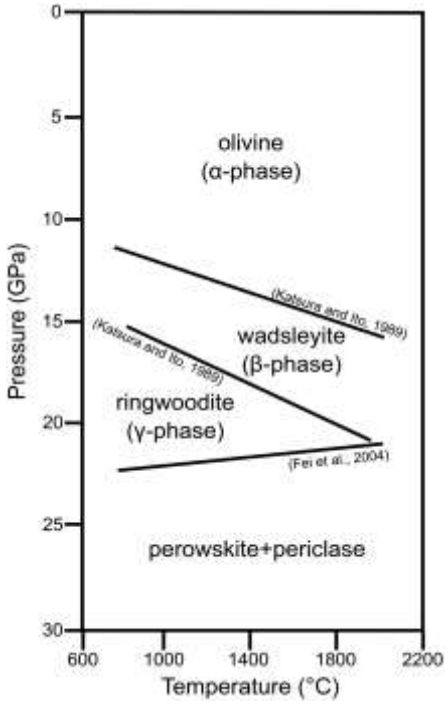

Figure A.5: Stability fields of olivine (α), wadsleyite (β), ringwoodite (γ) and perovskite + periclase in isochemical peridotitic mantle (based on *Katsura and Ito*, 1989 and *Fei et al.,* 2004).

Although the mineral reactions can increase the local temperature up to 60–70 °C (*van Hunen et al.,* 2001; *Afonso and Zlotnik*, 2011), *Negredo et al.* (2004) observed that the introduction of the latent heat in thermal models determines a variation in the maximum depth reach by the $\alpha - phase$ of less than 50 km inside the slab, while no differences have been observed outside the slab. Furthermore, *Blom* (2016) observed that the latent heat produced at the olivine→wadsleyite transformation is one order of magnitude smaller than the shear heating and two orders of magnitude smaller than the adiabatic heating.
Thus, the effects of the introduction of the latent heat can be considered negligible for what concerns the large-scale dynamics of the upper mantle.

Regarding the phase changes occurring in the oceanic and continental crust and in the sediments and plotted in the P-T diagram of Figure A.6, the density variations linked to different *P–T* conditions predicted by the models, have been computed by using Perple$_x$ (*Connolly*, 1990) program. Each component is characterized by particular bulk composition (*Borghesan*, 2011):

- the oceanic crust has the bulk composition of a mid-Atlantic ridge N-MORB (*Schilling et al.,* 1983);

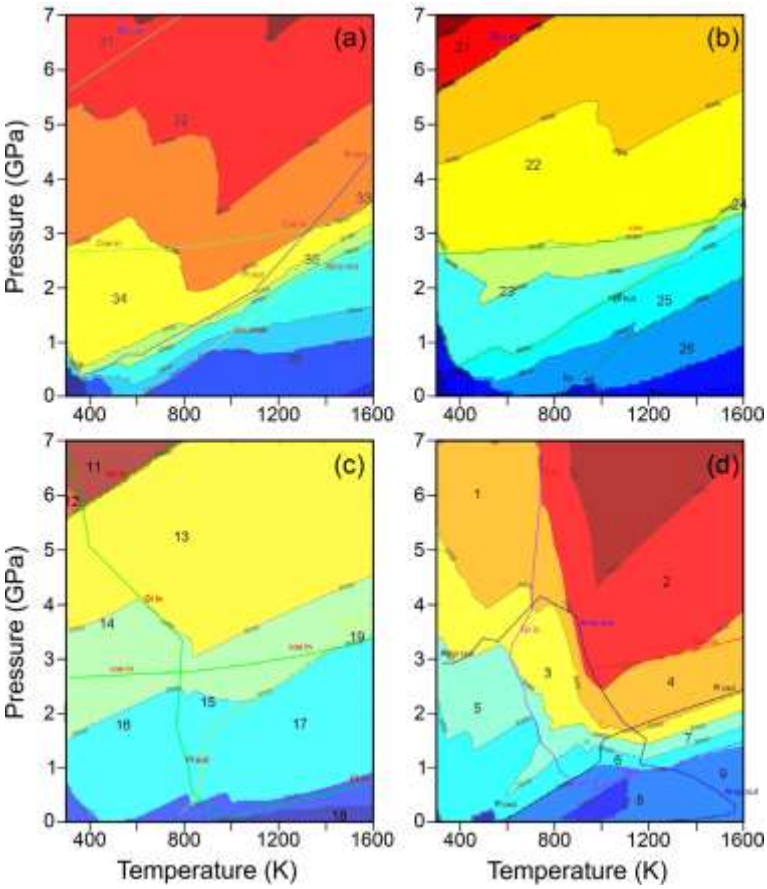

Figure A.6: Density contours related to phase changes in the (a) lower continental crust; (b) upper continental crust; (c) sediments and (d) oceanic crust. Gt, garnet; Amp, amphibole; Coe, coesite; Pl, plagioclase; Stv, stishovite; Ky, kyanite; Sill, sillimanite; And, andalusite; Mica, mica (from *Borghesan*, 2011).

- the continental crust has been separated into the upper crust, with the bulk composition of the Mucrone granite (*Oberhansli et al.,* 1985) and the lower crust, with the bulk composition of the Ivrea diorite (*Bigioggero et al.,* 1979);
- the sediments have the bulk composition of the Tre Valli Bresciane micaschist (*Origoni and Gregnanin*, 1983).

For each bulk composition, Perple*X* produced 10000 different densities for temperatures between 300 and 1600 K and pressures between 0 and 7 GPa (*Borghesan*, 2011) (Figure A.6) and at each time step the density is iterated with the pressure, driving the density changes due to phase change.

A.5.4 Coupling factor technique

Starting from the *split node* technique (*Jungels*, 1973; *Jungels and Frazier*, 1973), the degree of coupling has been implemented as described in Marotta *et al*. (2020), assigning at each node belonging to the discontinuity two different velocities, depending on the element to which it belongs. The *split node* technique is a method used to introduce a discontinuity in the displacement/velocity along fault planes within numerical computations based on the FE method. Normally, the displacement/velocity at nodes shared by more than one element is the same for each element. The *split nodes* are special nodes, in which the displacement/velocity is different depending on the element it belongs to. In this way, a generic differential slip/slip-rate $+\Delta\boldsymbol{u}$ can be assigned to a node when referring to the element on one side of the fault, while a differential slip/slip-rate $-\Delta\boldsymbol{u}$ is assigned to the same node when referring to the element on the other side of the faults. The fault is thus defined by a line of split nodes. The introduction of split nodes and the assembly of the vector of the charges and the stiffness matrix is simplified considering that this technique is implemented locally, and no degree of freedom is added to the nodes (*Melosh and Raefsky*, 1981). Since the original formulation of the *split nodes* requires that the slip/slip-rate is known *a priori*, it is not suitable for the modelling. This because it is not possible to know *a priori* the amount of the slip rate along the fault plane, leading to the results from the self-consistent thermomechanical evolution of the model. Therefore, the original formulation has been modified by introducing a coupling factor c_f that varies from 0 to 1 and indicates the percentage difference between the velocities at the two *split nodes* in such a way that:

$$\mathbf{u}_r = c_f \cdot \mathbf{u}_l \tag{A.53}$$

where $\mathbf{u}_l$ and $\mathbf{u}_r$ are the velocities of the same *split node* belonging to the left and right elements, respectively. Unlike the classical *split node* technique, which only involves modifying the load vector, this new technique also requires modification of the stiffness matrix.

Considering two quadratic triangular elements (Figure A.7) and assuming that 1 of the 6 nodes is a *split nodes* (node k, red circle in Figure A.7) with a coupling factor $c_f(k)$ different from 1. The velocity calculated in node k is equal to $\boldsymbol{u}(k)$ when node k is considered to belong

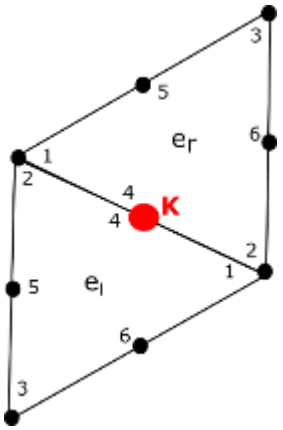

Figure A.7: Scheme used to implement the modified *slip node* technique.

to the left element e_l, while it is equal to $c_f(k) \cdot \boldsymbol{u}(k)$ when node k is considered to belong to the right element e_r. To simplify the implementation of the new technique, a coupling factor has been defined to all the nodes of the numerical grid initializing the array with the default value equal to 1. For the *slip node*, the value of the coupling factor changes into the actual value only when the *slip node* is treated as belonging to the right element. Its value remains unchanged when the same *slip node* is treated as belonging to the left element.

Following the standard formulation of the FE method, at the local scale of each element, the expression $\mathbf{K}^e \cdot \mathbf{u}^e = \mathbf{F}^e$ becomes:

$$\begin{bmatrix} K_{11} & K_{12} & K_{13} & K_{14} & K_{15} & K_{16} \\ K_{21} & K_{22} & K_{23} & K_{24} & K_{25} & K_{26} \\ K_{31} & K_{32} & K_{33} & K_{34} & K_{35} & K_{36} \\ K_{41} & K_{42} & K_{43} & K_{44} & K_{45} & K_{46} \\ K_{51} & K_{52} & K_{53} & K_{54} & K_{55} & K_{56} \\ K_{61} & K_{62} & K_{63} & K_{64} & K_{65} & K_{66} \end{bmatrix}^e \cdot \begin{bmatrix} u(1) & c_f(1) \\ u(2) & c_f(2) \\ u(3) & c_f(3) \\ u(4) & c_f(4) \\ u(5) & c_f(5) \\ u(6) & c_f(6) \end{bmatrix}^e = \begin{bmatrix} F(1) \\ F(2) \\ F(3) \\ F(4) \\ F(5) \\ F(6) \end{bmatrix}^e \tag{A.54}$$

where $\mathbf{K}^e$ is the element stiffness matrix, $\mathbf{u}^e$ is the vector of the element nodal displacement and $\mathbf{F}^e$ the vector of the element generalized nodal forces.

To obtain a symmetric stiffness matrix, the stiffness matrix and the load vector have been processed as follows:

$$\begin{bmatrix} K_{11}\cdot c_f(1) & K_{12}\cdot c_f(2) & K_{13}\cdot c_f(3) & K_{14}\cdot c_f(4) & K_{15}\cdot c_f(5) & K_{16}\cdot c_f(6) \\ K_{21}\cdot c_f(1) & K_{22}\cdot c_f(2) & K_{23}\cdot c_f(3) & K_{24}\cdot c_f(4) & K_{25}\cdot c_f(5) & K_{26}\cdot c_f(6) \\ K_{31}\cdot c_f(1) & K_{32}\cdot c_f(2) & K_{33}\cdot c_f(3) & K_{34}\cdot c_f(4) & K_{35}\cdot c_f(5) & K_{36}\cdot c_f(6) \\ K_{41}\cdot c_f(1) & K_{42}\cdot c_f(2) & K_{43}\cdot c_f(3) & K_{44}\cdot c_f(4) & K_{45}\cdot c_f(5) & K_{46}\cdot c_f(6) \\ K_{51}\cdot c_f(1) & K_{52}\cdot c_f(2) & K_{53}\cdot c_f(3) & K_{54}\cdot c_f(4) & K_{55}\cdot c_f(5) & K_{56}\cdot c_f(6) \\ K_{61}\cdot c_f(1) & K_{62}\cdot c_f(2) & K_{63}\cdot c_f(3) & K_{64}\cdot c_f(4) & K_{65}\cdot c_f(5) & K_{66}\cdot c_f(6) \end{bmatrix}^e \cdot \begin{bmatrix} u(1) \\ u(2) \\ u(3) \\ u(4) \\ u(5) \\ u(6) \end{bmatrix}^e = \begin{bmatrix} F(1) \\ F(2) \\ F(3) \\ F(4) \\ F(5) \\ F(6) \end{bmatrix}^e \quad \text{(A.55)}$$

Applying this method to a quadratic triangular element the new components of the stiffness matrix and the new load vectors to be inserted in the *SubMar* code are obtained.

Appendix B

Publications and abstracts realised during the Ph.D.

B.1 Paper on the PhD subject

Geophysical Journal International

Geophys. J. Int. (2020) **221**, 788–825
Advance Access publication 2020 January 16
GJI Gravity, Geodesy and Tides

doi: 10.1093/gji/ggaa029

The static and time-dependent signature of ocean–continent and ocean–ocean subduction: the case studies of Sumatra and Mariana complexes

A.M. Marotta, F. Restelli, A. Bollino, A. Regorda and R. Sabadini

Department of Earth Sciences 'A. Desio', Università degli Studi di Milano, L. Mangiagalli 34, *Milano* 20134, *Italy. E-mail: anna.maria.marotta@unimi.it*

Accepted 2020 January 15. Received 2019 December 24; in original form 2019 July 31

SUMMARY

The anomalous density structure at subduction zones, both in the wedge and in the upper mantle, is analysed to shed light on the processes that are responsible for the characteristic gravity fingerprints of two types of subduction: ocean–continent and ocean–ocean. Our modelling is then performed within the frame of the EIGEN-6C4 gravitational disturbance pattern of two subductions representative of the above two types, the Sumatra and Mariana complexes, finally enabling the different characteristics of the two patterns to be observed and understood on a physical basis, including some small-scale details. A 2-D viscous modelling perpendicular to the trench accounts for the effects on the gravity pattern caused by a wide range of parameters in terms of convergence velocity, subduction dip angle and lateral variability of the crustal thickness of the overriding plate, as well as compositional differentiation, phase changes and hydration of the mantle. Plate coupling, modelled within a new scheme where the relative velocity at the plate contact results self-consistently from the thermomechanical evolution of the system, is shown to have an important impact on the gravity signature. Beyond the already understood general bipolar fingerprint of subduction, perpendicular to the trench, we obtain the density and gravity signatures of the processes occurring within the wedge and mantle that are responsible for the two different gravity patterns. To be compliant with the geodetic EIGEN-6C4 gravitational disturbance and to compare our predictions with the gravity at Sumatra and Mariana, we define a *model normal Earth*. Although the peak-to-peak gravitational disturbance is comparable for the two types of subductions, approximately 250 mGal, from both observations and modelling, encompassing the highest positive maximum on the overriding plates and the negative minimum on the trench, the trough is wider for the ocean–ocean subduction: approximately 300 km compared to approximately 180 km for the ocean–continent subduction. Furthermore, the gravitational disturbance pattern is more symmetric for the ocean–ocean subduction compared to the ocean–continent subduction in terms of the amplitudes of the two positive maxima over the overriding and subducting plates. Their difference is, for the ocean–ocean type, approximately one half of the ocean–continent one. These different characteristics of the two types of subductions are exploited herein in terms of the different crustal thicknesses of the overriding plate and of the different dynamics in the wedge and in the mantle for the two types of subduction, in close agreement with the gravity data.

Key words: Numerical modelling; Gravity anomalies and Earth structure; Subduction zone processes; Asia.

Accepted on 15/01/2020 by the Geophysical Journal International. This subject has been treated in the thesis in Chapter 4.

Contents lists available at ScienceDirect

Tectonophysics

journal homepage: www.elsevier.com/locate/tecto

From rifting to oceanization in the Gulf of Aden: Insights from 2D numerical models

Arcangela Bollino *, Alessandro Regorda, Roberto Sabadini, Anna Maria Marotta

Università degli Studi di Milano, Department of Earth Science, L. Cicognara 7, 20129 Milano, Italy

ARTICLE INFO

Keywords:
2D numerical modeling
Continental rifting
Oceanic spreading
Gulf of Aden

ABSTRACT

We investigate the evolution of the Gulf of Aden from rift initiation to the development of active oceanic spreading center by means of 2D thermo-mechanical numerical models, in which the formation of oceanic crust and serpentinite due to the hydration of the uprising mantle peridotite has been implemented. Our analysis highlights that evolution of the models is characterized by four main tectonic phases: a) a first phase (phase I) characterized by low deformation rates throughout the divergent crustal blocks, except near the future ridge where a high crustal velocity gradient generates an intense strain rates; b) a second phase (phase II) during which the crust undergoes an intense, stable and widespread strain, with the localization of the thinning near the future ridge that ends into crustal breakup c) a third phase (phase III) that characterizes the post- crustal breakup evolution of the models during which a mechanical relaxation of the system and a continuum decreasing of the strain rate can be observed, until the occurrence of lithospheric breakup, and d) fourth phase (phase IV) that lasts up to the end of the evolution and during which the two continental blocks move rigidly. We also find that the timing of mantle serpentinization is not affected by the initial thermal configuration of the lithosphere, but a relationship with the crustal thickness can be observed. Rather, the timing of mantle partial melting strongly depends on the initial thermal conditions of both the lithosphere and the crust. We constrain the crustal and lithospheric thickness at 40 and 150 km, respectively, considering the timing of breakup that occurs 20 Myr after the onset of the extension for 0.05% percentage of mantle hydration (in agreement with magma-poor rift margins). Finally, model prediction supports the hypothesis that the Gulf of Aden developed as a slow passive rift of a thin lithosphere with a thick crust and the variation of the features along the passive margins could be related to a lateral variation in the amount of H_2O in the mantle, which determines different timing in the mantle melting.

Accepted on 09/07/2022 by Tectonophysics. This subject has been treated in the thesis in Chapter 6.

B.2 Abstract

EGU General Assembly 2020

New insights on the dynamics of the Sumatra and Mariana complexes inferred from the comparative analysis of gravity data and model predictions

A. Bollino[a], A.M.Marotta[a], F. Restelli[a], A. Regorda[a], R. Sabadini[a]

[a]Università degli Studi di Milano, Dipartimento di Scienze della Terra 'A. Desio', Milano, Italia

Subduction is responsible of surface displacements and deep mass redistribution. This rearrangement generates density anomalies in a wide spectrum of wavelength which, in turn, causes important anomalies in the Earth's gravity field that are visible as lineaments parallel to the arc-trench systems. In these areas, when the traditional analysis of the deformation and stress fields is combined with the analysis of the perturbation of the gravity field and its slow time variation, new information on the background environment controlling the tectonic loading phase can be disclosed.

Here we present the results of a comparative analysis between the geodetically retrieved gravitational anomalies, based on the EIGEN-6C4 model, and those predicted by a 2D thermo-chemical mechanical modeling of the Sumatra and Mariana complexes.

The 2D model accounts for a wide range of parameters, such as the convergence velocity, the shallow dip angle, the different degree of coupling between the facing plates. The *marker in cell* technique is used to compositionally differentiate the system. Phase changes in the crust and in the mantle and mantle hydration are also allowed. To be compliant with the geodetic EIGEN-6C4 gravity data, we define a *model normal Earth* considering the vertical density distribution at the margins of the model domain, where the masses are not perturbed by the subduction process.

Model prediction are in good agreement with data, both in terms of wavelengths and magnitude of the gravity anomalies measured in the surroundings of the Sumatra and Marina subductions. Furthermore, our modeling supports that the differences in the style of the gravity anomaly observed in the two areas is attributable to the different environments – ocean-ocean or ocean-continental subduction – that drives a significantly different dynamic in the wedge area.

BEGEO 2021 – 1° Congresso Nazionale dei Giovani Geoscienziati

New insights on the dynamics of the Sumatra and Mariana complexes inferred from the comparative analysis of gravity data and model predictions

Bollino A. [1*], Marotta A. M. [1], Restelli F. [1,2], Regorda A. [1], Sabadini R. [1]

Affiliation
[1] Department of Earth Sciences "Ardito Desio", University of Milan, L. Mangiagalli 34, 20133, Milan, Italy
[2] Department of Earth Sciences, Royal Holloway University of London, Egham, United Kingdom

Corresponding author: arcangela.bollino@unimi.it

Keywords: Numerical modelling; Gravity anomalies and Earth structure; Subduction zone processes

Subduction is responsible of surface displacements and deep mass redistribution. This rearrangement generates density anomalies in a wide spectrum of wavelengths which, in turn, causes important anomalies in the Earth's gravity field that are visible as lineaments parallel to the arc-trench systems. In these areas, when the traditional analysis of the deformation and stress fields is combined with the analysis of the perturbation of the gravity field and its slow time variation, new information on the background environment controlling the tectonic loading phase can be disclosed.

Here we present the results of a comparative analysis between the geodetically retrieved gravitational anomalies, based on the EIGEN-6C4 model, and those predicted by a 2D thermo-chemical mechanical modeling of the Sumatra and Mariana complexes, representative of the of two types of subduction: ocean–continent and ocean–ocean.

The 2D model accounts for a wide range of parameters, such as the convergence velocity, the shallow dip angle, the different degrees of coupling between the facing plates. The *marker in cell* technique is used to compositionally differentiate the system. Phase changes in the crust and in the mantle and mantle hydration are also allowed. To be compliant with the geodetic EIGEN-6C4 gravity data and to compare our predictions with the gravity at Sumatra and Mariana, we define a *model normal Earth* considering the vertical density distribution at the margins of the model domain, where the masses are not perturbed by the subduction process.

Model predictions are in good agreement with data, both in terms of wavelengths and magnitude of the gravity anomalies measured in the surroundings of the Sumatra and Marina subductions. Furthermore, our modeling supports that the differences in the style of the gravity anomaly observed in the two areas are attributable to the different environments – ocean-ocean or ocean-continental subduction – that drive a significantly different dynamic in the wedge area.

GNGTS 2021 – Gruppo Nazionale di Geofisica della Terra Solida – 39° Congresso Nazionale

The dynamic evolution of the Gulf of Aden: preliminary results from a 2D numerical model

A. Bollino[1], A. Regorda[1], R. Sabadini[1], A. M. Marotta[1]

[1]Università degli Studi di Milano, Department of Earth Science, Milano, Italy

Abstract

Gulf of Aden is a young oceanic basin that offers an excellent opportunity to understand breakup processes during extension. Regional stress field or thermal upwelling of the asthenosphere, inherited zones of weakness and the rheological structure of the lithosphere are the factors contributing to the initiation of rifting and deformation of lithosphere. We use a 2D thermo-mechanical model to simulate the formation of oceanic crust and serpentinite due to the hydration of upwelling mantle peridotite. Our preliminary results show that: a) four main tectonic phases develop during rifting, each one characterized by particular distributions of velocity gradients and strain rates inside divergent crustal blocks, which allow us to determine when breakup occurs; b) the timing of mantle serpentinization is not affected by the initial thermal configuration of the system but is related to crustal thickness; c) the timing of mantle partial melting strongly depends on the thermal conditions in both lithospheric plates.

Finally, the results obtained so far support the hypothesis that the Gulf of Aden developed as a slow passive rift in thin lithosphere with thick crust and that the variations in features along the passive margins could be related to lateral variations in the amount of H_2O in the mantle, which determines the different times of mantle melting. Further analyzes are underway in order to confirm these preliminary conclusions.

SIF – Società Italiana di Fisica 2022 – 108° Congresso Nazionale

Integration of numerical modelling and gravity data to disclose the dynamics of the Gulf of Aden

A. Bollino[1], A. Regorda[1], R. Sabadini[1], R. Barzaghi[2], A. M. Marotta[1]

[1]University of Milan, Department of Earth Science, Milano, Italy

[2]Politecnico di Milano, Department of Civil and Environmental Engineering, Milano, Italy

Abstract

Gulf of Aden is a young oceanic basin that offers an excellent opportunity to understand breakup processes during extension. Regional stress field or thermal upwelling of the asthenosphere, inherited zones of weakness and the rheological structure of the lithosphere are the factors contributing to the initiation of rifting and deformation of lithosphere. We use a 2D thermo-mechanical model to simulate the formation of oceanic crust and serpentinite due to the hydration of upwelling mantle peridotite. A strongly integration between modeling and gravitational data provided valuable constraints to our analysis.

Our preliminary results show that: a) four main tectonic phases develop during rifting, each one characterized by particular distributions of velocity gradients and strain rates inside divergent crustal blocks, which allow us to determine when breakup occurs; b) the timing of mantle serpentinization is not affected by the initial thermal configuration of the system but is related to crustal thickness; c) the timing of mantle partial melting strongly depends on the thermal conditions in both lithospheric plates; d) evolution of the model with crustal and lithospheric thickness of 40 and 150 km, respectively, well fit with the geodynamic reconstruction of the Gulf of Aden, considering the timing of break-up that occurs 20 Myr after the onset of the extension for 0.05 % percentage of mantle hydration (in agreement with magma-poor rift margins).

Finally, the results obtained so far support the hypothesis that the Gulf of Aden developed as a slow passive rift in thin lithosphere with thick crust and that the variations in features along the passive margins could be related to lateral variations in the amount of H_2O in the mantle, which determines the different times of mantle melting.

BIBLIOGRAPHY

Abers, G. A. (2000). Hydrated subducted crust at 100–250 km depth. *Earth and Planetary Science Letters*, *176*(3-4), 323-330.

Afonso, J.C. & Ranalli, G., 2004. Crustal and mantle strengths in continental lithosphere: is the jelly sandwich model obsolete? *Tectonophysics* 394(3–4), 221–232.

Afonso, J. C., & Zlotnik, S. (2011). The subductability of continental lithosphere: The before and after story. In *Arc-Continent Collision* (pp. 53-86). Springer, Berlin, Heidelberg.

Amante, C. & Eakins, B.W., 2009. ETOPO1 1 Arc-Minute Global Relief Model: Procedures, Data Sources and Analysis. NOAA Technical Memorandum NESDIS NGDC-2, National Geophysical Data Center, NOAA, doi:10.7289/V5C8276M.

Anderson, M.O. *et al.*, 2017. Geological interpretation of volcanism and segmentation of the Mariana back–arc spreading center between 12.7◦ N and 18.3◦ N, *Geochem. Geophys. Geosyst.,* 18(6), 2240–2274.

Arcay, D., Doin, M. P., & Tric, E. (2003). Effect of slab dehydration on the mantle wedge dynamics in subduction zones. In *EGS-AGU-EUG Joint Assembly* (p. 10547).

Arcay, D., Tric, E. & Doin, M.P. (2005). Numerical simulation of subduction zones. Effect of slab dehydration on the mantle wedge dynamics, *Phys. Earth planet. Inter.,* 149, 133–153.

Arcay, D., Lallemand, S., & Doin, M. P. (2008). Back-arc strain in subduction zones: Statistical observations versus numerical modeling. *Geochemistry, Geophysics, Geosystems*, *9*(5).

ArRajehi, A., McClusky, S., Reilinger, R., Daoud, M., Alchalbi, A., Ergintav, S., Gomez, F., Sholan, J., Bou-Rabee, F., Ogubazghi, G., Haileab, B., Fisseha, S., Asfaw, L., Mahmoud, S., Rayan, A., Bendik, R., Kogan, L. (2010). Geodetic constraints on

present-day motion of the Arabian Plate: Implications for Red Sea and Gulf of Aden rifting. *Tectonics*, *29*(3) https://doi.org/10.1029/2009TC002482.

Autin, J., Bellahsen, N., Leroy, S., Husson, L., Beslier, M.O., d'Acremont, E. (2013). The role of structural inheritance in oblique rifting: Insights from analogue models and application to the Gulf of Aden. *Tectonophysics*, *607*, 51-64. https://doi.org/10.1016/j.tecto.2013.05.041.

Autin, J., Leroy, S., Beslier, M.-O., d' Acremont, E., Razin, P., Ribodetti, A., Bellahsen, N., Robin, C., Al Toubi, K. (2010). Continental break-up history of a deep magma-poor margin based on seismic reflection data (northeastern Gulf of Aden margin, offshore Oman). *Geophysical Journal International*, *180*(2), 501-519. https://doi.org/10.1111/j.1365-246X.2009.04424.x

Bagley, B., & Nyblade, A. A. (2013). Seismic anisotropy in eastern Africa, mantle flow, and the African superplume. *Geophysical Research Letters*, *40*(8), 1500-1505.

Bassett, D., and Watts, A. B. (2015). Gravity anomalies, crustal structure, and seismicity at subduction zones: 1. Seafloor roughness and subducting relief. *Geochemistry, Geophysics, Geosystems*, *16*(5), 1508-1540.

Basuyau, C., Tiberi, C., Leroy, S., Stuart, G., Al-Lazki, A., Al-Toubi, K., Ebinger, C. (2010). Evidence of partial melting beneath a continental margin: case of Dhofar, in the Northeast Gulf of Aden (Sultanate of Oman). *Geophysical Journal International*, *180*(2), 520-534. https://doi.org/10.1111/j.1365-246X.2009.04438.x

Bauer, K., Neben, S., Schreckenberger, B., Emmermann, R., Hinz, K., Fechner, N., Gohl, K., Schulze, A., Trumbull, R.B., Weber, K. (2000). Deep structure of the Namibia continental margin as derived from integrated geophysical studies. *Journal of Geophysical Research: Solid Earth*, *105*(B11), 25829-25853. https://doi.org/10.1029/2000JB900227.

Bellahsen, N., Faccenna, C., Funiciello, F., Daniel, J. M., Jolivet, L. (2003). Why did Arabia separate from Africa? Insights from 3-D laboratory experiments. *Earth and Planetary Science Letters*, *216*(3), 365-381. https://doi.org/10.1016/S0012-821X(03)00516-8

Bellahsen, N., Fournier, M., d'Acremont, E., Leroy, S., Daniel, J. M. (2006). Fault reactivation and rift localization: Northeastern Gulf of Aden margin. *Tectonics*, *25(1)*. https://doi.org/10.1029/2004TC001626.

Bender, P.L., Wiese, D.N., Nerem, R.S. (2009). A possible dual-GRACE mission with 90

and 63 inclination orbits. In: Proc. of the 3rd International Symposium on Formation Flying, Missions and Technologies, Noordwijk (NL), April 2008.

Beniest, A. (2017). *From continental rifting to conjugate margins: insights from analogue and numerical modelling* (Doctoral dissertation, Université Pierre et Marie Curie-Paris VI).

Best, M.G. & Christiansen, E.H. (2001). *Igneous Petrology,* Blackwell Sci.

Beucher, R., Huismans, R. S. (2020). Morphotectonic Evolution of Passive Margins Undergoing Active Surface Processes: Large-Scale Experiments Using Numerical Models. *Geochemistry, Geophysics, Geosystems*, *21*(5), e2019GC008884. https://doi.org/ 10.1029/2019GC008884

Bigioggero, B., Boriani, A., Colombo, A.&Gregnanin, A. (1979). The 'Diorites' of the Ivrea Basic Complexs (Central Alps, Italy), *Memorie Scienze Geologiche,* **33,** 71–85.

Billen, I.M. & Hirth, G., 2007. Rheologic controls on slab dynamics, *Geochem. Geophys. Geosyst.,* **8**(8), 1–24.

Billen, M. I. (2008), Modeling the Dynamics of Subducting Slabs, Annual Review of Earth and Planetary Sciences, 36(1), 325–356, doi:10.1146/annurev.earth.36.031207.124129.

Blom, C. A. H. (2016). State of the art numerical subduction modelling with ASPECT; thermo-mechanically coupled viscoplastic compressible rheology, free surface, phase changes, latent heat and open sidewalls (Master's thesis).

Boillot, G. & Coulon, C. (1998). La Déchirure Continentale et L'ouverture Océanique: Géologie Des Marges Passives. Gordon and Breach, Amsterdam.

Bonatti, E., Cipriani, A., Lupi, L. (2015). The Red Sea: birth of an ocean. In *The Red Sea* (pp. 29-44). Springer, Berlin, Heidelberg.

Borghesan, I. (2011). Impatto delle trasformazioni di fase nella dinamica del cuneo di mantello, *MSc thesis*, Universit´a degli Studi di Milano.

Bosworth, W. (2015). Geological evolution of the Red Sea: historical background, review, and synthesis. In *The Red Sea* (pp. 45-78). Springer, Berlin, Heidelberg.

Bosworth, W., Huchon, P., McClay, K. (2005). The red sea and gulf of aden basins. *Journal of African Earth Sciences*, *43*(1-3), 334-378. https://doi.org/10.1016/j.jafrearsci.2005.07.020.

Bowling, J. C., & Harry, D. L. (2001). Geodynamic models of continental extension and the formation of non-volcanic rifted continental margins. *Geological Society, London, Special Publications*, *187*(1), 511-536.

Bradley, K.E., Feng, L., Hill, E.M., Natawidjaja, D.H. & Sieh, K., 2017. Implications of the diffuse deformation of the Indian Ocean lithosphere for slip partitioning of oblique plate convergence in Sumatra, *J. geophys. Res.,* **122**(1), 572–591.

Brockmann, Jan Martin; Schubert, Till; Mayer-Gürr, Torsten; Schuh, Wolf-Dieter (2019): The Earth's gravity field as seen by the GOCE satellite - an improved sixth release derived with the time-wise approach (GO_CONS_GCF_2_TIM_R6). GFZ Data Services. https://doi.org/10.5880/ICGEM.2019.003.

Brun, J.-P. (1999). Narrow rifts versus wide rifts: inferences for the mechanics of rifting from laboratory experiments. Philosophical Transactions of the Royal Society of London. Series A 357, 695–712.

Brune, S. (2014). Evolution of stress and fault patterns in oblique rift systems: 3-D numerical lithospheric-scale experiments from rift to breakup. Geochemistry, Geophysics, Geosystems, 15(8), 3392-3415.

Brune, S. (2018). Forces within continental and oceanic rifts: Numerical modeling elucidates the impact of asthenospheric flow on surface stress. *Geology*, *46*(2), 191-192.

Brune, S., Autin, J. (2013). The rift to break-up evolution of the Gulf of Aden: Insights from 3D numerical lithospheric-scale modelling. *Tectonophysics*, *607*, 65-79. https://doi.org/10.1016/j.tecto.2013.06.029.

Brune, S., Kolawole, F., Olive, J. A., Stamps, S., Buck, W. R., & Buiter, S. (2022). Geodynamics of continental rift initiation and evolution.

Buck, W.R., 1991. Modes of continental lithospheric extension. Journal of Geophysica Research 96, 20161–20178.

Burov, E. & Poliakov, A. (2003). Erosional forcing of basin dynamics: new aspects of syn- and post-rift evolution. *Geol. Soc. Spec. Publ.,* 212, 209–223.

Burov, E. (2007). The role of gravitational instabilities, density structure and extension rate in the evolution of continental margins. Geol. Soc. (Lond.) Spec. Publ.282, 139–156.

Cagnioncle, A. M., Parmentier, E. M., & Elkins-Tanton, L. T. (2007). Effect of solid flow above a subducting slab on water distribution and melting at convergent plate boundaries. *Journal of Geophysical Research: Solid Earth*, *112*(B9).

Cambiotti, G., Douch, K., Cesare, S., Haagmans, R., Sneeuw, N., Anselmi, A., ... & Sabadini, R. (2020). On earthquake detectability by the next-generation gravity mission. *Surveys in Geophysics*, *41*(5), 1049-1074.

Castle, J.C. & Creager, K.C. (1999). A steeply dipping discontinuity in the lower mantle beneath Izu-Bonin, *J. geophys. Res.,* 104(B4), 7279–7292.

Cerpa, N. G., Araya, R., Gerbault, M., & Hassani, R. (2015). Relationship between slab dip and topography segmentation in an oblique subduction zone: Insights from numerical modeling. *Geophysical Research Letters*, *42*(14), 5786-5795.

Cesare, S., Allasio, A., Anselmi, A., Dionisio, S., Mottini, S., Parisch, M., ... & Silvestrin, P. (2016). The European way to gravimetry: From GOCE to NGGM. *Advances in Space Research*, *57*(4), 1047-1064.

Channel, J.E., Mareschal, J.C. (1989). Delamination and asymmetric lithospheric thickening in the development of the Tyrrhenian Rift. In: Coward, M.P., Dietrich, D., Park, R.G. (Eds.), Alpine Tectonics. Geological Society, London, pp. 285–302.

Chenin, P., Schmalholz, S. M., Manatschal, G., Karner, G. D., 2018. Necking of the lithosphere: A reappraisal of basic concepts with thermo-mechanical numerical modeling. *Journal of Geophysical Research: Solid Earth*, *123*(6), 5279-5299. https://doi.org/10.1029/2017JB014155.

Chopra, P.N. & Peterson, M.S., 1981. The experimental deformation of dunite, *Tectonophysics,* 78, 453–473.

Christensen, U. R. (1984). Convection with pressure- and temperature-dependent non-Newtonian rheology. *Geophysical Journal of the Royal Astronomical Society*, **77**, 343–384.

Christensen, U. R. (1992). An Eulerian technique for thermomechanical modelling of lithospheric extension. *Journal of Geophysical Research*, 97, 2015–2036.

Christensen, U.R.& Yuen, D.A. (1985). Layered convection induced by phase transitions, *J. geophys. Res.,* 90(B12), 10291–10300.

Clague, D. A. (1987). Hawaiian xenolith populations, magma supply rates, and development of magma chambers. *Bulletin of Volcanology* 49(4), 577–87. https://doi.org/10.1007/BF01079963.

Clift, P., & Vannucchi, P. (2004). Controls on tectonic accretion versus erosion in subduction zones: Implications for the origin and recycling of the continental crust. *Reviews of Geophysics*, *42*(2).

Connolly, J.A.D., 1990. Multivariable phase-diagrams – an algorithm based on generalized thermodynamics, *Am. J. Sci.,* 290, 666–718.

Corbeau, J., Rolandone, F., Leroy, S., Al-Lazki, A., Stork, A. L., Keir, D., ... & Khanbari, K. (2014). Uppermost mantle velocity from Pn tomography in the Gulf of Aden. *Geosphere*, *10*(5), 958-968.

Corti, G., Bonini, M., Conticelli, S., Innocenti, F., Manetti, P., & Sokoutis, D. (2003). Analogue modelling of continental extension: a review focused on the relations between the patterns of deformation and the presence of magma. *Earth-Science Reviews*, *63*(3-4), 169-247.

Crameri, F., Schmeling, H., Golabek, G.J., Duretz, T., Orendt, R., Buiter, S.J.H., May, D.A., Kaus, B.J.P., Gerya, T.V., Tackley, P.J. (2012). A comparison of numerical surface topography calculations in geodynamic modelling: an evaluation of the 'sticky air'method. *Geophysical Journal International*, *189*(1), 38-54. https://doi.org/10.1111/j.1365-246X.2012.05388.x

Cruciani, C., E. Carminati, and C. Doglioni (2005). Slab dip vs. lithosphere age: No direct function, Earth and Planetary Science Letters, 238, 298–310, doi:10.1016/j.epsl.2005.07. 025.

Dahlen, F. A. (1990). Critical taper model of fold-and-thrust belts and accretionary wedges. *Annual Review of Earth and Planetary Sciences*, *18*, 55.

Dai, L., Li, S., Li, Z. H., Somerville, I., & Liu, X. (2017). Dynamic processes and mechanisms for collision to post-orogenic extension in the Western Dabie Orogen: Insights from numerical modeling. *Geological Journal*, *52*, 44-58.

Davies, J. H. (1999). The role of hydraulic fractures and intermediate-depth earthquakes in generating subduction-zone magmatism. *Nature*, *398*(6723), 142-145.

Deer, W.A., Howie, R.A. & Zussman, J. (1992). *An Introduction to the Rock-Forming Minerals,* 2nd edn, pp. 696, Longman.

Dionisio, S., Anselmi, A., Bonino, L., Cesare, S., Massotti, L., & Silvestrin, P. (2018). The "Next Generation Gravity Mission": challenges and consolidation of the system concepts and technological innovations. In *2018 SpaceOps Conference* (p. 2495).

Dixon, J. E., Leist, L., Langmuir, C., Schilling, J. G., 2002. Recycled dehydrated lithosphere observed in plume-influenced mid-ocean-ridge basalt. *Nature*, *420*(6914), 385-389. https://doi.org/10.1038/nature01215.

Donea, J. & Huerta, A., 2003. *Finite Element Methods for Flow Problems,* pp. 350, John Wiley & Sons.

Donea, J., Huerta, A. (2003). *Finite element methods for flow problems*. John Wiley & Sons.

Doré, T., & Lundin, E. (2015). Research focus: Hyperextended continental margins—knowns and unknowns. *Geology*, *43*(1), 95-96.

Dubois, J. & Diament, M. (1997). *G´eophysique,* Masson. dunite, *Tectonophysics,* 78, 453–473.

Duretz, T., Gerya, T. V., & May, D. A. (2011). Numerical modelling of spontaneous slab breakoff and subsequent topographic response. *Tectonophysics*, *502*(1-2), 244-256.

Ernst, W. G. and Liou, J. G. (2008). High-and ultrahigh-pressure metamorphism: Past results and future prospects. *American Mineralogist*, *93*(11-12), 1771-1786.

Faccenda, M. (2014). Water in the slab: A trilogy. *Tectonophysics*, *614*, 1-30.

Faccenna, C., Holt, A.F., Becker, T.W., Lallemand, S. & Royden, L.H., 2018. Dynamics of the Ryukyu/Izu-Bonin-Marianas double subduction system, *Tectonophysics,* 746, 229–238.

Farangitakis, G. P., Heron, P. J., McCaffrey, K. J. W., van Hunen, J., Kalnins, L. M. (2020). The impact of oblique inheritance and changes in relative plate motion on the development of rift-transform systems. *Earth and Planetary Science Letters*, *541*, 116277. https://doi.org/10.1016/j.epsl.2020.116277.

Fei, Y., Van Orman, J., Li, J., Van Westrenen, W., Sanloup, C., Minarik, W., ... & Funakoshi, K. I. (2004). Experimentally determined postspinel transformation boundary in Mg2SiO4 using MgO as an internal pressure standard and its geophysical implications. *Journal of Geophysical Research: Solid Earth*, *109*(B2).

Forsyth, D., and Uyeda, S., 1975, On the relative importance of the driving forces of plate motion: Geophysical Journal of the Royal Astronomical Society, v. 43, p. 163–200, https://doi.org/10.1111/j.1365-246X.1975.tb00631.x.

Fournier, M., Chamot-Rooke, N., Petit, C., Huchon, P., Al-Kathiri, A., Audin, L., ... & Merkouriev, S. (2010). Arabia-Somalia plate kinematics, evolution of the Aden-

Owen-Carlsberg triple junction, and opening of the Gulf of Aden. *Journal of Geophysical Research: Solid Earth*, *115*(B4).

Franke, D. (2013). Rifting, lithosphere breakup and volcanism: Comparison of magma-poor and volcanic rifted margins. *Marine and Petroleum geology*, *43*, 63-87.

Freeburn, R., Bouilhol, P., Maunder, B., Magni, V., & van Hunen, J. (2017). Numerical models of the magmatic processes induced by slab breakoff. *Earth and Planetary Science Letters*, *478*, 203-213.

Furlong, K. P., Chapman, D. S., 2013. Heat flow, heat generation, and the thermal state of the lithosphere. Annual Review of Earth and Planetary Sciences, 41, 385-410.

Gamage, S.S.N. (2017). Seismic activity near the Sunda and Andaman Trenches in the Sumatra subduction zone, *Int. J. Multidiscip. Stud.,* 4(2), doi:10.4038/ijms.v4i2.22 .

Gass, I. G., 1970. The evolution of volcanism in the junction area of the Red Sea, Gulf of Aden and Ethiopian rifts. Philosophical Transactions for the Royal Society of London. Series A, Mathematical and Physical Science

Geoffroy, L., Burov, E. B., & Werner, P. (2015). Volcanic passive margins: another way to break up continents. *Scientific reports*, *5*(1), 1-12.

Gerya, T. V., Stöckhert, B., & Perchuk, A. L. (2002). Exhumation of high-pressure metamorphic rocks in a subduction channel: A numerical simulation. *Tectonics*, *21*(6), 6-1.

Gerya, T.V. & Yuen, D.A., (2003). Rayleigh–Taylor instabilities from hydration and melting propel ‘cold plumes’ at subduction zones, *Earth planet. Sci. Lett.,* 212(1–2), 47–62.

Gerya, T.V., Yuen, D.A. & Maresch, W.V. (2004). Thermomechanical modelling of slab detachment, *Earth planet. Sci. Lett.,* 226(6), 101–116.

Gerya, T.V. & Stockhert, B. (2006). Two-dimensional numerical modeling of tectonic and metamorphic histories at active continental margins, *Int. J.Earth Sci. (Geol. Rundsch*.), 95(2), 250–274.

Gerya, T.V., Connolly, J. A., & Yuen, D. A. (2008). Why is terrestrial subduction one-sided? *Geology*, *36*(1), 43-46.

Gerya, T.V. (2010). *Numerical Geodynamic Modelling,* pp. 345, Cambridge Univ. Press.

Gerya, T.V. (2011). Future directions in subduction modeling, Journal of Geodynamics, 52(5), 344–378, doi:10.1016/j.jog.2011.06.005.

Gerya, T.V. (2013). Three-dimensional thermomechanical modeling of oceanic spreading initiation and evolution. Physics of the Earth and Planetary Interiors, 214, 35-52, doi:10.1016/j.pepi.2012.10.007.

Gibert, G., Gerbault, M., Hassani, R., & Tric, E. (2012). Dependency of slab geometry on absolute velocities and conditions for cyclicity: insights from numerical modelling. *Geophysical Journal International*, *189*(2), 747-760.

Globig, J., Fernàndez, M., Torne, M., Vergés, J., Robert, A., Faccenna, C., 2016. New insights into the crust and lithospheric mantle structure of Africa from elevation, geoid, and thermal analysis. *Journal of Geophysical Research: Solid Earth*, *121*(7), 5389-5424. https://doi.org/10.1002/2016JB012972.

Göğüş, O. H. (2015). Rifting and subsidence following lithospheric removal in continental back arcs. *Geology*, *43*(1), 3-6.

Gorczyk, W., Gerya, T.V., Connolly, J.A.D., Yuen, D.A. & Rudolph, M. (2006). Large-scale rigid-body rotation in the mantle wedge and its implications for seismic tomography, *Geochem. Geophys. Geosyst.,* **7**(5), 1–23, Q05018, doi:10.1029/2005GC001075

Green, H. W., W.-P. Chen, and M. R. Brudzinski (2010). Seismic evidence of negligible water carried below 400-km depth in subducting lithosphere., Nature, 467(7317), 828–831, doi:10.1038/nature09401.

Gueydan, F., Morency, C., Brun, J. P., 2008. Continental rifting as a function of lithosphere mantle strength. *Tectonophysics*, *460*(1-4), 83-93. https://doi.org/10.1016/j.tecto.2008.08.012.

Guillot, S., Hattori, K. H., de Sigoyer, J., Nägler, T., & Auzende, A. L. (2001). Evidence of hydration of the mantle wedge and its role in the exhumation of eclogites. *Earth and Planetary Science Letters*, *193*(1-2), 115-127.

Gulcher, A.J.P., Beaussier, S.J, and Gerya, T.V., 2019. On the formation of oceanic detachment faults and their influence on intra-oceanic subduction initiation: 3D thermomechanical modeling. Earth and Planetary Science Letters, 506, 195-208, doi:10.1016/j.epsl.2018.10.042.

Gutscher, M. A. (2016). Great subduction zone earthquakes: Advances in our understanding a decade after Sumatra, 2004. *Plate Boundaries Nat. Hazards*, *219*, 101.

Haagmans, R., Siemes, C., Massotti, L., Carraz, O., & Silvestrin, P. (2020). ESA's next-generation gravity mission concepts. *Rendiconti Lincei. Scienze Fisiche e Naturali*, *31*(1), 15-25.

Hackney, R. I., & Featherstone, W. E. (2003). Geodetic versus geophysical perspectives of the 'gravity anomaly'. *Geophysical Journal International*, *154*(1), 35-43.

Haenel, R., Rybach, L. & Stegena, L., 1988. *Handbook of Terrestrial Heat*- Hager, B.H., 1984. Subducted slabs and the geoid: constraints on mantle rheology and flow, *J. geophys. Res.,* 89(B7), 6003–6015.

Hager, B.H., O'Connell, R.J. & Raefsky, A., 1983. Subduction, back-arc spreading and global mantle flow, *Tectonophysics,* 99(2–4), 165–189.

Hall, R., Fuller, M., Ali, J.R. & Anderson, C.D., 1995. The Philippine Sea plate: magnetism and reconstructions, *Active Margins Marginal Basins Western Pacific,* 88, 371–404.

Hansen, S. E., Rodgers, A. J., Schwartz, S. Y., Al-Amri, A. M. (2007). Imaging ruptured lithosphere beneath the Red Sea and Arabian Peninsula. *Earth and Planetary Science Letters*, *259*(3-4), 256-265. https://doi.org/10.1016/j.epsl.2007.04.035.

Hébert, H., Deplus, C., Huchon, P., Khanbari, K., & Audin, L. (2001). Lithospheric structure of a nascent spreading ridge inferred from gravity data: the western Gulf of Aden. *Journal of Geophysical Research: Solid Earth*, *106*(B11), 26345-26363.

Heuret, A., & Lallemand, S. (2005). Plate motions, slab dynamics and back-arc deformation. *Physics of the Earth and Planetary Interiors*, *149*(1-2), 31-51.

Hirschmann, M. M. (2006). Water, melting, and the deep Earth H2O cycle. *Annu. Rev. Earth Planet. Sci.*, *34*, 629-653. https://doi.org/10.1146/annurev.earth.34.031405.125211.

Holt, A.F., Royden, L.H., Becker, T.W. & Faccenna, C. (2018). Slab interactions in 3-D subduction settings: The Philippine Sea Plate region, *Earth planet. Sci. Lett.,* 489, 72–83.

Honda, S., and M. Saito (2003), Small-scale convection under the back arc occurring in the low viscosity wedge, Earth and Planetary Science Letters, 216, 703–715, doi:10.1016/S0012-821X(03)00537-5.

Hu, J., & Gurnis, M. (2020). Subduction duration and slab dip. *Geochemistry, Geophysics, Geosystems*, *21*(4), e2019GC008862.

Huchon, P., Khanbari, K. (2003). Rotation of the syn-rift stress field of the northern Gulf of Aden margin, Yemen. *Tectonophysics*, *364*(3-4), 147-166. https://doi.org/10.1016/S0040-1951(03)00056-8.

Hughes, T.J.R., Liu, W. & Brooks, A. (1979). Finite element analysis of Incompressible viscous flows by the penalty function formulation, *J. Comp.Phys.,* 30**,** 1–60.

Hughes, T.J.R., Liu, W., Brooks, A., 1979. Finite element analysis of incompressible viscous flows by the penalty function formulation. *Journal of computational physics*, *30*(1), 1-60. https://doi.org/10.1016/0021-9991(79)90086-X.

Huismans, R. S., Beaumont, C. (2002). Asymmetric lithospheric extension: The role of frictional plastic strain softening inferred from numerical experiments. *Geology*, *30*(3), 211-214.

Huismans, R. S., Beaumont, C. (2003). Symmetric and asymmetric lithospheric extension: Relative effects of frictional-plastic and viscous strain softening. *Journal of Geophysical Research: Solid Earth*, *108*(B10).

Huismans, R. S., & Beaumont, C. (2014). Rifted continental margins: The case for depth-dependent extension. *Earth and Planetary Science Letters*, *407*, 148-162.

Huismans, R. S., Podladchikov, Y. Y., & Cloetingh, S. (2001). Transition from passive to active rifting: Relative importance of asthenospheric doming and passive extension of the lithosphere. *Journal of Geophysical Research: Solid Earth*, *106*(B6), 11271-11291.

Irifune, T. (1993). Phase transformations in the earth's mantle and subducting slabs: Implications for their compositions, seismic velocity and density structures and dynamics. *Island Arc*, *2*(2), 55-71.

Ismail-Zadeh, A., Korotkii, A., Schubert, G., & Tsepelev, I. (2007). Quasi-reversibility method for data assimilation in models of mantle dynamics. *Geophysical Journal International*, *170*(3), 1381-1398.

Ismail-Zadeh, A., & Tackley, P. (2010). *Computational methods for geodynamics*. Cambridge University Press.

Jarrard, R. D. (1986). Relations among subduction parameters. *Reviews of Geophysics*, *24*(2), 217-284.

Jones, C. H., Wernicke, B. P., Farmer, G. L., Walker, J. D., Coleman, D. S., McKenna, L. W., & Perry, F. V. (1992). Variations across and along a major continental rift: An

interdisciplinary study of the Basin and Range Province, western USA. *Tectonophysics*, *213*(1-2), 57-96.

Jourdon, A., Le Pourhiet, L., Mouthereau, F., May, D. (2020). Modes of propagation of continental breakup and associated oblique rift structures. *Journal of Geophysical Research: Solid Earth*, *125*(9), e2020JB019906.

Jungels, P.H. & Frazier, G.A. (1973). Finite element analysis of the residual displacements for an earthquake rupture: source parameters for the San Fernando earthquake, *J. geophys. Res.,* 78, 5062–5083.

Jungels, P.H. (1973), Models of tectonic processes associated with earthquakes, *PhD thesis*, pp. 207, California Institute Technology, Pasadena, California.

Katsura, T., & Ito, E. (1989). The system Mg2SiO4-Fe2SiO4 at high pressures and temperatures: Precise determination of stabilities of olivine, modified spinel, and spinel. *Journal of Geophysical Research: Solid Earth*, *94*(B11), 15663-15670.

Katz, R. F., Spiegelman, M., & Langmuir, C. H. (2003). A new parameterization of hydrous mantle melting. *Geochemistry, Geophysics, Geosystems*, *4*(9).

Keen, C.E., Stockmal, G.S., Welsink, H., Mudford, B. (1987). Deep crustal structure and evolution of the rifted margin northeast of Newfoundland: results from LITHOPROBE East. Canadian Journal of Earth Sciences 24, 1537–1549.

Keppie, D. F., Currie, C. A., & Warren, C. (2009). Subduction erosion modes: Comparing finite element numerical models with the geological record. *Earth and Planetary Science Letters*, *287*(1-2), 241-254.

Kerschhofer, L., Dupas, C., Liu, M., Sharp, T. G., Durham, W. B., & Rubie, D. C. (1998). Polymorphic transformations between olivine, wadsleyite and ringwoodite: mechanisms of intracrystalline nucleation and the role of elastic strain. *Mineralogical Magazine*, *62*(5), 617-638.

Kim, Y.M., Lee, S.M. & Okino, K. (2009). Comparison of gravity anomaly between mature and immature intra-oceanic subduction zones in the western Pacific, *Techtonophysics,* 474**,** 657–673.

King, S. D., & Anderson, D. L. (1998). Edge-driven convection. *Earth and Planetary Science Letters*, *160*(3-4), 289-296.

Kirby, S.H., 1983. Rheology of the lithosphere, *Rev. Geophys.,* 21(6), 1459– 1487.

Kong, X., Li, S., Wang, Y., Suo, Y., Dai, L., Geli, L., Zhang, Y., Guo, L. & Wang, P., 2018. Causes of earthquake spatial distribution beneath the Izu-Bonin-Mariana Arc, *J. Asian Earth Sci.,* 151, 90–100.

Koppers, A. A., Becker, T. W., Jackson, M. G., Konrad, K., Müller, R. D., Romanowicz, B., ... & Whittaker, J. M. (2021). Mantle plumes and their role in Earth processes. *Nature Reviews Earth & Environment*, *2*(6), 382-401.

Koptev, A., Cloetingh, S. and Ehlers, T. A. (2021). Longevity of small-scale ('baby') plumes and their role in lithospheric break-up. *Geophysical Journal International*, *227*(1), 439-471.

Korenaga, T., & Korenaga, J. (2016). Evolution of young oceanic lithosphere and the meaning of seafloor subsidence rate. *Journal of Geophysical Research: Solid Earth*, *121*(9), 6315-6332.

Kundu, B. & Gahalaut, V.K. (2011). Slab detachment of subducted Indo- Australian plate beneath Sunda arc, Indonesia, *J. Earth Syst. Sci.,* 120(2), 193–204.

Lallemand, S. (1999), La subduction ocèanic, Gordon and Breach Science Publishers.

Lallemand, S., Heuret, A., & Boutelier, D. (2005). On the relationships between slab dip, back-arc stress, upper plate absolute motion, and crustal nature in subduction zones. *Geochemistry, Geophysics, Geosystems*, *6*(9).

Larsen, H. C., Mohn, G., Nirrengarten, M., Sun, Z., Stock, J., Jian, Z., ... & Zhong, L. (2018). Rapid transition from continental breakup to igneous oceanic crust in the South China Sea. *Nature Geoscience*, *11*(10), 782-789.

Le Pichon, X. L., Henry, P., & Lallemant, S. (1993). Accretion and erosion in subduction zones: The role of fluids. *Annual Review of Earth and Planetary Sciences*, *21*, 307-331.

Leroy et al. (2012). From rifting to oceanic spreading in the Gulf of Aden: a synthesis. *Arabian Journal of Geosciences*, *5*(5), 859-901. https://doi.org/10.1007/s12517-011-0475-4.

Leroy, S., d'Acremont, E., Tiberi, C., Basuyau, C., Autin, J., Lucazeau, F., Sloan, H. (2010). Recent off-axis volcanism in the eastern Gulf of Aden: implications for plume–ridge interaction. *Earth and Planetary Science Letters*, *293*(1-2), 140-153. https://doi.org/10.1016/j.epsl.2010.02.036.

Li, Z. H. (2020). Flat subduction versus big mantle wedge: Contrasting modes for deep hydration and overriding craton modification. *Journal of Geophysical Research: Solid Earth*, *125*(8), e2020JB020018.

Liao, J., & Gerya, T. (2014). Influence of lithospheric mantle stratification on craton extension: Insight from two-dimensional thermo-mechanical modeling. *Tectonophysics*, *631*, 50-64.

Liao, J., Gerya, T. (2015). From continental rifting to seafloor spreading: insight from 3D thermo-mechanical modeling. *Gondwana Research*, *28*(4), 1329-1343.

Lister, G. S., Etheridge, M. A., & Symonds, P. A. (1986). Detachment faulting and the evolution of passive continental margins. *Geology*, *14*(3), 246-250.

Liu, L., J. Zhang, H. W. Green, Z. Jin, and K. N. Bozhilov (2007), Evidence of former stishovite in metamorphosed sediments, implying subduction to >350 km, Earth and Planetary Science Letters, 263(3-4), 180–191, doi:10.1016/j.epsl.2007.08.010.
Magazine, *62*(5), 617-638.

Magni, V., Bouilhol, P. and Van Hunen, J. (2014). Deep water recycling through time. *Geochemistry, Geophysics, Geosystems*, *15*(11), 4203-4216.

Malavieille, J., S. Guillot, P. Costa, J. M. Lardeaux, and V. Gardien (1990), Collapse of the thickened Variscan crust in the French Massif Central: Mont Pilat extensional shear zone and St. Etienne Late Carboniferous basin, Tectonophysics, 177(1-3), 139–149, doi: 10.1016/0040-1951(90)90278-G.

Malod, J.A. & Kemal, B.M., 1996. The Sumatra margin: oblique subduction and lateral displacement of the accretionary prism, *Geol. Soc., Lond., Spec. Publ.,* 106(1), 19–28.

Marotta, A.M., Barzaghi, R., Borghi, A. & Spelta, E. (2007). Gravity constraints on the dynamics of the crust–mantle system during Calabrian subduction, *Geophys. J. Int.,* 171, 977–985.

Marotta, A. M., Restelli, F., Bollino, A., Regorda, A., Sabadini, R. (2020). The static and time-dependent signature of ocean–continent and ocean–ocean subduction: the case studies of Sumatra and Mariana complexes. *Geophysical Journal International*, *221*(2), 788-825.

Marotta, A.M., Roda, M., Conte, K., Spalla, M.I. (2018). Thermo-mechanical numerical model of the transition from continental rifting to oceanic spreading: the case study of

the Alpine Tethys. *Geological Magazine*, *155*(2), 250-279. https://doi.org/10.1017/S0016756816000856.

Marotta, A. M., Spalla, M. I., Gosso, G. (2009). Upper and lower crustal evolution during lithospheric extension: numerical modelling and natural footprints from the European Alps. *Geological Society, London, Special Publications*, *321*(1), 33-72.

Marotta, A. M., E. Spelta, and C. Rizzetto (2006). Gravity signature of crustal subduction inferred from numerical modelling, Geophysical Journal International, 166, 923–938, doi: 10.1111/j.1365-246X.2006.03058.x.

McKenzie, D. (1978). Some remarks on the development of sedimentary basins. *Earth and Planetary science letters*, *40*(1), 25-32.

Mckenzie, D. A. N., & Bickle, M. J. (1988). The volume and composition of melt generated by extension of the lithosphere. *Journal of petrology*, *29*(3), 625-679.

Meda, M., Marotta, A. M., & Spalla, M. I. (2010). The role of mantle hydration in continental crust recycling in the wedge region. *Geological Society, London, Special Publications*, *332*(1), 149-172.

Melosh, H.J. & Raefsky, A. (1980). The dynamical origin of subduction zone topography, *J. geophys. Int.,* 60(3), 333–354.

Melosh, H.J. and Raefsky, A. (1981). A simple and efficient method for introducing faults into finite element computations, *Bull. seism. Soc. Am.,*71(5), 1391–1400.

Merle, O. (2011). A simple continental rift classification. *Tectonophysics*, *513*(1-4), 88-95.

Merle, O., Michon, L. (2001). The formation of the West European Rift: a new model as exemplified by the Massif Central area. Bulletin de la Société Géologique de France 172 (2), 213–221.

Michael, P. J. (1994). Evidence from trace elements and H20 for regionally distinctive sources of depleted MORB: implications for evolution of the depleted mantle. *Mineralogical Magazine*, *58*, 400.

Michael, P. J. (1995). Regionally distinctive sources of depleted MORB: Evidence from trace elements and H2O. *Earth and Planetary Science Letters*, *131*(3-4), 301-320. https://doi.org/10.1016/0012-821X(95)00023-6.

Michon, L., Merle, O. (2001). The evolution of the Massif Central Rift: spatio-temporal distribution of the volcanism. Bulletin de la Société Géologique de France 172(2), 201–211.

Miller, M.S., Gorbatov, A. & Kennett, B.L.N. (2005). Heterogeneity within the subducting Pacific slab beneath the Izu–Bonin–Mariana arc: evidence from tomography using 3D ray tracing inversion techniques, *Earth planet. Sci. Lett.,* 235(1–2), 331–342.

Miller, M.S., Gorbatov, A. & Kennett, B.L. (2006). Three-dimensional visualization of a near-vertical slab tear beneath the southern Mariana arc, *Geochem. Geophys. Geosyst.,* **7**(6), doi:10.1029/2005GC001110.

Moeremans, R., Singh, S.C., Mukti, M., McArdle, J. & Johansen, K. (2014). Seismic images of structural variations along the deformation front of the Andaman–Sumatra subduction zone: implications for rupture propagation and tsunami genesis, *Earth planet. Sci. Lett.,* 386**,** 75–85.

Moore, J. C., and Vrolijk, P. (1992). Fluids in accretionary prisms. *Reviews of Geophysics*, *30*(2), 113-135.

Moresi, L. N., Dufour, F. and Muhlhaus, H.-B. (2003).ALagrangian integration point finite element method for large deformation modeling of viscoelastic geomaterials. *Journal of Computational Physics*, 184, 476–497.

Moresi, L., and Solomatov, V. (1998). Mantle convection with a brittle lithosphere: thoughts on the global tectonic styles of the Earth and Venus. *Geophysical Journal International*, *133*(3), 669-682.

Morgan, P., Baker, B.H.E. (1983). Introduction — processes of continental rifting. Tectonophysics 94, 1–10.

Morgan, W.J. (1983). Hotspot tracks and the early rifting of the Atlantic. Tectonophysics 94, 123–139.

Morley, C.K. (1994). Interaction of deep and shallow processes in the evolution of the Kenya Rift. Tectonophysics 236, 81–91.

Moulik, P. & Ekstr¨om, G. (2016). The relationships between large-scale variations in shear velocity, density, and compressional velocity in the Earth's mantle, *J. geophys. Res.,* 121**,** 2737–2771.

Mulugeta, G. (1985). Dynamic models of continental rift valley systems. Tectonophysics 113, 49–73.

Mutter, J. C., Buck, W. R., & Zehnder, C. M. (1988). Convective partial melting: 1. A model for the formation of thick basaltic sequences during the initiation of spreading. *Journal of Geophysical Research: Solid Earth*, *93*(B2), 1031-1048.

Navon, O., & Stolper, E. (1987). Geochemical consequences of melt percolation: the upper mantle as a chromatographic column. *The Journal of Geology*, *95*(3), 285-307.

Negredo, A.M., Valera, J.L. & Carminati, E., 2004. TEMSPOL: a MATLAB thermal model for deep subduction zones including major phase transformations, *Comput. Geosci.,* 30**,** 249–258.

Nichols, A. R. L., Carrol, M. R., Hoskuldsson, A. (2002). Is the Iceland hot spot also wet? Evidence from the water contents of undegassed submarine and subglacial pillow basalts. *Earth and Planetary Science Letters*, *202*(1), 77-87. https://doi.org/10.1016/S0012-821X(02)00758-6.

Nielsen, C., Chamot-Rooke, N. & Rangin, C. (2004). From partial to full strain partitioning along the Indo-Burmese hyper-oblique subduction, *Marine Geology,* **209**(1–4), 303–327.

Nikishin, A. M., Ziegler, P. A., Stephenson, R. A., Cloetingh, S. A. P. L., Furne, A. V., Fokin, P. A., ... & Shalimov, I. V. (1996). Late Precambrian to Triassic history of the East European Craton: dynamics of sedimentary basin evolution. *Tectonophysics*, *268*(1-4), 23-63.

Nikolaeva, K., Gerya, T. V., Connolly, J. A. (2008). Numerical modelling of crustal growth in intraoceanic volcanic arcs. Physics of the Earth and Planetary Interiors, 171(1-4), 336-356.

Nonn, C., Leroy, S., Lescanne, M., Castilla, R., 2019. Central Gulf of Aden conjugate margins (Yemen-Somalia): Tectono-sedimentary and magmatism evolution in hybrid-type margins. *Marine and Petroleum Geology*, *105*, 100-123. https://doi.org/10.1016/j.marpetgeo.2018.11.053.

Oberhänsli, R., Hunziker, J. C., Martinotti, G., & Stern, W. B. (1985). Geochemistry, geochronology and petrology of Monte Mucrone: an example of Eo-Alpine eclogitization of Permian granitoids in the Sesia-Lanzo Zone, Western Alps, Italy. *Chemical Geology: Isotope Geoscience Section*, *52*(2), 165-184.

Oliveira V. C. Jr, Uieda L., Hallam K. A. T., Barbosa V. C. F. (2018). Should geophysicists use the gravity disturbance or the anomaly? *Geophysics*

Origoni, E.G. & Gregnanin, A. (1983). The cristalline basement of the Massiccio delle Tre Valli Bresciane: new petrographic and chemical data, *Memorie della Societ´a Geologica Italiana,* 26**,** 133–144.

Parsons, B. (1982). Causes and consequences of the relation between area and age of the ocean floor. *Journal of Geophysical Research: Solid Earth*, *87*(B1), 289-302.

Pearce, J. A., Reagan, M. K., Petronotis, K., Morgan, S., Almeev, R., Avery, A. J., ... & Whattam, S. A. (2015). Izu-Bonin-Mariana fore arc: Testing subduction initiation and ophiolite models by drilling the outer Izu-Bonin-Mariana fore arc; 30 July–29 September 2014. *Integrated Ocean Drilling Program: Preliminary Reports*, *352*.

Pérez-Gussinyé, M., Morgan, J. P., Reston, T. J. Ranero, C. R. (2006). The rift to drift transition at non-volcanic margins: Insights from numerical modelling. *Earth and Planetary Science Letters*, *244*(1-2), 458-473. https://doi.org/10.1016/j.epsl.2006.01.059.

Perez-Gussinye, M., Reston, T.J. (2001). Rheological evolution during extension at nonvolcanic rifted margins: onset of serpentinization and development of detachments

Petersen, K. D., Armitage, J. J., Nielsen, S. B., Thybo, H. (2015). Mantle temperature as a control on the time scale of thermal evolution of extensional basins. *Earth and Planetary Science Letters*, *409*, 61-70.

Petrunin, A. G., Kaban, M. K., El Khrepy, S., Al-Arifi, N. (2020). Mantle Convection Patterns Reveal the Mechanism of the Red Sea Rifting. *Tectonics*, *39*(2), e2019TC005829. https:// doi.org/10.1029/2019TC005829.

Quinquis, M.E.T. & Buiter, S.J.H. (2014). Testing the effects of basic numerical implementations of water migration on models of subduction dynamics, *J. geophys. Res.,* **5**(1), 537–555.

Ranalli, G. & Murphy, D.C. (1987). Rheological stratification of the lithosphere, *Tectonophysics,* 132(4), 281–295.

Rasul, N. M., Stewart, I. C., Nawab, Z. A. (2015). Introduction to the Red Sea: its origin, structure, and environment. In *The Red Sea* (pp. 1-28). Springer, Berlin, Heidelberg.

Rea, D. K., & Ruff, L. J. (1996). Composition and mass flux of sediment entering the world's subduction zones: Implications for global sediment budgets, great earthquakes, and volcanism. *Earth and Planetary Science Letters*, *140*(1-4), 1-12.

Regorda, A., Roda, M., Marotta, A. M., and Spalla, M. I. (2017). 2-D numerical study of hydrated wedge dynamics from subduction to post-collisional phases. *Geophysical Journal International*, *211*(2), 952-978.

Regorda, A., Spalla, M. I., Roda, M., Lardeaux, J. M., Marotta, A. M. (2021). Metamorphic facies and deformation fabrics diagnostic of subduction: Insights from 2D numerical models. *Geochemistry, Geophysics, Geosystems*, *22*(10), e2021GC009899.

Reilinger, R., McClusky, S., ArRajehi, A. (2015). Geodetic constraints on the geodynamic evolution of the Red Sea. In *The Red Sea* (pp. 135-149). Springer, Berlin, Heidelberg.

Reston, T., & Manatschal, G. (2011). Rifted margins: Building blocks of later collision. In *Arc-continent collision* (pp. 3-21). Springer, Berlin, Heidelberg.

Richards, M.A., Duncan, R.A., Courtillot, V.E., 1989. Flood basalts and hot-spot tracks: plume heads and tails. Science 246, 103e107.

Richter, M. J., Brune, S., Riedl, S., Glerum, A., Neuharth, D., Strecker, M. R., 2021. Controls on asymmetric rift dynamics: Numerical modeling of strain localization and fault evolution in the Kenya Rift. *Tectonics*, *40*(5), e2020TC006553

Roda M., Marotta A.M. and Spalla M.I. (2010); Numerical simulations of an ocean-continent convergent system: Influence of subduction geometry and manle wedge hydratation on crustal recycling. Geochem. Geophys. Geosyst., 11(5), 1-21.

Roda, M., A. M. Marotta, and M. I. Spalla (2011), The effects of the overriding plate thermal state on the slab dip in an ocean-continent subduction system, Compte Rendu Academie des Sciences Paris, 343(5), 323–330, doi:10.1016/j.crte.2011.01.005.

Roda, M., Regorda, A., Spalla, M. I., Marotta, A. M. (2018). What drives A lpine T ethys opening? Clues from the review of geological data and model predictions. *Geological Journal*, *54*(4), 2646-2664. https://doi.org/10.1002/gj.3316.

Roda, M., Spalla, M.I. & Marotta, A.M. (2012). Integration of natural data within a numerical model of ablative subduction: a possible interpretation for the Alpine dynamics of the Austroalpine crust, *J. Metamor.,* 30(9), 973–996.

Rooney, T. O., Nelson, W. R., Dosso, L., Furman, T., & Hanan, B. (2014). The role of continental lithosphere metasomes in the production of HIMU-like magmatism on the northeast African and Arabian plates. *Geology*, *42*(5), 419-422.

Rooney, T. O., Nelson, W. R., Dosso, L., Furman, T., Hanan, B. (2014). The role of continental lithosphere metasomes in the production of HIMU-like magmatism on the northeast African and Arabian plates. *Geology*, *42*(5), 419-422. https://doi.org/10.1130/G35216.1

Rowley, D. B., & Sahagian, D. (1986). Depth-dependent stretching: A different approach. *Geology*, *14*(1), 32-35.

Ruh, J.B.,Gerya, T.& Burg, J.P. (2013). High-resolution 3Dnumerical modeling of thrust wedges: influence of d′ecollement strength on transfer zones, *Geochem. Geophys. Geosyst.,* 14(4), 1131–1155.

Rupke, L.H., Morgan, J.P., Hort, M. & Connolly, J.A. (2004). Serpentine and the subduction zone water cycle, *Earth planet. Sci. Lett.,* 223(1-2), 17–34.

Rupke, L.H., Schmid,D.W., Perez-Gussinye, M.&Hartz, E. (2013). Interrelation between rifting, faulting, sedimentation, and mantle serpentinization during continental margin formation- including examples from the Norwegian Sea, *Geochem. Geophys. Geosyst.,* 14(10), 4351–4369.

Ruppel, C. (1995). Extensional processes in continental lithosphere. Journal of Geophysical Research 100, 24187–24215.

Sandwell, D. T., and W. H. F. Smith (2009), Global marine gravity from retracked Geosat and ERS-1 altimetry: Ridge segmentation versus spreading rate, J. Geophys. Res., 114, B01411, doi:10.1029/2008JB006008.

Schellart, W. P., & Rawlinson, N. (2013). Global correlations between maximum magnitudes of subduction zone interface thrust earthquakes and physical parameters of subduction zones. *Physics of the Earth and Planetary Interiors*, *225*, 41-67.

Schettino, A., Ranalli, G., Fierro, E., Pierantoni, P. P., Zanoni, D., Turco, E., Rasul, N., 2019. Rift–drift transition in the Red Sea: a rheological model of the early stage of seafloor spreading. Geophysical Journal International, 217(3), 1870-1893.

Schilling, J.G., Zajac, M., Evans, R., Johnston, T., White, W.M., Devine, J.D. & Kingsley, R. (1983). Petrologic and geochemical variations along the Mid-Atlantic Ridge from 29◦N to 73◦N, *Am. J. Sci.,* 283**,** 510–586.

Schlüter, H. U., Gaedicke, C., Roeser, H. A., Schreckenberger, B., Meyer, H., Reichert, C., ... & Prexl, A. (2002). Tectonic features of the southern Sumatra-western Java forearc of Indonesia. *Tectonics*, *21*(5), 11-1.

Schmeling, H. *et al.*, 2008. A benchmark comparison of spontaneous subduction models—towards a free surface, *Phys. Earth planet. Inter.,* 171**,** 198–223.

Schmeling, H. (2000). Partial melting and melt segregation in a convecting mantle. In *Physics and Chemistry of Partially Molten Rocks* (pp. 141-178). Springer,

Dordrecht.Sewell, G. (1982). TWODEPEP, a small general purpose finite element program. *Angewandte Informatik*, *24*(4), 249-253.

Schmidt, M. W., & Poli, S. (1998). Experimentally based water budgets for dehydrating slabs and consequences for arc magma generation. *Earth and Planetary Science Letters*, *163*(1-4), 361-379.

Scholz, C.H., Campos, J. (1995). On the mechanism of seismic decoupling and back-arc spreading at subduction zones. J. Geophys. Res. 100, 22103–22115.

Sdrolias,M., Roest,W.R.&M¨uller, R.D. (2004). An expression of Philippine Sea plate rotation: the Parece Vela and Shikoku basins, *Tectonophysics,* 394(1–2), 69–86.

Sen, G. (2014). Subduction Zone Magmas. In *Petrology* (pp. 209-242). Springer, Berlin, Heidelberg.

Sengör, A.M.C., Burke, K. (1978). Relative timing of rifting and volcanism on Earth and its tectonic implications. Geophysical Research Letters 5, 419–421.

Sewell, G. (1981). Twodepep: a small general purpose finite element program, IMSL Technical Report Series 8102.

Shapiro, N.M., Ritzwoller, M.H. & Engdahl, E.R. (2008). Structural context of the great Sumatra-Andaman Islands earthquake, *Geophys. Res. Lett.,* 35(L05301), doi:10.1029/2008GL033381.

Shinjo, R., Meshesha, D., Orihashi, Y., Haraguchi, S., Tamaki, K. (2015). Sr–Nd–Pb–Hf isotopic constraints on the diversity of magma sources beneath the Aden Ridge (central Gulf of Aden) and plume–ridge interaction. *Journal of Mineralogical and Petrological Sciences*, *110*(3), 97-110. https://doi.org/10.2465/jmps.141211.

Shuler, A., Nettles, M. (2012). Earthquake source parameters for the 2010 western Gulf of Aden rifting episode. *Geophysical Journal International*, *190*(2), 1111-1122. https://doi.org/10.1111/j.1365-246X.2012.05529.x

Silvestrin, P., Aguirre, M., Massotti, L., Leone, B., Cesare, S., Kern, M., Haagmans, R., (2012). The future of the satellite gravimetry after the GOCE mission. Int. Assoc. Geodesy Symp. 136 (2012), 223–230.

Simmons, N.A., Forte, A.M., Boschi, L. & Grand, S.P. (2010). GyPSuM: a joint tomographic model of mantle density and seismic wave speeds, *J. geophys. Res.,* 115**,** 1–24.

Stamps, D.S., Flesch, L.M., Calais, E. (2010). Lithospheric buoyancy forces in Africa from a thon sheet. International Journal of Earth Sciences 99, 1525–1533 (Geol. Rundsch.).

Stern, R. J. (2002). Subduction zones. *Reviews of geophysics*, *40*(4), 3-1.

Stern, R.J. & Gerya, T.V. (2018). Subduction initiation in nature and models: a review, *Tectonophysics,* 746**,** 173–198.

Syracuse, E. M., & Abers, G. A. (2006). Global compilation of variations in slab depth beneath arc volcanoes and implications. *Geochemistry, Geophysics, Geosystems*, *7*(5).

Tao, W. C., & O'connell, R. J. (1992). Ablative subduction: A two-sided alternative to the conventional subduction model. *Journal of Geophysical Research: Solid Earth*, *97*(B6), 8877-8904.

Tapley, B. D., Schutz, B. E., & Eanes, R. J. (1985). Station coordinates, baselines, and Earth rotation from LAGEOS laser ranging: 1976–1984. *Journal of Geophysical Research: Solid Earth*, *90*(B11), 9235-9248.Thielmann, M. & Kaus, B., 2012. Shear heating induced lithospheric-scale localization: does it result in subduction? *Earth planet. Sci. Lett.,* 359-360**,** 1–13.

Thielmann, M., & Kaus, B. J. (2012). Shear heating induced lithospheric-scale localization: Does it result in subduction?. *Earth and Planetary Science Letters*, *359*, 1-13.

Thieulot, C. (2014). ELEFANT: a user-friendly multipurpose geodynamics code. *Solid Earth Discussions*, *6*(2), 1949-2096.

Thompson, D.A., Hammond, J.O.S., Kendall, J.M., Stuart, G.W., Helffrich, G.R., Keir, D., Ayele, A., Goitom, B. (2015). Hydrous upwelling across the mantle transition zone beneath the Afar Triple Junction. *Geochemistry, Geophysics, Geosystems*, *16*(3), 834-846. https://doi.org/10.1002/2014GC005648.

Tugend, J., Gillard, M., Manatschal, G., Nirrengarten, M., Harkin, C., Epin, M. E., ... & Mcdermott, K. (2020). Reappraisal of the magma-rich versus magma-poor rifted margin archetypes. *Geological Society, London, Special Publications*, *476*(1), 23-47.

Turcotte, D.L. & Schubert, G., 2002. *Geodynamics,* 2nd edn, pp. 345, Cambridge.

Turner, S. P., George, R. M. M., Evans, P. J., Hawkesworth, C. J., Zellmer, G. F.(2000). Time-scales of magma formation, ascent and storage beneath subduction-zone volcanoes. *Philosophical Transactions of the Royal Society of London. Series A: Mathematical, Physical and Engineering Sciences*, *358*(1770), 1443-1464. https://doi.org/10.1098/rsta.2000.0598.

Ulmer, P., & Trommsdorff, V. (1995). Serpentine stability to mantle depths and subduction-related magmatism. *Science*, *268*(5212), 858-861.

Uyeda, S. (1987), Chilean vs Mariana type subduction zones with remarks on arc volcanism and collision tectonics, Geological Society of America, 18, 1–7.

Uyeda, S., and H. Kanamori (1979), Back-arc opening and the model of subduction, J. Geophys. Res., 84(8), 1049–1061, doi:10.1029/JB084iB03p01049.

van der Hilst, R. & Seno, T., (1993). Effects of relative plate motion on the deep structure and penetration depth of slabs below the Izu- Bonin and Mariana island arcs, *Earth planet. Sci. Lett.,* 120(3-4), 395–407.

van Dinther, Y., Morra, G., Funiciello, F., & Faccenna, C. (2010). Role of the overriding plate in the subduction process: Insights from numerical models. *Tectonophysics*, *484*(1-4), 74-86.

van Hunen, J., van den Berg, A.P. & Vlaar, N.J., 2001. Latent heat effects of the major mantle phase transitions on low-angle subduction, *Earth planet. Sci. Lett.,* 190**,** 125–135.

van Wijk, J.W., Cloetingh, S.A.P.L., (2002). Basin migration caused by slow lithospheric extension: Earth and Planetary Science Letters, v. 198, p. 275–288, https://doi.org/10.1016/S0012-821X(02)00560-5.

Veizer, J., & Jansen, S. L. (1985). Basement and sedimentary recycling-2: time dimension to global tectonics. *The Journal of Geology*, *93*(6), 625-643.

Von Huene, R., and S. Lallemand (1990), Tectonic erosion along the Japan and Peru convergent margins, Bulletin of the Geological Society of America, 102(6), 704–720, doi: 10.1130/0016 7606(1990)102<0704:TEATJA>2.3.CO;2.

Von Huene, R., and Scholl, D. W. (1991). Observations at convergent margins concerning sediment subduction, subduction erosion, and the growth of continental crust. *Reviews of Geophysics*, *29*(3), 279-316.

Von Huene, R., and Scholl, D. W. (1993). The return of sialic material to the mantle indicated by terrigeneous material subducted at convergent margins. *Tectonophysics*, *219*(1-3), 163-175.

Wada, I., & King, S. (2015). Dynamics of subducting slabs: numerical modeling and constraints from seismology, geoid, topography, geochemistry, and petrology. In *Mantle Dynamics* (pp. 339-391). Elsevier Inc..

Wang, Y., Zhang, L.F., Li, Z.H., Li, Q.Y. & Bader, T. (2019). The exhumation of subducted oceanic derived eclogites: insights from phase equilibrium and thermomechanical.

Watchorn, F., Nichols, G. J., Bosence, D. W. J. (1998). Rift-related sedimentation and stratigraphy, southern Yemen (Gulf of Aden). In *Sedimentation and Tectonics in Rift Basins Red Sea:-Gulf of Aden* (pp. 165-189). Springer, Dordrecht.

Watremez, L., Burov, E., d'Acremont, E., Leroy, S., Huet, B., Le Pourhiet, L., Bellahsen, N. (2013). Buoyancy and localizing properties of continental mantle lithosphere: Insights from thermomechanical models of the eastern Gulf of Aden. *Geochemistry, Geophysics, Geosystems*, *14*(8), 2800-2817. https://doi.org/10.1002/ggge.20179.

Watremez, L., Leroy, S., Rouzo, S., d'Acremont, E., Unternehr, P., Ebinger, C., Lucazeau, F., Al-Lazki, A. (2011). The crustal structure of the north-eastern Gulf of Aden continental margin: insights from wide-angle seismic data. *Geophysical Journal International*, *184*(2), 575-594. https://doi.org/10.1111/j.1365-246X.2010.04881.x.

Watts, A. B., and Talwani, M. (1974). Gravity anomalies seaward of deep-sea trenches and their tectonic implications. *Geophysical Journal International*, *36*(1), 57-90.

Wells, W.C. (Ed.) (1984). Spaceborne gravity gradiometers. NASA Conference Publication 2305, Greenbelt, Maryland.

Wenker, S., Beaumont, C. (2018). Effects of lateral strength contrasts and inherited heterogeneities on necking and rifting of continents. *Tectonophysics*, *746*, 46-63.

Wernicke, B. (1985). Uniform-sense normal simple shear of the continental lithosphere. *canadian Journal of earth sciences*, *22*(1), 108-125.

Wernicke, B. P., England, P. C., Sonder, L. J., & Christiansen, R. L. (1987). Tectonomagmatic evolution of Cenozoic extension in the North American Cordillera. *Geological Society, London, Special Publications*, *28*(1), 203-221.

Wernicke, B. (1981). Low-angle normal faults in the Basin and Range province: nappe tectonics in an extending orogen. Nature 291, 645–647.

Wessel, P., Smith, W. H., Scharroo, R., Luis, J., Wobbe, F. (2013). Generic mapping tools: improved version released. *Eos, Transactions American Geophysical Union*, *94*(45),

White, R., McKenzie, D. (1989). Magmatism at rift zones: the generation of volcanic continental margins and flood basalts. Journal of Geophysical Research 94, 7685e7729.

White, R.S. (1989). Initiation of the Iceland Plume and Opening of the North Atlantic. In: Extensional Tectonics and Stratigraphy of the North Atlantic Margins, pp.149e154.

Williamstown Report (1969). The Terrestrial Environment. In: W. Kaula (ed.). Solid-Earth and Ocean Physics: Application of Space and Astronomic Techniques, Report of a Study at Williamstown, Mass., to the NASA.

Wilson, J.T. (1966). Did the Atlantic close and then re-open? Nature 211, 676–681.

Wilson, M. (1989). Igneous Petrogenesis, A Global Tectonic Approach. Unwin Hyman, London. 466 pp.

Wilson, M. (1993). Magmatism and the geodynamics of basin formation. Sedimentary Geology 86, 5–29.

Wilson, M., Guiraud, R. (1992). Magmatism and rifting in Western and Central Africa, from Late Jurassic to recent times. Tectonophysics 213, 203–225.

Yamato, P., Agard, P., Burov, E., Le Pourhiet, L., Jolivet, L., & Tiberi, C. (2007). Burial and exhumation in a subduction wedge: Mutual constraints from thermomechanical modeling and natural P-T-t data (Schistes Lustrés, western Alps). *Journal of Geophysical Research: Solid Earth*, *112*(B7).

Zalesak, S. (1979). Fully multidimensional flux-corrected transport algorithms for fluids, Journal of computational physics, 31, 335–362.

Zhong, S. & Gurnis, M. (1992). Viscous flow model of a subduction zone with a faulted lithosphere: long and short wavelength topography, gravity and geoid, *Geophys. Res. Lett.,* **19**(18), 1891–1894.

Zhong, S.&Gurnis, M. (1994). Controls on trench topography from dynamic models of subducted slabs, *J. geophys. Res,* 99(15), 15 683–15 695.

Ziegler, P. A., & Cloetingh, S. (2004). Dynamic processes controlling evolution of rifted basins. *Earth-Science Reviews*, *64*(1-2), 1-50.

Zienkiewicz, O. C., and R. L. Taylor (2000). The Finite Element Method Volume 1: The Basis, vol. 1, 708 pp.

A ship in port is safe, but that's not what ships are built for: sail out to sea and do new things."

Grace Hopper